CHARACTERIZATION OF NANOPARTICLE AGGREGATES WITH LIGHT SCATTERING TECHNIQUES

Mariusz Woźniak

AIX-MARSEILLE UNIVERSITY

WROCŁAW UNIVERSITY OF TECHNOLOGY

Doctoral school:

Sciences pour l'Ingénieur: Mécanique, Physique, Micro et Nanoélectronique

PH.D. THESIS COMPLETED IN "COTUTELLE"

Fields: Mechanical-Engineering & Electronics

CHARACTERIZATION OF NANOPARTICLE AGGREGATES WITH LIGHT SCATTERING TECHNIQUES

Presented by

Mariusz WOŹNIAK

Marseille, the 19th October 2012

Composition of the jury:

Gérard GRÉHAN	Director of Research at CNRS, CORIA, University and INSA of Rouen	France	Reviewer
Loïc MÉÈS	Senior researcher at CNRS, LMFA, École Centrale de Lyon	France	Jury member
Janusz MROCZKA	Professor at Wrocław University of Technology, Member of the Polish Academy of Sciences	Poland	Supervisor
Fabrice ONOFRI	Director of Research at CNRS, IUSTI, Aix-Marseille University	France	Supervisor
Janusz SMULKO	Professor at Gdańsk University of Technology	Poland	Reviewer
Brian STOUT	Associate Professor at Institut Fresnel, Aix-Marseille University	France	Jury member
Séverine BARBOSA	Associate Professor at IUSTI, Aix-Marseille University	France	Guest
Alain JALOCHA	Researcher at CILAS, Orléans	France	Guest

Dedicated to my Parents

with love and gratitude

ACKNOWLEDGMENTS

This Ph.D. was completed as a co-shared thesis (French: “Cotutelle”) between the laboratory IUSTI UMR CNRS n°7343, Aix-Marseille University in Marseille, France, and the Chair of Electronic and Photonic Metrology Wrocław University of Technology in Wrocław, Poland. My work was supported by a Ph.D. grant from the French Embassy in Poland and by the Wrocław University of Technology. It was also embedded in the “ANR CARMINA” project performed in a collaboration with various laboratories and institutes (IUSTI – Aix-Marseille University, CORIA – University of Rouen, GREMI – University of Orleans, IRFM CEA – Cadarache). Therefore, I express my gratitude to all of these entities and agencies for their support to my work.

I would like to show my appreciation to the members of the jury who have accepted to evaluate this work, and more particularly the two reviewers Professor Janusz Smulko and Dr. Gérard Gréhan, as well as to the other members of the jury: Dr. Brian Stout, Dr. Loïc Méès, Dr. Séverine Barbosa and Dr. Alain Jalocha.

I am indebted to my two supervisors for all their support. Namely, to Professor Janusz Mroczka for his help during my stay in Poland, for introducing me to Dr. Fabrice Onofri and giving me opportunity to accomplish this Ph.D. in the framework of “Cotutelle”. I express my gratitude to Dr. Fabrice Onofri for welcoming me in France, supporting me scientifically during my research, as well as for introducing me to French culture.

I would like to acknowledge Professor Laifa Boufendi and his research group (GREMI UMR n°6606 CNRS, University of Orleans) for our cooperation on dusty plasmas. Particularly, for providing access to the plasma reactor and the reference data obtained by electron microscopy.

I acknowledge Dr. Jérôme Yon and his research group (UMR n°6614 CORIA, University and INSA of Rouen, France) for providing test sample of numerically generated DLCA aggregates and experimental raw data of diesel soot aggregates, as well as for the helpful information related to their analysis.

Sharing my time between France and Poland I met a lot of people who supported me every day. Therefore, I would like to express my gratitude to all my colleagues and employees of IUSTI and CEPM laboratories for all their help during my Ph.D. research.

Finally, for more reasons than one, I could not have completed my work without support of my loving family, especially my parents, my two brothers and my sisters-in-law.

The intellectual properties and the value of the intellectual properties of the work presented in this manuscript are equally divided between the Chair of Electronic and Photonic Metrology Wrocław University of Technology and the laboratory IUSTI UMR CNRS n°7343, Aix-Marseille University.

TABLE OF CONTENTS

LIST OF SYMBOLS AND ABBREVIATIONS

Symbols

δ_{TEM}	the mean background noise and TEM image offset
λ_0	laser wavelength in air
λ	laser wavelength in the considered medium
θ	scattering angle
σ_x	standard deviation of x-value
σ_p	standard deviation of particle radius
a	subscript for aggregate
C_n	particle concentration in number
C_v	particle concentration in volume
C_x	cross section (x = absorption, scattering or extinction)
$C_{\upsilon\kappa}^{2D}$, $C_{\upsilon\kappa}^{3D}$	2 and 3-dimensional overlapping factor of primary particles (monomers) in the aggregate
$d_{\upsilon\kappa}^{2D}$, $d_{\upsilon\kappa}^{3D}$	2 and 3-diemensional distance between centers of mass of primary particles (monomers)
d_p	diameter of a single particle (monomer), $d_p = 2r_p$
D_f	fractal dimension of the aggregate
g	gain of the optical conversion and imaging system
$G\left(k, R_g, D_f\right)$	structure factor
i	complex number
I	scattering intensity
I_0	incident beam intensity
$I(q)$	experimentally measured optical structure factor (OSF) of fractal-like aggregate
k	wave number $k = 2\pi/\lambda$
k_B	Boltzmann constant $k_B \approx 1.381\times10^{-23}$ $[JK^{-1}]$
k_f	fractal prefactor of the aggregate
k_p	imaginary part of particle (monomer) refractive index at λ_0 $(k_p \geq 0)$
K_m	electron path length within external medium
K_p	electron path length within particles (monomers)
L	length of the experimental setup
L^{2D}	length of the 2D projection of the aggregate

L^{3D}	total length of the aggregate in 3D space
m_e	real refractive index of the external medium for λ_0
$\tilde{m}_p$	complex refractive index of particles (monomers) at λ_0
m_p	real part of the particle (monomer) refractive index at λ_0
M_1, M_2	the first and the second momentum (i.e. mean value and variance) of the distribution of the number of monomers within aggregates
n_p	number of particles within an aggregate
p	subscript for particles (monomers)
q	magnitude of the scattering (wave) vector, $q = 2k\sin(\theta/2)$
Q_x	cross sections efficiency (x = absorption, scattering or extinction)
r_p	radius of a single particle (monomer)
R_b	minimum bounding sphere enclosing aggregate
R_e	external boundary sphere used in the DLA algorithm
R_g	radius of gyration of the aggregate
R_p	appearance sphere used in the DLA algorithm
R_S	radius in surface – radius of the sphere with surface equivalent to the one of the aggregate (or particle)
R_v	radius in volume – radius of the sphere with volume equivalent to the one of the aggregate (or particle)
$S(q)$	structure factor of fractal-like aggregate
$T(\lambda_i)$	beam transmission for λ_i wavelength
W^{2D}	width of the 2D projection of the aggregate
W^{3D}	total width of the aggregate in 3D space
x_p	size parameter (i.e. Mie parameter), $x_p = 2\pi r_p / \lambda$

Abbreviations and acronyms

abs	subscript for absorption (cross section, efficiency, etc.)
ext	subscript for extinction (cross section, efficiency, etc.)
sca	subscript for scattering (cross section, efficiency, etc.)
DLA	Diffusion Limited Aggregation
DLCA	Diffusion Limited Cluster Aggregation
HC	hexagonal close packed aggregate (hexagonal compact)
LES	Light Extinction Spectrometry

LMT	Lorenz-Mie Theory
Log.-Norm.	Log-Normal size distribution
LSQ	Least Square method
MBC	Modified Box-Counting
MBR	Minimum Bounding Rectangle
OSF	Optical Structure Factor
PDF	Probability Density Function
PSD	Particle Size Distribution
RGD	Rayleigh-Gans-Debye Theory
RDG-FA	Rayleigh-Debye-Gans Theory for Fractal Aggregates
RLCA	Reaction Limited Colloid Aggregation
SEM	Scanning Electron Microscopy
TEM	Transmission Electron Microscopy
T-M	T-Matrix Theory (method)

Chapter 1

INTRODUCTION

Undoubtedly, people have always been exposed to various nanoparticles via numerous natural phenomena, e.g. dust storms, volcanic ash, combustion, water evaporation, etc. At the same time, the human body has evolved to protect itself from potentially harmful influence of nanoparticles. However, from the technological point of view, for a long time we were not able to detect, control or use nanoparticles to any industrial application. The situation had changed with rapidly developing technologies in the last decades of the 20^{th} century.

Nowadays, nanoparticles and aggregates of nanoparticles are the subject of intensive research due to their unusual physical properties and potential technological impact. Basically, there are two primary factors that makes nanoparticles significantly different comparing to the bulk materials: surface effects and quantum effects (Buzea et al. 2007). Both of them influence any aspects related to the nanoparticles i.e. their chemical reactivity, mechanical, optical, electric and magnetic properties. In the same way, nanoparticles exhibit additional interesting and completely new properties, like strong ionic forces, unusual thermal diffusion or surface plasmons effects. They are also the subject of environmental and health concerns. Figure 1.1 shows some examples of nanoparticle aggregates encountered in various fields.

The surface effects are related to the fraction of atoms at the surface, which for nanomaterials is thousands of times larger than for the bulk ones. As an example, if we consider a single carbon microparticle with $60\,\mu m$ in diameter and $0.3\,\mu g$ mass, its surface area is equal to $0.01\,mm^2$ (Buzea et al. 2007). To have the same mass in carbon nanoparticles with diameter $60\,nm$ we need to take 1 billion particles. Their surface area is $11.3\,mm^2$ giving the ratio surface area to the particles volume around 1000 times higher than for the single microparticle. As the particles reactivity is more and less determined by their surface, we can

clearly see that reactivity of nanoparticles increases significantly comparing to the ordinary bulk materials, even at the microscale.

The quantum effects are related to the size of particles and appear as a sets of phenomena that are typical for single atoms rather than for particles or molecules (Roduner 2006). For instance, similarly as electrons in a single atom, quantum dots shows quantized energy spectra due to the electrons confinement. They demonstrate also quantified changes in their ability to accept or donate electrical charges. Yet another interesting result of the quantum confinement effect is that magnetic moments appear in nanoparticles of chemical compounds that are non-magnetic at a macroscale, e.g. gold, or platinum (Buzea et al. 2007).

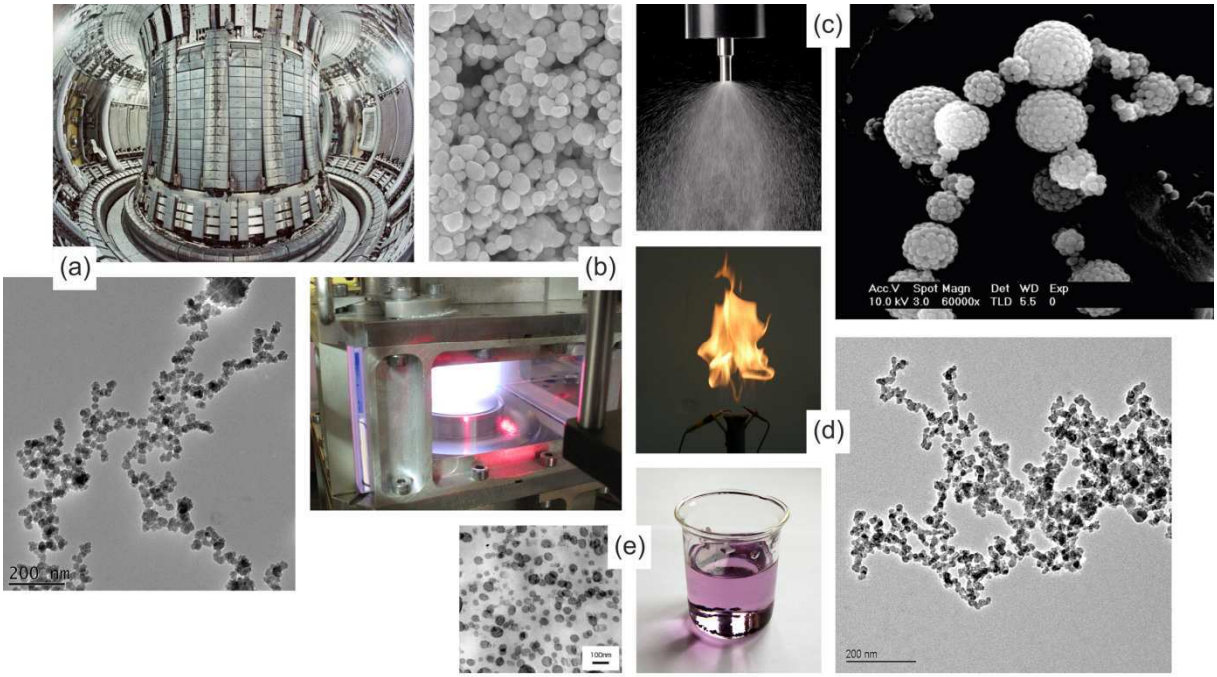

Figure 1.1. Nanoparticles in various fields: (a) thermonuclear reactor and dust produced during the nuclear reaction, (b) plasma reactor and nanopowder, (c) nozzle to produce aerosols with spray drying method and highly-ordered Buckyballs aggregates, (d) flame and soot, (e) suspension and aggregation.

All the aforementioned issues cause that ultra-fine dry powders (nanometer-sized aggregates, ceramics and crystals, quantum dots), nano-colloidal suspensions (slurries, nanofluids, emulsions, gels) or nano-sized aerosols (various dusts, fine-droplet liquid paints, carbonaceous aggregates) are the milestones of the future science.

As already pointed out above, nanoparticles and aggregates of nanoparticles are highly interesting from the scientific and technological points of view. Nonetheless, to understand, to monitor and to control their properties and formation mechanisms in various systems, it is fundamental to access to key parameters like particle size distribution (PSD) and particle number concentration (C_n). But, this is precisely a challenge from the metrological and experimental points of view. Sampling and off-line analyses (e.g. electron microscopy, electro-mobility, etc.) are the most widely used methods to characterize properties of nano

and microparticles (i.e. size, shape, elementary composition and specific surface area). However, for so reactive and fragile objects, the reliability and repeatability of such analyses may be questionable. For instance, the sampling procedure can be biased by the particle flow-field dynamics or the smallest particles can remain trapped in micro roughness of the sampling tool or the substract (like in tokamaks). Apart from that, aggregates can be broken down due to the rolling and collapsing effects or by the sampling procedure itself. For all the above mentioned reasons, optical particle sizing techniques appear to be very suitable for the in-situ and the in-line characterization of the morphological properties of nanoparticle systems.

Various optical methods have been developed to characterize particle systems, e.g. (Xu 2002). However, using them to characterize complex particles is not an easy and trivial task. In the next paragraphs, to illustrate our purposes, the advantage and limits of four optical techniques used to characterize nanoparticles form in combustion and plasma systems are briefly reviewed.

- *Particle Imaging Velocimetry* (PIV) and *Particle Tracking Velocimetry* (PTV) techniques (Stanislas et al. 2004) allow to measure the velocity of submicron particles. Both techniques relies on the illumination of the particle flow by two intense and successive pulsed laser sheets. The particles "image", recorded by a CCD camera localized at $\theta = 90°$, is just a bright spot whose size depends only on the point spread function (PSF) (Goodman 1996) of the imaging system. Using short time pulses (a few nanoseconds with a YAG laser) and a short time delays between the two successive pulses and images (down to few hundred nanoseconds with a typical PIV/PTV camera) allow to freeze particle motion and to measure velocities up to several hundred meters per second.

The only difference between PIV and PTV relies on the numerical algorithm used to obtain the velocity field. PIV estimates this field by measuring the global displacement of all particles within small interrogation windows (i.e. raw PIV images are meshed). Thus, based on a local flow field continuity assumption, PIV provides an Eulerian description of particulate media. On the other hand, PTV tracks each particle motion, providing an Lagrangian description of the particulate media (e.g. (Ouellette et al. 2006)). Therefore, PTV appears to be more appropriate for analyzing the spatial distribution of particles or particle properties linked to their charge and dynamics. Particle imaging techniques are basically constrained by the diffraction limit (Goodman 1996), making it impossible to image the surface and structure of sub-micron aggregates. Indeed, depth of view, optical magnification and aberrations, pixel size, particle size and refractive index, are also fundamental parameters that limit imaging technique capabilities.

However, imaging techniques can be used to characterize the size and the velocity of larger particles (see Figure 1.2 (a)). For this purpose, the PTV system must be operated in a *backlight* mode. In that configuration, the flow field is backlighted by a collimated beam,

produced by a double pulse flash lamp or a laser. When a laser is used, a diffusion plate or a fluorescence cell must be used to decrease the speckle noise level (Guenadou et al. 2008). The CCD camera is equipped with high magnification optics and placed in front of the lighting beam (i.e. $\theta = 0°$). With conventional systems, the minimum particle size that can be "measured" is $\approx 4\ \mu m$ for a working distance of $\approx 4\ mm$ and a field of view of $\approx 400 \times 400\ \mu m^2$. These techniques have been extensively used to infer the size of nanoparticles in colloids or fusion plasmas (where the nanoparticles inter-distances or velocities are connected to their electrical charge, and then, their size) but they are not really of practical use for other systems (see Table 1.1) (Onofri et al. 2011b).

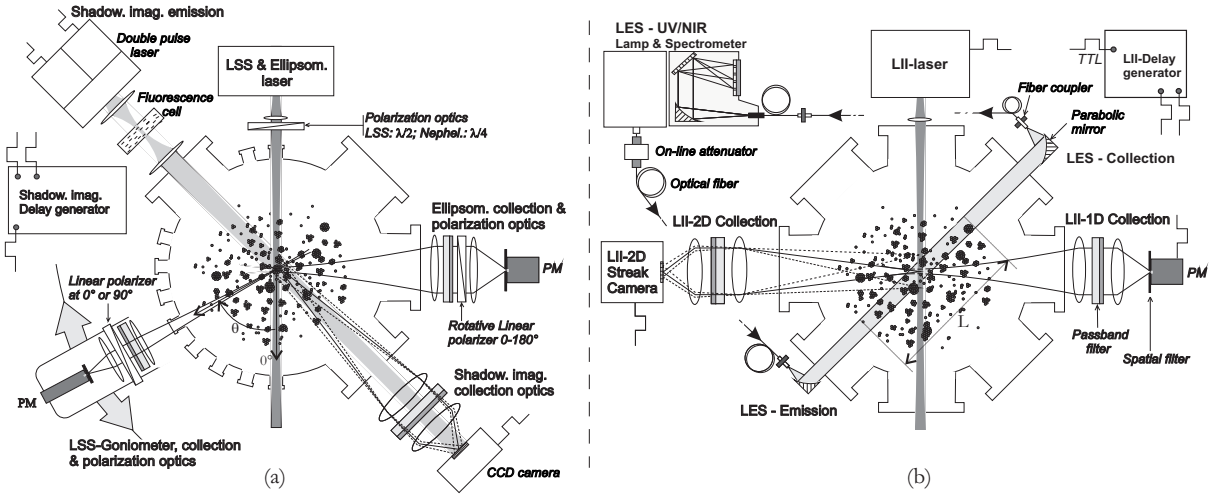

Figure 1.2. Basic experimental optical setups for (a) Shadowgraph imaging, Laser Light Scattering (LSS) and Ellipsometry techniques; (b) Light Extinction Spectroscopy (LES) and Laser Induced Incandescence (LII) techniques (Onofri et al. 2011b).

- *Laser Induced Incandescence (LII)* occurs when a laser beam encounters solid absorbing particles (Melton 1984; Schulz et al. 2006; Michelsen et al. 2007; Vander-Wal 2009). The absorbed energy causes an increase of the particle temperature. Simultaneously, particles lose energy via heat transfer with their surrounding. If the energy absorption rate is sufficiently high, the temperature can reach high levels where significant incandescence (essentially blackbody emission) and vaporization phenomena can occur. The inversion of the LII signal intensity and time-decay is done with a PSD model assumption, allowing the determination of the volume concentration and the mean size of all single particles (referred also as monomers) and all small aggregates within the measurement volume. It can be a local (the detector is a photomultiplier, PM) or a 2D measurement (the detector is a streak camera, with a time resolution of a few nanoseconds (De-Iuliis et al. 2005; Desgroux et al. 2008)), see Figure 1.2 (b). The LII basic setup is then composed of a pulsed laser, a focusing optics, a collection (1D) or an imaging optics. Although, this technique is still under development, it has been used with success in combustion science (i.e. to characterize soots). It is however

fundamentally limited to extremely small absorbing particles at low concentration (see Table 1.1).

- *The Laser Light Scattering (LLS)* (referred also as the Nepholometry technique) analyzes the angular scattering patterns produced by a sample of particles illuminated by focused and continuous laser beam, randomly or a linearly polarized (Xu 2002).

A LLS setup is generally, and basically, composed of a set of lenses, an interference filter centered onto the laser wavelength (to attenuate the optical background noise), a linear polarizer (to select parallel or/and perpendicular polarization), a spatial filter (to control the probe volume size) and a photomultiplier, see Figure 1.2 (a). Like most optical particle characterization techniques, LLS technique is limited to optically diluted particle systems although solutions have been proposed to correct multiple scattering effects with optical methods (Meyer et al. 1997; Onofri et al. 1999) or data inversion (Mokhtari et al. 2005; Tamanai et al. 2006). The main drawbacks of the LSS are that it cannot perform absolute particle concentration measurements, it requires wide optical accesses and a stationary process (i.e. regarding the scanning time). However, the LSS has two clear advantages: like the LII technique, it allows the detection of extremely small particles (e.g. monomers) at low concentration and, in addition, scattering diagrams are very sensitive to the morphology of aggregates (see Table 1.1 and reference (Onofri et al. 2011b) for additional inputs).

Table 1.1. Summary of key features of the various optical techniques.

Technique	Shadow-imag.	LES	LII	LSS	Ellipsometry
Illumination system	Flash lamp, pulsed laser and flurosc. cell, 0.1-100 *mJ*	Stabilized thermal source, 5-20 *W*	Pulsed laser, 50-700 mJ/cm^2	continuous wave laser, 0.5-5 *W*	continuous wave laser, 0.5-5 *W*
Detection system	CCD camera	Spectrometer	PM or streak camera	Rotat. system, PM and polarizer	PM with rotat. polarizer
Size range	$\approx 4\ \mu m$ to *cm*	10 *nm* – 2 μm	2 *nm* – 0.5 μm	10 *nm* – 2 *mm*	10 *nm* – 2 μm
Concentration	Relative	Absolute	Relative	Relative	Relative
Probe volume	Slab, $10^{-2}\ mm^3$ – $10^2\ cm^3$	Cylinder, cm^3 – $10^4\ cm^3$	Cubic or Slab, $10^{-3}\ mm^3$ – cm^3	Cubic, $10^{-3}\ mm^3$ – cm^3	Cubic, $10^{-3}\ mm^3$ – cm^3
Main advantage	Flow pattern size-velocity	Limited access, long distance	Low concentration	Fractal dimension, low concentration	Morphology, low concentration
Main drawbacks	Only large par. depth of view, speckle noise	Particle material spectrum needed	Only monomers and dilute aggregates	Wide optical access needed, Stationary flow	Stationary flow, Local meas.

- *Ellipsometry* infers the properties of particles from their ability to modify the polarization state of the scattered light. For this purpose a continuous wave (CW) laser is used

to produce a focused and polarized beam (i.e. circularly or linearly) that illuminates the particles within a small probe volume, see Figure 1.2 (a). Like the LSS, and for the same reasons, the collection optics is composed of a set of lenses, an interference filter, a spatial filter and a photomultiplier. Ellipsometry collection optics is ordinarily set at $\theta = 90°$, and it integrates a computer controlled polarizing optics (e.g. a linear polarizer fixed on a motorized goniometer, or a liquid crystal linear polarizer). In most studies, the latter component is simply used to analyze the light polarization phase-angle ψ and amplitude Δ (e.g. (Hong and Winter 2006)). Based on the Lorenz-Mie calculations, the inversion procedure consists on searching for the particle mean diameter and refractive index that allow to minimize differences observed between the theoretical and experimental values of ψ and Δ (Mishchenko et al. 2000). Indeed, light polarization is very sensitive to particle roughness and heterogeneity, making polarization techniques suitable for particle morphology investigations provided that an appropriate scattering models (like the T-Matrix or the DDA ones) is used. Among the drawbacks of this technique there is the fact that the measurement is local and that it requires well defined optical accesses, see Table 1.1 (Onofri et al. 2011b). The latter constraint make this technique totally unsuitable to characterize, for instance, dust in fusion devices.

One can conclude that very few methods allow the in-situ and time-resolved analysis, with limited optical accesses, of nanoparticle systems, and if there are, they usually use too simple light scattering model and inversion technique.

So that, the goal of this Ph.D. work was to contribute to the development of the two aforementioned optical methods: the Light Extinction Spectrometry (LES) and the Laser Light Scattering (LLS), and this, by using realistic and as accurate as possible particle and light scattering models, by developing dedicated inversion methods and validation experiments. All this work has been done with the objective to propose in fine an optical diagnosis that can be used both to perform laboratory experiments (mainly on colloidal suspensions) and experiments at long distance (fusion devices, aerosols, combustion).

Chapter 2 introduces the particle models we have developed to describes the morphology of two types of nanoparticle aggregates of interest, and with a fractal-like (plasmas, combustion systems) and buckyballs-like (aerosols, suspensions) shapes.

Chapter 3 summarize all the work done to determine the morphological parameters of fractal-like aggregates from electron microscopy images.

Chapter 4 reviews and discuss the physical and mathematical backgrounds of all the theories used in this work to predict the light scattering properties of nanoparticle and their aggregates: Lorenz-Mie theory, Rayleigh-based approximations (RGD, RDG-FA) and T-Matrix method.

Chapter 5 presents the algorithms and results obtained for the extraction of the morphological parameters of fractal aggregates from their scattering diagrams, the influence of single particles or the superposition of different populations of aggregates.

Chapter 6 details the basic principles as well as inversion techniques of extinction data recorded for fractal-like and buckyballs-like aggregates. Various experimental systems are considered and analyzed: aerosol of silica nanobeads and tungsten aggregates, dusty plasmas with silicone aggregates.

Chapter 7 is a general conclusion with perspectives for this work.

Chapter 8 contains references.

Chapter 9 and 10 are extended abstracts of this work, in French and in Polish languages respectively.

Chapter 2

MODELS FOR PARTICLE AGGREGATES

2.1. Introduction

Aggregation of nanoparticles occurs in numerous media and it has significant influence on the overall properties of the particle systems. For instance, although the chemical reactions and physical processes governing combustion systems, dusty plasmas or colloidal suspensions may be considered as rather different, they can lead to the formation of aggregates of nanoparticles with similar shapes. Nevertheless, from one case to another, the clusters may exhibit highly different dimensions or morphological properties. For example, they may contain from a few primary particles (called also monomers) up to several thousands of them. They may also take various shapes: from the dilute chain-like formations (Kim et al. 2003), through the typical fractal-like aggregates (Sorensen 2001), up to the dense and opaque cauliflower-like structures (Sharpe et al. 2003; Onofri et al. 2011b). To describe very dense and highly opaque aggregates with an overall shape close to the spherical one, buckyballs model (see section 2.5) (Toure 2010) may be applied. For highly ordered crystal structures one can also use hexagonal compact particle model (Holland et al. 1998).

The chapter is organized as follows. Section 2.2 presents a simplified overview of the physical background of the aggregation phenomena for colloidal suspensions according to the DLVO model. Section 2.3 is devoted to the numerical algorithm of the Diffusion Limited Aggregation (DLA) we have developed to reproduce the morphology of fractal-like aggregates. Section 2.4 compares DLA aggregates produced with our tunable algorithm with numerically generated DLCA aggregates provided by Dr. Jérôme Yon. Section 2.5 describes a mathematical and physical model to reproduce the morphology of highly ordered aggregates.

2.2. Physical basis of the aggregation in colloidal suspensions

2.2.1. Aggregation regimes

To characterize particle motion in a medium, the most commonly used parameter is the Knudsen number. It combines the mean free path l and the radius r_p of the particle:

$$Kn = \frac{l}{r_p}. \tag{2.1}$$

We define also the diffusion Knudsen number as $Kn_D = l_p / r_p$, where l_p is the persistence length of the particle (i.e. the distance over which a particle moves effectively in a straight line). Depending on the values of the Knudsen number, three different aggregation regimes are defined (Pierce et al. 2006): the "continuum regime" (referred also as the "Stokes" or "hydrodynamic regime", $Kn \ll 1$), the intermediate regime (called also the "slip regime", $Kn \sim 0$) and the "free molecular regime" ($Kn \gg 1$).

Most aggregation studies have been carried out in the continuum regime ($Kn \ll 1$), where particles motion between collisions is diffusive. This regime refers to aggregation in colloidal liquid suspensions or aerosols at low temperature and high pressure. In the continuum regime each particle experience a drag force that, for spherical particles, can be calculated as:

$$f = 6\pi\eta r_p, \tag{2.2}$$

where η is the dynamic viscosity of the medium. The diffusion constant for spherical particles is described by the Stokes-Einstein equation (Pierce et al. 2006):

$$D_{SE} = \frac{k_B T}{6\pi\eta r_p}, \tag{2.3}$$

where k_B is Boltzmann's constant and T is the medium temperature.

In the free molecular regime ($Kn \gg 1$) monomers have a similar mean free path as the molecules of the surrounding medium and the distance between monomers is significantly large. Due to the law describing the drag force of particles, this region is also called the Epstein regime. In this regime, the drag force of a single monomer is:

$$f = \frac{8}{3} r_p^2 \rho \left(\frac{2\pi k_B T}{m_m} \right)^{1/2} \left(1 + \frac{\beta_m \pi}{8} \right), \tag{2.4}$$

where ρ is the medium mass density, m_m is the molecular mass of the particles and β_m is the momentum accommodation coefficient. In the free molecular regime monomers move either ballistically or diffusively (Meakin 1984; Stasio et al. 2002; Babu et al. 2008). Usually, the limit between the diffusive and the ballistic motion, is found for diffusion Knudsen number smaller than $Kn_D \approx 1$. In that case, the diffusion constant is given by (Pierce et al. 2006):

$$D_{Ep} = \frac{3}{8\rho r_p^2}\left(\frac{m_m k_B T}{2\pi}\right)^{1/2}\left(1+\frac{\pi}{8}\beta_m\right)^{-1}. \tag{2.5}$$

During the ballistic motion the root mean square velocity of the monomers with mass m can be calculated as (Pierce et al. 2006):

$$v = \left(\frac{3k_B T}{m}\right)^{1/2}. \tag{2.6}$$

The intermediate regime (slip regime) is observed for $0.1 \le Kn \le 10$ (Pierce et al. 2006). Particles motion in this regime may be described introducing the Cunningham correction $C(Kn)$ into the Stokes-Einstein equations. Therefore, the diffusion constant is given as:

$$D = D_{SE} C(Kn), \tag{2.7}$$

with the corresponding drag force:

$$f = \frac{6\pi\eta r_p}{C(Kn)}. \tag{2.8}$$

Eqs. (2.1) – (2.8) refer to a single particle in various aggregation regimes. Nevertheless, they can be also apply to fractal aggregates. To do so, one must take into account that fractal aggregates are ramified, so to estimate the drag force or the diffusion constant, we must introduce the effective mobility radius R_m. In that case, regardless of the aggregate morphology, we can use Eqs. (2.1) – (2.8) with the R_m instead of the r_p.

2.2.2. Aggregation models (DLA, DLCA, RLCA)

In colloidal suspensions particles remain in a constant motion caused by the molecular collisions. This phenomenon, studied independently by Albert Einstein (1905) (Einstein 1956) and Marian Smoluchowski (1906) (Smoluchowski 1906), is widely known as the Brownian motion. Each particle experience a random walk like the one simulated on Figure 2.1. The latter figure shows 5000 steps of the motion of a single monomer in 3-dimensional space. Length scale in the presented figure is normalized by the step increment of the particle (i.e. increment step is equal to 1).

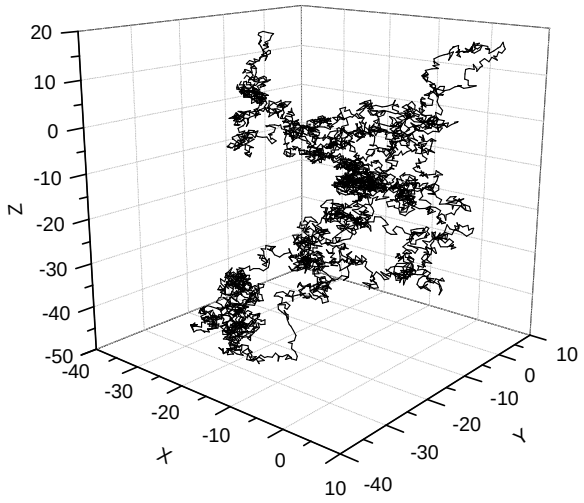

Figure 2.1. Simulated Brownian motion: 5000 steps of a single monomer in a 3-dimensional space (increment step equal to 1).

According to the DLVO model, the suspension remains stable against the aggregation (Lin et al. 1989), if the repulsive energy barrier caused by the electrostatic forces is much greater than $k_B T$ (where k_B is the Boltzmann constant and T is the temperature). In that case attractive, short-range van der Waals forces (proportional to the $1/r^6$, where r is a distance from the particle) are much weaker than the repulsive long-range, electrostatic forces between monomers (proportional to the $1/r^2$). To make the suspension unstable and hence trigger aggregation phenomena, we can modify the ionic balance of the system by changing the pH (neutralize the surface charges of the particles) adding tensio-actives to reduce the range of the electrostatic forces, etc. When the attractive van der Waals forces are no more balanced – they predominate causing aggregation. For dilute particle system the dynamics of this aggregation process is fundamentally limited by the ability of the primary particles to diffuse within the continuous medium, so that it is usually referenced as the Diffusion Limited Aggregation (DLA, e.g. (Witten and Sander 1981; Jullien and Botet 1987)). In that case, due to large distances between particles, diffusion of aggregates within a continuous medium is negligible. It is important to notice that in the suspension where repulsive energy barrier is greater than several $k_B T$ particles are still able to stick together but significant number of collisions is necessary. This is the fundamental requirement for the Reaction-Limited Colloid Aggregation (RLCA) (Lin et al. 1989). In contradiction to that, for the DLA process probability that two colliding particles stick together is close to unity. During the aggregation not only single monomers but also previously formed aggregates may collide. The process in which the DLA phenomena and clusterization occur simultaneously is called the Diffusion-Limited Cluster Aggregation (DLCA, e.g. (Weitz et al. 1985; Tang et al. 2000; Babu et al. 2008)). Its dynamics is limited by the ability of the previously formed clusters to diffuse within the continuous medium.

In the current part of this work, to generate synthetic aggregates, an fully adjustable (tunable) DLA-type code has been developed rather than a DLCA one. The main reason for that is that presented research requires aggregates with precisely defined parameters, strict self-similarity and thus scale-invariant properties (Theiler 1990). This requirement is not precisely satisfied for small aggregates produced in DLCA model (i.e. the power law nature of Eq. (2.13) is not satisfied) (Heinson et al. 2010). Furthermore, DLCA models should take into account physical (e.g. van der Waals', Coulomb's forces), mechanical (e.g. excluded volume, entanglement) and chemical (e.g. sintering, bonding) interactions and mechanisms that are not yet fully understood. But this is not the case as most DLCA as well as DLA models described in the literature assume only random motion of monomers and an irreversible sticking after their collision. They do not require any initial constraints regarding fractal dimension, fractal prefactor or number of monomers within aggregates. When simulation process is completed, the fractal parameters of the generated aggregates may be calculated.

The biggest advantage of the tunable DLA code developed in the current work is that it preserves all the fractal parameters (with a given accuracy) at each step of the aggregation process. This allows to avoid generation of multi-fractal aggregates (i.e. aggregates with different parameters at different scale or in a different part of the particle) and assures reliability and repeatability of the results. The detailed description of the DLA software and algorithm applied in this work can be found in section 2.3.

2.2.3. Scaling law for the aggregate growth rate

A complete characterization of the aggregating system requires to define aggregation kinetics and the structure of the growing aggregate. The cluster-cluster aggregation kinetics is governed by Smoluchowski equation (Zift et al. 1985). For sufficiently dilute systems of monodisperse monomers the Smoluchowski equation may be expressed in the relatively simple form (Sorensen et al. 1998; Stasio et al. 2002):

$$\frac{dC_n}{dt} = -\frac{1}{2} K_c C_n^2, \tag{2.9}$$

where K_c is the aggregation kernel, which specifies the aggregation rates, and C_n is the particle number concentration. The aggregate structure is well described by the number of monomers n_p, their mean radius $\bar{r}_p$ and the related PSD, as well as the fractal parameters: D_f, k_f and R_g (see Eq. (2.13) and description later on).

The aggregation kinetics may be characterized by the time evolution of the average mass of the aggregate $\bar{m} \sim t^z$. For the DLCA in colloidal suspension, the linear dependency of the aggregation kinetics was observed (Lin et al. 1989), so that $z=1$ and $\bar{m} = (t/t_0)^z$. Characteristic time t_0 is given by $t_0 = 3\eta / (8 k_B T C_{n,0})$, where η is the dynamic viscosity of the fluid and $C_{n,0}$ is the initial particle concentration. The aggregate mass distribution during the aggregation process may be found analytically using the Smoluchowski rate equations (Cohen

and Benedek 1982) which, with a good approximation, leads to the solution expressed by the following exponential form:

$$n(m) = \frac{n_a}{\bar{m}}\left(1 - \frac{1}{\bar{m}}\right)^{m-1}, \tag{2.10}$$

where $n_a = \sum n(m)$ is the total number of aggregates and $\bar{m} = \sum mn(m)/n_a$ is the mean mass of the aggregates.

Although there are initial similarities between the diffusion-limited and the reaction-limited cluster aggregation phenomena, both processes appear to be considerably different. The time evolution of the average mass of the aggregate in the RLCA is defined as $\bar{m} \sim e^{At}$, where A is a constant dependent on the sticking probability and the time between collisions of monomers. On the other way, the solution of Smoluchowski equations is given as:

$$n(m) \sim \bar{m}^{-\tau} e^{-m/m_c}, \tag{2.11}$$

where τ is a constant evaluated analytically, numerically and experimentally in the range $\tau = 1.5 - 1.9$ (Lin et al. 1989).

2.3. DLA aggregates

We define here aggregates as objects made of small elementary particles (monomers) that are stuck together and form a larger structure. It was shown that to describe and analyze aggregated particles we can apply the fractal-like model (Witten and Sander 1981). Its main concept is based on the self-similarity and structure invariance at each scale. The fractal theory may be applied regardless of the particular aggregation phenomena and specific conditions that have led to the cluster formation (Weitz and Oliveria 1984). Following this approach, in the fractal-like model the mass of the cluster M and its spatial dimension L, may be simply related as:

$$M \sim L^D, \tag{2.12}$$

where D is the Hausdorff or the so-called fractal dimension. It is always smaller than the Euclidian dimension. This relation describes the basic concept of the fractal-like aggregates and it is the fundamental dependency applied in the further morphological analysis.

2.3.1. Numerical model and algorithm of DLA aggregates

To define mathematically, and by a limited number of parameters, the morphology of particle aggregates, the so-called fractal equation (Forrest and Witten 1979; Bau et al. 2010) is commonly used:

$$n_p = k_f \left(\frac{R_g}{r_p}\right)^{D_f}, \tag{2.13}$$

where n_p and r_p represent respectively the number and the mean radius of the primary particles (monomers), D_f and R_g are the fractal dimension and the radius of gyration of the aggregate, and k_f is called the fractal prefactor (or structural coefficient).

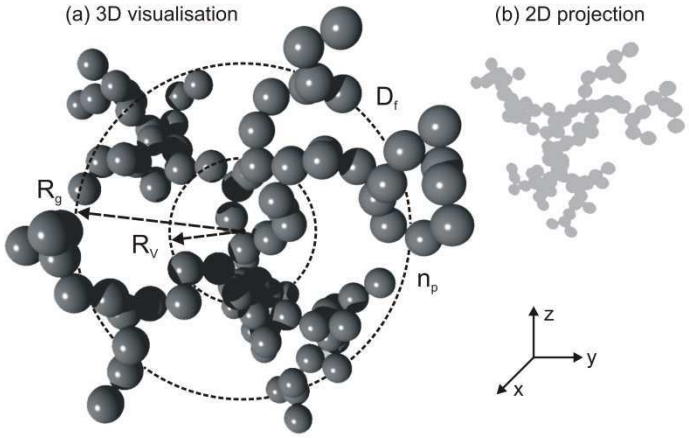

Figure 2.2. Numerically generated fractal aggregate with parameters: $n_p = 100$, $D_f = 1.80$, $k_f = 1.593$, $R_g = 9.97$, $R_v = 4.64$: (a) 3D rendering with POV-Ray software, (b) 2D projection of the aggregate.

As an example, Figure 2.2 (a) shows a 3D visualization (created with the POV-Ray software (POV-Ray 2004)) of the aggregate defined by $n_p = 100$ monomers, fractal dimension $D_f = 1.80$, fractal prefactor $k_f = 1.593$, radius of gyration $R_g = 9.97$ and equivalent radius in volume $R_v = 4.46$. Figure 2.2 (b) shows a 2D projection (the image of the aggregate as it is obtained in the zy plane).

In Eq. (2.13), and more particularly in this work, the fractal dimension and the radius of gyration are thought to be the key parameters to describe the morphology of aggregates. To define the radius of gyration, the centre of mass of the aggregate (x_a, y_a, z_a) must be previously specified. For the group of particles it may be defined as follows:

$$(x_a, y_a, z_a) = \frac{1}{\sum_{n=1}^{n_p} m_n}\left(\sum_{n=1}^{n_p} x_n m_n, \sum_{n=1}^{n_p} y_n m_n, \sum_{n=1}^{n_p} z_n m_n\right), \tag{2.14}$$

where (x_n, y_n, z_n) is the vector pointing to the $n-th$ particle with mass m_n. If we assume that all particles have the same unitary mass and radius m_0 and r_0 respectively, we can define the mass of the $n-th$ particle with radius $r_{p,n}$ as $m_n = m_0 r_{p,n}{}^3$. Using this assumption we can eliminate the mass of the particles in Eq. (2.14). The position of the centre of mass is now defined, so we can calculate the aggregate's radius of gyration. The latter quantity characterize the spatial distribution of mass in the aggregate. It is defined as a mean square distance of the particles from the centre of mass:

$$R_g = \sqrt{\frac{1}{n_p}\sum_{n=1}^{n_p}(\mathbf{r_0} - \mathbf{r_n})^2}, \tag{2.15}$$

where in the classical laboratory Cartesian and Spherical Coordinate Systems (x, y, z) and (r, θ, φ), $\mathbf{r_n}$ and $\mathbf{r_0}$ are vectors pointing respectively the $n-th$ particle and the centre of mass of the aggregate with radius of gyration R_g.

2.3.1.1. Aggregation algorithm

Figure 2.3 shows a flow chart of the DLA algorithm. An overview diagram of the geometry of the DLA algorithm is shown in Figure 2.4 (a). In the aggregation process all the primary particles are generated successively at a large distance R_p (also called appearance sphere) from the centre of mass of the aggregating cluster:

$$R_p \gg R_{g,n_p}, \tag{2.16}$$

where R_{g,n_p} describes the temporary radius of gyration of the growing aggregate. If during its random march the new particle moves out of the external boundary sphere with radius R_e, the particle is rejected and another particle is generated at the distance R_p. The definition of the boundary sphere with radius R_e, with $\mathrm{R_e} \geq R_p$ (ideally $\mathrm{R_e} \gg R_p$) is necessary to avoid particle's roaming far from the aggregate since this will significantly increase computational time. It is important to notice that here, the radiuses of appearance and external boundary spheres are not fixed. These values are continuously optimized. To do so, they are calculated as the sum of the additional constants (p and b for the appearance and the boundary spheres respectively) and multiplied by the radius of the minimum bounding sphere and by a factor called "appearance sphere multiplier". This procedure provides a wide range of possible relations between the R_b, R_p and R_e. For example, it is possible to turn off the multiplication and use only a constant difference between radiuses of the defined spheres.

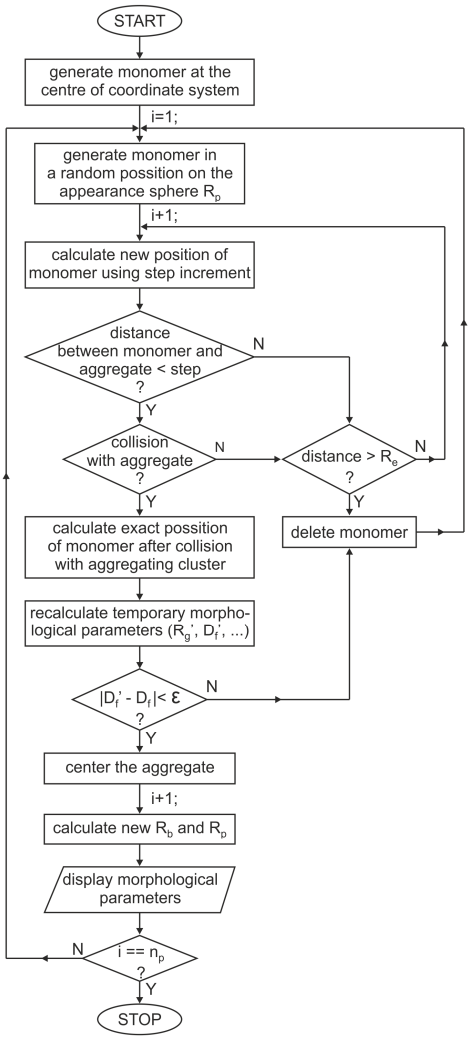

Figure 2.3. Schematic diagram of the DLA algorithm.

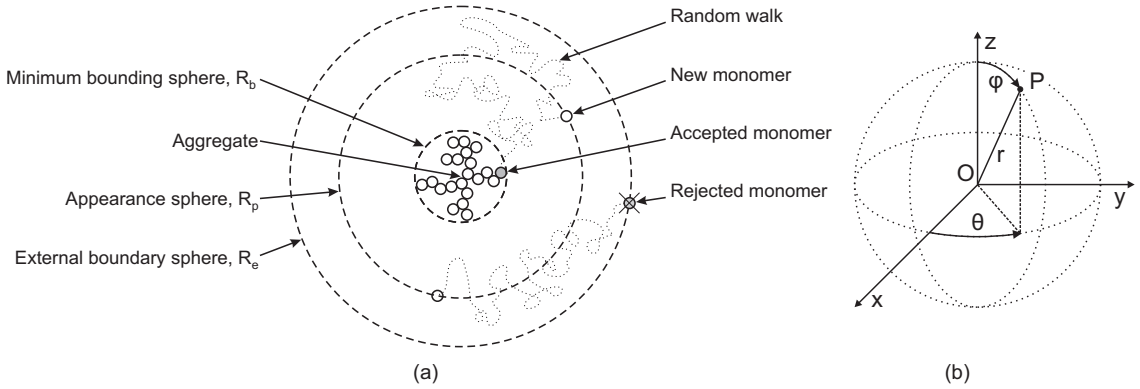

Figure 2.4. (a) Schematic diagram of the Diffusion Limited Aggregation (DLA) steps and parameters and (b) Spherical Coordinate System.

Figure 2.4 (b) presents the coordinate system of the DLA code. To avoid problems related with temporary position of the growing cluster at each step of the algorithm the centre of mass of the aggregate is relocated at the centre of the coordinate system. When the aggregation procedure is completed it is necessary to convert the spherical coordinates (r,θ,φ) to the classical laboratory Cartesian Coordinate System (x,y,z). To do so we can use the following mapping procedure:

$$\begin{aligned} x &= r\cos\theta\sin\varphi, \\ y &= r\sin\theta\sin\varphi, \\ z &= r\cos\varphi. \end{aligned} \tag{2.17}$$

The random motion of the primary particles is simulated by the decomposition of their trajectories into small step increments (e.g. $2r_p$) with a statistically true isotropic orientation. The latter is obtained by generating at each step random inclination and azimuth angles φ,θ with a uniform spherical distribution (Bird 1994). This procedure is not a trivial task because the intuitive approach is incorrect. Indeed, if we generate the inclination and azimuth angles φ,θ in the range $[0,\pi]$ and $[0,2\pi]$ respectively and transform them to the Spherical Coordinate System using Eq. (2.17), the points are not distributed uniformly. As an example, Figure 2.5 shows 5000 points generated on the surface of a unit sphere. It can be seen that their spatial distribution is denser at the poles. This problem is caused by the mapping procedure between the spherical and the Cartesian coordinates which does not preserve area (i.e. initial space is pinched and compressed at the poles). It is clear that random numbers generated in this way would strongly affect aggregation procedure and thus generated aggregates would be statistically elongated and oriented (anisotropic).

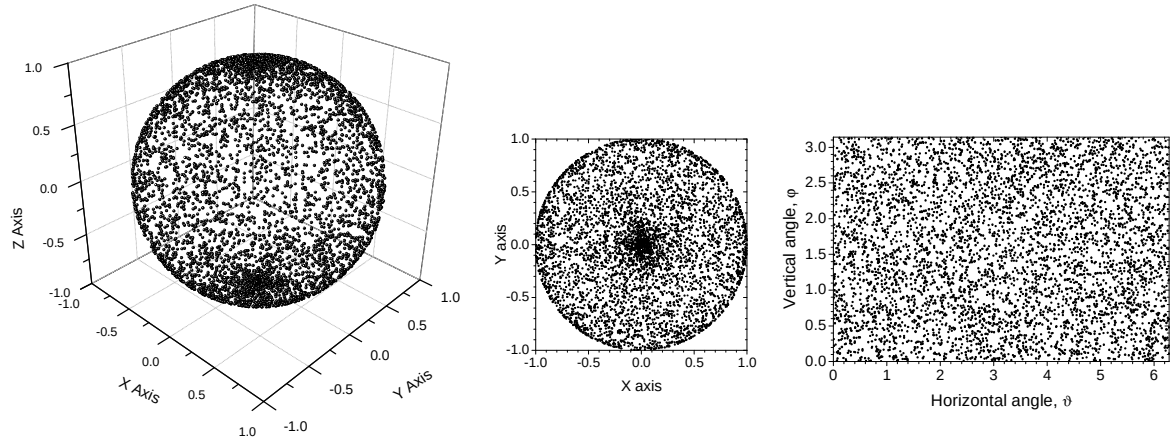

(a) (b) (c)

Figure 2.5. 5000 points generated on a surface of a unit sphere with the Uniform Distribution in the Cartesian Coordinates mapped to the Spherical Coordinate System: (a) 3D view, (b) top view of the region of the "north" pole and (c) angular distribution of the points.

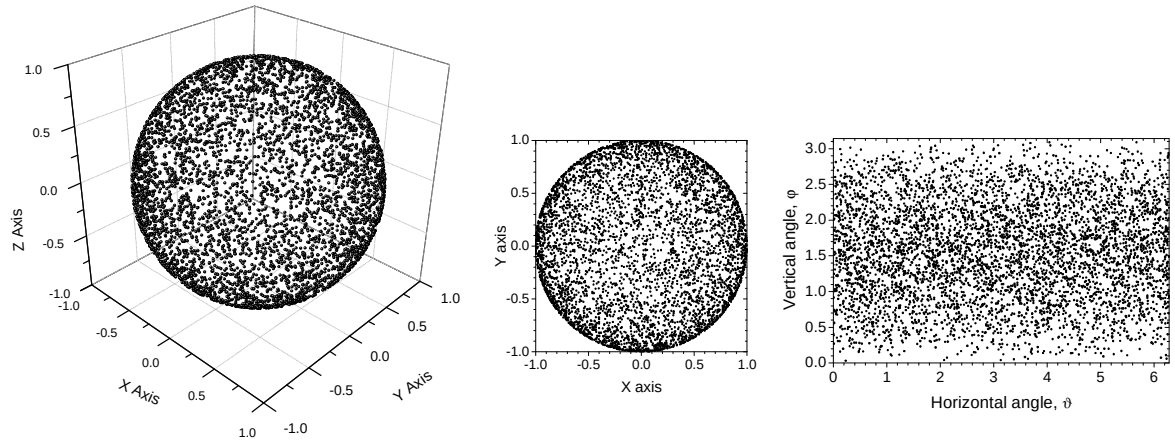

(a) (b) (c)

Figure 2.6. 5000 points generated on a surface of a unit sphere with the Uniform Spherical Distribution: (a) 3D view, (b) top view of the region of the "north" pole and (c) angular distribution of the points.

To avoid orientation problem and to find equations necessary for the generation of random points with the Uniform Spherical Distribution, it is necessary to consider the Jacobian matrix of the mapping procedure (Bird 1994):

$$J_F(r,\varphi,\theta)=\begin{bmatrix}\frac{\partial x}{\partial r} & \frac{\partial x}{\partial \varphi} & \frac{\partial x}{\partial \theta}\\ \frac{\partial y}{\partial r} & \frac{\partial y}{\partial \varphi} & \frac{\partial y}{\partial \theta}\\ \frac{\partial z}{\partial r} & \frac{\partial z}{\partial \varphi} & \frac{\partial z}{\partial \theta}\end{bmatrix}=\begin{bmatrix}\cos\theta\sin\varphi & r\cos\theta\cos\varphi & -r\sin\theta\sin\varphi\\ \sin\theta\sin\varphi & r\sin\theta\cos\varphi & r\cos\theta\sin\varphi\\ \cos\varphi & -r\sin\varphi & \cos\varphi\end{bmatrix}. \qquad (2.18)$$

The Jacobian determinant is independent of the azimuth angle θ but it is related with the inclination angle φ and radius r. However, if we consider an unit sphere we can cut out variable r. For the probability density function given by the Jacobian matrix one can find the

cumulative distribution function. Finally, using its inverse we can generate the inclination and azimuth angles φ, θ with uniform spherical distribution (Bird 1994):

$$\begin{aligned} \theta &= 2\pi\delta_1, \\ \varphi &= 2\arcsin\sqrt{\delta_2}, \end{aligned} \tag{2.19}$$

where, δ_1 and δ_2 are uniform distributions on $[0,1]$. As an example, Figure 2.6 shows 5000 points generated on a surface of a unit sphere. It is worth to compare the distribution of the angles φ and θ generated with both solutions (see Figure 2.5 (c) and Figure 2.6 (c)). It can be seen that now, the points are distributed equally on the entire surface of the given sphere (Figure 2.6).

2.3.1.2. Sticking process

Figure 2.7 shows a schematic diagram of a collision between a randomly marching monomer and an aggregating cluster. It should be noticed that for drawing considerations the increment step presented here (equal to $6r_p$) is significantly larger than the one used for our simulations (see Table 2.1). If the distance between the current position of the monomer (a) and any of the particles within the aggregating cluster is smaller than the increment step, the possibility of a collision must be considered. In that case, new coordinates of the monomer (b) are calculated with the typical procedure described above. However, the algorithm also verifies whether during the current increment step (i.e. between positions (a) and (b)) the monomer collides with the aggregate or not. If an intersection occurs (see Figure 2.7), the coordinates of the marching particle are recalculated the exact contact position (c).

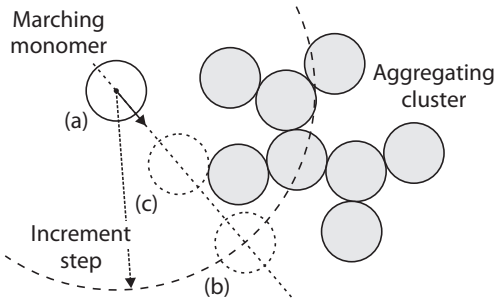

Figure 2.7. Schematic diagram of a collision between a randomly marching monomer and aggregating cluster: (a) current position of the monomer, (b) new position of the monomer without collision, (c) position of the monomer at the collision point.

The procedure described above does not fulfill all requirements for the aggregation process. In fact, the collision and sticking between a single monomer and an aggregate of $n_p - 1$ particles, is only effective when the following inequality is satisfied:

$$\left(\frac{R_{g,n_p}}{R_{g,n_p-1}}\right)^{D_f-\varepsilon} \le \frac{n_p}{n_p-1} \le \left(\frac{R_{g,n_p}}{R_{g,n_p-1}}\right)^{D_f+\varepsilon}, \tag{2.20}$$

where ε is an accuracy parameter on the fractal dimension. In the DLA software this value may be adjusted on demand. Nevertheless, in the present study it was fixed at $\varepsilon = 10^{-2}$ as smaller values greatly increase computational time without noticeable improvements in morphological characteristics of the aggregates. Something important to understand is that Eq. (2.20) allows ensuring at each aggregation step that Eq. (2.13) is nearly verified and thus, that the scaling properties of all aggregates are conserved at all scales.

During the aggregation process we assume that particles stick together like hard spheres in contact, i.e. exactly in one point and any additional displacement after their collision is impossible. From a macroscopic point of view both assumptions, especially the latter, seem to be incorrect. It is obvious that velocity of a fast moving object after a collision with a larger one decreases significantly but due to the principle of inertia and the law of conservation of the linear momentum, the colliding particle should in most cases remains in motion. This is not necessarily the case of nanoparticles which are mostly sensitive to adhesion and short range forces (e.g. Van der Waals forces). Nevertheless, it is common to simplify this problem and ignore particle displacement after collision (Witten and Sander 1981; Babu et al. 2008).

2.3.1.3. Overlapping factor

In some particle systems, due to additional processes (e.g. melting, polymerization, deposition or collision impact), primary particles may be entangled by more than a single point of contact, and they can also significantly overlap. For example, overlapping may be encountered when aggregation process occurs at high temperature (e.g. during combustion or in a plasma system), so it may be necessary to take into account and model this phenomenon. Figure 2.8 shows a schematic diagram of the overlapping of 2 particles with radiuses $r_{p,1}$, $r_{p,2}$ and their centers of mass distant each other by $d_{\upsilon\kappa}^{3D}$.

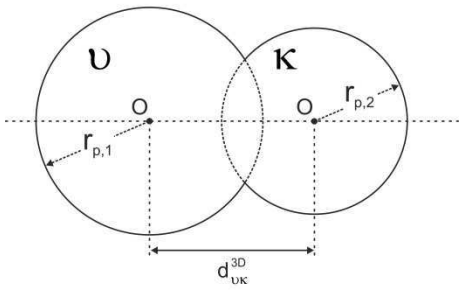

Figure 2.8. Schematic diagram of the three dimensional overlapping factor $C_{\upsilon\kappa}^{3D}$ for 2 spherical particles with radiuses r_{p1}, r_{p2} and their centers of mass distant each other by $d_{\upsilon\kappa}^{3D}$.

To quantify overlapping effect, it is convenient to define a 3D overlapping factor based on the true Euclidian inter-distance $d_{\upsilon\kappa}^{3D}$ between the particles' centers of mass (Brasil et al. 1999):

$$C_{\upsilon\kappa}^{3D} = \frac{\left(r_{p,1} + r_{p,2}\right) - d_{\upsilon\kappa}^{3D}}{r_{p,1} + r_{p,2}}, \tag{2.21}$$

where $C_{\upsilon\kappa}^{3D} < 0$ for monomers that are not in contact, $C_{\upsilon\kappa}^{3D} = 0$ for hard spheres in contact and $C_{\upsilon\kappa}^{3D} \in (0,1]$ for partially to fully overlapped spheres. If we consider only monodisperse particles within an aggregate, Eq. (2.21) may be simplified to:

$$C_{\upsilon\kappa}^{3D} = \left(2r_p - d_{\upsilon\kappa}^{3D}\right) / 2r_p . \tag{2.22}$$

As an example, for diesel soot aggregates, depending on the sampling and storage protocols, Wentzel et al. (Wentzel et al. 2003) have found an overlapping factor in the range $C_{\upsilon\kappa}^{3D} = 0.10 - 0.29$, while Ouf et al. (Ouf et al. 2010) reported $C_{\upsilon\kappa}^{3D} = 0.16 - 0.30$. We have found similar value ($C_{\upsilon\kappa}^{3D} = 0.20 \pm 0.05$) for the experimental sample of diesel soot particles (Yon et al. 2011) during the TEM-based analysis (see chapter 3). Estimated overlapping factor was also applied to model artificial fractal-like aggregates.

In what follows, to numerically account for overlapping (Brasil et al. 1999), we first generate an aggregate of hard spheres in contact. Next, we can take into account for $C_{\upsilon\kappa}^{3D}$ by progressively increasing the radiuses of monomers within an aggregate while maintaining the position of their centers. At the same time it is necessary to perform a scaling down procedure to keep the initial value of the particle radius. Described steps are depicted in Figure 2.9.

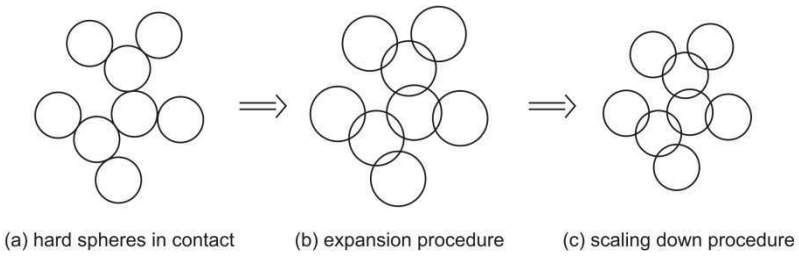

Figure 2.9. Numerical procedure for overlapping: (a) an aggregate with hard spheres in contact, (b) the aggregate with expanded radiuses of monomers, (c) the aggregate after scaling down procedure.

Figure 2.10 compares radius of gyration of the aggregates with fractal dimension equal to 1.80 and various number of monomers for different overlapping factors (from 0 to 0.5). It can be seen that the overlapping factor has a linear influence on the radius of gyration.

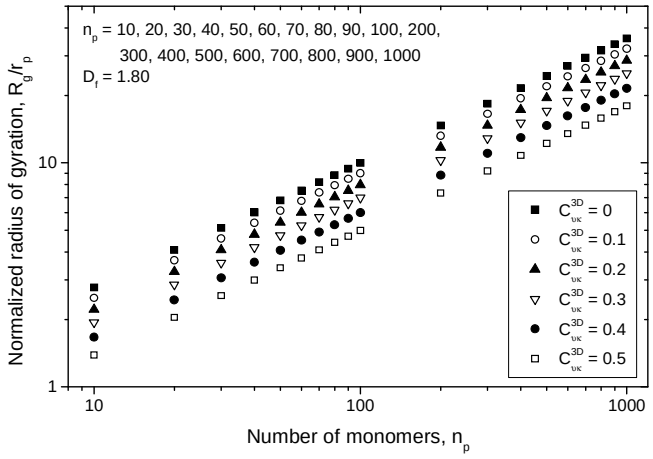

Figure 2.10. Radius of gyration as a function of the number of monomers in the aggregate with fractal dimension equal to 1.80, for various overlapping factors.

2.3.1.4. Fractal prefactor

Another important parameter in the DLA model is the fractal prefactor k_f appearing in Eq. (2.13). The physical meaning and values of this constant has been extensively discussed in the literature. Even for the same particle system its value differ significantly between various authors. As an example, for soot aggregates it can vary from 1.23 to 3.5 (e.g. (Puri et al. 1993; Cai et al. 1995; Koylu et al. 1995; Ouf et al. 2010)). As already mentioned, there are many attempts to explain this spreading (Brasil et al. 1999; Sorensen 2001; Bau et al. 2010). The most common idea is that it accounts for monomers overlapping, as well as their shape which can also differ significantly from the spherical one (Puri et al. 1993).

In this work, like some authors (Sorensen and Roberts 1997; Brasil et al. 1999; Bau et al. 2010) did before, this parameter was set constant, with a value corresponding to the one found for an infinitely large hexagonal close packed (hexagonal compact, HC) aggregate of monodisperse hard spheres in contact. The underlying idea being that this aggregate has the highest possible compactness in a 3D space. Sorensen et al. (Sorensen and Roberts 1997) proposed a correlation between k_f and D_f:

$$k_f = p(d)\left(\frac{D_f + 2}{D_f}\right)^{D_f/2}, \tag{2.23}$$

where $p(d)$ is a compactness factor (called also sphere packing fraction):

$$p(d) = \frac{V_{SPH}}{V_{PR}}, \tag{2.24}$$

where V_{PR} and V_{SPH} are volumes of the elementary spatial object and volume of the particles contained in this object respectively. For monodisperse hexagonal compact aggregate $p(d) = \pi / \left(3\sqrt{2}\right) \simeq 74\%$. Thus using Eq. (2.24) in Eq. (2.23) the fractal prefactor for a monodisperse hexagonal compact aggregate is equal to:

$$k_f = \left(\pi / 3\sqrt{2}\right)\left(5/3\right)^{3/2} \approx 1.593. \tag{2.25}$$

The same argument has been found by Lapuerta et al. (Lapuerta et al. 2010) and also similar value was previously supported by Sorensen et al. (Sorensen and Roberts 1997).

The overall procedure described in this section allows to generate synthetic aggregates (i.e. sets of spheres coordinates) for a large range of fractal dimensions, radiuses of gyration and number of primary particles only limited by the computational time.

2.3.1.5. Particle Size Distribution

The size distribution of a large variety of particle systems can be approximated by analytical particle size distribution (PSD) like the Gaussian, log-normal, power, Gamma ones. For most results presented in the current work we have assumed that we have monodisperse particles. We did it since in a lot of systems (e.g. aerosol of nanoparticles, plasma) the radius of particles has a low standard deviation. Nevertheless, in some cases it may be also interesting to consider polydisperse particles. To do so, in this work, we use the log-normal distribution which depends on two parameters μ, s (Xu 2002):

$$f(r_p) = \frac{1}{r_p s\sqrt{2\pi}} \exp\left[-\frac{1}{2}\left(\frac{\ln r_p - \mu}{s} \right)^2 \right]. \tag{2.26}$$

The parameters μ, s, the mean radius $\bar{r}_p$ and the related standard deviation σ_p are given by:

$$s = \sqrt{\ln\left(\sigma_p{}^2 / \bar{r}_p{}^2\right) + 1}, \qquad \mu = \ln \bar{r}_p - s^2/2, \tag{2.27}$$

$$\bar{r}_p = \exp\left[\mu + s^2/2\right], \qquad \sigma_p^2 = \bar{r}_p{}^2\left[\exp\left(s^2\right) - 1\right]. \tag{2.28}$$

Looking at Figure 2.14 and Figure 2.16, where aggregates with a high polydispersity ($\sigma_p = 0.5$) are presented, one may have the impression that there are too many large monomers and the given size distribution is not preserved. This is pure subjective effect – the observer is more sensitive to the larger objects than the smaller ones. To verify the correctness of the generated distribution, we have performed dedicated simulations. Figure 2.11 shows the particles size distribution estimated for 100 clusters of 1000 polydisperse monomers (i.e. 100 000 particles) with the log-normal distribution and the initial standard deviation equal to (a) $\sigma_p = 0.10$ and (b) $\sigma_p = 0.30$. Clearly, estimated values are in a perfect agreement with the initial ones.

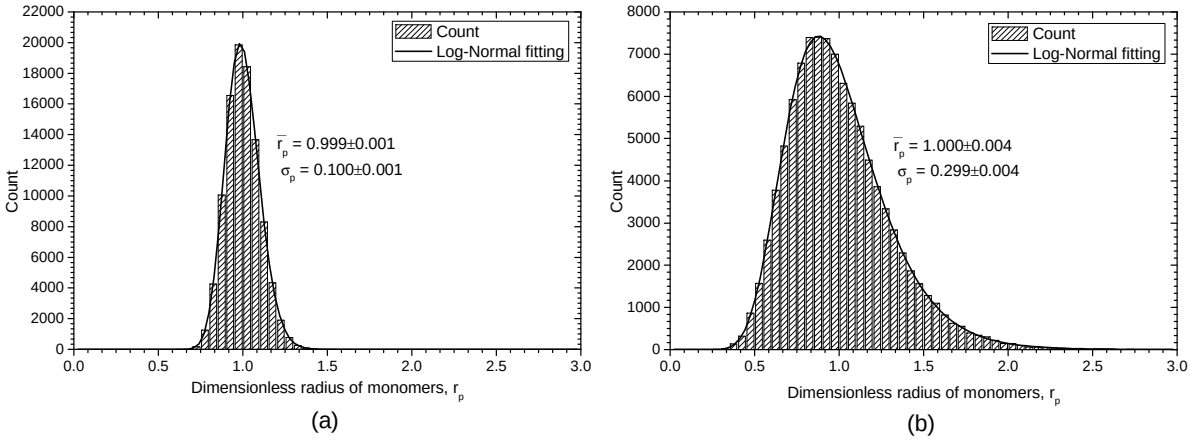

Figure 2.11. Particle Size Distribution (PSD) of monomers for 100 aggregates of 1000 polydisperse monomers with initial standard deviation (a) $\sigma_p = 0.10$ and (b) $\sigma_p = 0.30$.

2.3.1.6. Diffusion Limited Aggregation Software

A screen copy of the DLA software developed according to the algorithm described above is shown in Figure 2.12. In the main window six separate panels may be found. The most important is panel (a), which allows to specify the parameters of aggregation (e.g. number and radius of monomers, radius of gyration, radius of appearance and external boundary spheres, etc.). Panel (b) is used to rotate the aggregate on demand according to the laboratory coordinate system, while panel (c) enables to perform serial calculations (loop over n_p, D_f, R_g, k_f). Panel (d) is a progress bar. All the coordinates of the aggregating monomers and the parameters of the forming cluster are displayed in the preview window (e). Finally, panel (f) gathers together general control buttons and enables to export and import data to various format files. Particularly, it is possible to generate output files that can be directly used with the POV-Ray 3D rendering software (POV-Ray 2004) and also text files that may be post-processed and used as the input files for light scattering codes.

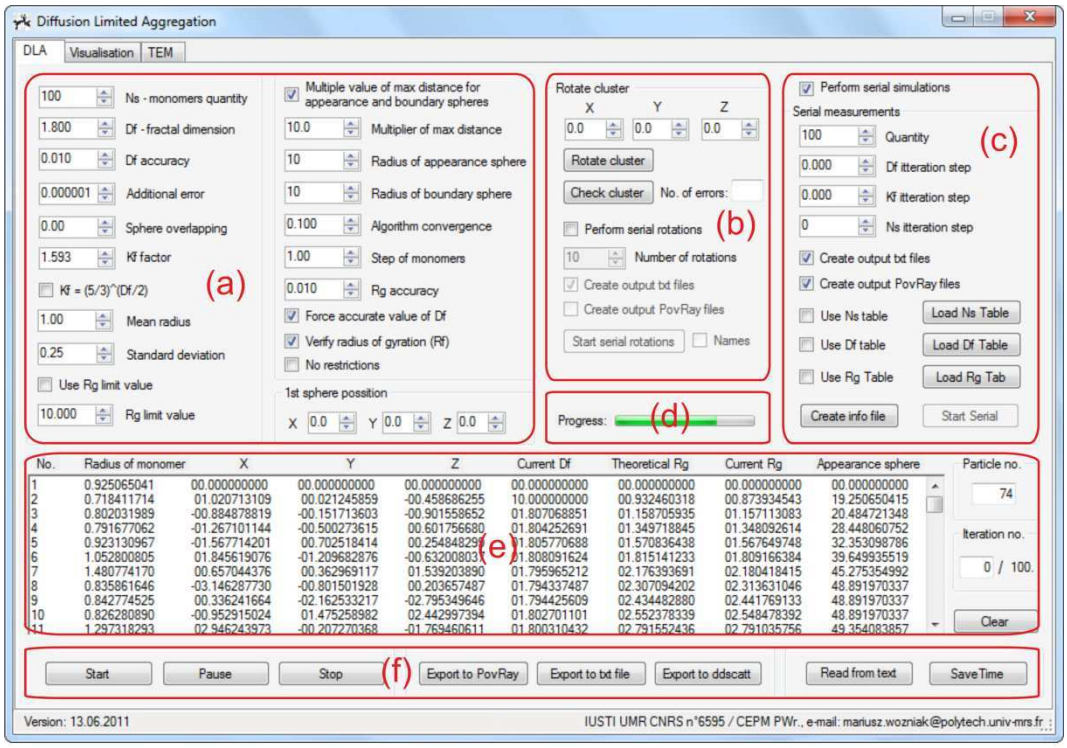

Figure 2.12. Screen copy of the DLA software main tab: (a) aggregation parameters, (b) cluster rotation panel, (c) serial simulation panel, (d) progress bar, (e) preview window and (f) general control buttons.

2.3.2. Numerical results of the DLA aggregation – examples

2.3.2.1. Aggregates with a 3D rendering view

Figure 2.13 - Figure 2.19 show typical synthetic fractal-like aggregates generated with the DLA software. These aggregates were simulated for monodisperse monomers with dimensionless radius set to $r_p = 1$ as well as polydisperse monomers with mean radius $\overline{r}_p = 1$ and various fractal parameters (fractal dimension, radius of gyration, etc.). Their 3D renderings were generated with the POV-Ray software (POV-Ray 2004).

Fractal aggregates presented in Figure 2.13 (a) and Figure 2.13 (b) have different fractal dimensions ($D_f = 1.50$ and $D_f = 1.75$ respectively) and radiuses of gyration ($R_g = 32.85$ and $R_g = 19.95$) although they contain the same number of monodisperse monomers ($n_p = 300$) and thus they have the same radius in volume $R_v = r_p \sqrt[3]{n_p} \approx 6.69$. Figure 2.14 shows aggregates with the same parameters as in Figure 2.13 but with a significant polydispersity in radius of monomers (log-normal distribution with standard deviation $\sigma_p = 0.50$). The 2D images obtained for the 3 main projection planes (xy, xz and yz) are also shown. The large disk sheathes the radius of gyration while the smaller one corresponds to the radius in volume.

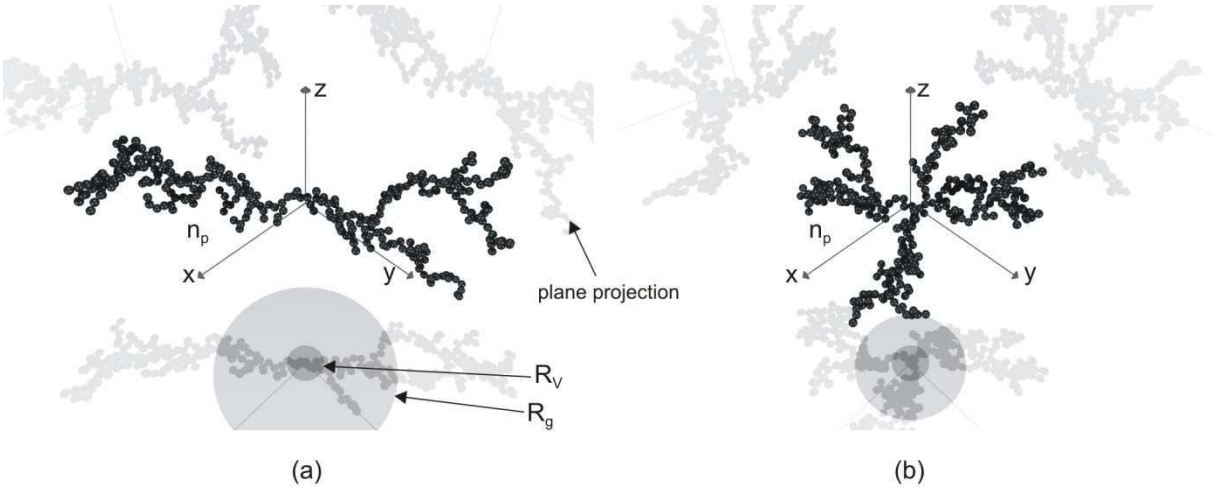

Figure 2.13. Fractal aggregates of 300 monodisperse monomers with the same radius in volume $R_v = 6.69$ but various fractal dimensions and radiuses of gyration: (a) $D_f = 1.50$, $R_g = 32.85$, (b) $D_f = 1.75$, $R_g = 19.95$.

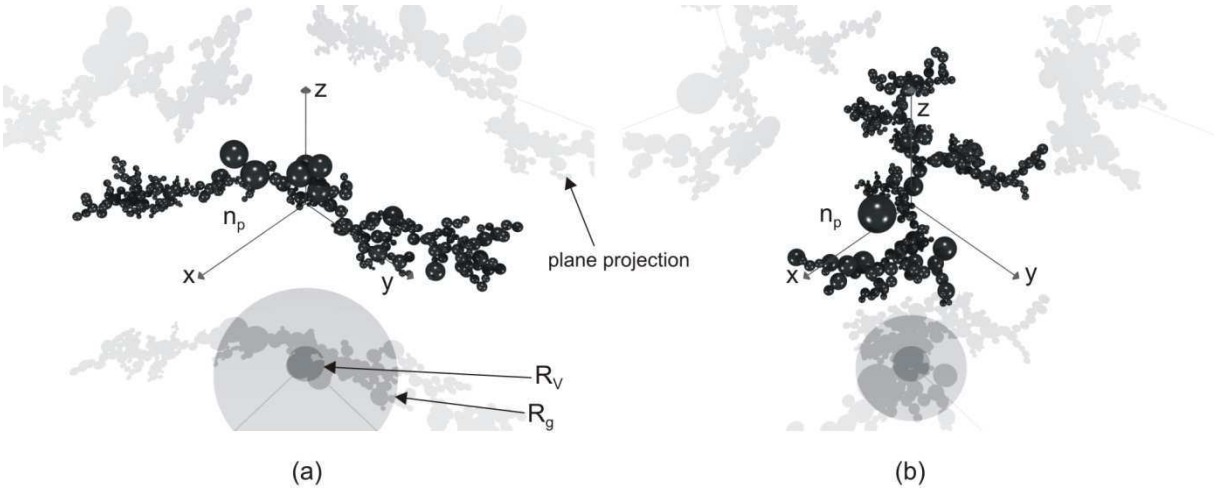

Figure 2.14. Fractal aggregates of 300 polydisperse monomers (log-normal distribution, $\sigma_p = 0.5$) with the same radius in volume $R_v = 6.69$ but various fractal dimensions and radiuses of gyration: (a) $D_f = 1.50$, $R_g = 32.85$, (b) $D_f = 1.75$, $R_g = 19.95$.

Fractal aggregates presented in Figure 2.15 (a) and Figure 2.15 (b) have different fractal dimensions ($D_f = 2.00$ and $D_f = 2.25$ respectively) and radiuses of gyration ($R_g = 12.87$ and $R_g = 17.71$) but they have the same number of monodisperse monomers $n_p = 500$ and thus the same equivalent radius in volume $R_v = r_p \sqrt[3]{n_p} \approx 7.94$. Figure 2.16 shows aggregates with the same parameters as Figure 2.15 but the PSD of monomers is polydisperse (log-normal distribution with standard deviation $\sigma_p = 0.50$).

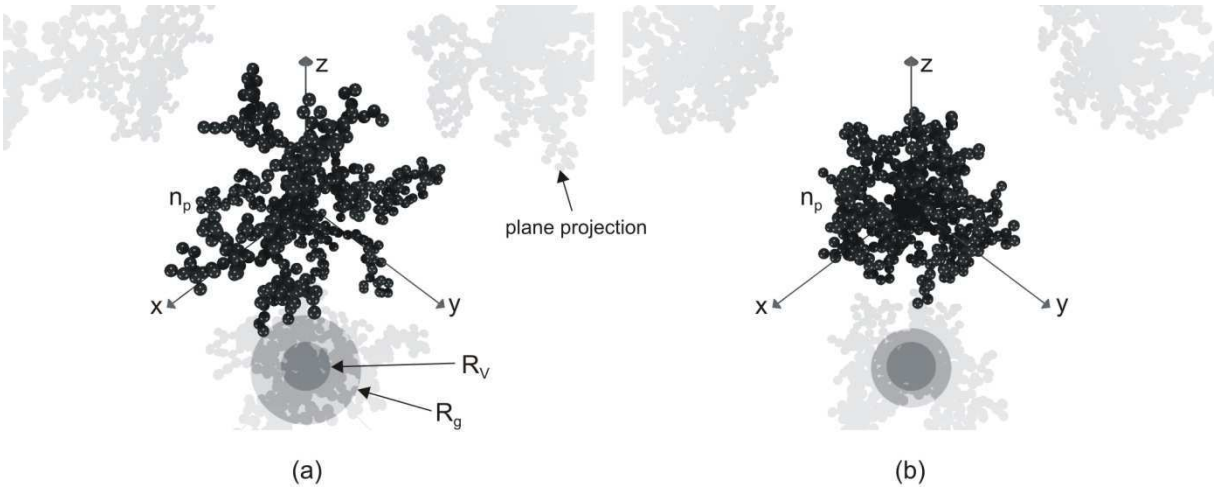

Figure 2.15. Fractal aggregates of 500 monodisperse monomers with the same radius in volume $R_v = 7.94$ but various fractal dimensions and radiuses of gyration: (a) $D_f = 2.00$, $R_g = 17.71$, (b) $D_f = 2.25$, $R_g = 12.87$.

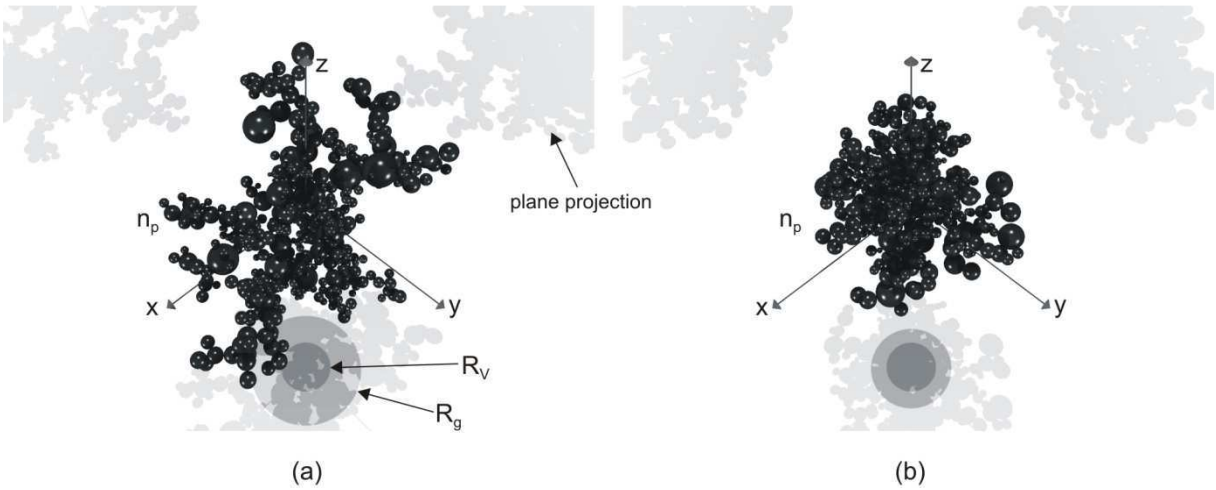

Figure 2.16. Fractal aggregates of 500 polydisperse monomers (log-normal distribution, $\sigma_p = 0.5$) with the same radius in volume $R_v = 7.94$ but various fractal dimensions and radiuses of gyration: (a) $D_f = 2.00$, $R_g = 17.71$, (b) $D_f = 2.25$, $R_g = 12.87$.

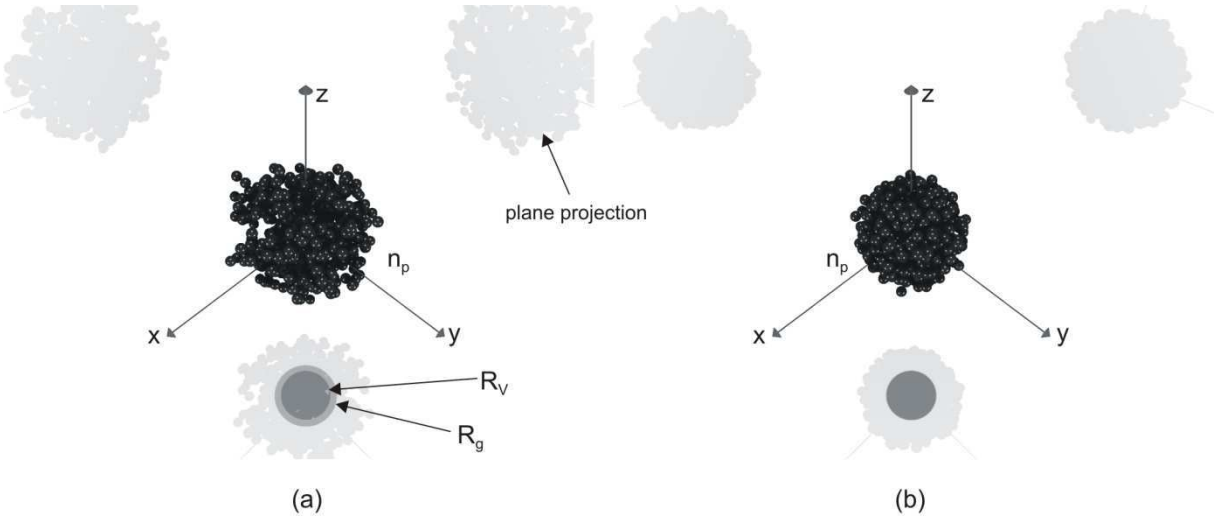

Figure 2.17. Fractal aggregates of 500 monodisperse monomers with the same radius in volume $R_v = 7.94$ but various fractal dimensions and radiuses of gyration: (a) $D_f = 2.50$, $R_g = 9.98$, (b) $D_f = 2.75$, $R_g = 8.10$.

In the same way, fractal aggregates presented in Figure 2.17 (a) and Figure 2.17 (b) have different fractal dimensions equal $D_f = 2.50$ and $D_f = 2.75$ respectively, different radiuses of gyration $R_g = 9.98$ and $R_g = 8.10$ but the same number of monodisperse primary particles $n_p = 500$ and the same equivalent radius in volume $R_v = r_p \sqrt[3]{n_p} \approx 7.94$.

Figure 2.18 and Figure 2.19 present aggregates with a much more significant number of monomers ($n_p = 10\ 000$), the same equivalent radius in volume $R_v = r_p \sqrt[3]{n_p} \approx 21.54$ but different fractal dimensions and radiuses of gyration. Figure 2.18 presents aggregates with (a) $D_f = 1.75$, $R_g = 147.97$ and (b) $D_f = 2.00$, $R_g = 79.22$. Figure 2.19 presents aggregates with (a) $D_f = 2.25$, $R_g = 48.73$ and (b) $D_f = 2.50$, $R_g = 33.06$.

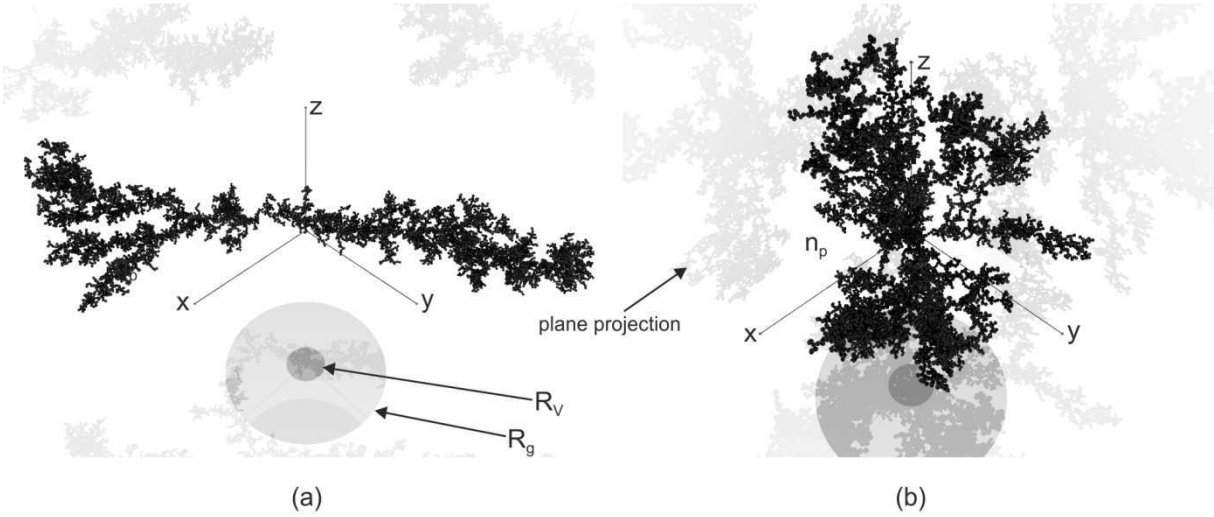

Figure 2.18. Fractal aggregates of 10 000 monodisperse monomers with the same equivalent radius in volume $R_v = 21.54$ but various fractal dimensions and radiuses of gyration: (a) $D_f = 1.75$, $R_g = 147.97$, (b) $D_f = 2.00$, $R_g = 79.22$.

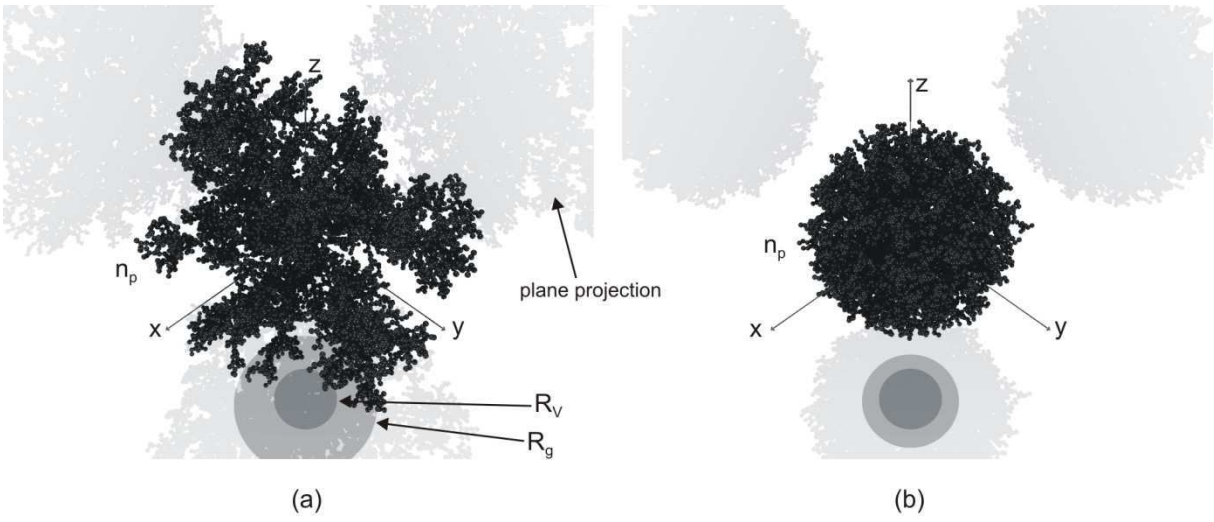

Figure 2.19. Fractal aggregates of 10 000 monodisperse monomers with the same equivalent radius in volume $R_v = 21.54$ but various fractal dimensions and radiuses of gyration: (a) $D_f = 2.25$, $R_g = 48.73$, (b) $D_f = 2.50$, $R_g = 33.06$.

2.3.2.2. Morphological parameters

Working with fractal aggregates one must be aware that aggregates with the same number of monomers, but various fractal dimensions may have totally different radiuses of gyration. Figure 2.20 shows the evolution of the radius of gyration (normalized by the mean radius of monomers) of aggregates versus the number of monomers. Results presented here were obtained for the aggregates of monodisperse particles with hard spheres in contact and a wide range of fractal dimensions (from 1.20 to 2.80). For instance, it can be seen that for two 1000-monomer aggregates with a fractal dimensions equal to 1.20 and 2.80 respectively, the ratio between the radiuses of gyration is higher than 20.

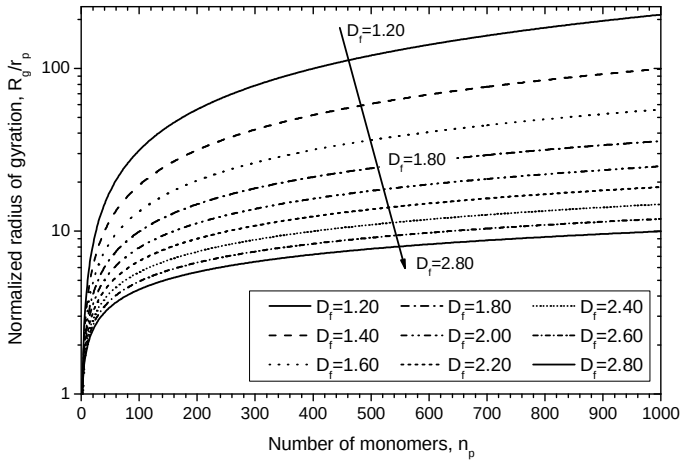

Figure 2.20. Radius of gyration as a function of the number of monomers in the aggregate for various fractal dimensions and monodisperse monomers with a single point of contact.

To describe the characteristic size of a fractal aggregate the radius of gyration is widely used. Nevertheless, it is not the only one characteristic length that can be used for this purposes. To do so, we can calculate the radius in volume R_v (i.e. the radius of a sphere with a volume equivalent to the volume of all the monomers within an aggregate), the radius of the minimum bounding sphere R_b (i.e. the sphere with the minimum radius which contains entire aggregate) or the maximum length of the aggregate in the 3-dimensional space L^{3D}. Figure 2.21 shows a comparison between the aforementioned characteristic lengths as a function of the fractal dimension for aggregates with (a) $n_p = 100$ and (b) $n_p = 500$ monomers.

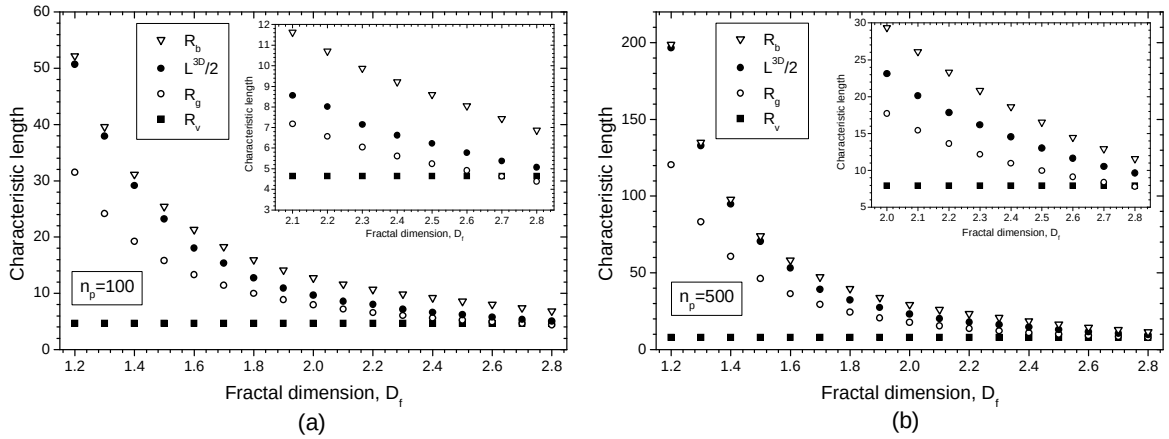

Figure 2.21. Comparison between 4 characteristic lengths of aggregates (radius of gyration R_g, radius in volume R_v, radius of minimum bounding sphere R_b and maximum length of aggregate L^{3D}) versus the fractal dimension and for: (a) $n_p = 100$ and (b) $n_p = 500$.

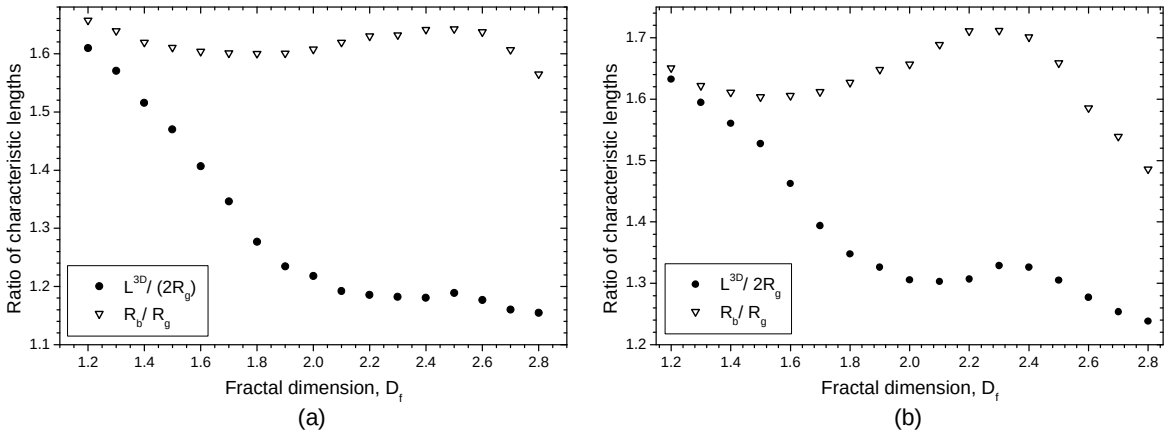

Figure 2.22. Comparison between $L^{3D}/\left(2R_g\right)$ and R_b / R_g ratios versus the fractal dimension and for: (a) $n_p = 100$ and (b) $n_p = 500$.

Moreover, the ratio between the presented characteristic lengths is not constant. Figure 2.22 shows that the values of $L^{3D}/\left(2R_g\right)$ and R_b / R_g are changing as a function of the fractal dimension. Numerical simulations comparing the different solutions of the presented problem and the results obtained for the various light scattering models are presented and discussed in chapter 4 of the current work.

2.3.2.3. Accuracy on aggregation parameters

Created in this research DLA code is called fully adjustable (or tunable) because in contradiction to the ordinary DLA solutions it preserves fractal parameters at each step of the aggregation. As an example, Figure 2.23 (a) and Figure 2.23 (b) show the evolution of the fractal dimension during the aggregation process for $n_p = 100$ monomers and D_f equal 1.80 ± 0.01 and 2.50 ± 0.01 respectively. We can ensure that the generated aggregates are not multi-fractals and that they have true auto-similarity properties.

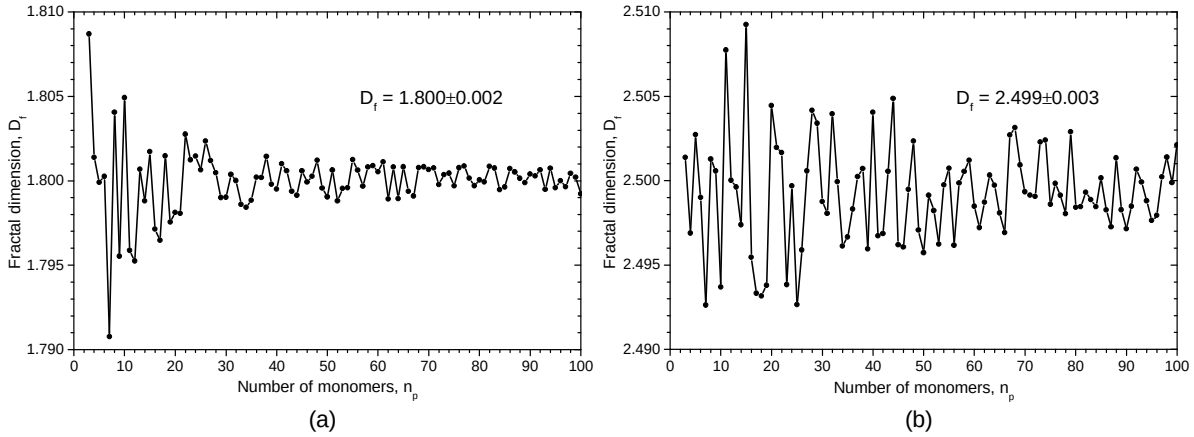

Figure 2.23. Accuracy of the fractal dimension for the following aggregation steps for clusters of 100 monodisperse monomers with imposed values: (a) $D_f = 1.80 \pm 0.01$ and (b) $D_f = 2.50 \pm 0.01$.

However, for very low or very high fractal dimensions (e.g. $D_f = 1.20$ or $D_f = 2.80$) the aggregation parameters cannot be preserved at the beginning of the aggregation. This comes directly from the fact that for so extreme parameters fractal equation (2.13) is not satisfied for a few monomers. In such case, the aggregation process may be stucked. The only way to deal with this problem is to decrease the accuracy imposed at the beginning of the aggregation process. This option allows to start aggregation with a lower (or higher) D_f than the initial one, afterwards, the code converges rapidly to the imposed value. As an example, Figure 2.24 shows the evolution of the fractal dimension of an aggregation of 100 monodisperse monomers with $D_f = 2.80 \pm 0.01$ when aforementioned option was used.

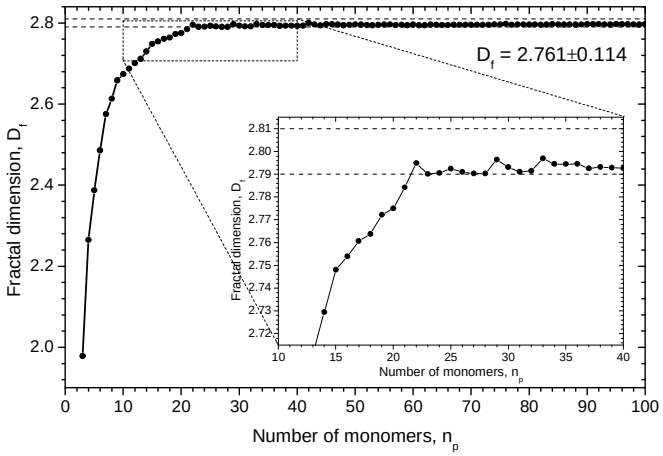

Figure 2.24. Accuracy of the fractal dimension for the following aggregation steps for cluster of 100 monodisperse monomers with $D_f = 2.80 \pm 0.01$.

In some way we could say that this aggregate is multi-fractal for $n_p \leq 25$. However, it makes no sense to use (or apply) a fractal dimension for an object which do not contain more than tens of monomers.

2.3.2.4. Computational time of DLA algorithm

Another important issue related to the DLA is the computational time. DLA algorithm is very time-consuming, especially if we use extreme parameters (i.e. very high or low fractal dimension, significant number of monomers, etc.) or if we impose a high accuracy of these parameters. As an example, Figure 2.25 shows the aggregation time of aggregates (a) with different fractal dimensions versus the number of monomers and (b) for a given number of monomers versus the fractal dimension.

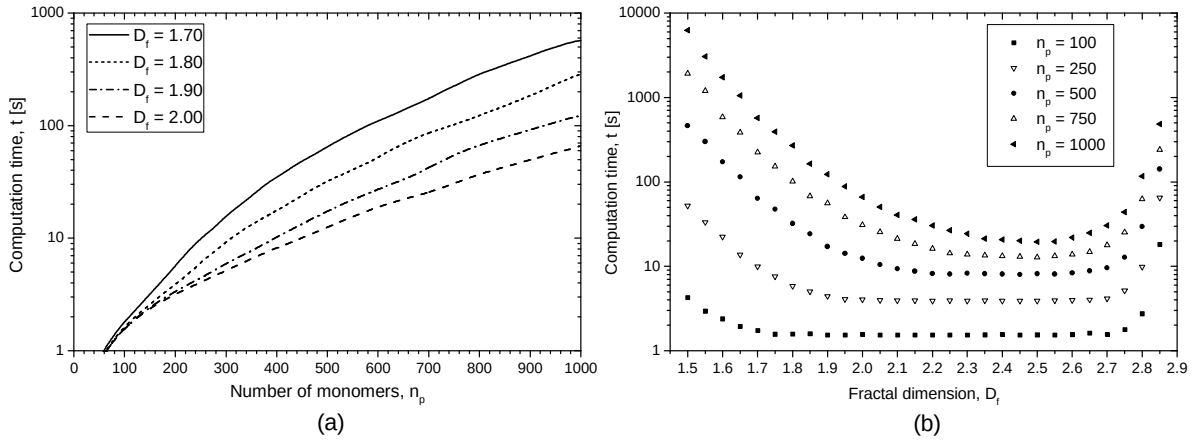

Figure 2.25. Computational time of the DLA software: (a) aggregates with different fractal dimensions versus the number of monomers, (b) aggregates with different numbers of monomers versus the fractal dimension.

The calculations were performed with an up-to date personal computer (dual core CPU $2\times2.8\,GHz$ and $4\,GB$ of RAM memory) for the parameters shown in Table 2.1. Figure 2.25 (a) shows a power-law relation between the number of monomers and the computational time. This behavior of the DLA algorithm is partly due to the fact that the radius of appearance sphere R_p is calculated as a multiple value of the radius of gyration. In that case a fast increase of the radius of gyration versus the number of monomers (see Figure 2.20) causes the power-law growth of the volume fraction that may be explored by the randomly marching new monomer. Obviously, it significantly extends computational time.

Figure 2.25 (b) shows the computational time of aggregates versus the fractal dimension. It should be noticed that an aggregate with a low fractal dimension has a large radius of gyration, which is growing fast for increasing number of monomers (see Figure 2.20). As a consequence it increases the radiuses of the appearance and the external boundary spheres. Moreover, a dilute aggregate occupies only a small fraction of the volume defined by the external boundary sphere so the probability of a collision with a randomly marching monomer is extremely low. Because of the aforementioned issues, computational time of the DLA algorithm might be significantly extended. The situation is opposite for aggregates with high fractal dimension. In that case, the external boundary sphere is several times smaller so numerous collisions between free monomers and an aggregate may occur. Nevertheless, due

to the high compactness of the aggregate only certain positions of particle satisfy equation (2.20), so most of the colliding monomers are rejected. This effect also extend aggregation time (see Figure 2.25). However, as mentioned previously, high precision of the fractal dimension or the other parameters does not cause significant improvements of morphological characteristics. Therefore, accuracy imposed during the extensive simulations should be a compromise between morphological requirements and algorithm execution time.

Table 2.1 shows typical parameters used for the aggregation with our DLA code. Beside all the parameters that have already been explained, an additional field called “No restriction” is depicted. When checked, our code works as typical DLA software which during the aggregation process does not impose any constraints regarding the fractal dimension, fractal prefactor or radius of gyration. In that case, each collision between randomly walking monomer and aggregate results in a irreversible connection.

Table 2.1. Typical parameters for the aggregation simulations.

D_f accuracy	± 0.01	Radius of appearance sphere (*p*)*	5.0
R_g accuracy	± 0.01	Radius of boundary sphere (*b*)**	5.0
fractal prefactor k_f	1.593	Monomer step increment	2.0
Multiple value of max distance for appearance and boundary spheres	Yes	Force accurate value of D_f	Yes
		Verify radius of gyration	Yes
Appearance sphere multiplier (*mult*)*	2.0	No restrictions	No

* radius of appearance sphere is calculated as $R_p = mult \times R_b + p$, where R_b is the radius of boundary sphere, *mult* is the “appearance sphere multiplier” and *p* is the input parameter.

** radius of external boundary sphere is calculated as $R_e = R_p + b$, where b is the input parameter.

2.4. A Comparison between DLA and DLCA aggregates

Numerous computer simulations (e.g. (Meakin 1983; Weitz et al. 1985; Chakrabarty et al. 2007)) have shown that the fractal dimension of DLCA aggregates is in the range $D_f = 1.70 - 1.80$. Similar values have been found experimentally. As an example, the TEM-based analysis (Koylu et al. 1995; Chakrabarty et al. 2007; Ouf et al. 2010), depending on the sampling and storage protocol, report $D_f = 1.65 - 1.85$. Investigations with static light scattering (Sorensen et al. 1992a; Wang and Sorensen 1999; Sorensen 2001) and small angle X-ray scattering (SAXS) (Rieker et al. 2000; Boffa et al. 2009) techniques have also reported similar values.

2.4.1. Numerical test sample of the DLCA aggregates

In this paragraph we analyze numerical test sample of the DLCA aggregates (Yon et al. 2008) provided by Dr. Jérôme Yon. The parameters of this sample correspond to those of real

aggregates produced by a diesel flame. The aggregates are composed of polydisperse monomers having a log-normal distribution with mean radius of monomers $\overline{r}_p = 17.10\ nm$ and its standard deviation of $\sigma_p = 3.43\ nm$. The test sample contains 7240 various aggregates (i.e. sets of coordinates of the monomers) with a number of monomers within aggregates from 1 to 6725 and radius of gyration from $R_g = 0.18\overline{r}_p$ to $R_g = 92\overline{r}_p$. Figure 2.26 shows the distribution of (a) the number of monomers and (b) the normalized radius of gyration for the given population of aggregates. Looking at both figures, it can be seen that the test sample contains a significant number of very small aggregates (with $n_p < 10$ and $R_g < 2\overline{r}_p$).

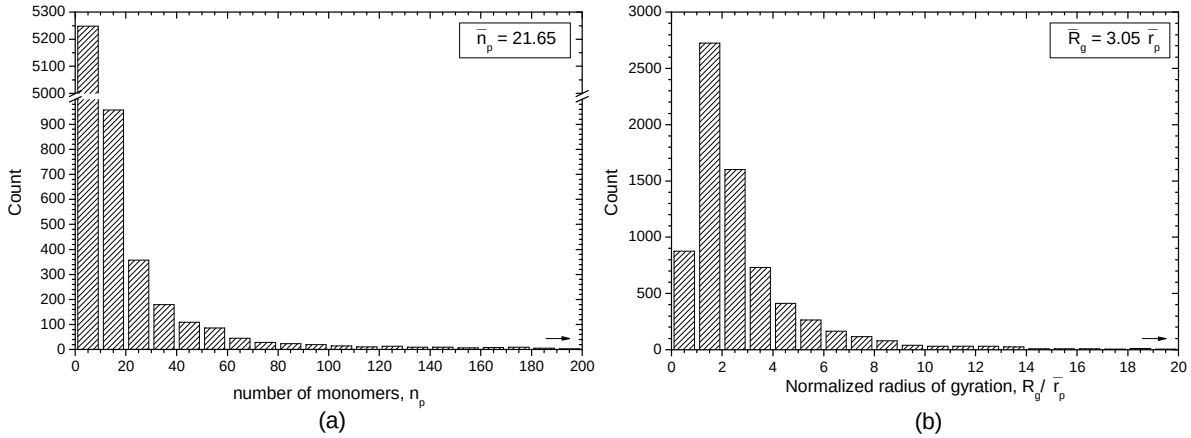

Figure 2.26. Distribution of (a) the number of monomers and (b) the normalized radius of gyration of the numerical test sample of DLCA aggregates.

2.4.2. Estimation of the "global" fractal dimension

The test sample of DLCA aggregates was generated during the spontaneous aggregation without any initial constraints regarding the fractal dimension and fractal prefactor. The only initially fixed parameters describe the size distribution of monomers (log-normal distribution with $\overline{r}_p = 17.10\ nm$ and $\sigma_p = 3.43\ nm$). Therefore, the fractal dimension and fractal prefactor are unknown and must be estimated. D_f can be evaluated from the slope of a linear regression, in log-log scale, of the number of monomers n_p versus the ratio $R_g / \overline{r}_p$:

$$\ln\left(n_p\right) = \ln k_f + D_f \ln\left(\frac{R_g}{\overline{r}_p}\right). \tag{2.29}$$

With Eq. (2.29) we can only access to an average or "global" fractal dimension for the entire sample and it is not necessary to determine k_f to obtain D_f. However, the fractal prefactor is simply estimated as an intersection point of the regression line and $oy-\text{axis}$.

Figure 2.27 shows the number of monomers versus normalized radius of gyration for the numerical test sample of the DLCA aggregates in the log-log scale. It is clear that the curve shown in Figure 2.27 exhibits two different slopes for $\log\left(R_g / \overline{r}_p\right) < 0.4$ (referred to as region "A" latter on) or $\log\left(R_g / \overline{r}_p\right) > 0.4$ (referred as region "B"). It should be noticed that the first

range corresponds to the aggregates with $\log\left(R_g / \overline{r}_p\right) \leq 0.4$ (i.e. $R_g / \overline{r}_p \leq 2.512$). In this range, aggregates are very small (approximately with $n_p < 8$), so they do not exhibit true fractal properties. Thus, due to their size we cannot define them as self-similar objects, so it is doubtful to estimate their fractal properties.

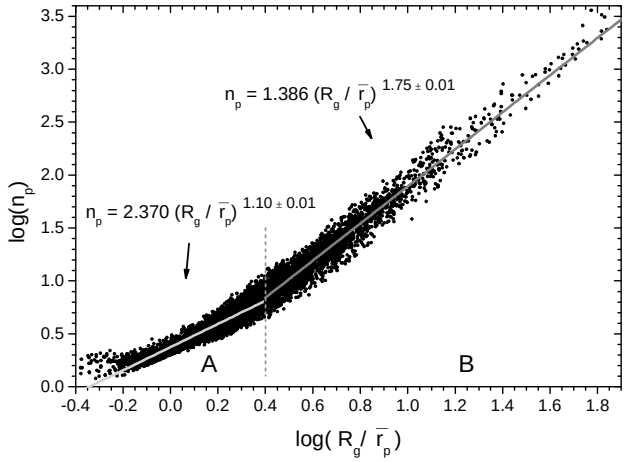

Figure 2.27. Number of monomers versus normalized radius of gyration for the numerical test sample of the DLCA aggregates (Yon et al. 2008) in the log-log scale.

This sample is not homogenous. The first slope may be interpreted as the first stage of the aggregation, where mainly DLA process occurs. The second slope could be attributed to aggregates produced simultaneously by DLA and DLCA phenomena. The "global" fractal dimension estimated in the region "A" is equal to $D_f = 1.10 \pm 0.01$ with the fractal prefactor $k_f = 2.370$. Figure 2.28 shows the estimation of the fractal dimension for the selected 2654 aggregates of the DLCA sample from the region "B". The "global" fractal dimension estimated for these aggregates is significantly larger than for the previous case, it is equal to $D_f = 1.75 \pm 0.01$ with the fractal prefactor $k_f = 1.386$.

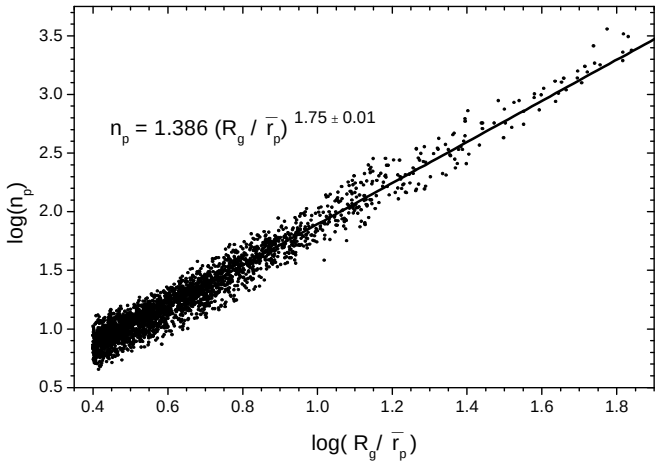

Figure 2.28. Estimation of the fractal dimension for synthetic aggregates: raw data points and linear regression (the log-log scale) of the number of monomers versus the $R_g / \overline{r}_p$ ratio.

An alternative way to determine k_f is to use the slope of a linear regression fitting n_p versus the $\left(R_g / \overline{r}_p\right)^{D_f}$. Figure 2.29 shows estimation of the fractal prefactor for the previous sample of aggregates. It can be seen that in this case, the estimation procedure is strongly biased by the strong non-linearity in the distribution of the raw data points. Thus, the fractal prefactor evaluated in this method equal to $k_f = 1.518$ is mainly determined by the largest aggregates.

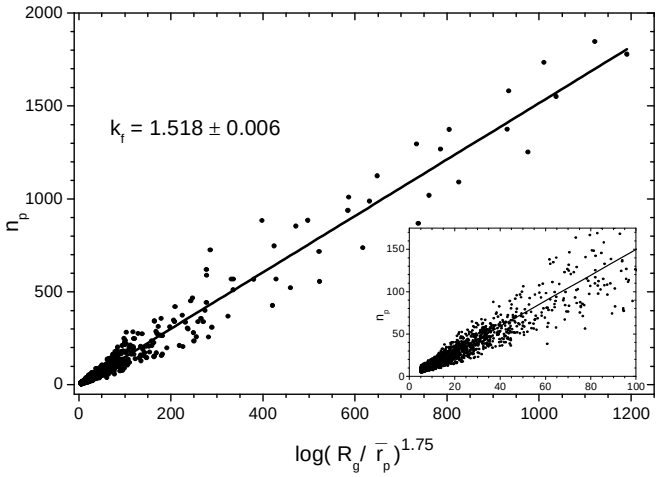

Figure 2.29. An alternative methods for estimation of the fractal prefactor: (b) raw data points and linear regressions of the plot of the number of monomers versus the $\left(R_g / \overline{r}_p\right)^{D_f}$.

2.4.3. Non-homogeneity of the fractal dimension

Looking at the high dispersion of the raw data points presented in Figure 2.28 one may conclude that the fractal dimension of the sample of the DLCA aggregates is not homogenous. Indeed, to fully characterize the aggregates, rather than a "global" fractal dimension, various D_f for each aggregate must be evaluated. To do so, we fixed k_f to 1.386 and use it in the fractal equation (2.13) for each aggregate separately. Figure 2.30 shows the histogram of the fractal dimensions evaluated for 2654 aggregates from the region "B" of the sample of DLCA aggregates. A similar histogram is obtained for all the aggregates (from both regions) satisfying the fractal equation (i.e. with $n_p \geq 3$), see Figure 2.31.

Analyzing Figure 2.30 and Figure 2.31 it can be noticed that the fractal dimension of DLCA aggregates is highly polydisperse. The average value evaluated for the aggregates with $R_g > 2.512\overline{r}_p$ is equal to $D_f = 1.754$ and it is in a perfect agreement with previously estimated the "global" value $D_f = 1.75 \pm 0.01$. The average value of the fractal dimension for all the aggregates with $n_p \geq 3$ is significantly larger: $D_f = 1.915$. Nevertheless, as mentioned previously, self-similarity properties of small aggregates are questionable.

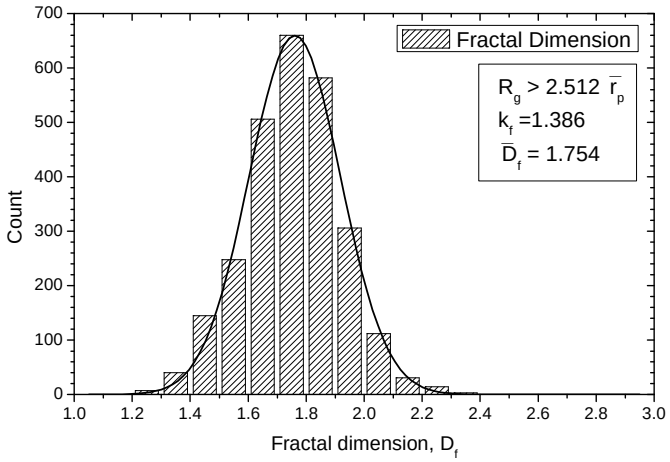

Figure 2.30. Distribution of the fractal dimension of the DLCA aggregates with $\log\left(R_g / \overline{r}_p\right) > 0.4$.

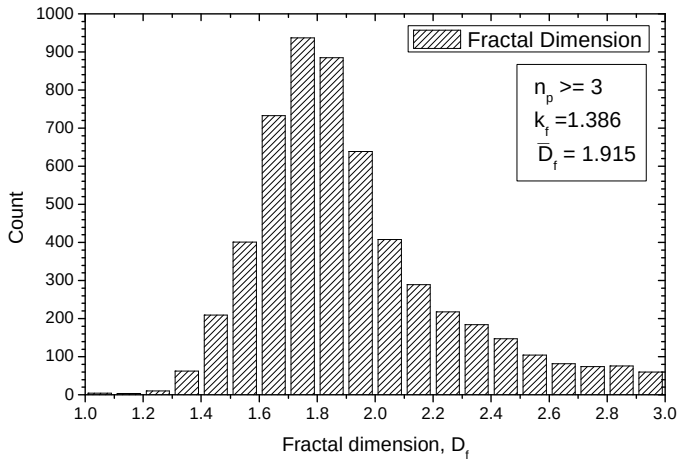

Figure 2.31. Distribution of the fractal dimension of the DLCA aggregates with $n_p \geq 3$.

2.4.4. Sticking DLA aggregates

The most intuitive way to generate DLCA aggregates is to stick together two (or more) DLA aggregates. Using this procedure (not so rigorous from the physical point of view), it is possible to generate DLCA aggregates and compare morphological differences between DLA and DLCA aggregates regarding their parameters. As an example, we stick together pairs of aggregates with $n_p = 100$ monomers and various fractal dimensions ($D_f = 1.25$, 1.50, 1.75, 2.00, 2.25, 2.50 and 2.75). For each fractal dimension we used 100 different pairs of aggregates and stick them for 1000 random orientations in 3-dimensional space. Distribution of the resulting fractal dimension is shown in Figure 2.32.

Looking at the distributions of the fractal dimension presented in Figure 2.32 we conclude that collision between two aggregates with the same fractal dimension leads to the lower average value of D_f for aggregates with medium or high fractal dimension ($D_f > 1.50$). For dilute aggregates ($D_f < 1.50$) the average fractal dimension after collision is smaller than the initial one. At the same time, the standard deviation of the D_f is significantly decreasing

when fractal dimension increases. It is a direct consequence of the fact, that dilute aggregates may stick together in much more different configurations than the opaque ones.

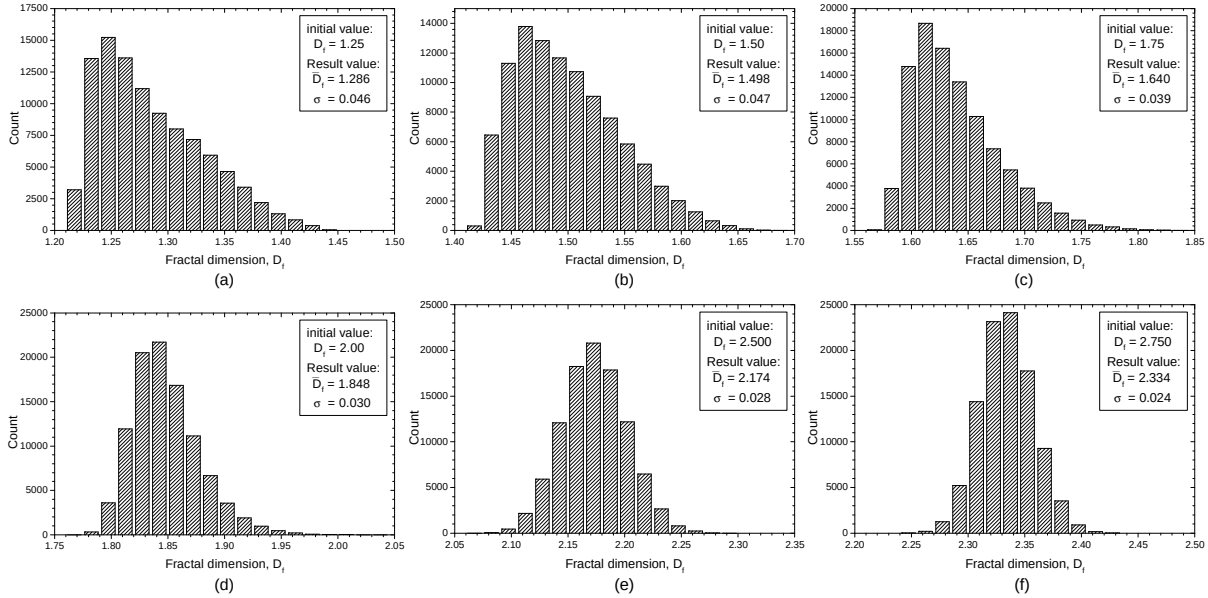

Figure 2.32. Distribution of the fractal dimension of 10000 aggregates with the total number of $n_p = 200$ monomers generated by sticking 100 pairs of aggregates with $n_p = 100$ for 1000 random orientations of each of them. Initial fractal dimension of aggregates: (a) $D_f = 1.25$ (b) $D_f = 1.50$, (c) $D_f = 1.75$, (d) $D_f = 2.00$, (e) $D_f = 2.50$, (f) $D_f = 2.75$.

As an example of the sticking procedure described above, Figure 2.33 - Figure 2.35 show some of the generated aggregates. All of them contain $n_p = 200$ monomers and have the same equivalent radius in volume $R_v = 5.85$ but different fractal dimensions. They were generated by sticking the aggregates with various fractal dimensions and radiuses of gyrations.

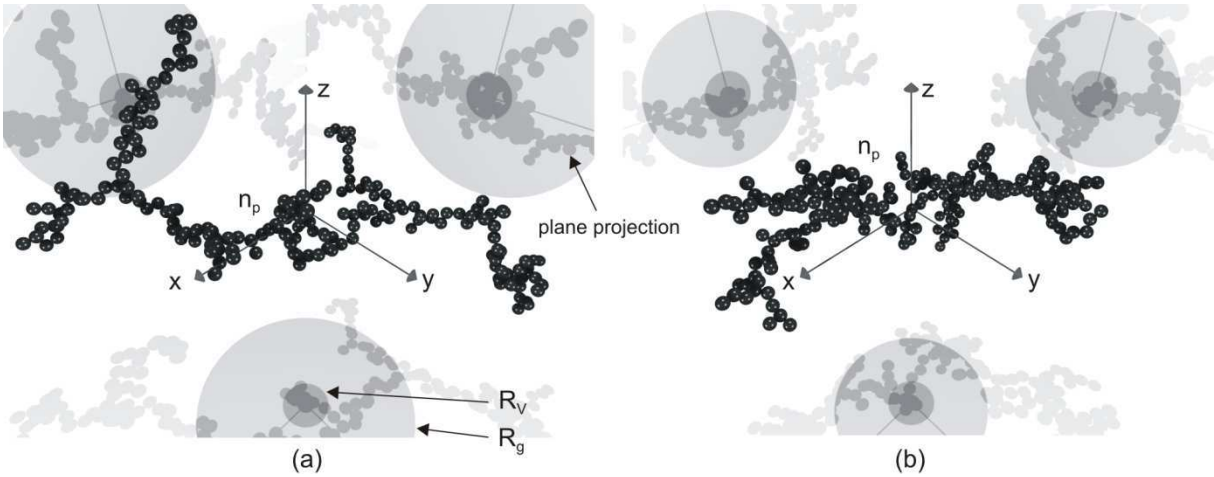

Figure 2.33. Fractal aggregates with the total number of $n_p = 200$ monomers and the same equivalent radius in volume $R_v = 5.85$ but various fractal dimensions and radiuses of gyration: (a) $D_f = 1.484$, $R_g = 25.93$ and (b) $D_f = 1.662$, $R_g = 18.31$ generated by sticking two aggregates of $n_p = 100$ monomers with: (a) $D_f = 1.50$, $R_g = 15.80$ and (b) $D_f = 1.75$, $R_g = 11.41$.

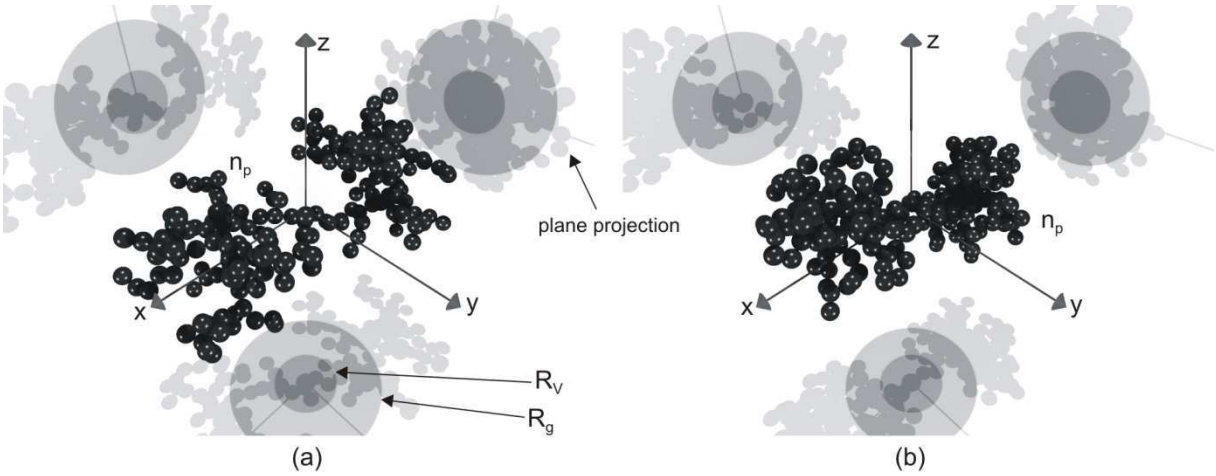

Figure 2.34. Fractal aggregates with the total number of $n_p = 200$ monomers and the same equivalent radius in volume $R_v = 5.85$ but various fractal dimensions and radiuses of gyration: (a) $D_f = 1.866$, $R_g = 13.32$ and (b) $D_f = 1.977$, $R_g = 11.52$ generated by sticking two aggregates of $n_p = 100$ monomers with: (a) $D_f = 2.00$, $R_g = 7.92$ and (b) $D_f = 2.25$, $R_g = 6.30$.

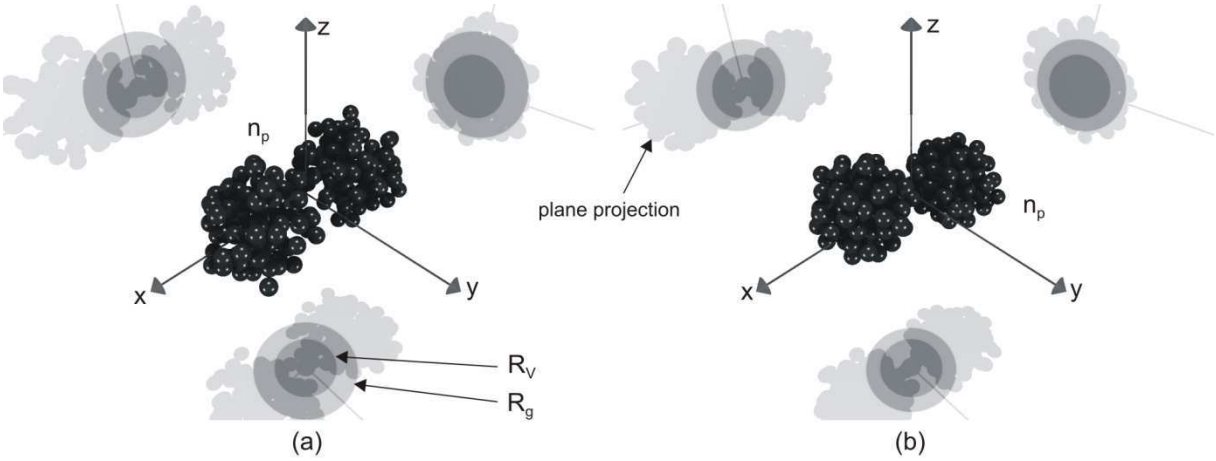

Figure 2.35. Fractal aggregates with the total number of $n_p = 200$ monomers and the same equivalent radius in volume $R_v = 5.85$ but various fractal dimensions and radiuses of gyration: (a) $D_f = 2.192$, $R_g = 9.07$ and (b) $D_f = 2.233$, $R_g = 7.94$ generated by sticking two aggregates of $n_p = 100$ monomers with: (a) $D_f = 2.50$, $R_g = 5.23$ and (b) $D_f = 2.75$, $R_g = 4.51$.

2.5. Buckyballs aggregates

2.5.1. Introduction

The regular aggregates of silica nanobeads formed by the spray drying method (see Figure 2.36) show strong, if not astonishing, similarity to the morphology of the "fullerene" or "buckyballs" molecules: (i.e. Carbon (C_{60} , C_{540}), Bore (B_{80} , B_{92}), etc.).

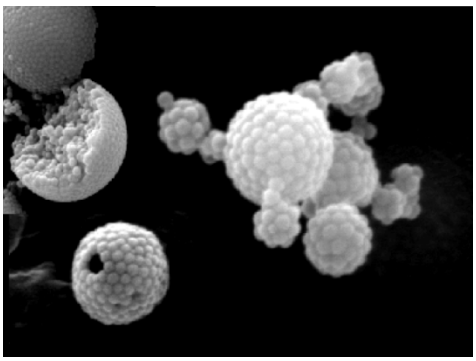

Figure 2.36. Aggregates of silica nanobeads with a Buckyball shape (size: from few tens of nanometers to one or two micrometers).

Each of the latter molecules is formed by a set of atoms localized at the vertices of a close and regular (but not fully) polyhedron having pentagons and hexagons faces ($4, 6, 8, 10$), see Figure 2.37. On the other hand, it is known from Euler's Theorem ("12 pentagons rule") that any *regular* and close polyhedron must contains 12 pentagonal faces, whereas it can contains any number of hexagonal faces (i.e. the number of hexagon may follow other constraints like the overall sphericity of the polyhedron). Based on the clear evidence that the silica nanobeads observed are also organized in a pentagonal and hexagonal lattice, we naturally came to the idea that a geodesic dome model is the most suitable to describe the morphology of buckyballs of silica nanobeads that we were (initially) observed experimentally (Toure 2010; Barbosa et al. 2012; Onofri et al. 2012a).

If the geodesic dome model is commonly used to produce geodesic surfaces that fit rather well the spherical (or other convex) surfaces, the particularity and novelty of our model is that we place silica nanobeads almost *in contact* at the vertices of the regular and convex polyhedron generated with this method (Toure 2010).

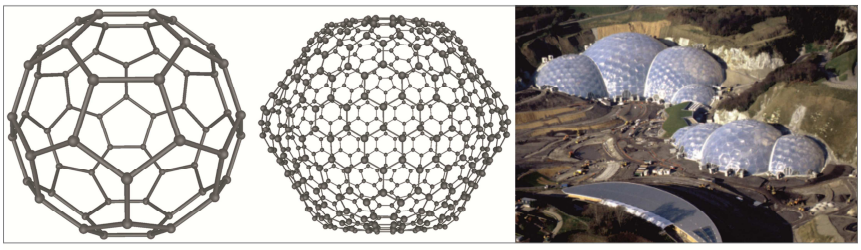

Figure 2.37. From left to right: fullerene (C_{60} , C_{540}) - Geodesic Domes (Eden, Germany) (Toure 2010).

2.5.2. Geodesic dome model to describe Buckyballs morphology

To generate a geode, we first need to select a regular polyhedron. Among the five platonic solids (regular polyhedra: tetrahedron, octahedron, hexahedron, icosahedron and dodecahedron), we have chosen the icosahedron, since it better fit the spherical shape. The icosahedron is composed of $n_{Face} = 20$ identical equilateral triangular faces, $n_{Edg.} = 30$ edges and $n_{Vert.} = 12$ vertices. By placing a monomer at each of its vertices, we obtain a buckyball of $n_p = 12$ identical monomers. It should be noticed that these monomers will be at the same time at the center of the faces of the dual polyhedron of the icosahedron (i.e. the dodecahedron with $n_{Face} = 12$, $n_{Edg.} = 30$ and $n_{Vert.} = 20$). Basically, our model to describe large buckyballs (i.e. $n_p \geq 12$) is composed of four steps (Toure 2010): (i) description of various properties of the icosahedron and the related buckyballs, (ii) decomposition of each face of the icosahedron into smaller regular triangles, (iii) projection of the related new vertices on the sphere circumscribed to the icosahedron and (iv) optimization of the radius of the monomers that will be localized at each projected vertex position.

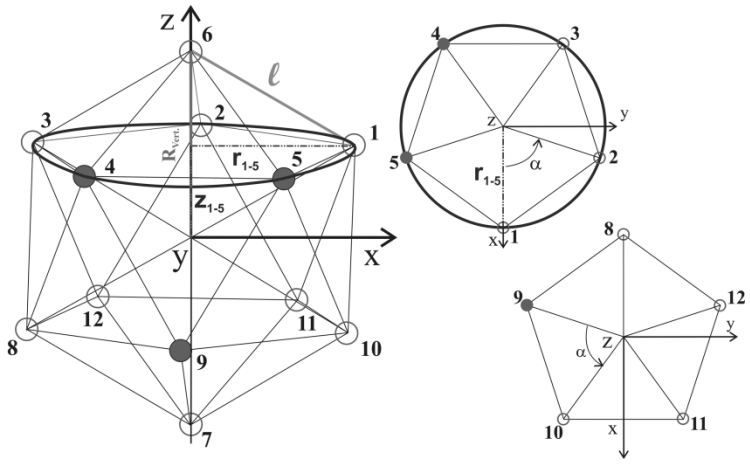

Figure 2.38. Illustration of some parameters of the icosahedron.

2.5.2.1. Some important relations in the icosahedron

We first calculate the coordinates of the vertices of the icosahedron of edge length *l*. The radius of the sphere circumscribed that passes through all vertices of the icosahedron (see Figure 2.38) is equal to:

$$R_{Vert.} = l \sin\alpha = l \sin\frac{2\pi}{5}. \tag{2.30}$$

To find the coordinates of the vertices of the icosahedron, located at the center of the (x, y, z) Cartesian system (see Figure 2.38), we first calculate the intersection plain of the sphere circumscribed to the icosahedron and the sphere of radius l centered on the vertices 6. It should be noticed that all vertices 1, 2 3, 4 and 5 pertain to this intersection plan which equation may be deduced from:

$$\begin{cases} x^2 + y^2 + z^2 = R_{Vert.}^2, \\ (x-0)^2 + (y-0)^2 + (z - R_{Vert.})^2 = l^2. \end{cases} \tag{2.31}$$

The equation of the intersection plain and the third coordinate of the vertices 1-5 are:

$$z \equiv z_{1-5} = R_{Vert.} - l^2 / (2R_{Vert.}) = l \left[\sin\alpha - (2\sin\alpha)^{-1} \right]. \tag{2.32}$$

With Eqs. (2.30) and (2.32), and with the equation of the circumscribed sphere, we obtained for the radius of the circle passing by the vertices 1-5:

$$r_{1-5} = l\sqrt{1 + 1(4\cos^2\alpha - 1)}. \tag{2.33}$$

Finally, the coordinates of the vertices 1, 2, 3, 4, 5 are $(X,Y,Z) = (r_{1-5}\cos(n\alpha),\ r_{1-5}\sin(n\alpha),\ z_{1-5})$ with *n=0, 1, 2, 3, 4* respectively. By symmetry, the coordinates of the vertex *7* are equal to $(0,0,-R_{Vert.})$ and those of vertices *8, 9, 10, 11* and *12* to $(r_{1-5}\cos(n\alpha+\pi),\ r_{1-5}\sin(n\alpha+\pi),\ -z_{1-5})$ respectively.

By placing monomers at the icosahedron vertices, i.e. $l = 2r_p$, we obtain for the radius of the circumscribed sphere passing by the center of all monomers:

$$R_{Vert.} = 2r_p \sin\alpha, \tag{2.34}$$

and the circumscribed sphere touching the buckyball of $n_p = 12$ external diameter:

$$R_e = r_p (2\sin\alpha + 1). \tag{2.35}$$

It may also be useful to derive the radius of the monomers from the external radius of the buckyball:

$$r_p = (2\sin\alpha + 1)^{-1} R_e. \tag{2.36}$$

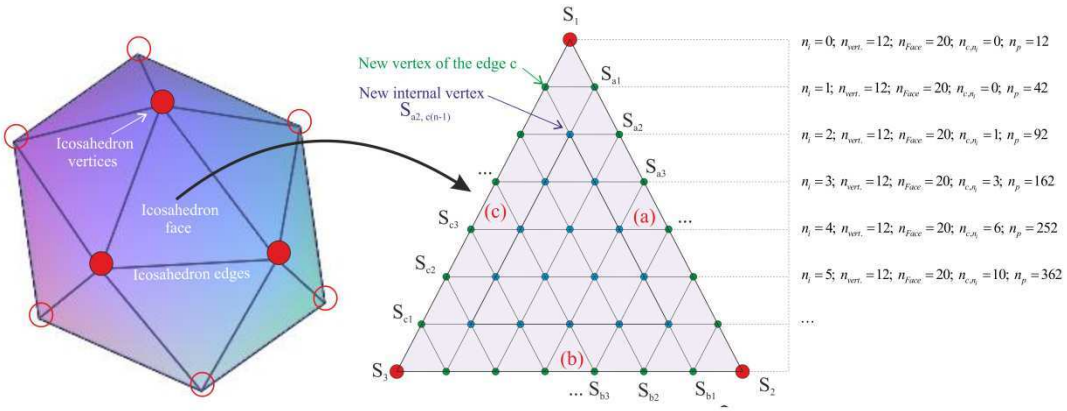

Figure 2.39 Geodesic dome model: decomposition of the icosahedron elementary faces into smaller regular triangular faces.

2.5.2.2. Building large and regular polyhedron

To build larger buckyballs with the geodesic dome model, each edge of the icosahedron is divided into $n_i + 1$ line segments of equal length (see Figure 2.39), where $n_i \geq 0$ is an integer number corresponding to the number of new vertices introduced along each nominal edge

(noted *a, b, c* in Figure 2.39). By drawing line segments of equal length, passing through these new vertices and being at the same time parallel to the edges of the face of the icosahedron, we produce new regular triangles. These smaller triangles are defined by the vertices located on the edges of the face of the icosahedron face plus the ones that are inside the corresponding icosahedron face. So that for each face of the icosahedron we obtain n_i^2 smaller identical equilateral triangular faces and a total number of vertices equal to n_p. As a first step, we evaluate empirically the relation between n_p and n_i, with $n_p = 12,\ 42,\ 92,\ 162,\ 252,\ 362,...$ for $n_i = 0,\ 1,\ 2,\ 3,\ 4,\ 5,...$ respectively (see Figure 2.39). It is easy to show that the values of n_p evolve as:

$$\begin{aligned} n_{p,n_i=0} &= n_{Vert.}, \\ n_{p,n_i>0} &= n_{Vert.} + n_{Face}\left(\frac{3n_i}{2} + n_{c,n_i}\right), \end{aligned} \tag{2.37}$$

where the coefficient $3/2$ accounts for the fact that the vertices on the edges of the triangular faces of the icosahedron are common to two of its adjacent faces (green symbols in Figure 2.37 (a)). n_{c,n_i} stands for the number of vertices inside the considered icosahedron face (i.e. ball symbols in Figure 2.39) with $n_{c,ni} = 0,\ 1,\ 3,\ 6,\ 15,\ 21,...$ when $n_i = 0,\ 1,\ 2,\ 3,\ 4,\ 5,...$ respectively. The number of the internal vertices obeys the arithmetic progression:

$$n_{c,n_i=0} = 0;\ \ n_{c,n_i>0} = 2n_{c,n_i} - n_{c,n_i-1} + 1 = \frac{n_i\left(n_i-1\right)}{2}. \tag{2.38}$$

Finally, the total number of vertices of the buckyballs is:

$$\begin{cases} n_i = 0,\ \ n_p = n_{Ver}, \\ n_i > 0;\ \ n_p = n_{Ver} + \dfrac{n_i\left(n_i+2\right)n_{Face}}{2}. \end{cases} \tag{2.39}$$

Later on, it will be useful to have an expression relying $n_i > 1$ to n_p:

$$n_i = \sqrt{1 + 2\left(\frac{n_p - n_{Ver}}{n_{Face}}\right)} - 1. \tag{2.40}$$

The edge length of a buckyball of $n_p = f\left(n_i\right)$ monomers can be derived from its *approximated*[1] edge length (in Figure 2.37 (a)):

$$l \equiv \left(2n_i + 1\right)r_p. \tag{2.41}$$

Thus we finally obtain for the external radius of the buckyball of n_p particles:

$$\frac{R_{Vert.}}{r_p} = \left[2\left(\sqrt{1 + 2\left(\frac{n_p - n_{Ver}}{n_{Face}}\right)} - 1\right) + 1\right]\sin\frac{2\pi}{5} + 1. \tag{2.42}$$

The coordinates of the new vertices, are more particularly those located on the edges *a, b, c:* S_{ai}, S_{bi}, S_{ci} (see Figure 2.39), can be derived with simple linear relations from the coordinates

[1] It is only an approximation since the monomer will be not fully monodisperse (see later on).

of the icosahedron vertices. As an example, for the edge *a*, the coordinates of the vertices are, with $i = 0,\ 1,\ ...,\ n_i$, given by:

$$X_{ai} = X_1 + \frac{i}{n_i + 1}(X_2 - X_1);\ Y_{ai} = Y_1 + \frac{i}{n_i + 1}(Y_2 - Y_1);\ Z_{ai} = Z_1 + \frac{i}{n_i + 1}(Z_2 - Z_1). \qquad (2.43)$$

A similar procedure can be used to deduce the coordinate of the vertices inside each face of the icosahedron (Toure 2010; Onofri et al. 2012a).

2.5.2.3. Projection of the circumscribed sphere

To obtain large buckyballs with a spherical shape, the vertices of all small equilateral triangles are projected onto the circumscribed sphere. This is simply done with a homothetic transformation of center $(0,0,0)$ and similitude ratio γ (see Figure 2.40 (a)). We found for the coordinates X', Y' and Z' of the projected vertices:

$$X' = \gamma X\ ;Y' = \gamma Y\ ;X' = \gamma Z\ ,with\ \ \gamma = R_{Vert.} / \sqrt{X^2 + Y^2 + Z^2}. \qquad (2.44)$$

Figure 2.40 (a) shows the vertices on the regular polyhedron (in black) and their projected image onto the circumscribed sphere. At all of these projected vertices a monomer will be set. However, due to the projection onto the circumscribed sphere, the edges of the projected triangles are curved and they have slightly different lengths (i.e. in Figure 2.40 (a) the length noted ℓ and ℓ^+ are clearly different). For molecules this implies that the interaction forces are slightly different between each atom. For buckyballs, this distortion implies that the monomers are necessary slightly polydisperse and/or not fully in contact (5 or 6 points).

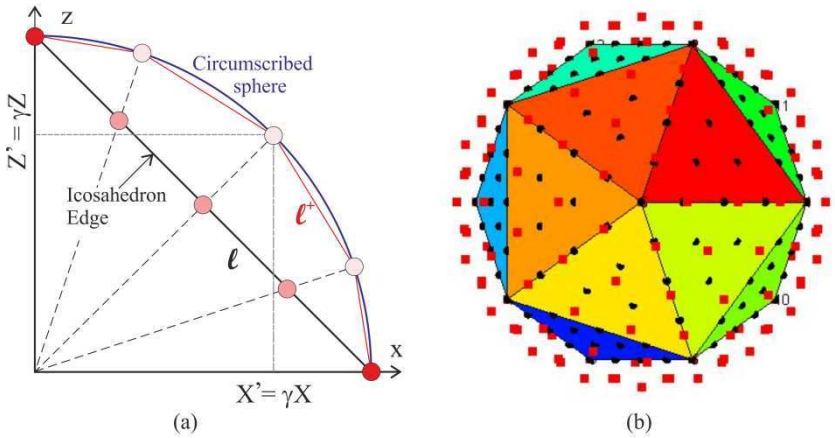

Figure 2.40 Projection of the vertices on the circumscribed sphere (Toure 2010; Onofri et al. 2012a).

2.5.2.4. Optimization of the radius of each monomer

As the buckyball of 12 monomers is directly build from the icosahedron, it is easy to conclude that all monomers are in contact with their five neighbors and that they are

monodisperse when $r_p = R_{Vert.}$. For larger buckyballs, one additional step is necessary to minimize gaps and overlapping between the monomers. To do so, keeping constant the position of each monomer, the size of each monomer is adjusted iteratively until we obtain each monomer is in contact with at least another one (the monomer size distribution remains narrow, see Figure 2.44). With this procedure, the maximum contact point is only ensured for the monomers that are at the center of the pentagon's (i.e. 5 contacts). The fact that all monomers are not strictly in contact could be a problem to simulate the scattering properties of metallic aggregates (i.e. plasmon resonances). However, for buckyballs of dielectric spheres, this accuracy is thought to be far enough.

2.5.2.5. Filling Buckyballs

Even if there are some experimental evidences that aggregates of silica nanobeads may be empty (like those produced with the geodesic dome model), the great majority of them seem to be filled with nanobeads. Unfortunately, we do not have any information about the internal packing structure. Then, as a first step and to make the things simple, we have developed two filling procedures using (i) hexagonal compact (HC) aggregate and (ii) fractal aggregate with the maximum compactness achievable with our DLA code (i.e. $D_f = 2.88$) imposed before the filling procedure. These two solutions, allow to obtain buckyballs with a volume fraction about 50%. For the HC case, the Buckyballs with $n_p = 12,\ 42,\ 92,\ 162,\ 252,\ 362,...$ contain finally $n_{p,HC} = 13,\ 44,\ 111,\ 249,\ 509,\ 749,...$ nanoparticles. For the filling procedure with fractal aggregates, the buckyballs contain $n_{p,D_f} = 13,\ 44,\ 111,\ 234,\ 434,\ 709,...$ nanoparticles respectively.

2.5.3. Numerical examples

All the aforementioned algorithms, for the modeling of small to large buckyballs that are empty (shell) or filled, were implemented under MATLAB environment. Figure 2.41 shows 3D-rendering views (with POV-Ray (POV-Ray 2004)) of shell-buckyballs containing $n_p = 12,\ 42,\ ...,\ 1002$ monomers (normalized radiuses). All monomers with radius $r_p < 1$ are pointed out in black. One can remark that the latter monomers are localized at the center of the pentagons whatever, for the largest buckyballs, they spread out all around the pentagons.

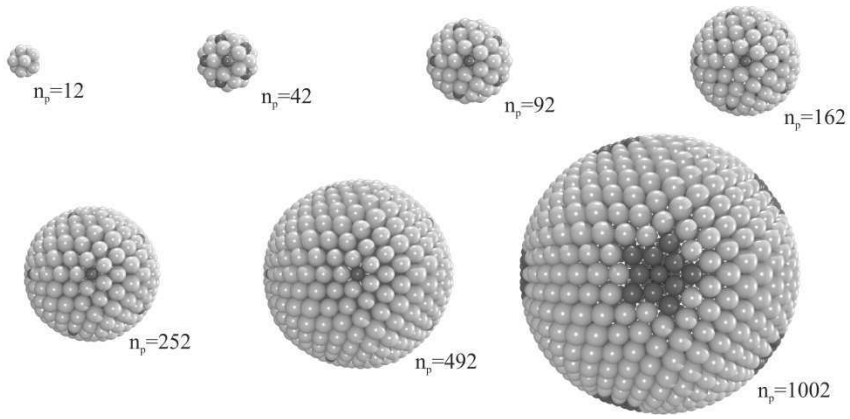

Figure 2.41. 3D-rendering of buckyballs with increasing number of monomers n_p.

Figure 2.42 shows a compact and dilated ($\times 1.5$) buckyball with $n_p = 92$. The bonds between each monomer and its closest neighbors are also illustrated. Figure 2.43 shows synthetic TEM images of a buckyball which is empty ($n_p = 162$) or filled with hexagonal compact ($n_{p,HC} = 162 + 87$) or fractal ($n_{p,D_f} = 162 + 72$) aggregates. Figure 2.44 shows all inter-distances, and the related statistics, between the monomers of the buckyballs of $n_p = 42$ and $n_p = 362$ monomers. For both cases, the standard deviation of the monomers inter-distances is below 7.2% with a standard deviation of the radiuses of less than 11% and 8% respectively.

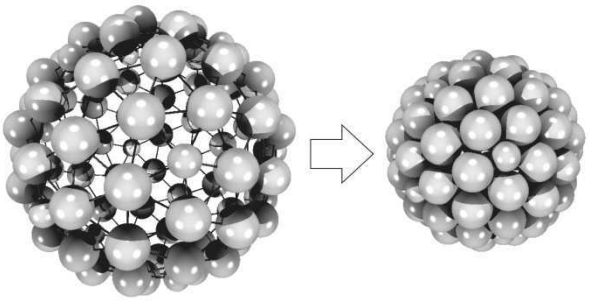

Figure 2.42. Buckyball of $n_p = 92$ monomers: dilated and compact forms with an illustration of monomers "bonds".

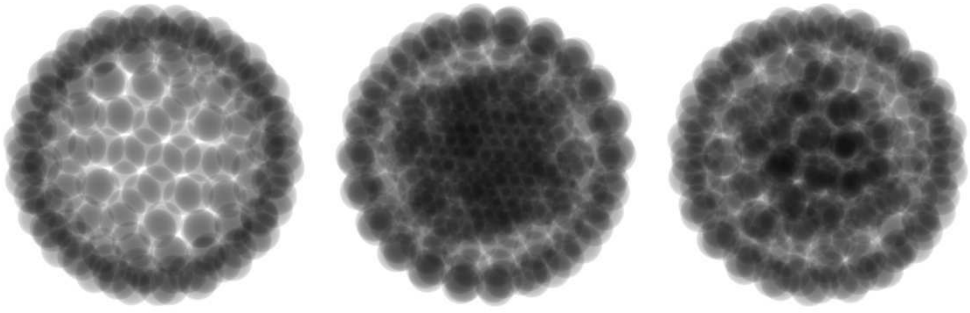

Figure 2.43. Synthetic TEM images generated for the same geodesic dome parameters. Buckyballs: (a) empty ($n_p = 162$, volume fraction 32%) or filled with (b) an hexagonal compact ($n_{p,HC} = 162 + 87$ spheres, volume fraction 52%) or (c) a fractal aggregate ($n_{p,D_f} = 162 + 72$ spheres, $D_f = 2.88$, volume fraction 49%).

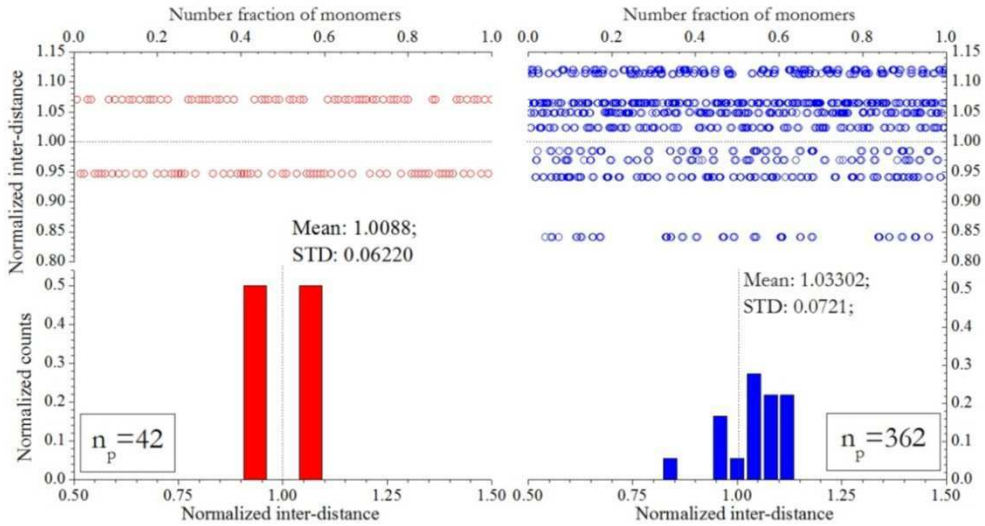

Figure 2.44. Normalized monomers inter-distances for empty buckyballs of $n_p = 42$ and $n_p = 362$ monomers.

2.6. Conclusion

In this chapter we have introduced two particle models to describe the morphology of nanoparticle aggregates. The first of them, the fractal-like model, is based on the self-similarity concept or structure invariance at each scale. Its basic assumptions are well known and widely used in the literature to describe DLA, DLCA or RLCA aggregates. However, we have developed a tunable DLA algorithm and code which deliberately avoid any complex physical, mechanical or chemical dependencies. It is however a universal and well-defined model, which provides reproducible results. This particle model is used throughout this manuscript to test the developed algorithms, to calibrate the morphological analysis obtained by electron microscopy (Chapter 3), to test the light scattering models (Chapter 4) as well to inverse experimental data (Chapter 6). The second model, referenced hare as the Buckyballs model, allows to produce highly symmetrical aggregates that have been observed experimentally. This model is used to inverse experimental light extinction spectra obtained for aerosol of silica nanobeads aggregates (Chapter 6).

Chapter 3

TEM-BASED METHODS FOR THE ANALYSIS OF FRACTAL-LIKE AGGREGATES

3.1. Introduction

In this work the two privileged experimental approaches to investigate aggregates of nanoparticles are used: the light extinction and the small angle scattering techniques. They provide an on-line and in-situ analysis of various particle systems. However, up to now for most scientists, the Transmission Electron Microscopy (TEM) and X-ray scattering techniques remain the reference methods to characterize soot aggregates (e.g., (Hessler et al. 2002; Braun et al. 2004; Mitchell et al. 2009)) or dust formed in plasma systems (e.g. (Sharpe et al. 2003; Arnas et al. 2005; Glenzer and Redmer 2009)). Indeed, even though TEM-based analyses are known to be partly biased due to sampling and storage procedures (e.g. (Koylu et al. 1995; Chakrabarty et al. 2009; Ouf et al. 2010)) they offer fundamental advantages over optical techniques. For instance, they allow a direct measurement of the two-dimensional (2D) projected image of each collected aggregate over a huge size range, while being at the same time only slightly sensitive to the properties of primary particle material. All the aforementioned issues explain why over the last decades a huge effort has been devoted to develop global Transmission Electron Microscopy (TEM) based method for estimating the size distribution and average fractal dimension of collected samples. However, this global approach is not suitable for aggregate samples that do not have homogeneous fractal dimension.

As an example, Figure 3.1 (Woźniak et al. 2012a; Woźniak et al. 2012b) shows TEM-based analyses of 543 soot aggregates produced by a diesel flame (Yon et al. 2011). Several results, which will be detailed and discussed throughout this chapter, are presented in this figure:

(i) the number distribution of the normalized radius of gyration; (ii) typical binarized TEM images of soot aggregates with their fractal dimension estimated by the proposed Modified Box-Counting method (MBC, see below) and (iii) the fractal dimension of the whole sample estimated with the conventional Minimum Bounding Rectangle method (MBR, see below). With the MBR method we found a rather typical value for the average fractal dimension of diesel soot: $D_f = 1.88 \pm 0.01$ (e.g. (Yon et al. 2011)). Nonetheless, from a quick view of TEM images, one may intuit that the smallest aggregates have a significantly greater fractal dimension than the largest ones. If such a correlation exists (i.e. the experimental sample is multi-fractal), this could have major implications for our understanding of aggregation and growing mechanisms. To clarify this point, one must be able to estimate the fractal dimension at different size scales (i.e. as we did with the MBC method) and to quantify the error made.

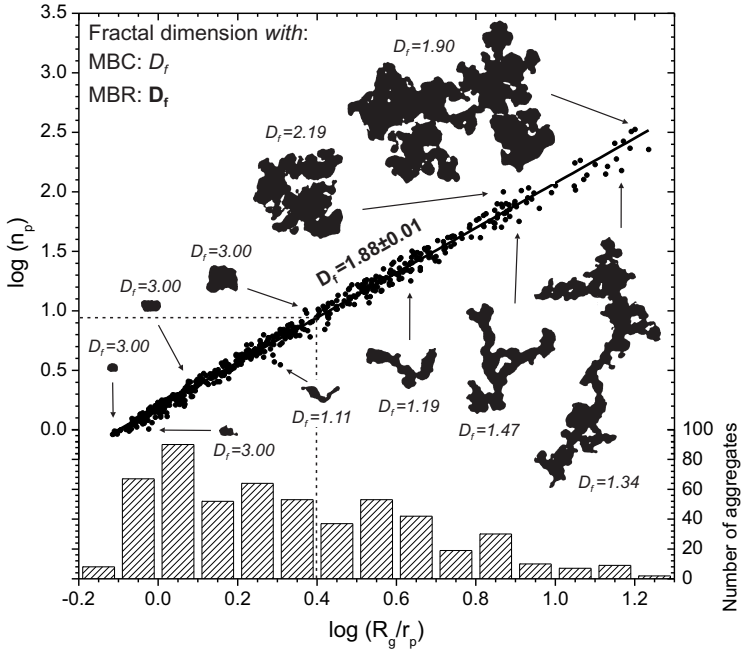

Figure 3.1. TEM-based analyses of an experimental sample of diesel soot: number distribution of their normalized radius of gyration and estimated fractal dimension. The fractal dimension is obtained with the conventional Minimum Bounding Rectangle method (single value, in bold) and the Modified Box-Counting method (for each aggregate, in italic) (Woźniak et al. 2012b).

Thus, in this chapter we present the work done to discuss and develop two approaches for detecting correlations between the fractal dimension and the radius of gyration of a limited sample of fractal-like nanoparticle aggregates (Woźniak et al. 2012a; Woźniak et al. 2012b). The chapter is organized as follows. Section 3.2 presents the model developed to simulate synthetic TEM images of fractal aggregates, as well as the pre-processing schemes used to filter out TEM images and extract the overlapping factor of particle image pairs. Section 3.3 details the principle of and improvements on two methods used to estimate the morphological properties of aggregates on the basis of their TEM images. Section 3.4 presents and discusses

the results obtained with these methods when applied to experimental and synthetic test samples. Section 3.5 is an overall conclusion.

It should be noticed that, this chapter mostly presents analysis of the experimental diesel soot aggregates (Yon et al. 2011) as well as synthetic test samples generated with our DLA-TEM software. However we analyze also silicon carbide (SiC) nanoaggregates provided by CILAS company, which have, indeed, rather similar properties than diesel soot.

3.2. Modeling and images pre-processing schemes

3.2.1. Modeling of TEM images

To obtain synthetic TEM images, a simple macroscopic model for electron absorption was used. Assuming a single scattering regime and amorphous primary particles, electron propagation and absorption were described by a ray path model and the Beer-Lambert law. It was further assumed here that TEM optical conversion and imaging systems are linear.

Figure 3.2 outlines the modeling procedure, where x_0y_0 and xy are respectively the default emission and imaging planes, parallel to each other, while electrons (i.e. rays) propagate along z. L is the inter-distance between the planes that are both discretized into $N\times M$ elements, with $i=1,...,N$ and $j=1,...,M$. With I_0 being the initial intensity of an incident electron beam and I_L the intensity of the corresponding transmitted beam, the transmission rate T for the beam (i,j) is given by:

$$T_L(i,j)=\frac{I_L(i,j)}{I_0}=\exp\left[-K_p\sum_{n=1}^{\underline{p}(i,j)}l_{p,n}-K_m\sum_{q=1}^{\underline{m}(i,j)}l_{m,q}\right], \tag{3.1}$$

where $l_{p,n}$, $l_{m,q}$, $\underline{p}(i,j)$, $\underline{m}(i,j)$, K_p and K_m respectively represent the electron path lengths within the $n-th$ primary particle and within the $g-th$ external medium gap, the number of primary particles and external medium gaps crossed by the ray (i,j), and the primary particle and external medium absorption constants. All the path lengths $l_{p,n}$, $l_{m,q}$ were determined by calculating the geometric intersection points between each incident ray and the surface of all primary particles within the aggregates. TEM images were simulated by transforming the transmission matrix into a gray-level image:

$$I_{TEM}(i,j)=gT_L(i,j)-\delta_{TEM}, \tag{3.2}$$

where g is the overall gain of the optical conversion and imaging system, and δ_{TEM} the mean background noise and offset of the TEM image. Ideally, with an 8-bit camera and an infinite signal-to-noise ratio, we find that $g=255$ and $\delta_{TEM}=0$. This simple model and the related Windows-based DLA-TEM code can also take into account parameters such as the contrast, brightness or gamma factor of the imaging system. Regarding the difficulty to find tabulated data for K_p, we just estimate its value from experimental TEM images. For nearly spherical primary particles, by measuring their radius and the minimum gray levels of their experimental TEM image, we find that:

$$K_p = -\ln\left[\left(Min\left\{I_{TEM}(i,j)\right\} + \delta_{TEM}\right) / gI_0\right] / r_p. \tag{3.3}$$

Figure 3.2 shows a typical synthetic aggregate of hard spheres in contact (3D-rendering with POV-Ray software (POV-Ray 2004)) and its associated TEM image (produced with the algorithm described above, with $D_f = 1.50$, $n_p = 25$, $R_g / r_p = 6.27$, $N = M = 1024$, $K_p = 1$, $K_m = 0$).

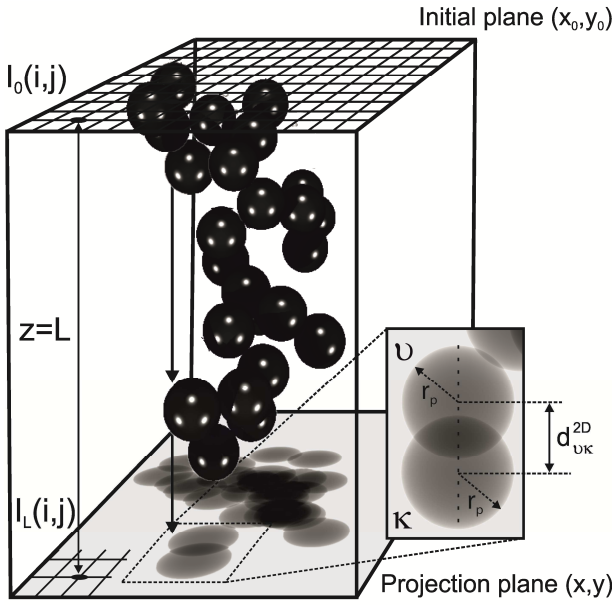

Figure 3.2. 3D rendering with the POV-Ray software and 2D TEM image (with our model) of a synthetic aggregate with: $D_f = 1.50$, $n_p = 25$, $R_g / r_p = 6.27$.

This algorithm has been implemented in the DLA software, tab "TEM" (see Figure 3.3). The TEM tab of the software is composed of six separate panels. The most important is panel (a), that allows to specify the parameters of TEM-imaging (e.g. resolution, grayscale levels, values for K_p, K_m, etc.). Panel (b) is a progress bar, while panel (c) shows a preview of the TEM image. Panel (d) provides the information about the resolution of the final image. Panel (e) gathers together general control buttons and enables to import data (text files with coordinates of spheres produced in the DLA tab of the software) and export synthetic TEM images. Finally, panel (f) may be used to perform serial calculations for a set of input files (coordinates of monomers in each aggregate).

Figure 3.4 shows example synthetic TEM images for various projection planes (columns) of the simulated aggregates of $n_p = 200$ monomers with $r_p = 1$ and different fractal dimensions (rows): (a) $D_f = 1.60$, (b) $D_f = 1.80$, (c) $D_f = 2.00$. It can be seen that the morphological parameters of the presented aggregates vary significantly for different rotation angles (and thus the projection planes). The latter remark explains why to analyze aggregates from TEM images it is necessary to proceed a large number of samples.

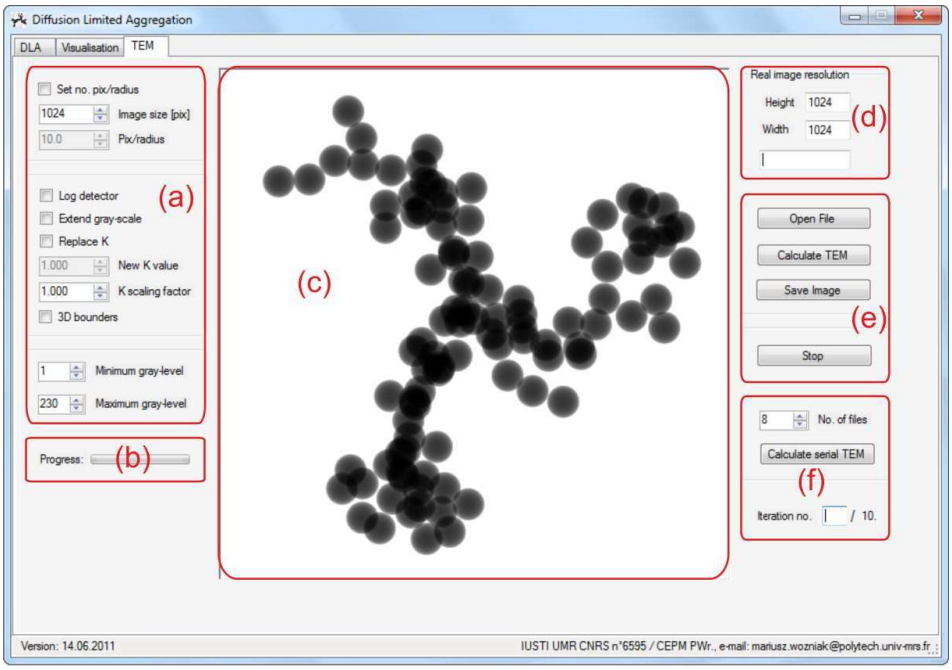

Figure 3.3. Screen copy of the TEM software: (a) parameters of the TEM imaging, (b) progress bar, (c) preview window, (d) image resolution, (e) general control buttons, (f) serial simulation panel.

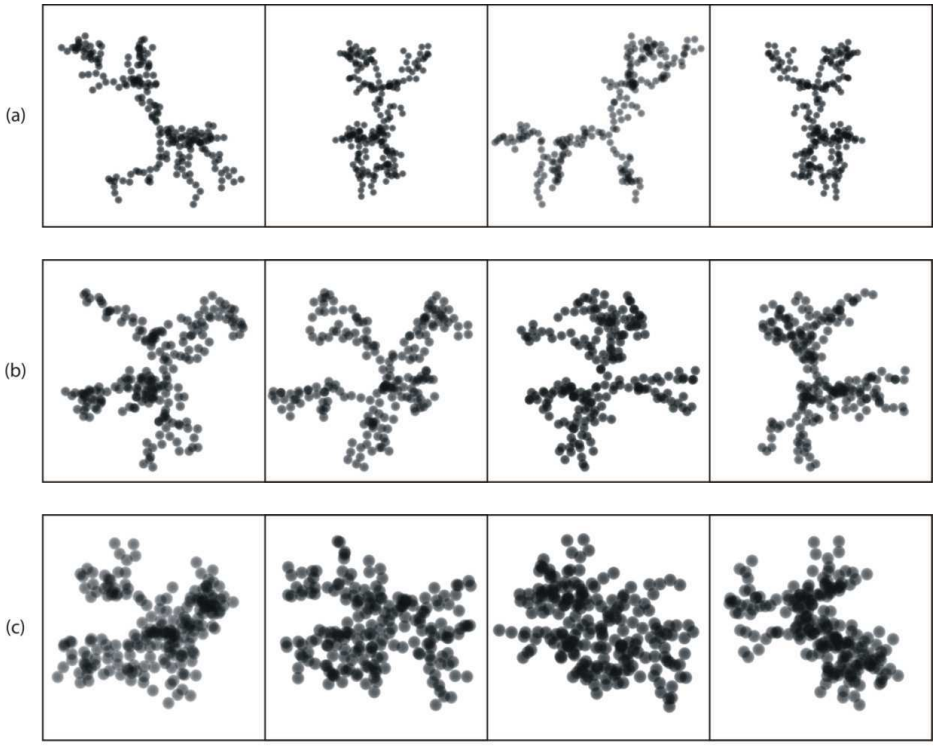

Figure 3.4. Synthetic TEM images for various projection planes (columns) of DLA aggregates with $n_p = 200$ with $r_p = 1$ and different fractal dimensions (rows): (a) $D_f = 1.60$, (b) $D_f = 1.80$, (c) $D_f = 2.00$.

3.2.2. Overlapping factor and projection errors

The zoom in Figure 3.2 highlights the fact that TEM images of neighbor particles ν and κ, with a radius r_p and a Euclidian inter-distance $d_{\nu\kappa}^{2D}$ overlap with a two-dimensional overlapping factor:

$$C_{\upsilon\kappa}^{2D} = \left(2r_p - d_{\upsilon\kappa}^{2D}\right) / 2r_p. \tag{3.4}$$

This overlapping may be attributed to physical reasons i.e. 3-dimensional overlapping of particles discussed previously in section 2.3.1 as well as 3D to 2D projection bias. In fact, for aggregates of spherical particles with statistically random orientations, the average 2D overlapping factor of all pairs (υ,κ) of neighboring hard spheres in contact does not depend on the fractal dimension. It is a pure geometrical coefficient that can be derived by averaging the inter-distance $d_{\upsilon\kappa}^{3D}$ with the help of Eq. (2.19) and the proper boundary values $\gamma_1 = 0$ and $\gamma_2 = 1$:

$$\bar{d}_{\upsilon\kappa}^{2D} = \frac{1}{\gamma_2 - \gamma_1}\int_{\gamma_1}^{\gamma_2} d_{\upsilon\kappa}^{3D}\varphi(\delta_2)\,dx = \frac{\pi}{2}r_p. \tag{3.5}$$

Using Eqs. (2.22) and (3.5) we find that for two hard spheres in contact:

$$\bar{C}_{\upsilon\kappa}^{2D} = \left(2\bar{r}_p - \bar{d}_{\upsilon\kappa}^{2D}\right) / 2\bar{r}_p \approx 0.215. \tag{3.6}$$

The same procedure can be used for partially overlapping spheres. From numerical simulations performed on 1000 pairs (υ,κ) of spheres with random orientations and with various overlapping factors $\bar{C}_{\upsilon\kappa}^{3D} = 0,\ 0.05,\ ...,\ 1$, we find that the relation between the two overlapping factors is nearly linear:

$$\bar{C}_{\upsilon\kappa}^{3D} = \zeta_1\bar{C}_{\upsilon\kappa}^{2D} - \zeta_2, \tag{3.7}$$

where ζ_1 and ζ_2 are linear regression constants, with $\zeta_1 = 1.27 \pm 0.01$ and $\zeta_2 = 0.27 \pm 0.01$. The latter values are comparable with those found by Brasil et al. (Brasil et al. 1999).

It now remains to find how we can estimate $\bar{C}_{\upsilon\kappa}^{2D}$ from TEM images. Image processing algorithms and blob analysis techniques fail to detect all primary particles within the TEM images of a fractal aggregate, especially when its fractal dimension approaches, and all the more when it exceeds 2. Consequently, all authors, including ourselves, try to estimate this inter-distance "manually". This is done by selecting a few branches of the fractal aggregate which are as far as possible both elongated and parallel to the TEM image projection plane. Obviously this is a totally subjective approach. However, in order to obtain a rough estimate of the degree of error, let us consider that we have managed to select branches that are not tilted more than $\pm 30°$ in respect to the projection plane. In that case, for $\bar{C}_{\upsilon\kappa}^{3D} = 0$ and by using Eq. (3.5) with the appropriate boundary values $\gamma_1 = 0.25$ and $\gamma_2 = 0.75$, we find that $\bar{C}_{\upsilon\kappa}^{2D} \approx 0.043$. The error made is only 4.3%.

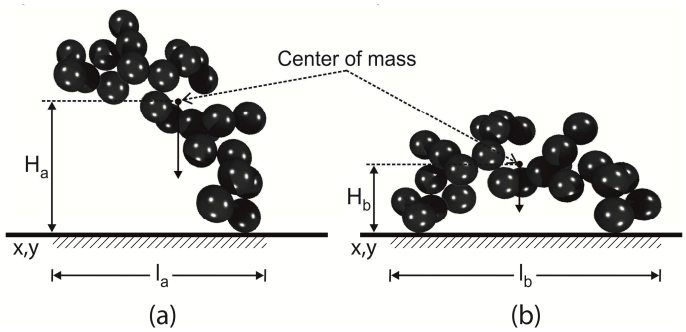

Figure 3.5. Sketch of aggregates contact model: (a) single-contact point or (b) multi-contact points (with lengths $l_b \geq l_a$ for the 1D-projection).

The aggregate of Figure 3.2 seems to be stuck onto the projection plane by a single contact point. For particles which are sensitive to the force of gravity, this position would clearly be unstable as it does not minimize the aggregate potential energy. This is not necessarily the case for nano- and small micro-aggregates that are mostly sensitive to adhesion and short-range forces (e.g. Van der Waals forces when soot aggregates are deposited on a TEM grid). Thus, depending on the sampling procedure used to collect aggregates, the balance of adhesion forces and collapsing or rolling effects, we may be confronted with the two cases outlined in Figure 3.5. The single contact point case is a direct result of the DLA & TEM algorithms: aggregates are randomly oriented in space and consequently with regard to the projection plane (i.e. on the simulated TEM Grid). The multi-contact point case can be modeled roughly by iterating on all possible orientations of the aggregate until the distance H (between its center of mass and the projection plane) reaches a minimum. It is obvious that the latter assumption leads to the greatest projection length and surface area. Comparison between projected lengths for randomly oriented aggregates and for aggregates with the multi-contact point scheme is shown in Figure 3.6. For each D_f the results were averaged over 50 different clusters. Something important to notice is also that aggregates with the same parameters may exhibit different projection lengths and surface areas. It is a direct consequence of their random orientation onto TEM grid. Of course, this effect is much less noticeable if the multi-contact point case is taken into account. So it is not surprising that, the standard deviation for the randomly oriented aggregates is significantly higher than for aggregates with the multi-contact points case. It can be also seen from Figure 3.6 that the differences between both approaches decrease rapidly when increasing D_f so that with a good accuracy we can neglect this issue for aggregates with a fractal dimension higher than $D_f = 2.0$.

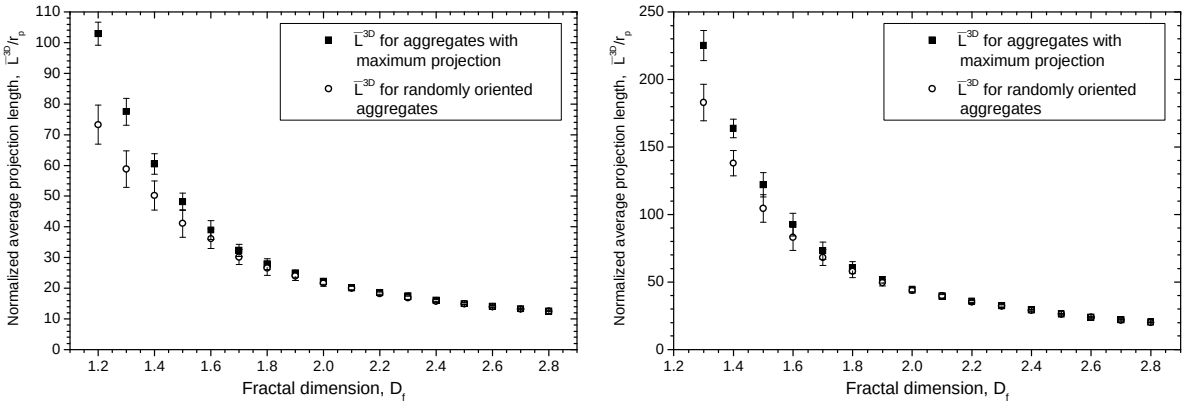

Figure 3.6. Comparison between maximum projection length averaged over 50 synthetic aggregates as a function of the fractal dimension for randomly oriented aggregates and for aggregates with the multi-contact point scheme: clusters with (a) $n_p = 100$ and (b) $n_p = 400$ monomers.

Similar questioning regarding influence of the collapsing or rolling effects to the estimation procedure have been discussed by Oh and Sorensen (Oh and Sorensen 1997) and by Brasil et al. (Brasil et al. 1999). Brasil et al. assumes that an aggregate after touching the collecting surface rolls until 2 and finally 3 contact points are reached. If these effect is not properly considered, the number of primary particles n_p and the fractal prefactor k_f may be overestimated up to $10-15\%$ (Brasil et al. 1999). Due to the lack of information on aggregate deposition mechanisms, all results presented here (except those of Figure 3.25) were obtained with the single-contact point model.

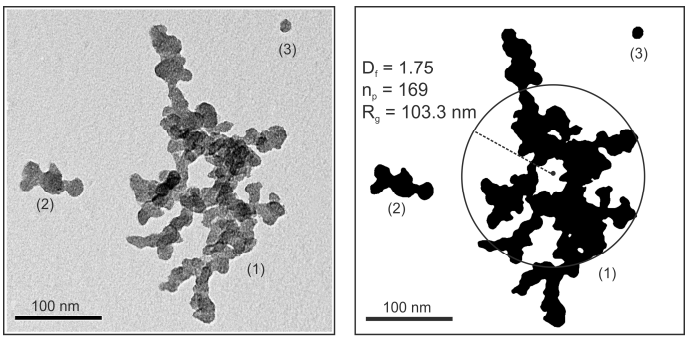

Figure 3.7. Example of large (1) and small (2-3) diesel soot aggregates (Yon et al., 2011): (a) raw TEM image (the contrast was enhanced for the purpose of publication); (b) pre-processed image showing the morphological parameters estimated for the largest aggregate.

3.2.3. Pre-processing of TEM images

Prior to perform a morphological analysis, each raw TEM image was pre-processed (i.e. spatially filtered out to remove background noise and low-frequency gradients) and binarized, see Figure 3.7. Next, the mean radius and overlapping factor of the primary particles were estimated "manually" by measuring several dozen of single, and pair, of particle images. Thus, for each aggregate, we looked for its bounding rectangle with a

minimal surface. Each minimum bounding rectangle was defined by its length L^{2D}, its width W^{2D} and its orientation within the original raw TEM image. Finally, each embedded TEM image was rotated to obtain conventional rectangular-shaped and oriented images (these steps are depicted in Figure 3.8 (a) and (b)).

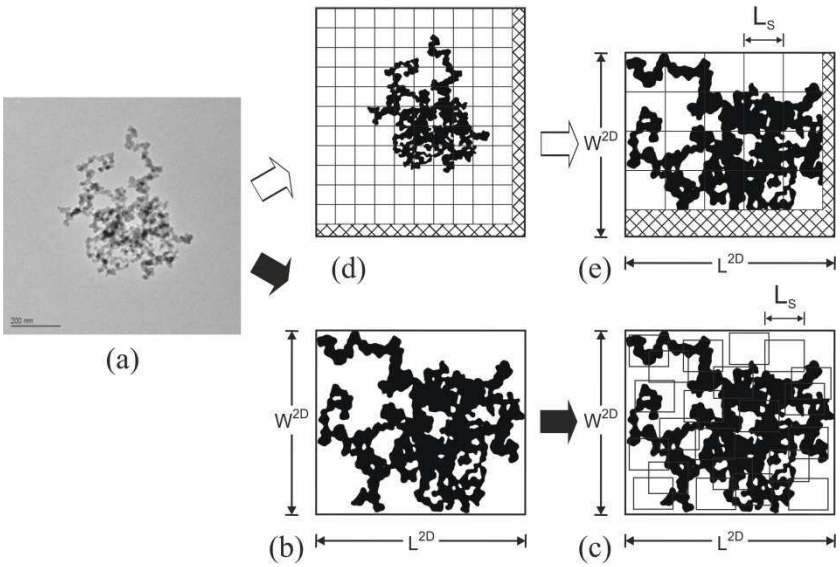

Figure 3.8. Chart of some of the pre-processing and morphological steps: (a) raw image; (b) pre-processed image (filtered, rectangle bounded and rotated); (c) random sampling scheme of the MBC method; (d) image with additional bounders (hatched area); (e) classical box-counting algorithm with regular mesh.

3.3. Methods for estimating the morphological parameters

3.3.1. Minimum Bounding Rectangle (MBR) method

Although the first method discussed here is the most widely used (e.g., (Samson et al. 1987; Megaridis and Dobbins 1990; Koylu and Faeth 1992; Cai et al. 1995; Chakrabarty et al. 2009; Ouf et al. 2010)), its name is not well established. Thus, for the sake of convenience and in view of the fact that it is fundamentally based on the determination of the properties of the smallest rectangle containing each aggregate, we will refer to it as the "Minimum Bounding Rectangle (MBR)" method. Example images of the raw aggregates (left column) and after binarization with visualization of the minimum bounding rectangles (right column) have been shown in Figure 3.9.

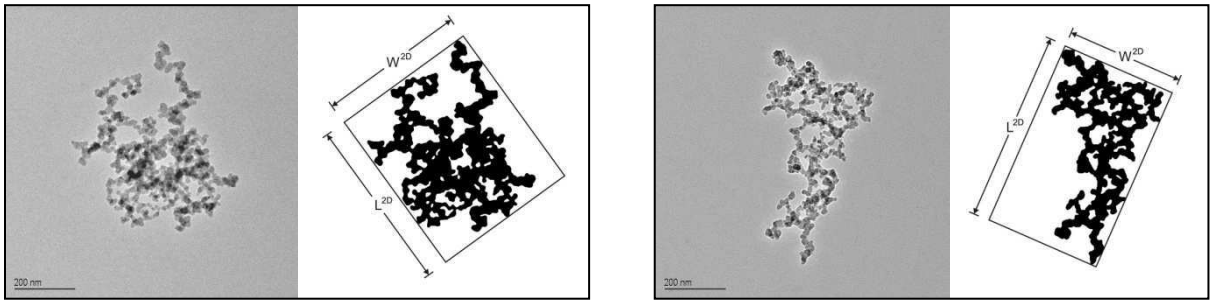

Figure 3.9. Example of SiC aggregates: raw images (left) and images after binarization with visualization of the minimum bounding rectangles (right).

3.3.1.1. Radius of gyration

The radius of gyration of a fractal aggregate can be estimated from its characteristic lengths in a two-dimensional space, and more particularly the length L^{2D} of its minimum bounding rectangle. The value of the ratio $L^{2D}/\left(2R_g\right)$ is generally considered to be a constant nevertheless its value varies between 1.49 and 1.78 from one author to another (Puri et al. 1993; Koylu et al. 1995; Brasil et al. 1999). In fact, our simulations reported in Figure 3.10 show that for small aggregates (i.e. like those in Figure 3.1) with $D_f = 1.40$ to 2.80, the ratio $L^{2D}/\left(2R_g\right)$ varies from 1.26 to 1.53 with the mean value of $L^{2D}/\left(2R_g\right) = 1.43 \pm 0.06$.

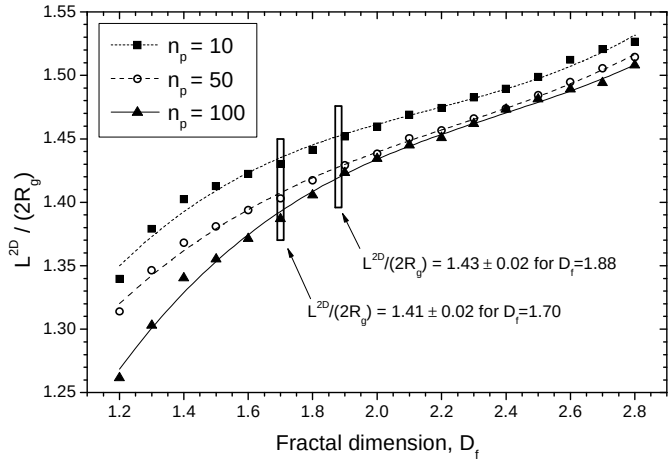

Figure 3.10. Numerical estimation of the dependency of $L^{2D}/\left(2R_g\right)$ versus the fractal dimension and for various values of the number of primary particles within the aggregate.

The radius of gyration can also be estimated from a characteristic length derived from the surface area of the minimum bounding rectangle. This characteristic length $\sqrt{L^{2D}W^{2D}}$ is commonly used to relate the morphological parameters to each other thanks to an equation which is formally identical to the fractal equation (e.g. (Koylu and Faeth 1992; Chakrabarty et al. 2009):

$$n_p = k_{LW}\left(\frac{\sqrt{L^{2D}W^{2D}}}{r_p}\right)^{D_f}, \tag{3.8}$$

where k_{LW} is a 2D structural factor playing the same role than k_f in Eq. (2.13). Using Eqs. (2.13) and (3.8), it comes that the radius of gyration can be estimated with:

$$R_g = \frac{\sqrt{L^{2D}W^{2D}}}{\beta}, \tag{3.9}$$

where $\beta = \left(k_f / k_{LW}\right)^{1/D_f}$. The value of the latter parameter was estimated by Koylu et al. (Koylu et al. 1995) to be equal to $\beta \approx 2.34$ for rather large soot particles ($D_f = 1.70$ and $n_p \geq 100...1000$). However, it should be mentioned that although β is explicitly fractal dimension dependent, a large number of authors have used this value of $\beta \approx 2.34$ for their own problems, forgetting that it was estimated for specific aggregates. Unfortunately, our simulations show that although β is indeed fractal dimension dependent, it also depends slightly on the number of primary particles within the aggregates, see Figure 3.11). This is why, in what follows, we distinguish between the cases in which β is either variable (as it needs to be and as it is ensured by using the calibration curves shown in Figure 3.11) or constant (only for comparison with the literature).

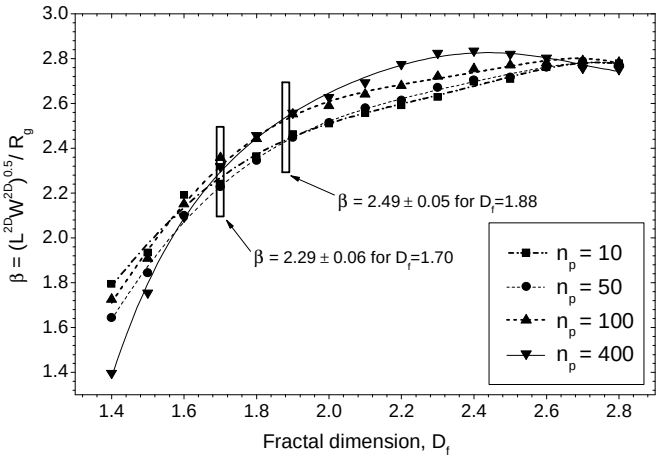

Figure 3.11. Numerical estimation of the dependency of β versus the fractal dimension and for various values of the number of primary particles within the aggregate.

Figure 3.12 compares the radius of gyration estimated with two different characteristic lengths. To evaluate R_g for the synthetic aggregates of (a) $n_p = 100$ and (b) $n_p = 400$ monomers the ratios of $L^{2D}/(2\times 1.49)$ and $\sqrt{L^{2D}W^{2D}}/2.34$ were used. The results have been compared with the initial values of the radius of gyration. It can be seen that in both methods the standard deviation is quite significant for small fractal dimension and it decreases rapidly for increasing value of D_f. Projection errors caused by random orientation of the aggregates during TEM imaging are responsible for these effects.

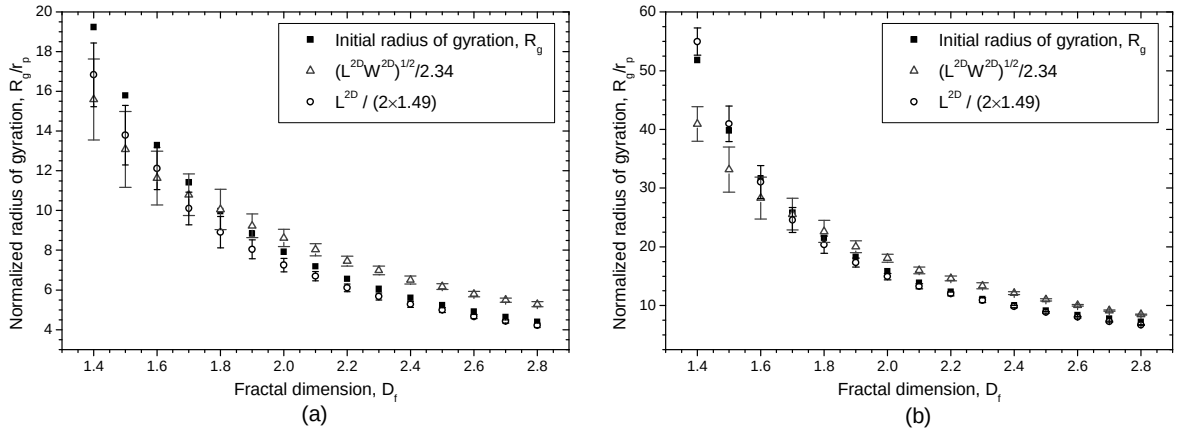

Figure 3.12. Comparison between the radius of gyration estimated with two different characteristic lengths ($L^{2D}/(2\times1.49)$ and $(L^{2D}W^{2D})^{1/2}/2.34$) for synthetic aggregates with (a) $n_p = 100$ and (b) $n_p = 400$ monomers versus fractal dimension.

3.3.1.2. Number of primary particles

The number of primary particles within an aggregate was estimated from the measurement of its projected surface area A_a and that A_p of the primary particles, and also by using an equation which is formally identical to the fractal equation:

$$n_p = k_a \left(\frac{A_a}{A_p} \right)^{\alpha}, \tag{3.10}$$

where α and k_a are parameters that have been evaluated experimentally (Megaridis and Dobbins 1990; Koylu et al. 1995) or numerically (Oh and Sorensen 1997; Brasil et al. 1999). Depending on the work and combustion systems considered, the values of these parameters are in the ranges: $\alpha = 1.07 - 1.10$ and $k_a = 1.10 - 1.30$. For all results presented below, to be consistent with other authors, we use the values $k_a = 1.155$ and $\alpha = 1.095$ derived by Koylu et al. (Koylu et al. 1995) since this work was found to be the most convincing. Nonetheless, according to the numerical results presented in Figure 3.13 the parameter α significantly varies with the fractal dimension and the number of monomers. The average values evaluated from Figure 3.13 for $D_f = 1.70$ and $D_f = 1.88$ are equal to 1.091 ± 0.008 and 1.104 ± 0.007 respectively. Estimations for these parameters are in a good agreement with the results supported by the aforementioned authors. This also explains why to be consistent with the literature, the parameter α was set to $\alpha = 1.095$.

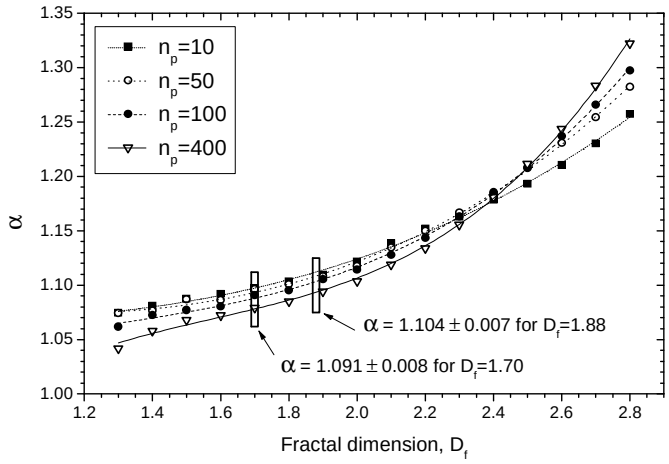

Figure 3.13. Numerical estimation of the dependency of the exponent α versus the fractal dimension, for various values of the number of monomers within the aggregate.

3.3.1.3. Fractal dimension

The fractal dimension can be estimated by posing the equality between Eqs. (3.8) and (3.10) and by measuring the properties r_p, A_p, A_a and $L^{2D}W^{2D}$ of many aggregates:

$$\ln\left[k_a\left(\frac{A_a}{A_p}\right)^{\alpha}\right] = \ln n_p = \ln k_{LW} + D_f \ln\left(\frac{\sqrt{L^{2D}W^{2D}}}{r_p}\right). \tag{3.11}$$

With Eq. (3.11) we can only access to an average or "global" fractal dimension for the entire sample, since D_f is simply derived from the slope of a linear regression (see (Koylu et al. 1995) and like it is done in Figure 3.1). It is not necessary to determine k_{LW} to obtain D_f. However, with a view to the main aim of this work, we found it more meaningful in Figure 3.1 (as in all other Figures) to display along the x-axis the values of the normalized radius of gyration R_g / r_p rather than the quantity $\sqrt{L^{2D}W^{2D}} / r_p$. To do so, our procedure consists in obtaining D_f directly from the slope given Eq. (3.11), and then to use Eq. (3.9) (with β constant or variable) to obtain R_g / r_p. r_p is deduced, like A_p, A_a, L^{2D} and W^{2D}, by means of a classical "blob" analysis performed in MATLAB environment.

3.3.2. Modified Box-Counting (MBC) method

The Box-Counting method is a well-established method for estimating the fractal dimension (Minkowski dimension) of infinite mathematical objects (such as the well-known Cantor and Sierpinski sets, and also strange attractors) (Theiler 1990). To do so, the 2D image of the object is successively binarized and covered with square boxes (i.e. interrogating windows) with a scale of L_s, where $s = 1,...,S$ refers to the analyzing scale. At each scale s, N_s boxes contain a fragment of the fractal object (at least one dark pixel). Thus, the basic underlying idea is that the evolution of N_s versus L_s expresses the self-similarity properties of the fractal aggregate over the considered scales, which implies that (compare also with Eq. (2.12)):

$$N_s \sim L_s^{-D_f}, \tag{3.12}$$

or, more formally (Theiler 1990), that

$$D_f = -\lim_{L_s \to 0} \frac{\ln N_s}{\ln L_s}. \tag{3.13}$$

One major feature of this method is that it allows one to estimate the fractal dimension of single objects, making it very suitable for detecting a correlation between the morphological properties of all aggregates within a small sample. However, with real particle aggregates and their TEM images, we have to deal with their size and resolution limits. As a direct consequence, the limit of Eq. (3.13) (which is taken to ensure invariance over smooth coordinate changes) cannot be reached. Additionally, in most cases the images of fractal aggregates cannot be decomposed at all scales into an integer number of square boxes. Therefore the total surface area of the analyzing boxes is not the same at all scales. To solve these problems, we developed a Modified Box-Counting (MBC) algorithm which provides several major improvements. First, the minimum bounding rectangle method is used to reject any surrounding parts of the TEM image that contain no fractal elements but which could strongly influence the box-counting analysis (see example aggregate with surrounding parts and regular Cartesian meshes of boxes in Figure 3.8 (d)). Second, to overcome the problem related to multiple subwindows and blank zones, analyzing boxes are not generated along regular Cartesian meshes (like shown in Figure 3.8 (e)) but are distributed randomly with uniform distribution within the TEM image (this step is depicted in Figure 3.8 (c)). Thirdly, at each scale, the number of non empty boxes is normalized by the total surface area of all boxes generated at the corresponding scale. Finally, the fractal dimension of uniform fractal aggregates (i.e. which are not multi-fractal) (Theiler 1990)) is no longer estimated from the limit given in Eq. (3.13) but from the slope (Foroutan-pour et al. 1999) of the linear regression performed on the raw data points obtained at all scales:

$$\ln\left(\frac{N_s}{\sum L_s^2}\right) = -D_f \ln\left(L_s\right) + \ln b, \tag{3.14}$$

where b is an arbitrary constant.

For the conventional box counting method (Theiler 1990; Kaye 1994; Foroutan-pour et al. 1999) as for the newly introduced one, the choice of the set of analyzing boxes, and more particularly the minimum and maximum box sizes, is a determining factor. For the sake of convenience, and since we are looking for self-similarity properties, we can use the dimension of one pixel as the unitary scale. For the minimum box size, the choice is guided by the need to maintain a reasonable signal-to-noise ratio and the capacity of the method to probe the low scale "porosity" of the aggregate image. The latter condition is particularly important for aggregates with a high fractal dimension (e.g. $D_f \geq 2$). On the basis of the above remarks and also a stability analysis performed with the DLA-TEM algorithms, the smallest analyzing box size was set to $L_1 = 2$ pixels. To set the maximum box size, we can first observe that the

maximum dimension of fractal aggregate images rarely exceeds a few hundred pixels. We also came to the conclusion, as did Foroutan-pour et al. (Foroutan-pour et al. 1999) for the conventional box-counting method, that problems linked to the maximum box scale can be ignored if the maximum box dimension does not exceed $\approx 25\%$ of the maximum length scale of the aggregate image. In this work therefore, the maximum box scale was limited to $L/4$. After several test with various sets of boxes and due to the form of Eq. (3.14) we finally chose to build a set of $S=17$ boxes which were nearly logarithmically distributed with $\mathbf{L}_s = [2,\ 3,\ 4,\ 5,\ 6,\ 8,\ 10,\ 13,\ 16,\ 20,\ 25,\ 32,\ 40,\ 50,\ 63,\ 79,\ 100]$. As an illustration, Figure 3.14 shows the pre-processed image of a soot aggregate, together with the raw data points and the corresponding linear regression obtained with the MBC method. The uniformity at all scales of this aggregate is clear. However, when processing synthetic aggregates, we found a systematic shift between the nominal fractal dimension and that deduced from the slope of the linear regression. This shift, which depends both on D_f and n_p, is attributed to the finite dimension of the aggregates considered here (i.e. $R_g / r_p \leq 20$ for all synthetic and experimental aggregates). Consequently, in order to obtain an accurate estimation of the fractal dimension we were obliged to use, as we did for the MBR method, numerical calibration curves. The latter were derived from the analysis of the TEM images of thousands of synthetic aggregates with different fractal dimensions ($D_f = 1.2,\ 1.3,\ ...,\ 2.8$) and numbers of primary particles ($n_p = 5,\ 10,\ 20,\ 30,\ 50,\ 100,\ 400$).

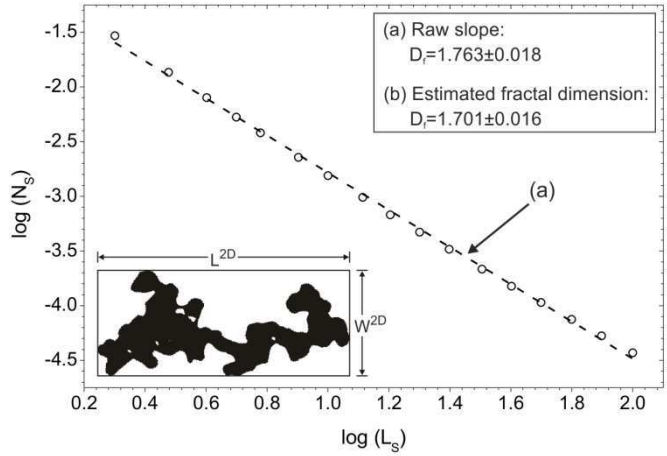

Figure 3.14. MBC method: raw data points and linear regression on the box count versus the box length scale of the boxes for a large diesel soot: (a) raw slope; (b) calibrated slope (i.e. fractal dimension); (c) corresponding pre-processed TEM image.

Figure 3.15 (a) shows examples of these calibration curves. It can be seen that for reasonably large aggregates (i.e. for $n_p \geq 100$) the calibration curves of the MBC method are less and less dependent on the size of aggregates (as it must be for objects with auto-similarity properties). For smaller aggregates, MBC calibrations curves just tell us that we are not dealing with true fractal objects. It is the reason why, we have to use various calibration curves. Figure 3.15 (b) compares the calibration curve of the optimal set of $S=17$ boxes for

$n_p = 100$ monomers with some other possible solutions that were also tested. It is worth to notice that we set an almost constant sensitivity in a wide range of the raw slope D (up to the initial fractal dimension equal to $D_f = 2.40$).

Due to this overall procedure, the deviation between the mean estimated fractal dimension and the nominal one is typically less than 1% for numerical aggregates with $R_g / r_p \geq 2.5$ (see for instance Figure 3.21). It should be noticed that, with the MBC method there is no specific way to determine either the number of primary particles or the radius of gyration. Therefore, below, like with the MBR method, these morphological parameters are deduced using Eqs. (3.9) and (3.10).

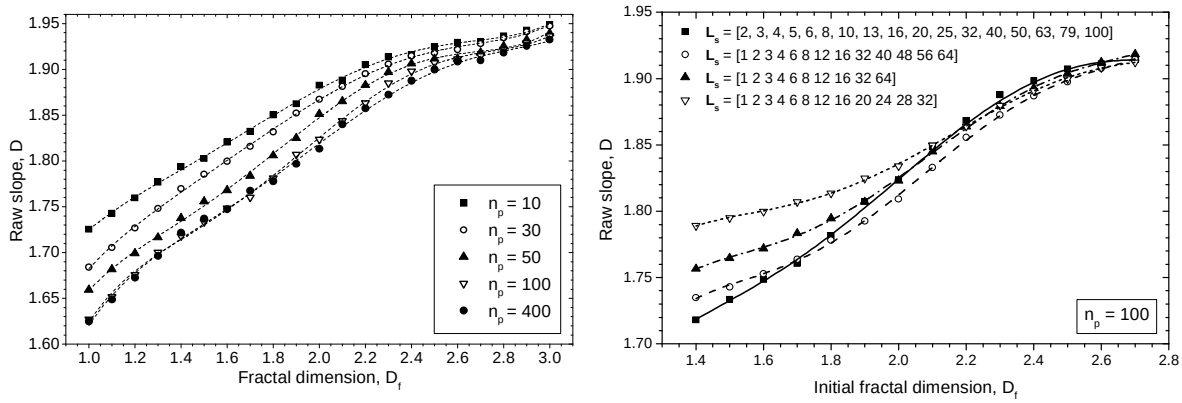

Figure 3.15. (a) Some of the numerical calibration curves of the MBC method and (b) comparison between the numerical calibration curves for different sets of boxes $\mathbf{L}_s$.

3.4. Results and Discussion

All the previous models and methods were tested on an experimental test sample of 543 images of soot aggregates produced by a diesel flame (Yon et al. 2011) (see Figure 3.1 and Figure 3.7) and silicon dioxide particles (CILAS company, e.g. see Figure 3.9) as well as synthetic aggregates generated with the DLA-TEM algorithm. The morphological properties of the synthetic aggregates were chosen to be as similar as possible to those obtained with the experimental soot sample: normalized radius of gyration ($R_g / r_p = 1, ..., 17.2,$ with $r_p = 8.2\ nm$); number of primary particles ($n_p = 1, ..., 334$); size distribution in number (see Figure 3.1); a constant overlapping factor ($C_{\upsilon\kappa}^{3D} = 0.20 \pm 0.05$); a fractal dimension which is either constant ($D_f = 1.88$, as we found with the classical MBR technique in Figure 3.1), or variable (to cross-check the sensitivity of the MBC method). For both experimental and synthetic TEM images, the equivalent diameter of the primary particles was about 20 pixels.

3.4.1. The Minimum Bounding Rectangle (MBR) method

For small variations of the fractal dimension, one can assume that β is nearly constant. In that case, the most direct way to detect correlations using the MBR technique is to calculate

the derivative of Eq. (3.11) with respect to $\ln\left(\sqrt{L^{2D}W^{2D}}/r_p\right)$. Thus, we can estimate the fractal dimension with:

$$D_f = d\left(\ln\left[\left(\frac{A_a}{A_p}\right)^{\alpha}\right]\right) / d\left(\ln\frac{\sqrt{L^{2D}W^{2D}}}{r_p}\right). \tag{3.15}$$

Figure 3.16 shows the evolution of this derivative for the raw experimental data points (see Figure 3.1) that have been re-sampled and smoothed beforehand (i.e. adjacent-averaging with a bandwidth $\log\left(R_g/r_p\right)=\pm 0.2$). These results suggest that the fractal dimension of aggregates with a small to intermediate size $\left(\log\left(R_g/r_p\right)=0...0.8\right)$ decreases as their size increases. For the largest aggregates $\left(\log\left(R_g/r_p\right)\geq 0.8\right)$, the statistics are too poor to draw any reasonable conclusion on the evolution of the derivative. For the smallest aggregates $\left(\log\left(R_g/r_p\right)\leq 0\right)$, which are statistically the most common in this experimental sample, the results seem to be biased too. This may be related to a classic data filtering problem or more probably to the fact that the smallest aggregates do not have a fractal structure. To our opinion, the derivative method is not of great help for analyzing such sample since this method is very sensitive to the statistical noise (a larger sample would be preferable) and it does not contain any calibration method which could take into account the doubtful auto-similarity of the smallest aggregates.

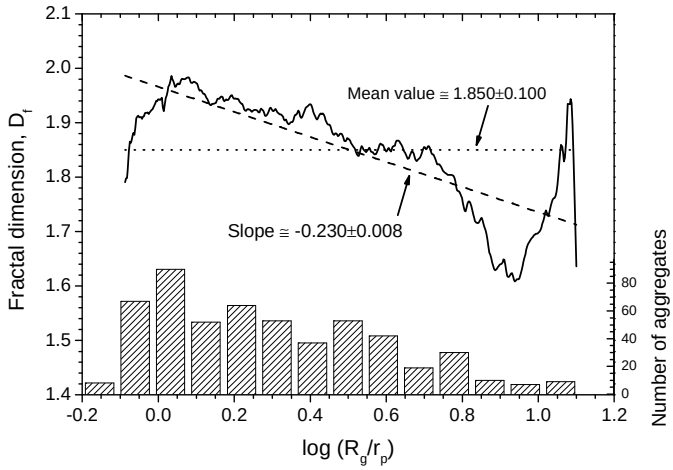

Figure 3.16. MBR with the derivative method: estimated fractal dimension versus the normalized radius of gyration of the experimental aggregates (the corresponding number-weighted size distribution is shown at the bottom).

With the MBR method, a second way to detect a relationship between D_f and R_g is to perform low-pass and high-pass analyses, i.e. the linear regression is performed on limited aggregate size ranges. Figure 3.17 shows the results obtained for the following ranges: $R_g/r_p>2$, $R_g/r_p>4$, $R_g/r_p>6$, $R_g/r_p<8$, $R_g/r_p<6$ and $R_g/r_p<3$. In Figure 3.17 (a) the parameter β is set constant with $\beta=2.34$ for the mean fractal dimension $D_f=1.88\pm 0.01$, whereas in Figure 3.17 (b) β is variable (i.e. full calibration curves are used, see Figure 3.11). From Figure 3.17 (a) it appears that, as suggested by the derivative method, the largest

aggregates have a lower fractal dimension than the smallest ones, with $D_f = 1.68 \pm 0.08$ for $R_g / r_p > 6$ and $D_f = 1.95 \pm 0.02$ for $R_g / r_p < 3$ respectively. However, this trend is much weaker when β is variable.

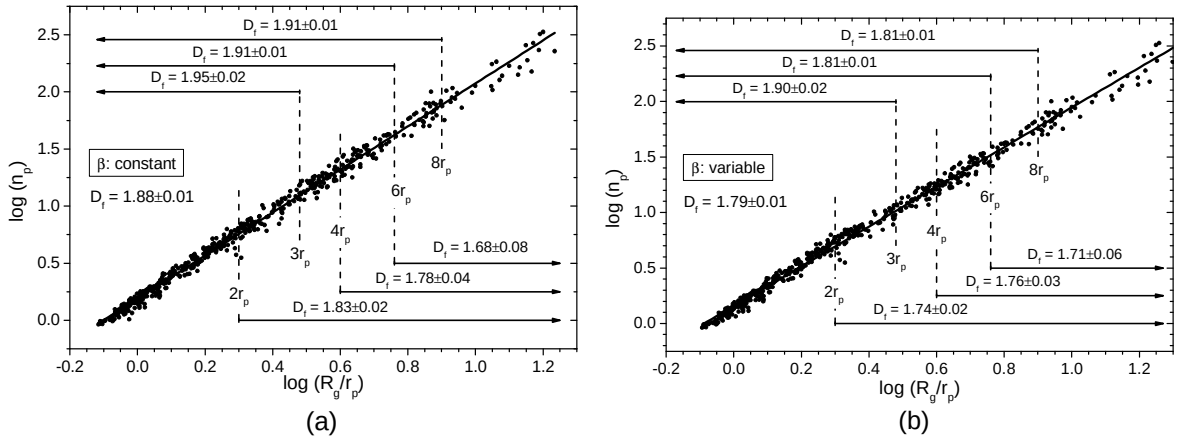

Figure 3.17. MBR with the low- and high-pass methods: raw data points and linear regressions obtained for the experimental test samples of diesel soot when (a) β is constant or (b) β is variable.

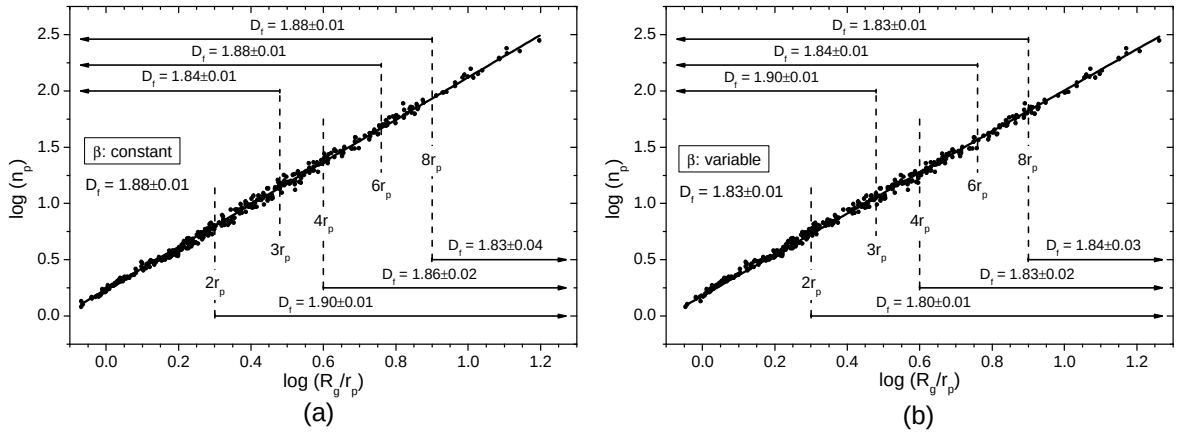

Figure 3.18. MBR with the low- and high-pass methods: raw data points and linear regressions obtained for synthetic aggregates with the same fractal dimension ($D_f = 1.88$ as in Figure 3.17 (a)), when (a) β is constant or (b) β is variable.

To clarify this point, Figure 3.18 (a) and (b) show the results obtained for similar synthetic aggregates with $D_f = 1.88$. Surprisingly, we also find here that the largest aggregates have a larger fractal dimension than the smallest ones. In our opinion, the most convincing explanation for these rather destabilizing results is that the experimental sample is not homogeneous. From Figure 3.1 it was already possible to infer that, unlike large aggregates, small aggregates do not exhibit any self-similarity or scaling properties. In the same way, it is easy to show that fractal equation (Eq. (2.13)) is not verified for $n_p = 1$ and 2. What we put forward with the latter arguments is that it is meaningless to look for a fractal dimension for the small aggregates considered here, or for an average fractal dimension for a non-homogeneous sample (which is however typical for soot aggregates (Yon et al. 2011)). In other words, the results of Figure 3.18 are less confusing than we thought at first; they

simply rely on a set of parameters that are not consistent with our particle model (i.e. Eq. (2.13) is not satisfied over all the aggregates size range).

Figure 3.19 shows the MBR analysis preformed for the experimental samples of silicon carbide (SiC) provided by CILAS company. In Figure 3.19 (a) the parameter β is set constant with $\beta = 2.34$ for the mean fractal dimension $D_f = 1.82 \pm 0.09$, while in Figure 3.19 (b) β is variable for the mean fractal dimension equal to $D_f = 1.83 \pm 0.09$. The high standard deviation of the values found for D_f should be attributed to the small number of the experimental samples (only 48 aggregates!) and the narrow range of their radiuses of gyration ($0.7 < \log(R_g / r_p) < 1.2$), compare with Figure 3.17). The problem is that, as a multi-scale analysis, the MBR method requires a large number of aggregates with a wide range of size (i.e. like those in Figure 3.17 and Figure 3.18). If those requirements are not satisfied, accuracy of the estimation significantly decrease. Analyzing Figure 3.19 (a) and Figure 3.19 (b) it can be also noticed that regardless of the different assumptions for the parameter β, the estimations of the fractal dimensions are close. This is due to the fact that those aggregates are large enough (number of monomer of each cluster is higher than $n_p = 30$) to exhibit self-similarity and scaling properties.

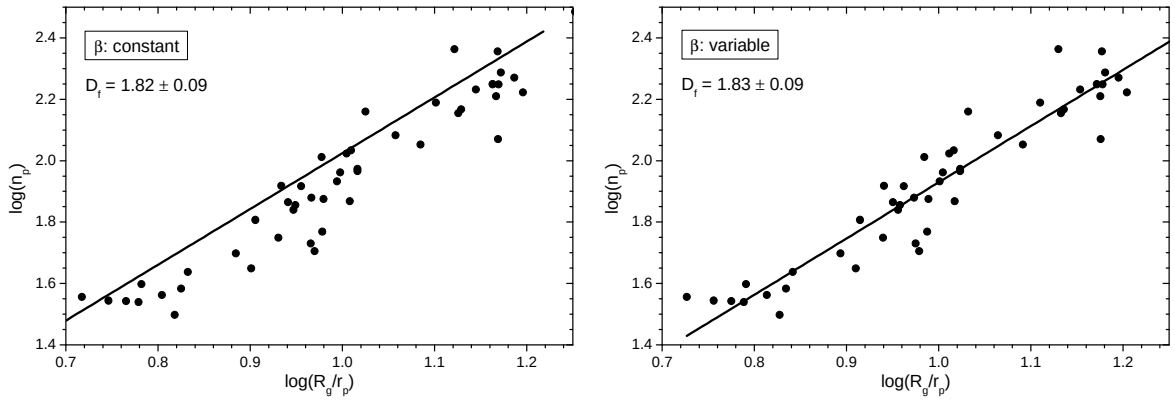

Figure 3.19. MBR: raw data points and linear regressions obtained for the experimental test samples of SiC aggregates when (a) β is constant or (b) β is variable.

A third alternative to detect correlations with the MBR method is to perform a band-pass analysis, i.e. to analyze sub-samples with the same width. Figure 3.20 shows, for the experimental sample, the results obtained with a band width of $\log(R_g / r_p) = \pm 0.2$ when β is either constant or variable. D_f evolves roughly like a stair-stepped function. For a variable β and very small-sized aggregates $(\log(R_g / r_p) \approx 0.2)$ the average fractal dimension is about $D_f \approx 2.0$; whereas for intermediate-sized $(\log(R_g / r_p) \approx 0.4 - 0.8)$ and large-sized $(\log(R_g / r_p) > 0.8)$ aggregates it is about $D_f \approx 1.73$ and $D_f \approx 1.69$ respectively. Although in the latter region the results are quite noisy they fit rather well with those presented in Figure 3.16 and Figure 3.17. The error bars are large but this is the price to pay to obtain a local

estimation of the fractal dimension and thus to avoid smoothing and boundary effects observed with the derivative and the low-pass/high-pass methods.

3.4.2. The Modified Box-Counting (MBC) method

Figure 3.20 also shows statistical results found with the MBC method when applied to the experimental soot sample. The local median, mean values and related standard deviations of D_f were calculated for the sub-samples with a band width of $\log\left(R_g / r_p\right) = \pm 0.05$. For mean values, two cases were considered depending on whether all data points were used for the statistics or only those with $D_f < 3$ (i.e. other data points are considered as artifacts of the MBC method). Note that for drawing considerations, the raw data points are not shown in Figure 3.20 but they are visible in Figure 3.25.

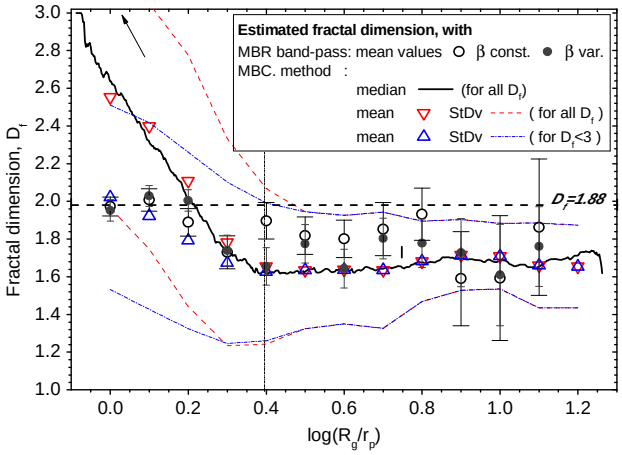

Figure 3.20. MBC and MBR band-pass methods applied to the experimental test sample: comparison of the evolution of the fractal dimension versus the aggregates normalized radius of gyration.

Several important remarks can be drawn from Figure 3.20. First of all, for rather small aggregates $\left(\log\left(R_g / r_p\right) \le 0.4\right)$ the mean fractal dimension increases as R_g / r_p decreases. For $\log\left(R_g / r_p\right) \approx 0$ we obtain $D_f \approx 2.05$ and $D_f \approx 2.55$ when, respectively, either all data points are considered for the statistics or only those with $D_f < 3$. A similar tendency was also brought to light with the MBR method. But since the minimum analyzing scale ($L_1 = 2$ pixels) in this region is no longer totally negligible compared to the diameter of the primary particles, the results obtained with the MBC method must be viewed with caution. One additional problem with this region is that the pre-processing procedure may also introduce a certain amount of bias by artificially decreasing the internal porosity, or by increasing the roughness, of TEM images. On the other hand, for intermediate- and large-sized aggregates, Figure 3.20 shows that the MBC method seems to predict a fairly constant value for the fractal dimension (based on either the two mean values or the median value) of about $D_f \approx 1.66 \pm 0.04$ for $\log\left(R_g / r_p\right) \ge 0.4$.

In order to determine whether or not we can be confident in the capacity of the MBC method to detect such small evolutions, we analyzed two new sets of synthetic aggregates with a slightly increasing and a slightly decreasing (number-weighted) fractal dimension, see Figure 3.21. The latter figure shows clearly the capabilities of the MBC method. The discrepancy observed for intermediate-sized aggregates in Figure 3.20 could also be attributed to a statistical weighting problem. In fact, with the MBC method the statistical values correspond to the moments of the number distribution of all estimated fractal dimensions. On the other side, with the MBR method, the nature of the statistical values is not so trivial since the fractal dimension is obtained from the slope of a linear regression applied to different aggregates. Additionally, these aggregates are ordered according to a characteristic length which is derived from a surface area. One clear advantage of the MBC method is that the number-weighted distribution of D_f can be easily converted to a volume-weighted distribution (or mass-weighted, i.e. directly connected to the number of primarily particles within the aggregate). Thus, Figure 3.22 shows the number- and the volume-weighted histograms for (a) all the analyzed samples and (b) for the aggregates with $R_g > 2.5r_p$. Both figures confirm that the largest aggregates have smaller fractal dimensions. The average volume-weighted fractal dimension is equal to $D_f = 1.74$ for all the aggregates and equal to $D_f = 1.65$ for the aggregates bigger than $R_g > 2.5r_p$.

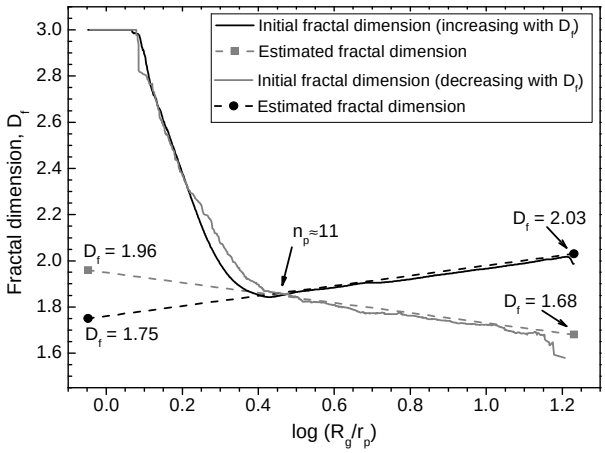

Figure 3.21. MBC methods applied to synthetic aggregates whose fractal dimension slightly increases, or slightly decreases, with the normalized radius of gyration.

Similar histograms were also prepared for the synthetic TEM images of the aggregates with $D_f = 1.88$ (see Figure 3.23). The average and the average volume-weighted fractal dimensions are equal to $D_f = 2.03$ and $D_f = 1.83$ respectively. Those values seem to be in a contradiction with the initial fractal dimension $D_f = 1.88$. Nevertheless, to evaluate the results we must take into account the limitations of the MBC method. As mentioned previously, it might be doubtful to estimate fractal dimension of the aggregates that do not satisfy fractal equation (Eq. (2.13)). We should also keep in mind that the MBC analysis of the "aggregates" consisting of only one particle is meaningless and as a result provides fractal dimension

$D_f \geq 3.00$. Therefore, to interpret Figure 3.23 we should consider results of the estimation equal to $D_f = 3.00$ or greater as artifacts of the MBC method and do not use them for statistics. In that case the average and the average volume-weighted values are equal to $D_f = 1.88$ and $D_f = 1.86$ respectively, and they are in a perfect agreement with the initial fractal dimension. It should be also noticed that a wide spreading in the fractal dimensions shown in the histograms is mainly caused by the fact that aggregates with the same D_f may have very different projected images (as shown clearly in Figure 3.4).

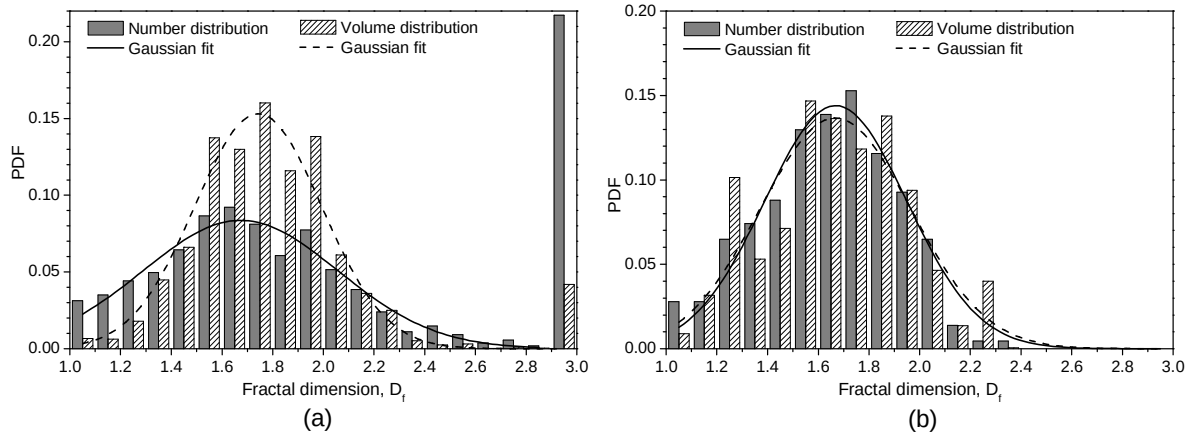

Figure 3.22. MBC method: comparison of the number-weighted and volume-weighted distributions of the fractal dimension for (a) all the experimental samples of diesel soot aggregates and (b) for the aggregates with $R_g > 2.5r_p$.

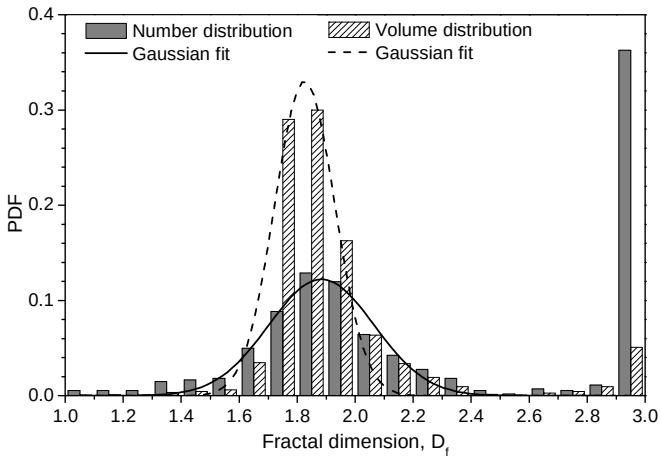

Figure 3.23. MBC method: comparison of the number-weighted and volume-weighted distributions of the fractal dimension for the synthetic aggregates.

Figure 3.24 shows the number- and the volume-weighted histograms for the experimental samples of silicon carbide. The average fractal dimension equal to $D_f = 1.81$ is in a very good agreement with the previously evaluated with the MBR method results equal to $D_f = 1.82$ and $D_f = 1.83$ for the constant and variable β case respectively. The average volume-weighted fractal dimension is estimated as $D_f = 1.89$.

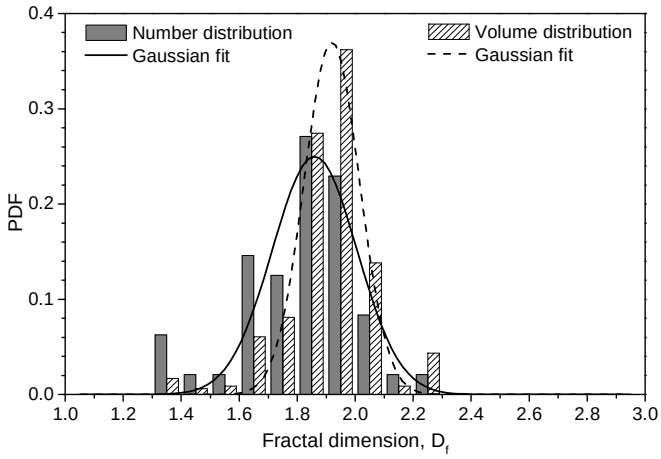

Figure 3.24. MBC method: comparison of the number-weighted and volume-weighted distributions of the fractal dimension for the SiC samples.

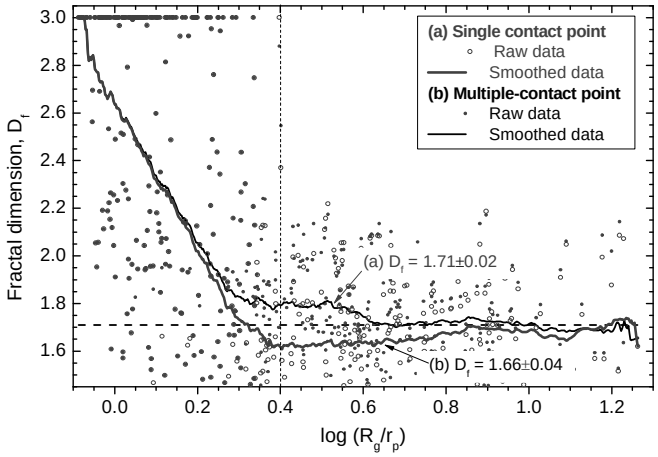

Figure 3.25. MBC method: influence of the single-contact and multiple-contact models on the estimation of the fractal dimension of experimental aggregates.

The differences observed in Figure 3.20, between the predictions of the MBR and MBC methods may also be related to the "problem" of single-contact or multi-contact points. Both methods require calibration curves derived from the prior analysis of synthetic TEM images, but we have then choose whether to generate the synthetic aggregates with a single-contact or with a multi-contact point model. Figure 3.25 examines the influence of this choice on the fractal dimension estimated with the MBC method (median value, as in Figure 3.20). As we intuited early on, we systematically obtain a higher fractal dimension with the multi-contact point model. But the most interesting thing here is that for this experimental sample, the differences are only significant for intermediate-sized aggregates, with $D_f \approx 1.66 \pm 0.04$ and $D_f \approx 1.71 \pm 0.02$ respectively. This indicates once more that there is no point defining a global fractal dimension for this sample. The difference observed in Figure 3.25 could be considered as an indication that, depending on their size, the aggregates are not all deposited (i.e. collected and attached) in the same way onto the TEM grid. The latter remark could have considerable physical implications; however, for the moment we do not have any physical

criteria with which to choose whether the single-contact point model or the multi-contact point model is the more appropriate.

3.5. Conclusion

In this chapter we have developed various models and numerical tools to evaluate more accurately the morphological parameters of fractal-like aggregates from TEM images. This is important for the general scientific community as well to get necessary comparisons with optical methods. We have investigated and tested a classical method (called the “MBR method”) and we have introduced a new one, named “MBC method”.

We found that, the classical MBR method is fundamentally inappropriate for detecting correlations between the morphological parameters of fractal-like particle aggregates as it is based on the analysis of their self-similarity properties over a large size range. To overcome this limitation of the MBR method we investigated solutions which are simple to implement, such as the calculation of a local derivative or the use of high-pass, low-pass or band-pass filters. However, the results obtained were found to be quite noisy and even questionable. In order to obtain a better resolution we introduced the MBC method, which estimates the fractal dimension of each aggregate from its own self-similarity properties. MBC validity was tested successfully on synthetic aggregates whose fractal dimension was independent of (constant) or correlated with (linear increase or decrease) aggregate size. For the experimental sample, the predictions of the MBC method were found to be much more convincing than those obtained with the MBR-based methods, and we show that the average fractal dimension of the soot samples is much lower (with $D_f = 1.66 \pm 0.02$ for small to large aggregates and a single-contact point model) than that found with the classical MBR method ($D_f = 1.88 \pm 0.02$). Nevertheless, the analysis of the silicon carbide samples shows that for aggregates large enough both methods provide very similar results ($D_f = 1.82 \pm 0.09$ and $D_f = 1.81 \pm 0.01$ for the MBR and MBC methods respectively).

Chapter 4

LIGHT SCATTERING THEORIES AND MODELS

4.1. Introduction

In this chapter we review and discuss the physical and mathematical backgrounds of all theories used in this work to predict the light scattering properties of nanoparticles and their aggregates: Lorenz-Mie theory, Rayleigh-based approximations (RGD, RDG-FA) and T-Matrix method.

4.2. Lorenz-Mie theory

Since it was introduced in the year 1908 by Gustav Mie (Mie 1908), the theory referred here as the "Lorenz-Mie theory" (LMT), is the most important and widely used theory for the description of the light scattering and absorption properties of small particles (e.g. (Bohren and Huffman 1998)). The LMT describes in an exact manner the interaction between an monochromatic electromagnetic plane wave and a homogeneous, isotropic, nonmagnetic and spherical particle defined by its diameter d_p and its complex refractive index $\tilde{m}_p$. It solves the Maxwell's wave equations using the method of separation of variables, in the spherical

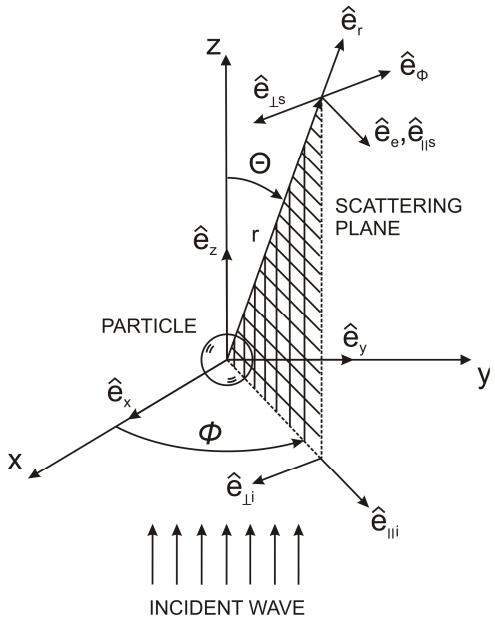

Figure 4.1. Light scattering by an arbitrary particle (Bohren and Huffman 1998)

coordinates with appropriate boundary conditions. External medium must be nonabsorbing. The LMT is used as a reference case for nearly all particle light scattering techniques (e.g. (Xu 2002)). Figure 4.1 shows the geometry and coordinate system of the problem solved LMT (Bohren and Huffman 1998). The plane wave propagates in the *z*-axis direction. The center of the particle is considered as the origin point O of the Cartesian as well as the Spherical Coordinate Systems. The orthonormal basis vectors $\hat{e}_x, \hat{e}_y, \hat{e}_z$ are in the directions of the positive *x*, *y* and *z* axes. The scattering plane is determined by a scattering direction $\hat{e}_r$ and the forward direction $\hat{e}_z$. It might be also defined in the spherical coordinates by the azimuthal angle ϕ. In the next paragraphs, we summarize the basic mathematics and results of this theory.

4.2.1. Solutions to the vector wave equations

The time harmonic electromagnetic field $(\mathbf{E},\mathbf{H})$ in a linear, isotropic, homogenous medium must satisfy simultaneously two wave equations (for the electric E and magnetic H fields):

$$\begin{cases} \nabla^2\mathbf{E} + k^2\mathbf{E} = 0, \\ \nabla^2\mathbf{H} + k^2\mathbf{H} = 0. \end{cases} \tag{4.1}$$

where $k^2 = \omega^2\varepsilon\mu$ is the wave vector, ω the wave pulsation, ε and μ the medium electrical permittivity and permeability respectively. This problem can be solved by considering the scalar wave equation:

$$\nabla^2\psi + k^2\psi = 0, \tag{4.2}$$

where ψ is a function related to the spherical harmonics by $\nabla\times(\mathbf{r}\psi) = \mathbf{M}$ and $\mathbf{N} = (\nabla\times\mathbf{M})/k$. The scalar wave equation may be expressed in the spherical coordinate system as:

$$\frac{1}{r}\frac{\partial}{\partial r}\left(r^2\frac{\partial\psi}{\partial r}\right) + \frac{1}{r^2\sin\theta}\frac{\partial}{\partial\theta}\left(\sin\theta\frac{\partial\psi}{\partial\theta}\right) + \frac{1}{r^2\sin\theta}\frac{\partial^2\psi}{\partial\phi^2} + k\psi^2 = 0. \tag{4.3}$$

The key idea of the Lorenz-Mie theory is to use a separation variable method (SVM) to find particular solutions of the equation (4.3):

$$\psi(r,\theta,\phi) = R(r)\Theta(\theta)\Phi(\phi). \tag{4.4}$$

Using Eq. (4.4) in Eq. (4.3) three separated equations are derived (where m and n are separation constants):

$$\begin{cases} \dfrac{d^2\Phi}{d\phi^2} + m\phi^2 = 0, & (\mathrm{a}) \\ \dfrac{1}{\sin\theta}\dfrac{d}{d\theta}\left(\sin\theta\dfrac{d\Theta}{d\theta}\right) + \left[n(n+1) - \dfrac{m^2}{\sin^2\theta}\right] = 0, & (\mathrm{b}) \\ \dfrac{d}{dr}\left(r^2\dfrac{dR}{dr}\right) + \left[k^2r^2 - n(n+1)\right]R = 0. & (\mathrm{c}) \end{cases} \tag{4.5}$$

The linearly independent solutions of Eq. (4.5)-(a) are of the following type:

$$\begin{cases} \Phi_e = \cos(m\phi), \\ \Phi_o = \sin(m\phi). \end{cases} \tag{4.6}$$

where subscripts e and o denote even and odd respectively.

The solutions of Eq. (4.5)-(b) that are finite at $\theta = 0$ and $\theta = \pi$ are the Legendre's polynomials $P_n^m(\cos\theta)$ and the associated Legendre's functions. To find the solutions of Eq. (4.5)-(c) the dimensionless variable $\rho = kr$ and the function $Z = R\sqrt{\rho}$ are introduced. Thus, Eq. (4.5)-(c) can then be rewritten as:

$$\rho \frac{d}{d\rho}\left(\rho \frac{dZ}{d\rho}\right) + \left[\rho^2 - \left(n - \frac{1}{2}\right)^2\right] Z = 0. \tag{4.7}$$

The linearly independent solutions of Eq. (4.7) are combinations of spherical Bessel's functions of the first and second kind j_n, y_n, $k_n^{(1)}$, $k_n^{(2)}$. Thus, the solutions of Eq. (4.5) that satisfy the scalar wave equation in spherical coordinates are of the following form (Bohren and Huffman 1998):

$$\begin{aligned} \psi_{emn} &= \cos(m\phi) P_n^m(\cos\theta) z_n(kr), \\ \psi_{omn} &= \sin(m\phi) P_n^m(\cos\theta) z_n(kr). \end{aligned} \tag{4.8}$$

4.2.2. The internal and scattered fields

In the linear optics the scattered $(\mathbf{E}_S, \mathbf{H}_S)$ and internal fields $(\mathbf{E}_1, \mathbf{H}_1)$ are simply proportional to incident field. They can be expanded in infinite series of vector spherical harmonics with complex coefficients:

$$\begin{cases} \mathbf{E}_p = \sum_{n=1}^{\infty} E_n \left(c_n \mathbf{M}_{o1n}^{(1)} - i d_n \mathbf{N}_{e1n}^{(1)}\right) \\ \mathbf{H}_p = \dfrac{-k_p}{\omega \mu_p} \sum_{n=1}^{\infty} E_n \left(d_n \mathbf{M}_{e1n}^{(1)} - i c_n \mathbf{N}_{o1n}^{(1)}\right) \end{cases} \quad \begin{cases} \mathbf{E}_s = \sum_{n=1}^{\infty} E_n \left(i a_n \mathbf{N}_{e1n}^{(3)} - b_n \mathbf{M}_{o1n}^{(3)}\right) \\ \mathbf{H}_s = \dfrac{k}{\omega \mu} \sum_{n=1}^{\infty} E_n \left(i b_n \mathbf{N}_{o1n}^{(3)} - a_n \mathbf{M}_{e1n}^{(3)}\right) \end{cases} \tag{4.9}$$

where $E_n = i^n E_0 (2n+1) / n(n+1)$.

In Eq. (4.9) the coefficients a_n, b_n are referred as the "external scattering coefficients" or "Mie coefficients". c_n, d_n are the "internal scattering coefficients". Tangential components of the electromagnetic fields have to fulfill boundary conditions onto the particle surface:

$$\begin{cases} \left[\mathbf{E}_p(\mathbf{X}) - \mathbf{E}_e(\mathbf{X})\right] \times \hat{\mathbf{n}} = 0, \\ \left[\mathbf{H}_p(\mathbf{X}) - \mathbf{H}_e(\mathbf{X})\right] \times \hat{\mathbf{n}} = 0, \end{cases} \tag{4.10}$$

which gives:

$$\begin{cases} E_{i\theta} + E_{s\theta} = E_{p\theta} \\ H_{i\theta} + H_{s\theta} = H_{p\theta} \end{cases} \quad \begin{cases} E_{i\phi} + E_{s\phi} = E_{p\phi} \\ H_{i\phi} + H_{s\phi} = H_{p\phi} \end{cases} \tag{4.11}$$

Introducing the Ricatti-Bessel functions defined as:

$$\psi_n(\rho) = \rho j_n(x_p), \quad \xi_n(x) = \rho h_n^{(1)}(x_p) \tag{4.12}$$

the following relations are derived for the external scattering coefficients (Bohren and Huffman 1998):

$$a_n = \frac{\tilde{m}_p \psi_n(\tilde{m}_p x_p)\psi'_n(x_p) - \psi_n(x_p)\psi'_n(\tilde{m}_p x_p)}{\tilde{m}_p \psi_n(\tilde{m}_p x_p)\xi'_n(x_p) - \xi_n(x_p)\psi'_n(\tilde{m}_p x_p)},$$
$$b_n = \frac{\psi_n(\tilde{m}_p x_p)\psi'_n(x_p) - \tilde{m}_p \psi_n(x_p)\psi'_n(\tilde{m}_p x_p)}{\psi_n(\tilde{m}_p x_p)\xi'_n(x_p) - \tilde{m}_p \xi_n(x_p)\psi'_n(\tilde{m}_p x_p)}. \quad (4.13)$$

The coefficients a_n, b_n can be computed efficiently by using the logarithmic derivatives of the Riccati-Bessel functions:

$$a_n = D_n^{(3)} \frac{\tilde{m}_p D_n^{(1)}(x_p) - D_n^{(1)}(\tilde{m}_p x_p)}{\tilde{m}_p D_n^{(2)}(x_p) - D_n^{(1)}(\tilde{m}_p x_p)},$$
$$b_n = D_n^{(3)} \frac{D_n^{(1)}(x_p) - \tilde{m}_p D_n^{(1)}(\tilde{m}_p x_p)}{D_n^{(2)}(x_p) - \tilde{m}_p D_n^{(1)}(\tilde{m}_p x_p)}. \quad (4.14)$$

where

$$D_n^{(1)}(z) = \frac{\psi'_n(z)}{\psi_n(z)}, \quad D_n^{(2)}(z) = \frac{\xi'_n(z)}{\xi_n(z)}, \quad D_n^{(3)}(z) = \frac{\psi_n(z)}{\xi_n(z)}. \quad (4.15)$$

4.2.3. Expressions for the phase functions and extinction cross sections

In the far field, the relations between the incident and scattered electrical fields can be expressed for the two main polarization components (parallel $\parallel$ and perpendicular $\perp$ to the scattering plane (see Figure 4.1)) as:

$$\begin{pmatrix} E_{s\parallel} \\ E_{s\perp} \end{pmatrix} = \frac{e^{ik(r-z)}}{-ikr} \begin{pmatrix} S_2 & S_3 \\ S_4 & S_1 \end{pmatrix} \begin{pmatrix} E_{i\parallel} \\ E_{i\perp} \end{pmatrix}. \quad (4.16)$$

For a spherical particle we have $S_3 = S_4 = 0$ and S_1, S_2 are given by:

$$S_1 = \sum_{n=1}^{\infty} \frac{(2n+1)}{n(n+1)} (a_n \pi_n + b_n \tau_n),$$
$$S_2 = \sum_{n=1}^{\infty} \frac{(2n+1)}{n(n+1)} (a_n \tau_n + b_n \pi_n), \quad (4.17)$$

where:

$$\pi_n = \frac{P_n^1}{\sin\theta}, \quad \tau_n = \frac{dP_n^1}{\sin\theta}. \quad (4.18)$$

Using the Poynting vector it is possible to derive the relations for the scattering intensities $i_{\parallel} \sim |S_2|^2$ and $i_{\perp} \sim |S_1|^2$.

On the other way, the total scattering, extinction and absorption cross sections can be calculated as:

$$C_{p,sca} = \frac{2\pi}{k^2}\sum_{n=1}^{\infty}(2n+1)\left(|a_n|^2 + |b_n|^2\right) \qquad \text{(a)}$$

$$C_{p,ext} = \frac{2\pi}{k^2}\sum_{n=1}^{\infty}(2n+1)\,\mathrm{Re}\{a_n + b_n\} \qquad \text{(b)} \qquad (4.19)$$

$$C_{p,abs} = C_{p,ext} - C_{p,sca} \qquad \text{(c)}$$

Numerically, the infinite expansion series are truncated for

$$n_{stop} = x_p + 4x_p^{1/3} + 2, \qquad (4.20)$$

where $x_p = \pi d_p / \lambda$ and λ are the size parameter and the wavelength of the incident beam. Note that, according to the localization principle (van der Hulst 1957), the expansion term n may be interpreted as rays that impinge onto the particle surface at distance R_n from the axis:

$$R_n = \left(n + \frac{1}{2}\right)\frac{\lambda}{2\pi}. \qquad (4.21)$$

It is important to notice that since it was introduced, the Lorenz-Mie theory has been widely extended (see Gouesbet's review (Gouesbet 2009)). Nowadays, this method may be used also for the scattering of an arbitrary beam by a homogeneous sphere (Barton et al. 1988; Gouesbet et al. 1988), a multilayered or heterogeneous sphere (Onofri et al. 1995), a circular cylinder or a spheroid (Ren et al. 1997). Numerous computer codes and applications using the LMT have been developed (see e.g. (Wriedt 2009)).

4.3. Rayleigh theory and Rayleigh-Gans-Debye (RGD) theory

If we deal with particles with a complex shape, usually it is impossible to solve the scattering problem in an exact manner (i.e. a SVM is not possible). Thus, one strategy is to find an approximate method that provides results with a satisfactory degree of accuracy. Usually, this kind of approximation is valid only for certain particles (e.g. small compared to the wavelength) and some specific conditions (e.g. angular range, refractive index close to unity, etc.). These limits are part of the price to pay to get a simple and numerically stable (approximate) solution. An example of such an approximation is the Rayleigh-Gans-Debye (RGD) theory, which is widely used to analyze fractal-like aggregates of nanoparticles.

4.3.1. Rayleigh theory

If we consider a particle much smaller than the wavelength, each part of the particle experiences almost the same homogeneous electric field (quasistatic field approximation). Therefore, the light scattered by this particle is the same as if it was scattered from an oscillating dipole radiating in nearly all directions. This scattering is called Rayleigh scattering. Its basic underlying assumptions are given by the following equations (Bohren and Huffman 1998; Xu 2002):

$$\begin{aligned} x_p &\ll 1, \\ \left|\tilde{m}_p\right| x_p &\ll 1. \end{aligned} \tag{4.22}$$

where $x_p = 2\pi r_p / \lambda$ is the size parameter and $\tilde{m}_p$ is the complex refractive index of particles. The amplitude functions are described as:

$$\begin{pmatrix} S_1 & S_4 \\ S_3 & S_2 \end{pmatrix} = ik^3 x_p \begin{pmatrix} 1 & 0 \\ 0 & \cos\theta \end{pmatrix}, \tag{4.23}$$

If the incident light is linearly polarized the angular distribution of the scattered light depends on the polarization:

$$\begin{pmatrix} I_\perp \\ I_\parallel \end{pmatrix} = I_0 \frac{16\pi^4 {r_p}^6}{r^2\lambda^4} \left|\frac{\tilde{m}_p^2 - 1}{\tilde{m}_p^2 + 2}\right|^2 \begin{pmatrix} 1 & 0 \\ 0 & \cos^2\theta \end{pmatrix}, \tag{4.24}$$

where r is the observation distance. For unpolarized incident light we have:

$$I = \frac{1}{2}\left(I_\parallel + I_\perp\right) = I_0 \frac{8\pi^4 {r_p}^6}{r^2\lambda^4} F\left(\tilde{m}_p\right). \tag{4.25}$$

For latter convenience, the following optical factors are commonly introduced:

$$E(\tilde{m}_p) = \mathrm{Im}\left(\frac{\tilde{m}_p^2 - 1}{\tilde{m}_p^2 + 2}\right), \qquad F(\tilde{m}_p) = \left|\frac{\tilde{m}_p^2 - 1}{\tilde{m}_p^2 + 2}\right|^2. \tag{4.26}$$

So that we get for the two main polarizations:

$$\begin{aligned} I_{p,\perp}(\theta) &= k^4 r_p^6 F\left(\tilde{m}_p\right) && \text{(a)} \\ I_{p,\parallel}(\theta) &= I_{p,\perp}(\theta)\cos^2\theta && \text{(b)} \end{aligned} \tag{4.27}$$

and the cross sections:

$$\begin{aligned} C_{p,abs} &= 4\pi k r_p^3 E\left(\tilde{m}_p\right) && \text{(a)} \\ C_{p,sca} &= \frac{8}{3}\pi k^4 r_p^6 F\left(\tilde{m}_p\right) && \text{(b)} \\ C_{p,ext} &= C_{p,abs} + C_{p,sca} && \text{(c)} \end{aligned} \tag{4.28}$$

From Eq. (4.28) it can be seen that according to the Rayleigh theory the scattering cross section is proportional to r_p^6, while the absorption cross section is proportional to r_p^3. Thus, for absorbing particles that are much smaller than the wavelength it is common to neglect the scattering cross section when calculating the extinction ($C_{p,ext} \simeq C_{p,abs}$). As an example, Figure 4.2 shows the cross sections of a single particle (monomer) of soot (complex refractive index $\tilde{m}_p = 1.57 + 0.56i$ (Dalzell and Sarofim 1969)) versus its radius. It can be seen that, for the Rayleigh calculations the ratio $C_{p,abs} / C_{p,sca}$ is larger than 100 for the particle with $r_p \le 22\ nm$ ($x_p \le 0.26$) and larger than 10 for $r_p \le 47\ nm$ ($x_p \le 0.56$). Figure 4.2 compares also Rayleigh to T-Matrix calculations, which are considered to be exact for this case (see section 4.5). Clearly, there is almost a perfect agreement between both theories for radius of particle up to several dozens of nanometers.

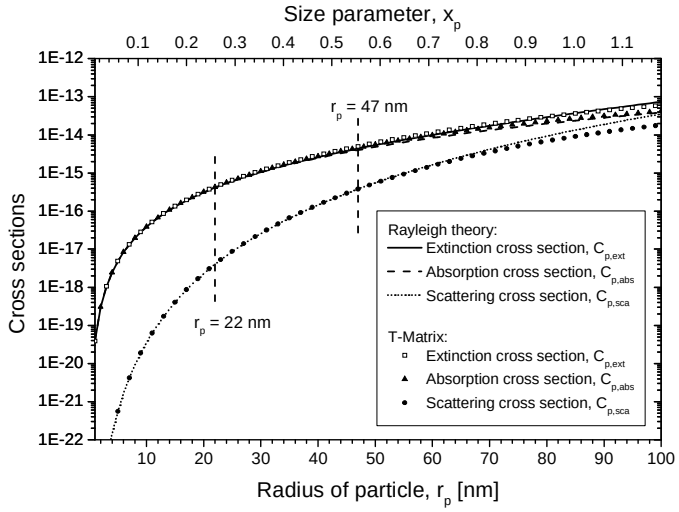

Figure 4.2. Comparison between the extinction, absorption and scattering cross sections of spherical particle of soot ($\tilde{m}_p = 1.57 + 0.56i$) versus its radius and for the incident wavelength $\lambda = 532\ nm$ - Rayleigh and T-Matrix calculations.

The Rayleigh differential scattering cross section of a spherical particle (where Ω stands for a solid angle) (Kerker 1969) is given as:

$$\frac{dC_{p,sca}}{d\Omega} = k^4 r_p^6 F\left(\tilde{m}_p\right). \tag{4.29}$$

4.3.2. Rayleigh-Gans-Debye (RGD) theory

The Rayleigh-Gans-Debye (RGD) theory is used for particles small compared to the wavelength and suspended in a medium with similar optical properties. Its applicability is limited to particle and media satisfy the following assumptions (Bohren and Huffman 1998):

$$\begin{aligned} &\left|\tilde{m}_p - 1\right| \ll 1, \\ &kd_p \left|\tilde{m}_p - 1\right| \ll 1. \end{aligned} \tag{4.30}$$

where d_p is the particle diameter. The basic assumption of the RGD theory is that a particle initially too large to be treated as a single dipole can be decomposed into an assembly of single structureless scattering elements. Each of them separately satisfies the Rayleigh theory and thus may be successfully analyzed. Due to the small size of the particle we can neglect the phase shift corresponding to any element and assume that the phase difference between elements is determined only by their position. In the framework of the RGD theory, the amplitude functions are given by:

$$\begin{pmatrix} S_1 & S_4 \\ S_3 & S_2 \end{pmatrix} = \frac{ik^3\left(\tilde{m}_p - 1\right)V}{2\pi} f\left(\theta,\varphi\right) \begin{pmatrix} 1 & 0 \\ 0 & \cos\theta \end{pmatrix}, \tag{4.31}$$

where $f\left(\theta,\varphi\right)$ is referred as a "form factor" that depends on the shape of the particle of volume V:

$$f\left(\theta,\varphi\right) = \frac{1}{V}\int_V e^{i\delta} dV. \tag{4.32}$$

For a spherical particle, the volume integral given by Eq. (4.32) simplifies to a convenient analytical form:

$$f(\theta)=\frac{3}{u^3}(\sin u-u\cos u), \tag{4.33}$$

where $u=2x_p\sin(\theta/2)$. Using Eqs. (4.31) and (4.33) we can derive the dependency for the scattering matrix elements. For the perpendicular and parallel polarization we get the following expressions for the scattered intensities:

$$\begin{aligned} S_1S_1^* &= \left[\frac{3}{u^3}(\sin u-u\cos u)\right]^2 \qquad \text{(a)} \\ S_2S_2^* &= \left[\frac{3}{u^3}(\sin u-u\cos u)\right]^2\cos^2\theta \qquad \text{(b)} \end{aligned} \tag{4.34}$$

Figure 4.3 shows the intensity scattered for the (a) perpendicular and (b) parallel polarization, by a spherical particle with $r_p=200\ nm$ for an incident wavelength $\lambda=200\ nm$ according to the RGD theory. It should be noticed that a log-log scale is used to show the evolution of the scattering intensities versus the magnitude of the scattering wave vector q:

$$q=2k\sin\left(\frac{\theta}{2}\right). \tag{4.35}$$

It is worth to notice, that for the perpendicular polarization we have a decay of the scattered intensity $I(q)\sim q^{-4}$.

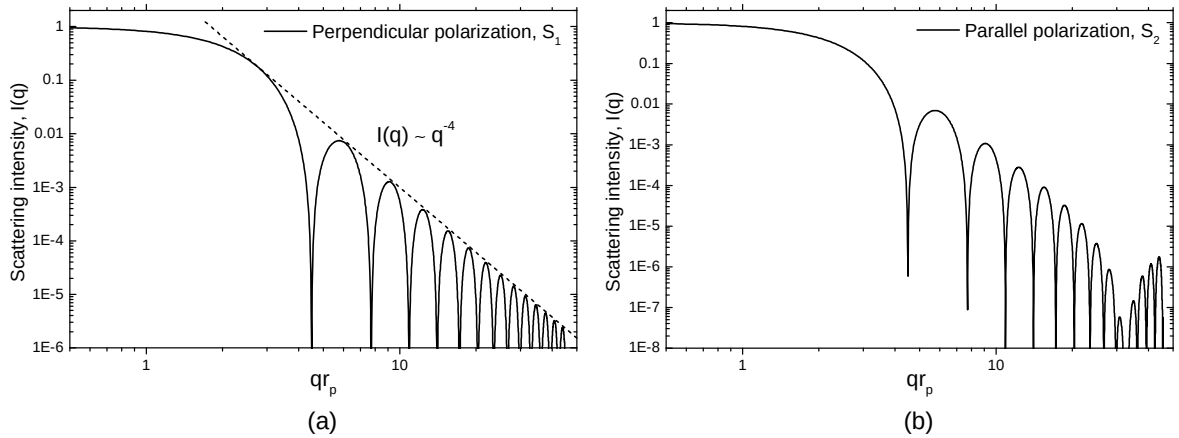

Figure 4.3. Scattering of a spherical particle according to the RGD theory: (a) perpendicular and (b) parallel polarization.

In the RGD framework, it is possible to estimate scattering properties of an aggregate of spherical particles[2] that are small compared to the wavelength. To do so, it is necessary to consider that multiple scattering effects and self interactions between the particles are negligible, so that the scattering intensity can be calculated as (Bohren and Huffman 1998):

$$I_{a,\gamma}(\theta)=n_p^2I_{p,\gamma}(\theta), \tag{4.36}$$

[2] These particles are referred as "monomers" in the other chapters of this manuscript.

where $\gamma = \parallel$ or $\perp$ and $I_{p,\gamma}(\theta)$ is the scattering intensity of the single particle (calculated with the Rayleigh theory, see Eq. (4.27)). The cross sections of the aggregate are expressed as:

$$\begin{aligned} C_{a,abs} &= n_p C_{p,abs} \qquad \text{(a)} \\ C_{a,sca} &= n_p^2 C_{p,sca} \qquad \text{(b)} \end{aligned} \tag{4.37}$$

where $C_{p,abs}$ and $C_{p,sca}$ are the cross sections of the single particle (see Eqs. (4.28)).

As an example, Figure 4.4 compares results of the RGD theory and the T-Matrix. It shows the cross sections of soot aggregates of (a) $n_p = 20$ and (b) $n_p = 100$ monomers with fractal dimension $D_f = 1.80$ and refractive index $\tilde{m}_p = 1.57 + 0.56i$ (Dalzell and Sarofim 1969). It can be noticed that the RGD and Rayleigh theories use similar relations for the cross sections. For aggregates sufficiently small compared to the wavelength (with the small radius of particle and/or the limited number of monomers within the aggregate) the scattering cross section may be neglected ($C_{a,ext} \simeq C_{a,abs}$). If we consider the soot aggregate with $n_p = 20$ monomers and $\tilde{m}_p = 1.57 + 0.56i$ (see Figure 4.4 (a)) the ratio $C_{a,abs} / C_{a,sca}$ is larger than 10 if $r_p \leq 17\ nm$ ($x_p \leq 0.20$). For this value of r_p and a fractal dimension of $D_f = 1.80$, we derived as an estimation that $R_g \leq 69.2\ nm$. For the aggregate presented in Figure 4.4 (b) the critical value $r_p \leq 10\ nm$ ($x_p \leq 0.12$) corresponds to $R_g \leq 99.7\ nm$. In addition, both subfigures clearly show that for sufficiently small size parameters, the RGD results are in a very good agreement with the T-Matrix solution.

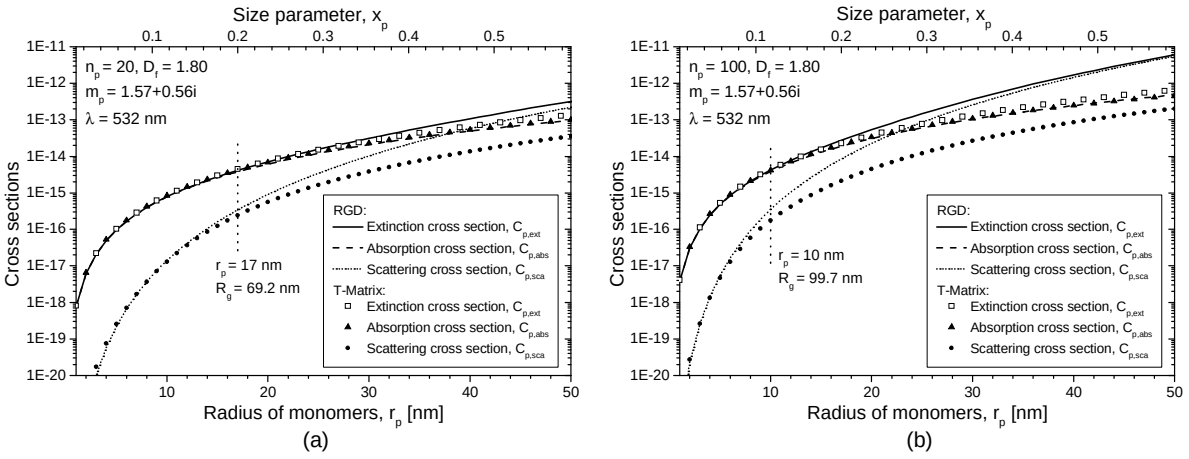

Figure 4.4. Comparison between RGD and T-Matrix: cross sections of soot aggregates versus the radius of monomers ($D_f = 1.80$, $\tilde{m}_p = 1.57 + 0.56i$, $\lambda = 532\ nm$) with (a) $n_p = 20$ and (b) $n_p = 100$.

4.4. Rayleigh-Debye-Gans theory for Fractal Aggregates (RDG-FA)

4.4.1. General assumptions

One major limitation of the basic RGD theory for spherical particles is that it do not account for the morphology of aggregates. It should be also noticed that the RGD theory assumptions (Eqs. (4.30)) are rarely satisfied for soot, silicon, silicon dioxide or tungsten aggregates in which we are interested in (Chapters 5 and 6). In some cases, the RDG-FA solves the former

problem. In addition, it is compatible with the underlying idea that it is better to avoid requiring an *a priori* knowledge about the relative positions (i.e. sets of coordinates) of all monomers within the aggregate. Thus, it is more suitable to describe in a "global" way the structure of the aggregate by parameters such as D_f, k_f, R_g, n_p and r_p.

4.4.2. Scattering intensity and cross sections

According to the RDG-FA approximation, the intensity scattered at angle θ, by an aggregate of spherical particles, is given by (Dobbins and Megaridis 1991):

$$\begin{aligned} I_{a,\perp}(\theta) &= n_p^2 I_{p,\perp}(\theta)\, f\left(q, R_g, D_f\right) \qquad \text{(a)} \\ I_{a,\parallel}(\theta) &= I_{a,\perp}(\theta)\cos^2\theta \qquad \text{(b)} \end{aligned} \tag{4.38}$$

The form factor (known also as the shape factor) $f\left(q, R_g, D_f\right)$ of fractal aggregate has been widely investigated. According to Dobbins and Megaridis (Dobbins and Megaridis 1991) it has two forms depending on the scattering regime considered, i.e. the (a) Guinier (small-angles) or the (b) power law (large-angles) regimes:

$$\begin{aligned} f\left(q, R_g, D_f\right) &= \exp\left(-\frac{q^2 R_g^2}{3}\right), \quad q^2 R_g^2 \le 1.5 D_f \text{ (Guinier regime)} \qquad \text{(a)} \\ f\left(q, R_g, D_f\right) &= \left(q^2 {R_g}^2\right)^{-D_f/2}, \quad q^2 R_g^2 > 1.5 D_f \text{ (Power-law regime)} \qquad \text{(b)} \end{aligned} \tag{4.39}$$

where q is the amplitude of the scattering (wave) vector, defined in Eq. (4.35). The absorption, scattering and extinction cross sections are given by:

$$\begin{aligned} C_{a,abs} &= n_p C_{p,abs} \qquad \text{(a)} \\ C_{a,sca} &= n_p^2 C_{p,sca} G\left(k, R_g, D_f\right) \qquad \text{(b)} \\ C_{a,ext} &= C_{a,abs} + C_{a,sca} \qquad \text{(c)} \end{aligned} \tag{4.40}$$

where $C_{p,abs}$ and $C_{p,sca}$ are the absorption and scattering cross sections of a single particle and $G\left(k, R_g, D_f\right)$ is a structure factor (Dobbins and Megaridis 1991). For a fractal aggregate this new factor is defined as follows:

$$G\left(k, R_g, D_f\right) = \left(1 + \frac{4}{3D_f} k^2 R_g^2\right)^{-D_f/2}. \tag{4.41}$$

As an example, Figure 4.5 shows a comparison between the extinction, absorption and scattering cross sections of soot aggregates with (a) $n_p = 20$ and (b) $n_p = 100$ monomers, the fractal dimension of $D_f = 1.80$ and refractive index equal to $\tilde{m}_p = 1.57 + 0.56i$ (Dalzell and Sarofim 1969). We found that for the small size parameters considered here, the RDG-FA fits pretty well the T-Matrix results.

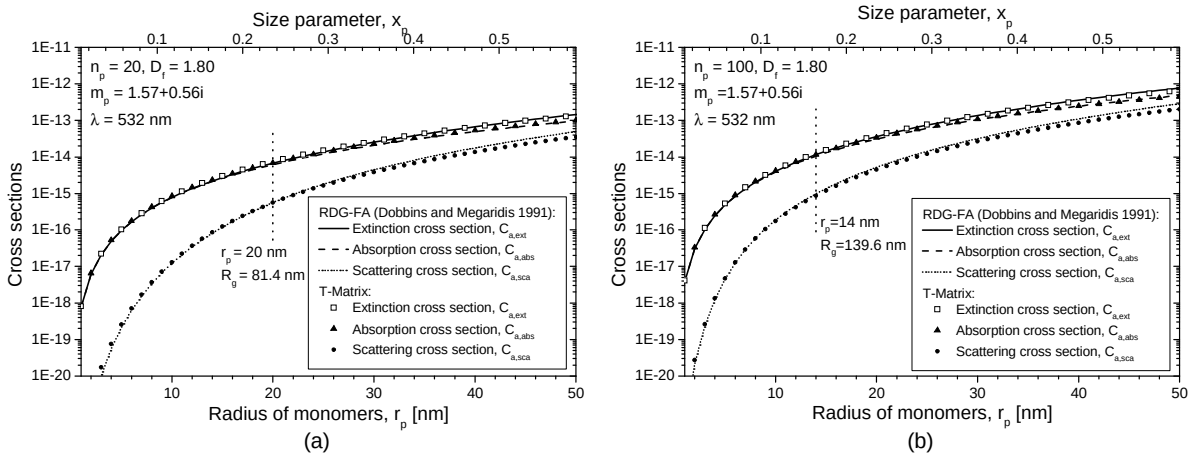

Figure 4.5. Comparison between RDG-FA (Dobbins and Megaridis 1991) and T-Matrix: the cross sections of the soot aggregates versus the radius of monomers within the aggregate with (a) $n_p = 20$ and (b) $n_p = 100$; $D_f = 1.80$, $\tilde{m}_p = 1.56 + 0.57i$; incident wavelength $\lambda = 532\ nm$.

If we compare results presented in Figure 4.4 and Figure 4.5, it can be noticed that according to the RDG-FA theory, the scattering cross section increases slower for increasing radius of monomers than with the RGD theory. This is a direct consequence of the structure factor, $G\left(k, R_g, D_f\right)$ which appears in Eq. (4.40)-(b) and takes into account the radius of gyration and the fractal dimension of the aggregate. The scattering cross section for the aggregate of soot with $n_p = 100$ monomers and fractal dimension $D_f = 1.80$ calculated according to the RDG-FA theory is compared with the RGD calculations in Figure 4.6. Additionally, the latter figure presents also structure factor $G\left(k, R_g, D_f\right)$ for the given aggregate.

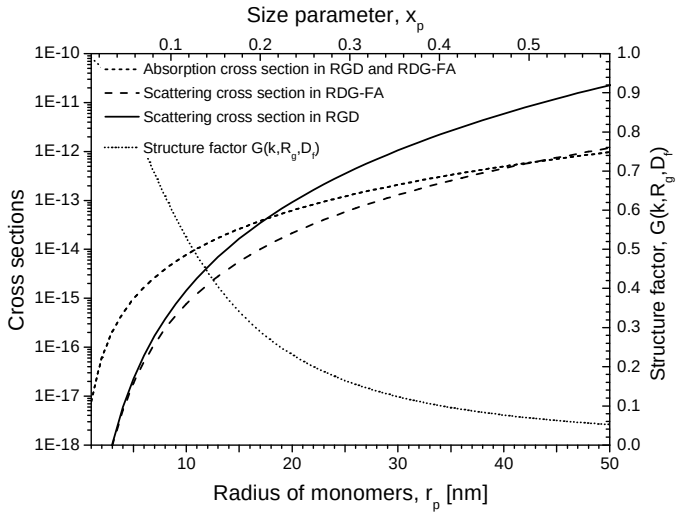

Figure 4.6. Comparison between the scattering cross sections calculated according to the RGD and RDG-FA (Dobbins and Megaridis 1991) theories for the aggregate of soot with $n_p = 100$, $D_f = 1.80$ and $R_g = 9.97 r_p$.

As clearly pointed out above, according to the RGD theory the scattering cross section is directly proportional to the n_p^2, so it rapidly increases as the number of monomers increases. But, as there is no assumption of multiple scattering effects between monomers in the RGD theory, the consequence is that the RGD strongly overestimates the scattering cross section of

large (and dense) aggregates. In contradiction to that, in the RDG-FA theory, the structure factor $G\left(k,R_g,D_f\right)$ introduces an "asymptotic saturation" of the scattering cross section for large values of R_g and D_f, see Figure 4.7. We remark also that the structure factor decreases more rapidly as r_p increases, for aggregates with a large monomers and a large fractal dimension.

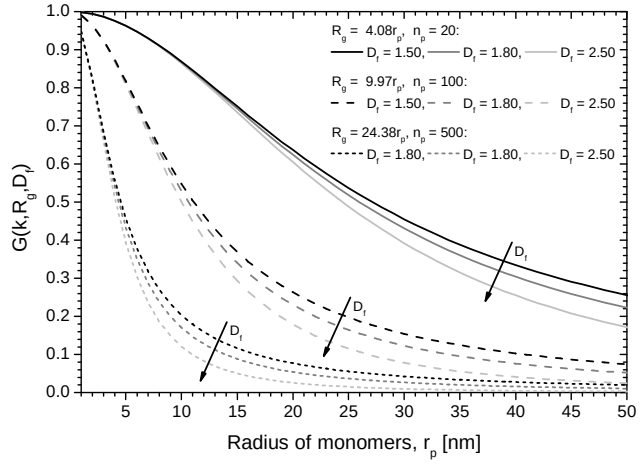

Figure 4.7. Evolution of the structure factor of the RDG-FA theory versus the radius of monomers.

With the RDG-FA, the differential scattering cross section of an ensemble of aggregates is expressed by:

$$\frac{dC_{a,sca}}{d\Omega} = n_p^2 \frac{dC_{p,sca}}{d\Omega} S(q), \tag{4.42}$$

where $S(q)$ is an structure factor:

$$\begin{aligned} &S(q)=1, && qR_g<1 && \text{(a)} \\ &S(q)=C\left(qR_g\right)^{-D_f}, && qR_g>1 && \text{(b)} \end{aligned} \tag{4.43}$$

where $C \simeq 1.0$ is an empirical constant (Sorensen 2001). The intensity I_S of the scattered light measured by a detector, which subtends a given solid angle relative to the scattering volume in a given distance, is described as (Sorensen et al. 1992a):

$$I_S = c_0 I_0 C_n \frac{dC_{a,sca}}{d\Omega}, \tag{4.44}$$

where C_n is a particles number concentration. Combining Eqs. (4.29) and (4.42):

$$I_S = c_0 I_0 C_n n_p^2 \frac{dC_{p,sca}}{d\Omega} S(q). \tag{4.45}$$

Using equation (4.29) in Eq. (4.45) we obtain:

$$I_S = c_0 I_0 C_n n_p^2 k^4 r_p^6 F\left(\tilde{m}_p\right) S(q). \tag{4.46}$$

In the Rayleigh regime Eq. (4.46) is expressed as:

$$\begin{aligned} &I_S = c_0 I_0 C_n n_p^2 k^4 r_p^6 F\left(\tilde{m}_p\right) && \text{monodisperse aggregate} && \text{(a)} \\ &I_S = c_0 I_0 M_2 k^4 r_p^6 F\left(\tilde{m}_p\right) && \text{polydisperse aggregate} && \text{(b)} \end{aligned} \tag{4.47}$$

where M_2 is the second momentum (i.e. variance) of the distribution of the number of monomers within aggregates.

4.4.3. Scattering-extinction analysis

According to Sorensen et. al (Sorensen et al. 1992a) a comparison between the scattering and the extinction measurements enables to determine the volume-equivalent sphere radius (R_v) of the aggregate by combining scattering and extinction (SE) analysis $R_{SE} = R_v$. This relation can be used to estimate the fractal dimension of soot aggregates as well as the radius of single particles within aggregates.

The extinction transmittance is given by the equation:

$$I_T = I_0 exp\left(-\tau_{ext} L\right), \tag{4.48}$$

where τ_{ext} is the turbidity and L is the probed length of the system (i.e. cloud of monodisperse aggregates). The total extinction is the sum of the absorption and scattering cross sections:

$$C_{a,ext}^{T} = C_n \left(C_{a,abs} + C_{a,sca}\right), \tag{4.49}$$

where C_n is the number density of particles. From Eqs. (4.40)-(a) and (4.40)-(b), Eq. (4.49) becomes:

$$C_{a,ext}^{T} = C_n \left(n_p C_{p,abs} + n_p^2 C_{p,sca} G\left(kR_g\right)\right). \tag{4.50}$$

Using Eqs. (4.40) (a)-(b) and (4.28) (a)-(b) in Eq. (4.50) we obtain (Sorensen et al. 1992a):

$$C_{a,ext}^{T} = C_n \left[4\pi n_p k r_p^3 E(\tilde{m}_p) + \frac{8}{3}\pi n_p^2 k^4 r_p^6 F(\tilde{m}_p) G\left(kR_g\right)\right]. \tag{4.51}$$

If we consider the extinction in the Rayleigh limit where $C_{a,abs} \gg C_{a,sca}$ (see Figure 4.2) then the total extinction expressed by Eq. (4.51) can be simplified to:

$$\begin{aligned} C_{a,ext} &\simeq 4\pi n_p C_n k r_p^3 E\left(\tilde{m}_p\right) \qquad \text{monodisperse} \quad \text{(a)} \\ C_{a,ext} &\simeq 4\pi M_1 k r_p^3 E\left(\tilde{m}_p\right) \qquad \text{polydisperse} \quad \text{(b)} \end{aligned} \tag{4.52}$$

where M_1 is the first momentum of the PSD function, i.e. the total number of monomers per unit volume:

$$M_1 = \frac{3 C_n n_p}{4\pi r_p^3}. \tag{4.53}$$

Particles volume fraction is expressed by the following equations:

$$\begin{aligned} C_v &= C_n n_p \frac{4\pi r_p^3}{3} \qquad \text{monodisperse} \quad \text{(a)} \\ C_v &= M_1 \frac{4\pi r_p^3}{3} \qquad \text{polydisperse} \quad \text{(b)} \end{aligned} \tag{4.54}$$

Using Eqs. (4.52) (a-b) in Eqs. (4.54) (a-b) respectively, we obtain:

$$C_v = \frac{C_{a,ext}}{3kE\left(\tilde{m}_p\right)} \quad \text{monodisperse} \quad \text{(a)}$$
$$C_v = \frac{C_{a,ext}}{3kE\left(\tilde{m}_p\right)} \quad \text{polydisperse} \quad \text{(b)} \tag{4.55}$$

Combining Eq. (4.47)-(a) with Eq. (4.52) and using volume equivalent sphere radius $R_v^3 = n_p r_p^3$ we derive a set of two equations for the volume equivalent radius and the number particle density:

$$R_{SE}^3 = R_v^3 = r_p^3 \frac{M_2}{M_1} = r_p^3 n_p = \frac{4\pi}{k^3} \frac{E\left(\tilde{m}_p\right)}{F\left(\tilde{m}_p\right)} \frac{I_S / I_0 c_0}{C_{a,ext}}, \tag{4.56}$$

$$C_n = \frac{M_1}{s_2} = \left(\frac{k}{4\pi}\right)^2 \frac{F\left(\tilde{m}_p\right)}{E\left(\tilde{m}_p\right)^2} \frac{C_{a,ext}^2}{I_S / I_0 c_0}, \tag{4.57}$$

It must be pointed out that Eq. (4.56) is based on the assumption that the ratio of any two consecutive moments of the distribution is a mean size. So that, in the latter case, the ratio M_2 / M_1 provides the average number of monomers per aggregate $\overline{n}_p$.

Combination of Eq. (4.56) with the fractal equation (Eq. (2.13)) leads to the following expression (Sorensen et al. 1992a):

$$R_{SE} = k_f^{\,1/D_f} n_p^{\,1/3-1/D_f} R_g. \tag{4.58}$$

The latter equation shows that log-log plot of the experimental values of R_{SE} (i.e. evaluated with the scattering and extinction measurements) versus R_g should be linear with $D_f / 3$. The interception point between the given plot and the $x-$axis provides the estimate of r_p. The approach described above was successfully used by Sorensen (Sorensen et al. 1992a; Sorensen 2001) to evaluate fractal dimension of the aggregates of soot using scattering data (particularly I_S, R_g and $C_{a,ext}$) recorded at various positions above the burner. To cancel out influence of the fractal prefactor k_f and number of monomers r_p, Sorensen performed relative analysis i.e. using fixed point in the flame as a reference point. One key assumption introduced in this model, which may be somehow questionable, is that the number of monomers is determined by the combustion reaction and it becomes constant afterwards.

4.4.4. RDG-FA theory for soot aggregates

We have shown in section 4.4.2, how the RDG-FA theory can be used to estimate optical properties of fractal-like aggregates. However, in the literature there exist several formulations for the structure factor $G\left(k, R_g, D_f\right)$ than the one used here (Sorensen 2001). The other formulation that is the most widely used was derived by Koylu and Faeth (Koylu and Faeth 1992; Farias 1997). Within the power-law regime ($k^2 R_g^{\,2} > 3D_f / 8$):

$$G\left(k,R_g,D_f\right)=\frac{\beta}{2}\left(3-3\beta+2\beta^2\right)-\frac{k^2{R_g}^2}{3}\beta^2\left(3-4\beta+3\beta^2\right)+\left(4k^2{R_g}^2\right)^{-\frac{D_f}{2}}\times$$
$$\times\left[\frac{3}{2-D_f}-\frac{12}{\left(6-D_f\right)\left(4-D_f\right)}-3\beta^{1-\frac{D_f}{2}}\left(\frac{1}{2-D_f}-\frac{2\beta}{4-D_f}+\frac{2\beta^2}{6-D_f}\right)\right], \tag{4.59}$$

where:

$$\beta=\frac{3D_f}{8k^2{R_g}^2}. \tag{4.60}$$

In the Guinier regime ($k^2{R_g}^2\le 3D_f/8$) $\beta=1$, Eq. (4.59) reduces to:

$$G\left(k,R_g,D_f\right)=1-\frac{2k^2{R_g}^2}{3},\quad kR_g\ll 1. \tag{4.61}$$

If scattering diagram is dominated by the power-law regime (i.e. $\beta\cong 0$) Eq. (4.59) yields:

$$G\left(k,R_g,D_f\right)=\left(\frac{3}{2-D_f}-\frac{12}{\left(6-D_f\right)\left(4-D_f\right)}\right)\left(4k^2{R_g}^2\right)^{-D_f/2},\quad kR_g\gg 1. \tag{4.62}$$

The formulation derived by Koylu and Faeth is much more complex and formally quite different from the one introduced by Dobbins and Megaridis (see Eq. (4.41)). However, the numerical results obtained with both equations are not so different for small and medium size aggregates.

4.4.4.1. Numerical examples for the cross sections

As an example of the RDG-FA theory, Figure 4.8 and Figure 4.9 show the absorption and the extinctions cross sections predicted according to the RDG-FA (equations formulated by Dobbins and Megaridis as well as Koylu and Faeth) and the T-Matrix theories. It can be seen that for aggregates with $n_p=20$ monomers (Figure 4.8), both solutions of the RDG-FA theory are in a very good agreement with the T-Matrix for radius of single monomers increasing from $r_p=1\,nm$ up to the $r_p=30-40\,nm$ (i.e. size parameter $x_p\simeq 0.35-0.47$). The absorption cross section according to the RDG-FA is predicted accurately in the entire range of the r_p, while significant differences appear only for extinction. If we consider larger aggregate (e.g. with $n_p=100$, see Figure 4.9) differences between the RDG-FA and T-Matrix theories can be already seen for $r_p=20-30\,nm$ ($x_p\simeq 0.24-35$). The latter behavior of the RDG-FA theory is caused by the fact that for large aggregates the power-low regime has a much larger influence to the total scattering that the Guinier regime. It can be also seen that in the given example extinction cross section calculated according to Koylu and Faeth for $r_p>40\,nm$ is significantly overestimated comparing to the other solution.

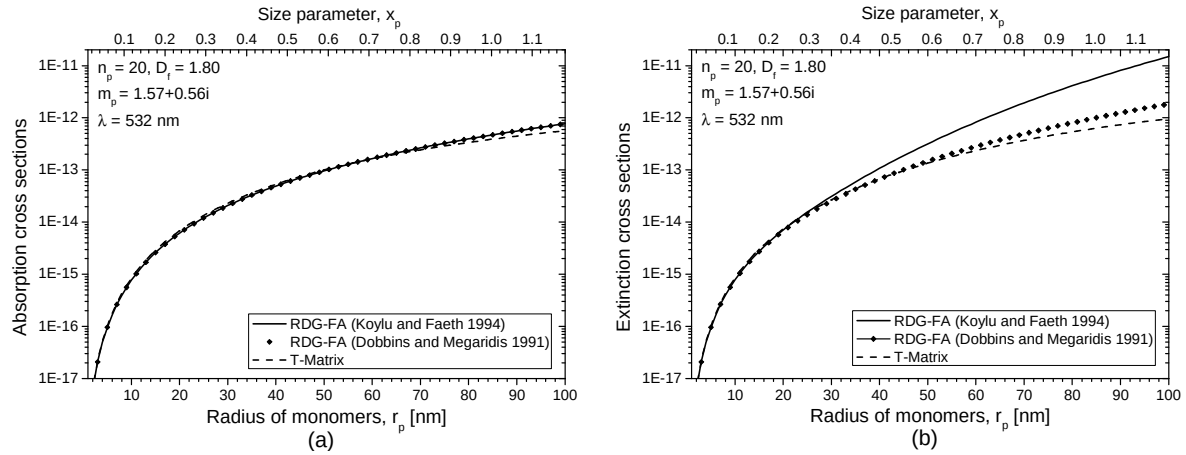

Figure 4.8. A comparison between the (a) absorption and (b) extinction cross sections of soot aggregates versus the radius of monomers with $n_p = 20$, $D_f = 1.80$, $\tilde{m}_p = 1.57 + 0.56i$, $\lambda = 532\ nm$ according to RDG-FA theory and T-Matrix method.

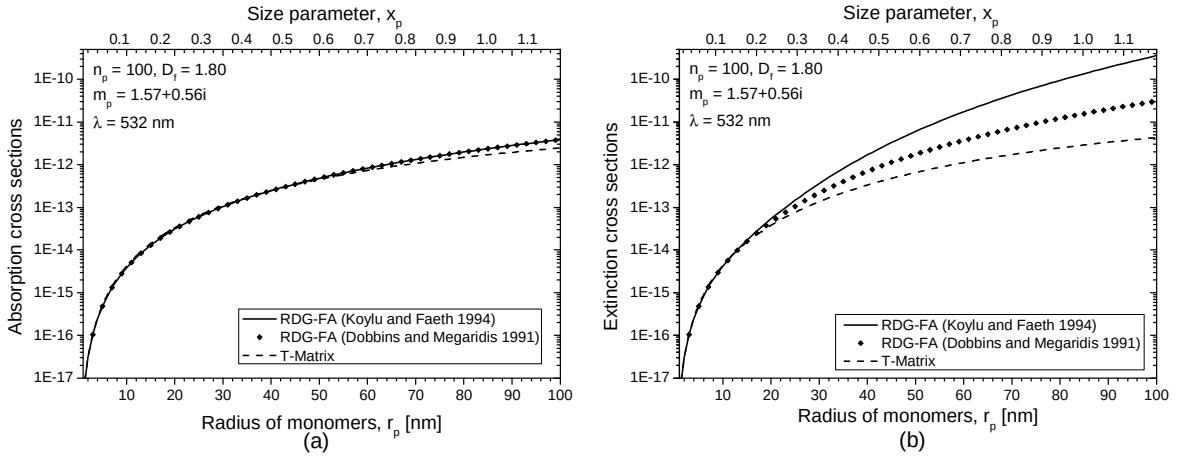

Figure 4.9. A comparison between the (a) absorption and (b) extinction cross sections of soot aggregates versus the radius of monomers with $n_p = 100$, $D_f = 1.80$, $\tilde{m}_p = 1.57 + 0.56i$, $\lambda = 532\ nm$ according to RDG-FA theory and T-Matrix method.

Figure 4.10 evaluates the range of validity of the RDG-FA theory with the second formulation of the structure factor (Koylu and Faeth 1994) compared to the T-Matrix results. It presents isole-maps of the percent deviation of the absorption cross sections for aggregates with $D_f = 1.80$ and (a) $n_p = 16$, (b) $n_p = 64$ and (c) $n_p = 256$. Size parameter and refractive index were chosen as $x_p = 0.01 - 1.00$ and $\left|\tilde{m}_p - 1\right| = 0.1 - 2.0$ (where $\tilde{m}_p = m_p + ik_p$ and $\tilde{m}_p = k_p + 1$) respectively. These parameters we chosen to compare our results with the simulations presented by Farias et al. (Farias et al. 1996; Farias 1997). The RDG-FA and T-Matrix theories agree within 10% in the region (1), $10 - 30\%$ in the region (2) and more than 30% in the region (3). Figure 4.11 presents similar results, for scattering cross sections.

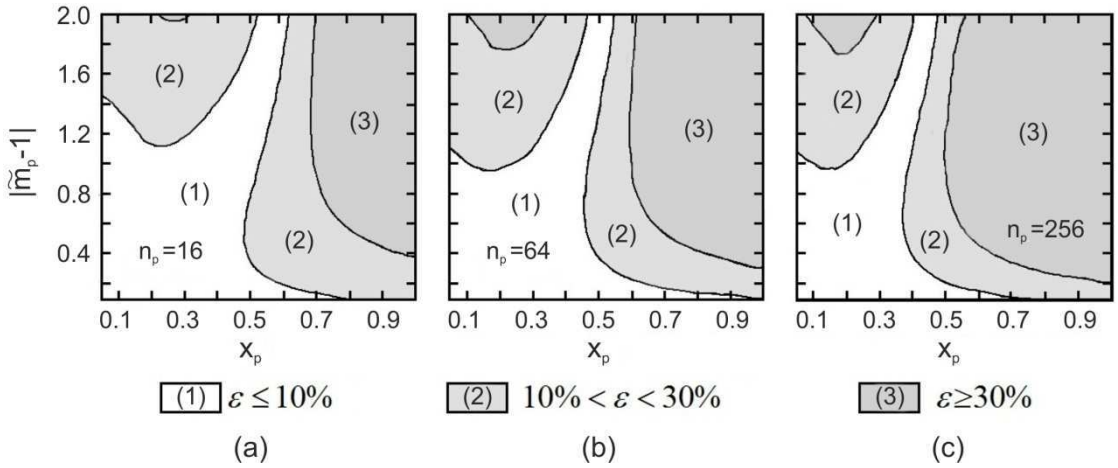

Figure 4.10. Percent deviation between RDG-FA approximation and T-Matrix results for the absorption cross section of fractal aggregates $D_f = 1.80$ with various size parameters (x_p) and various number of monomers.

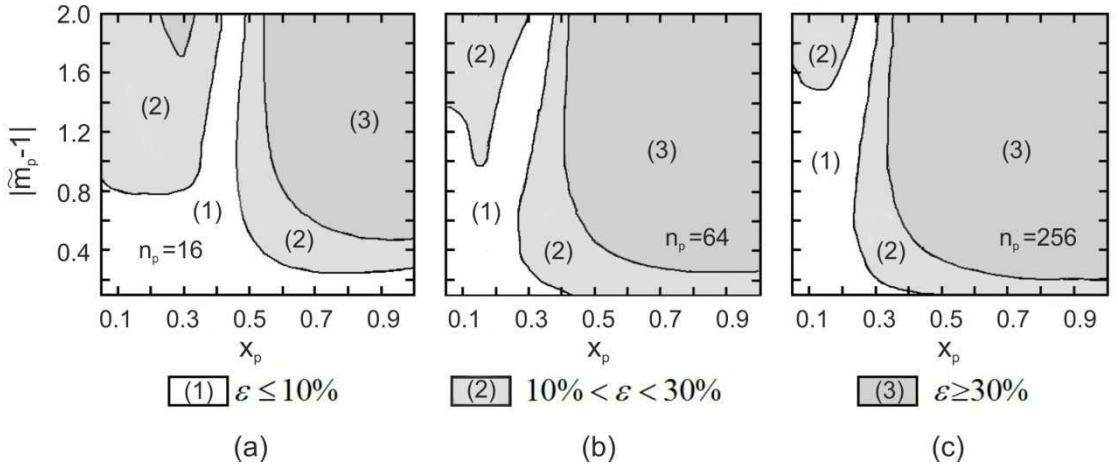

Figure 4.11. Like in Figure 4.10 but for scattering cross sections.

From Figure 4.10 and Figure 4.11 it can be seen that the RDG-FA theory provides results with a reasonably good accuracy for aggregates with small size parameter and relatively small refractive index. When predicting absorption cross section, accuracy better than 10% can be reached for $|\tilde{m}_p - 1| < 1$ and $x_p < 0.4$ regardless of the number of monomers within aggregate. The same accuracy for scattering cross section can be obtained when $|\tilde{m}_p - 1| < 0.8$ and $x_p < 0.25$. It should be noticed that accuracy better than 10% when predicting absorption as well as scattering cross section cover a wide variety of soot aggregates. For instance, size parameter equal to $x_p = 0.25$ corresponds to $r_p \simeq 21\,nm$ if the incident wavelength $\lambda = 532\,nm$ is used. This value exceed typical radiuses of single monomers of soots aggregates generated during the combustion of various chemical compounds (Ouf 2006).

4.4.4.2. Numerical examples for the scattering diagrams

Figure 4.12 compares the RDG-FA and T-Matrix results for intermediate size soot aggregates (i.e. $n_p = 100$, $r_p = 25\,nm$, $R_g = 249\,nm$ and $R_g = 322\,nm$) while Figure 4.13 and Figure 4.14 for the large ones ($n_p = 500, r_p = 25\,nm, R_g = 515 - 909\,nm$). The refractive index of particles is equal to $\tilde{m}_p = 1.57 + 0.56i$ (Dalzell and Sarofim 1969). Aggregates are investigated with perpendicularly or parallel polarized incident plane wave with $\lambda = 532\,nm$ (green laser diode). The scattering intensities are plotted versus the scattering vector q (see chapter 5).

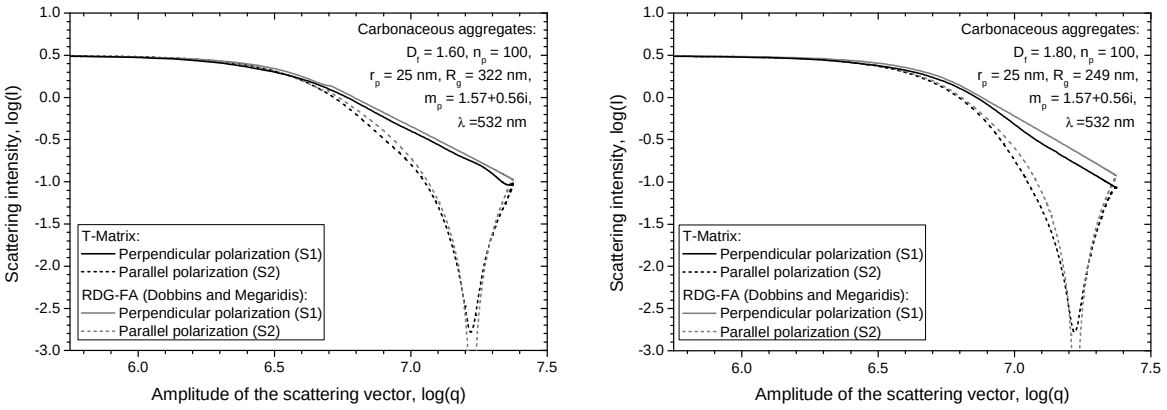

Figure 4.12. A comparison between RDG-FA and T-Matrix predictions for the scattering diagrams of soot aggregates with intermediate size ($n_p = 100, r_p = 25\,nm$).

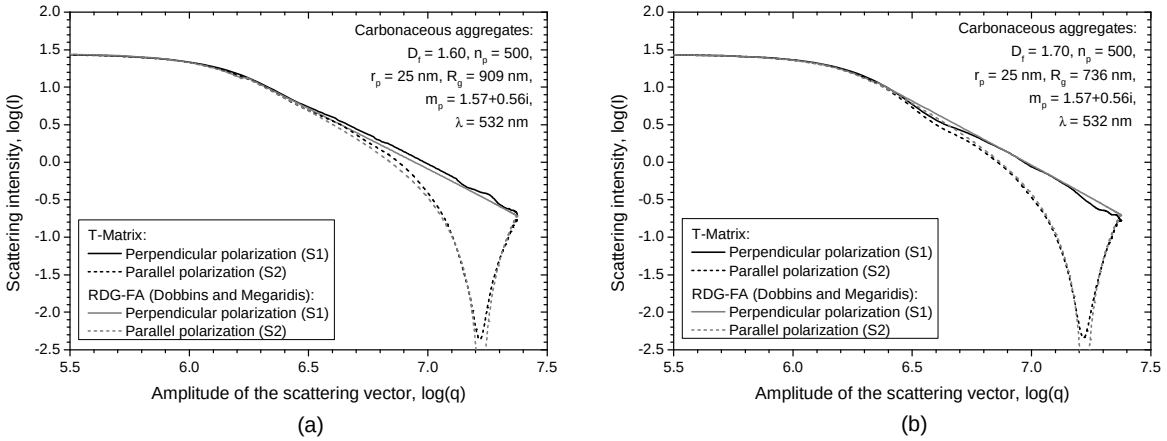

Figure 4.13. A comparison between RDG-FA and T-Matrix predictions for the scattering diagrams of soot aggregates with intermediate size ($n_p = 500$, $r_p = 25\,nm$).

From Figure 4.12 – Figure 4.14 it can be seen that scattering diagrams for the aggregates with small fractal dimensions ($D_f = 1.60$) fit rather well for all the scattering angles. At the same time for the $D_f \geq 1.80$ they significantly differ for the intermediate values of q. However, it should be noticed that for the larger values of the scattering vector q the decay in the power-law region are very similar with the RDG-FA and the T-Matrix. For a more quantitative comparison of this power-law region we can use the algorithm developed in chapter 5, see Table 4.1.

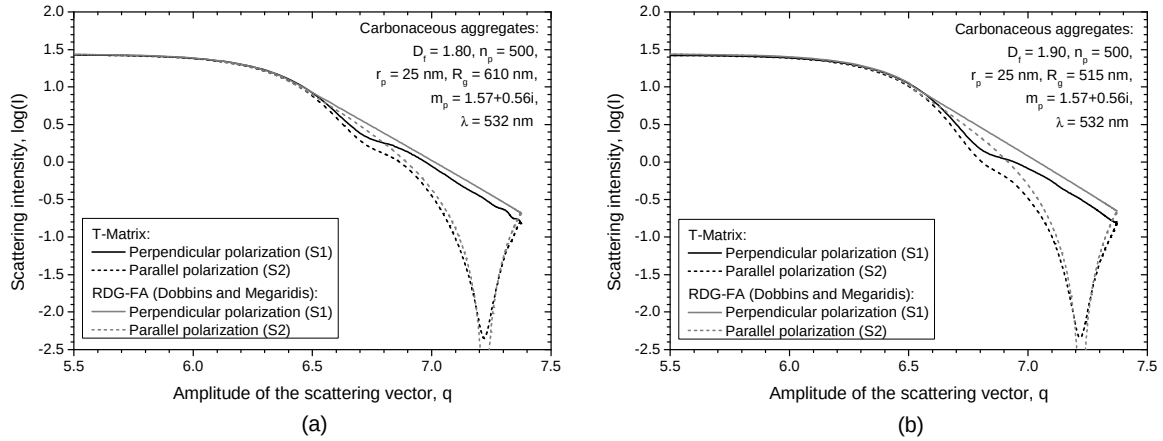

Figure 4.14. A comparison between RDG-FA and T-Matrix predictions for the scattering diagrams of soot aggregates with intermediate size ($n_p = 500$, $r_p = 25\ nm$).

Table 4.1 compares the results obtained with both light scattering model and the SSE algorithm. The results fit rather well. To our opinion, the differences between the expected and the estimated values must be attributed more to the SSE algorithm limitations than to the T-Matrix inaccuracy, see chapter 5.

Table 4.1. Summary of the fractal dimension estimated for the scattering diagrams of soot aggregates predicted with T-Matrix and RDG-FA theories, analyzed with the SEE algorithm.

Reference figure:	Figure 4.12		Figure 4.13		Figure 4.14	
Initial D_f	1.60±0.01	1.80±0.01	1.60±0.01	1.70±0.01	1.80±0.01	1.90±0.01
Estimated D_f	1.63±0.01	1.84±0.01	1.62±0.01	1.73±0.01	1.84±0.01	1.95±0.01

Table 4.2. Summary of the radiuses of gyration estimated for the scattering diagrams of soot aggregates predicted with T-Matrix and RDG-FA theories, analyzed with the SEE algorithm.

Reference figure:		Figure 4.12		Figure 4.13		Figure 4.14	
Fractal dimension		1.60	1.80	1.60	1.70	1.80	1.90
Initial R_g [nm]		322	249	909	736	610	515
T-Matrix	Estimated R_g [nm]	350	275	921	766	640	541
	R_g accuracy [nm]	19	17	51	42	33	25
RDG-FA	Estimated R_g [nm]	355	266	958	783	646	532
	R_g accuracy [nm]	21	18	55	45	30	29

Results presented in Table 4.2 appear to be much more interesting. The latter table compares the radius of gyration estimated with the Guinier analysis (see chapter 5) for the scattering diagrams predicted by the RDG-FA as well as T-Matrix theories. It can be seen that generally, both approximation provide similar accuracy: the results typically do not differ more than

10%. What is more, systematic overestimation that can be seen in Table 4.2, is results of the Guinier analysis properties rather than the RDG-FA or T-Matrix predictions, see chapter 5.

4.5. T-Matrix method

4.5.1. Introduction

The T-Matrix method (known also as Null-field Method or Extended Boundary Condition Method, EBCM) is one of the most powerful and commonly used methods to calculate light scattering by various nonspherical particles. Solution proposed by Waterman (Waterman 1965) in 1965 has been widely extended and improved. Several different computational codes using T-Matrix approach have been developed (e.g. (Barber and Hill 1990; Mishchenko et al. 1996; Auger et al. 2007; Nieminen et al. 2007)). They might be apply to the analysis of various particle systems (e.g. (Doicu et al. 2006; Martin 2006; Binek 2007)). In the present work we use the Fortran code developed by Mackowski and Mishchenko (Mackowski and Mishchenko 1996; Mishchenko et al. 1996; Mishchenko 2009). Different versions of this code are available on-line on the website of the NASA Goddard Institute for Space Studies (Mishchenko et al. 2012). We have slightly modified this code to allow, for instance, MPI parallelized calculations.

The T-Matrix is based on the direct solution of the Maxwell's equations. Therefore, it is an exact method to calculate scattering properties of rather complex-shaped particles or ensemble of spherical particles. It is very popular due to the fact that it provides high accuracy and relatively short computational time comparing to the other competitive solutions (e.g. discrete dipole approximation (Draine and Flatau 1994)) that can be used in order to solve such a complex scattering problems.

4.5.2. T-Matrix assumptions

The T-Matrix method is based on the principle that the electromagnetic field outside of a regular surface S containing a scattering object, is equivalent to that which would be produced by electric currents distributed on the surface S. Inside the surface S, the scatterer do not produce any electric or magnetic field (thus, the T-Matrix is also known as the null-field method). Therefore, we can express the total field (incident and scattered) outside of the surface S as surface integrals. The latter assumption is not valid on the surface S itself. It is valid only inside the inscribed sphere or outside of the circumscribed sphere of the surface S. The equivalent surface currents are then expressed as the sum of n-spherical harmonics with unknown coefficients. Within the inscribed sphere, the equation $E=0$ is transformed into a linear system of equations which connects the unknown coefficients of the scattered field with known coefficients of the incident one. This relation is given in a matrix notation as a transition matrix, known also as a Matrix **T**.

The T-Matrix formulation can be extended to the multiple scatterers (i.e. particles) problem. To do so, Matrix **T** must be associated to each particle of the system (Auger et al. 2007). Thus, it contains properties of the scattering particles and takes into account influence of the other particles. It leads to the N coupled linear equations, where N is equal to the number of particles to be analyzed.

4.5.3. T-Matrix formulation

If we consider an arbitrary nonspherical particle in the spherical coordinate system with the origin inside the particle, suspended in the homogenous, linear, isotropic and nonabsorbing medium, an incident plane electromagnetic wave can be expressed as (Mishchenko et al. 1996):

$$\mathbf{E^{inc}}(\mathbf{R}) = \mathbf{E^{inc}} \exp(ik\mathbf{n_{inc}}\mathbf{R}) = (E_\theta^{inc}\boldsymbol{\theta}_{\mathbf{inc}} + E_\varphi^{inc}\boldsymbol{\varphi}_{\mathbf{inc}}) \exp(ik\mathbf{n_{inc}}\mathbf{R}), \tag{4.63}$$

where $\mathbf{R}$ is the radius vector with the origin at the origin of the coordinate system, $\mathbf{n_{inc}}$ is the unit vector pointing the incident direction of the electromagnetic wave, $\boldsymbol{\varphi}_{\mathbf{inc}}$ and $\boldsymbol{\theta}_{\mathbf{inc}}$ are perpendicular unit vectors such as $\mathbf{n_{inc}} = \boldsymbol{\theta}_{\mathbf{inc}} \times \boldsymbol{\varphi}_{\mathbf{inc}}$ and $\exp(-i\omega t)$ is the time factor. In the far-field region ($kR \gg 1$), the scattered wave takes spherical shape and can be expressed as follows:

$$\mathbf{E^{sca}}(\mathbf{R}) = E_\theta^{sca}(R, \mathbf{n_{sca}})\boldsymbol{\theta}_{\mathbf{sca}} + E_\varphi^{sca}(R, \mathbf{n_{sca}})\boldsymbol{\varphi}_{\mathbf{sca}}, \qquad \mathbf{n_{sca}} = \mathbf{R}/R, \quad kR \gg 1, \tag{4.64}$$

where $\mathbf{n_{sca}} = \boldsymbol{\theta}_{\mathbf{sca}} \times \boldsymbol{\varphi}_{\mathbf{sca}}$ and $R = |\mathbf{R}|$. Moreover, the relation between the incident and the scattered wave can be expressed as:

$$\mathbf{R}\mathbf{E}^{sca}(\mathbf{R}) = 0, \tag{4.65}$$

$$\begin{bmatrix} E_\theta^{sca} \\ E_\varphi^{sca} \end{bmatrix} = \frac{\exp(ikR)}{R}\mathbf{S}(\mathbf{n}_{sca}, \mathbf{n}_{inc}) \begin{bmatrix} E_\theta^{inc} \\ E_\varphi^{inc} \end{bmatrix}, \tag{4.66}$$

where $\mathbf{S}$ is an (2×2) amplitude scattering matrix which transforms linearly the incident electric vector components E_θ^{inc}, E_φ^{inc} to the scattered ones. The incident and the scattered fields are expressed using the vector spherical functions $\mathbf{M_{mn}}$ and $\mathbf{N_{mn}}$ as follows (Mishchenko et al. 1996):

$$\mathbf{E^{inc}}(\mathbf{R}) = \sum_{n=1}^{\infty}\sum_{m=-n}^{n}\left[a_{mn}\mathbf{RgM_{mn}}(k\mathbf{R}) + b_{mn}\mathbf{RgN_{mn}}(k\mathbf{R})\right], \tag{4.67}$$

$$\mathbf{E^{sca}}(\mathbf{R}) = \sum_{n=1}^{\infty}\sum_{m=-n}^{n}\left[p_{mn}\mathbf{M_{mn}}(k\mathbf{R}) + q_{mn}\mathbf{N_{mn}}(k\mathbf{R})\right], \qquad R > r_0, \tag{4.68}$$

where p_{mn}, q_{mn} are the scattered field coefficients, a_{mn}, b_{mn} are the incident field coefficients and the vector spherical functions are:

$$\mathbf{M_{mn}}(k\mathbf{R}) = (-1)^m d_n h_n^{(1)}(kR)\mathbf{C_{mn}}(\theta)\exp(im\varphi), \tag{4.69}$$

$$\mathbf{N_{mn}}(k\mathbf{R}) = (-1)^m d_n \left(\frac{n(n+1)}{kR}h_n^{(1)}(kR)\mathbf{P_{mn}}(\theta) + \frac{1}{kR}\left[kRh_n^{(1)}(kR)\right]'\mathbf{B_{mn}}(\theta)\right)\exp(im\varphi). \tag{4.70}$$

where:

$$\begin{aligned} \mathbf{B_{mn}}(\theta) &= \boldsymbol{\theta}\frac{d}{d\theta}d_{0m}^{n}(\vartheta) + \boldsymbol{\varphi}\frac{im}{\sin\theta}d_{0m}^{n}(\theta), \qquad \text{(a)} \\ \mathbf{C_{mn}}(\theta) &= \boldsymbol{\theta}\frac{im}{\sin\theta}d_{0m}^{n}(\vartheta) - \boldsymbol{\varphi}\frac{d}{d\theta}d_{0m}^{n}(\theta), \qquad \text{(b)} \end{aligned} \tag{4.71}$$

and

$$\mathbf{P_{mn}}(\theta) = \mathbf{R}d_{0m}^{n}(\theta)/R, \tag{4.72}$$

$$d_n = \left[\frac{2n+1}{4\pi n(n+1)}\right]^{1/2}, \tag{4.73}$$

where r_0 is the radius of the circumscribed sphere containing ensemble of scattering particles (e.g. an aggregate) and $d_{0m}^{n}(\theta)$ are the Wigner d-functions (Mishchenko et al. 1996). Functions $\mathbf{RgM_{mn}}$ and $\mathbf{RgN_{mn}}$ can be obtained from Eqs. (4.69) and (4.70) by replacing spherical Henkel functions $h_n^{(1)}$ by spherical Bessel functions j_n.

The expansion coefficients for the plane incident wave are expressed as:

$$\begin{aligned} a_{mn} &= 4\pi(-1)^m i^n d_n \mathbf{C}_{\mathbf{mn}}^{*}(\theta_{inc})\mathbf{E^{inc}}\exp(-im\varphi_{inc}), \qquad \text{(a)} \\ b_{mn} &= 4\pi(-1)^m i^{n-1} d_n \mathbf{B}_{\mathbf{mn}}^{*}(\theta_{inc})\mathbf{E^{inc}}\exp(-im\varphi_{inc}), \qquad \text{(b)} \end{aligned} \tag{4.74}$$

where asterisk indicates complex conjugation. Finally, the relation between the scattered and the incident field coefficients is described by the transition matrix (Matrix **T**) as follows:

$$p_{mn} = \sum_{n'=1}^{\infty}\sum_{m'=-n'}^{n'}\left[T_{mnm'n'}^{11}a_{m'n'} + T_{mnm'n'}^{12}b_{m'n'}\right], \tag{4.75}$$

$$q_{mn} = \sum_{n'=1}^{\infty}\sum_{m'=-n'}^{n'}\left[T_{mnm'n'}^{21}a_{m'n'} + T_{mnm'n'}^{22}b_{m'n'}\right]. \tag{4.76}$$

In a matrix notation Eqs. (4.75) and (4.76) can be expressed as:

$$\begin{bmatrix}\mathbf{p}\\ \mathbf{q}\end{bmatrix} = \mathbf{T}\begin{bmatrix}\mathbf{a}\\ \mathbf{b}\end{bmatrix} = \begin{bmatrix}\mathbf{T^{11}} & \mathbf{T^{12}}\\ \mathbf{T^{21}} & \mathbf{T^{22}}\end{bmatrix}\begin{bmatrix}\mathbf{a}\\ \mathbf{b}\end{bmatrix}. \tag{4.77}$$

Eq. (4.77) shows one of the biggest advantages of the T-Matrix solution: the elements of the Matrix **T** depend only on the morphological parameters of the scattering particles (i.e. shape, size parameters, refractive index) and their orientation regarding the coordinate system (Onofri 2007). As a result, for a given aggregate, Matrix **T** has to be calculated only once and then it can be used to evaluate the particle scattering properties for any incident and scattering directions. Total extinction, absorption and scattering cross sections for an aggregate can be calculated with the following equations:

$$\begin{aligned} C_{a,ext} &= -\frac{2\pi}{k^2}\mathrm{Re}\left\{\sum_{n=1}^{\infty}\sum_{m=-n}^{n}\left[T_{mnmn}^{11} + T_{mnmn}^{22}\right]\right\}, \qquad (a) \\ C_{a,sca} &= \frac{2\pi}{k^2}\sum_{n=1}^{\infty}\sum_{n'=1}^{\infty}\sum_{m=-n}^{n}\sum_{m'=-n'}^{n'}\sum_{i=1}^{2}\sum_{j=1}^{2}\left|T_{mnm'n'}^{ij}\right|^2, \qquad (b) \\ C_{a,abs} &= C_{a,ext} - C_{a,sca}. \qquad (c) \end{aligned} \tag{4.78}$$

4.5.4. The coordinate system and the displayed quantities

During calculations, T-Matrix code uses spherical coordinate system. However, as an input parameters coordinates of monomers within an aggregate must be given in the classical laboratory Cartesian system. Thus, the coordinate system and the displayed quantities are as follows (see also Figure 4.15):

- The incident, plane wave with linear polarization, is propagating along the Z axis, (see Figure 4.15). The scattered intensity is calculated in the "scattering plane" XZ ($Y=0$) for a given scattering angle θ.
- The polarization is parallel when $E_{\perp}=0$ and $E_{\parallel}$ is parallel to axis X (i.e. intensity usually written as $I_{\parallel}$ or S_2).
- The polarization is perpendicular when $E_{\parallel}=0$ and $E_{\perp}=Y$ (usually written as $I_{\perp}$ or S_1).
- The degree of linear polarization of the scattered light is also given with $P=-S_{12}/S_{11}=(S_1-S_2)/(S_1+S_2)$, where S_{11} and S_{12} are two of the 16 real coefficients of the T-Matrix solution.

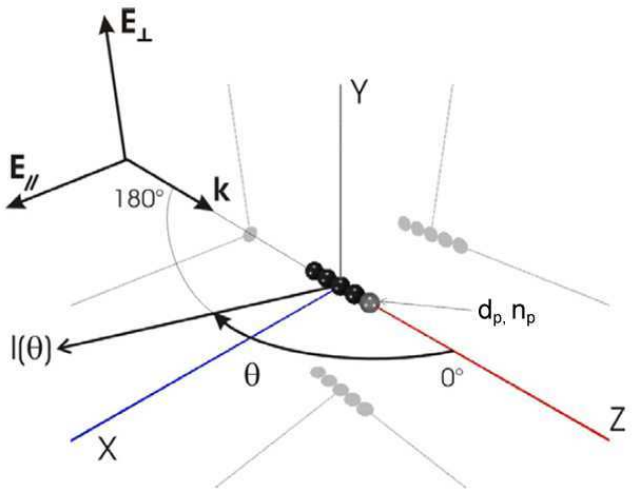

Figure 4.15. Coordinate system for the light scattering calculations and particles orientation in the T-Matrix calculations (Onofri 2007).

4.5.5. Example numerical results

4.5.5.1. Optical characteristics of various fractal aggregates

With linear optics, one of the most fundamental approach to characterize the size distribution of large particles is to analyze their scattering diagrams, i.e. the intensity I versus the scattering angle θ for large particles (e.g. in the Fraunhofer, the rainbow or critical angle regions) or versus the scattering vector q for nano- and micro aggregates.

Figure 4.16 compares the scattering diagrams of single aggregate of silicon dioxide monomers in water with various orientations. The incident plane wave is (a) perpendicular and (b) parallel polarized with wavelength $\lambda=532\ nm$ The parameters of the aggregate are:

$D_f = 1.80$, $n_p = 101$, $r_p = 55\,nm$, $R_g = 550\,nm$. The scattering diagram averaged over 500 various aggregates, with exactly the same parameters, is also shown. The influence of the aggregate orientation (with respect to the incident plane wave and the scattering plane) is really significant. At the same time, the main influence of the averaging procedure seems to damp all resonances.

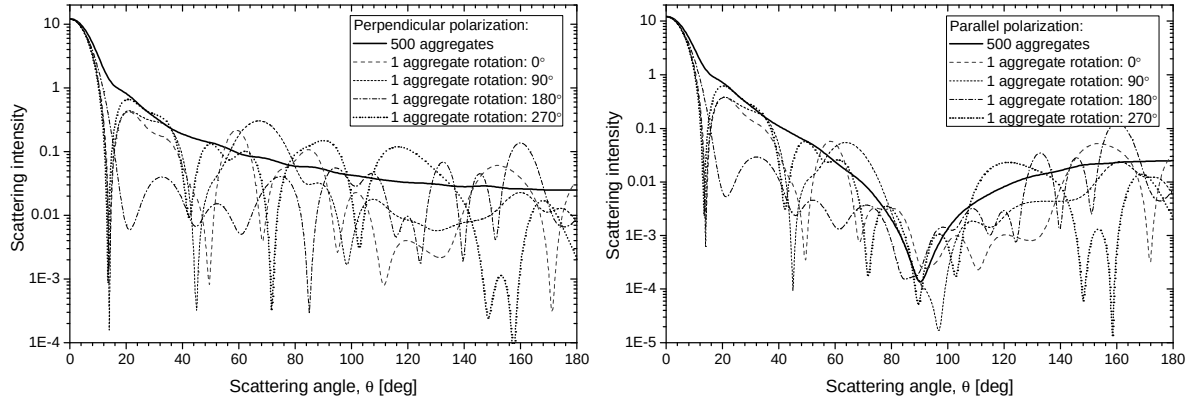

Figure 4.16. Scattering diagrams for a single aggregate of silicon dioxide monomers rotated around the x axis by $0°$, $90°$, $180°$ and $270°$ and results average over 500 aggregates with the same parameters: (a) perpendicular and (b) parallel polarization of light.

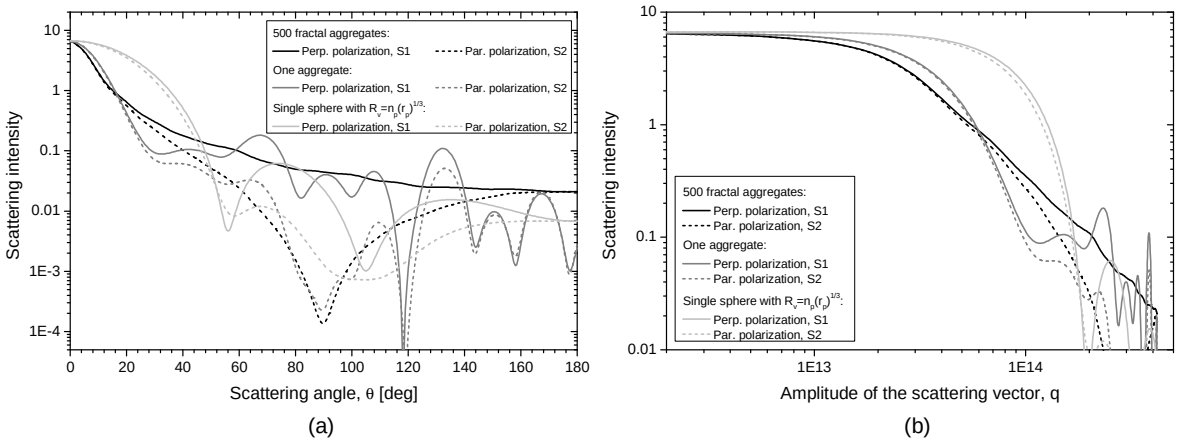

Figure 4.17. Scattering intensity averaged over 500 fractal aggregates, for a single aggregate and single sphere with radius $R_v = r_p \sqrt[3]{n_p} = 218.8\,nm$ versus (a) scattering angle and (b) amplitude of the scattering wave vector q; perpendicular polarization.

Figure 4.17 compares the scattering diagrams of a single silicon dioxide aggregate in water with the one of a single sphere with radius equal to the radius in volume of the aggregate, with $D_f = 1.60$, $n_p = 63$, $r_p = 55\,nm$, $R_g = 550\,nm$. Only the forward scattering exhibits some similarities. In some extent this may be understood with the RDG-FA approximation, as in that case we have $I(\theta = 0) \propto n_p^2$. For the other scattering regions, the scattering diagrams are totally different.

4.5.5.2. Averaging procedure for the scattering diagrams

From the previous results we can really conclude that to model the scattering diagrams of aqueous colloidal suspension or aerosols of complex-shaped aggregates, it is necessary to cancel out orientation effects using a numerical averaging procedure. This is particularly important because in practice we are usually probing thousands of millions of nanoparticles and aggregates, not a single aggregate with a particular orientation.

Therefore, as a standard procedure, all the scattering diagrams presented in this work were averaged over 500 different aggregates with exactly the same fractal properties. This sample was chosen as a compromise between calculation accuracy and computational time.

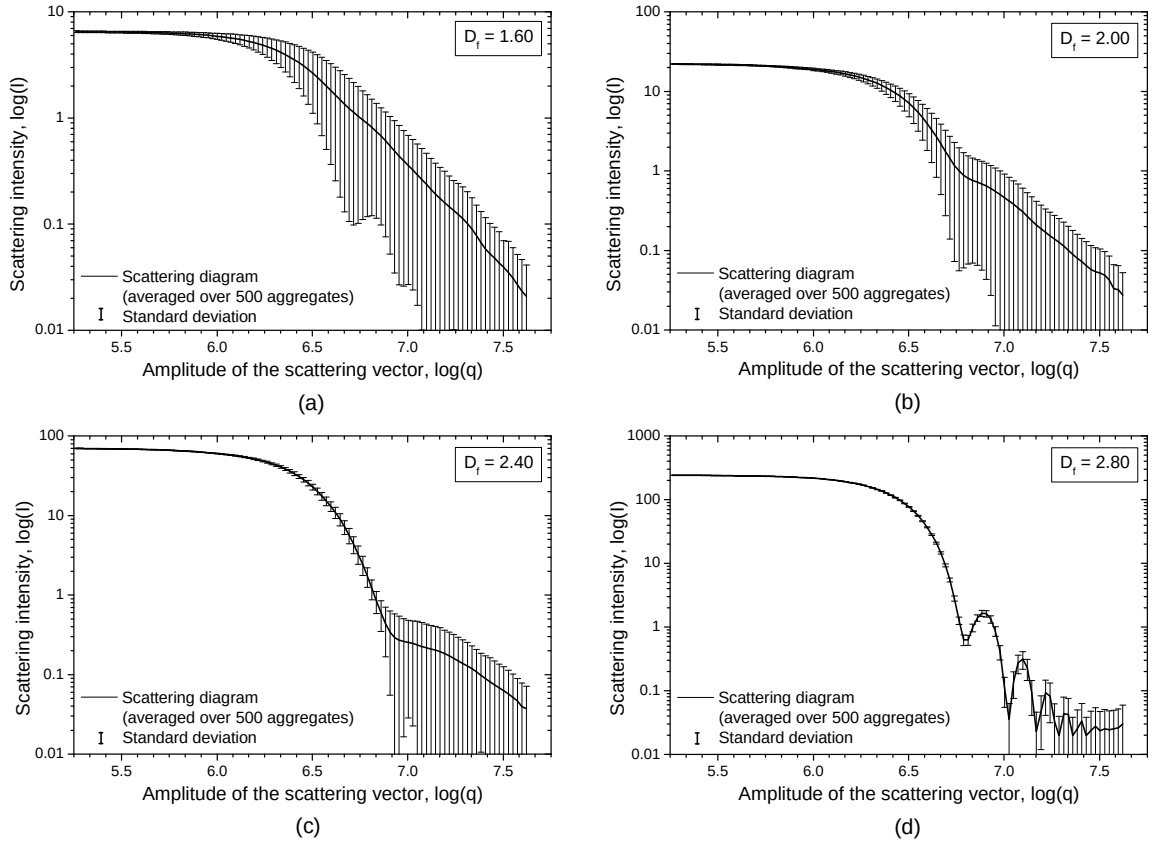

Figure 4.18. Scattering diagrams of the aqueous suspension of SiO_2 aggregates with $r_p = 55\,nm$, $R_g = 550\,nm$, (a) $D_f = 1.60$, (b) $D_f = 2.00$, (c) $D_f = 2.40$ and (d) $D_f = 2.80$; perpendicular polarization.

As an example, Figure 4.18 shows the scattering diagrams of the aqueous suspension of silicon dioxide (SiO_2) monomers with $r_p = 55\,nm$, $R_g = 550\,nm$ and $D_f = 1.60 - 2.80$. We present scattering diagrams averaged over 500 various aggregates with the same parameters and the standard deviations (STD) related to the averaging procedure. We found that for aggregates with low and medium fractal dimensions the differences are non-negligible. The standard deviation decreases as the fractal dimension increases. For $D_f = 2.80$ it is almost insignificant for the small scattering angles (small values of q) and it becomes noticeable only for the larger ones.

Similar conclusions can be drawn from Figure 4.19. The latter presents the relative differences between the scattering diagrams of the silicon dioxide aggregates ($r_p = 55\,nm$, $R_g = 550\,nm$, $D_f = 1.6$, $n_p = 64$) depending on the number of aggregates used for the averaging procedure (i.e. 500, $100-400$; 500 being considered as a reference case). The relative difference between the results averaged over 500 and 400 aggregates is smaller than 1% for the entire scattering diagram. Moreover, the improvements related to the increasing number of aggregates by 100 are relatively smaller at each step. It clearly shows that averaging over 500 aggregates provides enough high accuracy. This value of 500 was found to be a good compromise for all cases (aerosol, plasmas, etc.) threaded in this Ph.D. work.

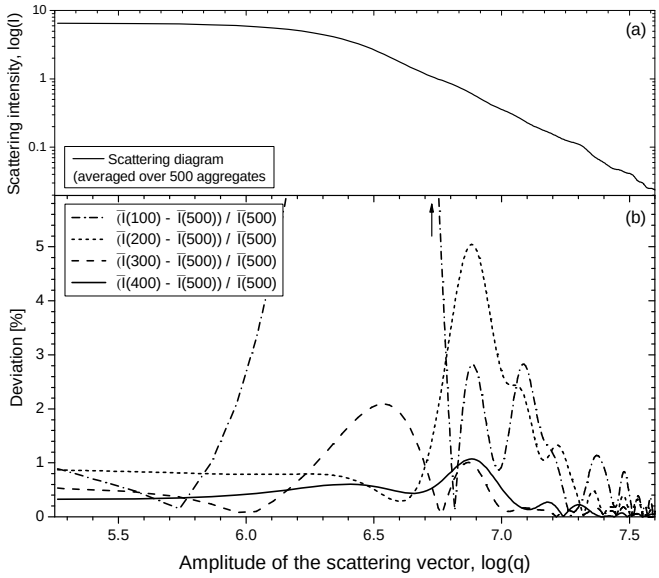

Figure 4.19. (a) Scattering diagrams of silicon dioxide aggregates ($r_p = 55\,nm$, $R_g = 550\,nm$, $D_f = 1.6$, $n_p = 64$) averaged over 500 different aggregates with the same parameters and (b) deviation between the scattering diagrams averaged over a smaller number of monomers.

4.5.5.3. Averaging procedure for the extinction profiles

It is also necessary to average extinction spectra to cancel out orientation effects as well as any sensitivity to aggregates with a non fully representative shape. However, the total cross sections (and thus extinction and scattering coefficients) are much less sensitive to the orientation of aggregates than scattering diagrams (see previous section). We found that an averaging over 50 aggregates is a good compromise. As an example, Figure 4.20 shows the extinction coefficient (i.e. extinction cross section normalized by the surface of the sphere with volume equivalent to the one of the aggregate, see section 6.4.1 for more details) of aggregates of amorphous silicon monomers $r_p = 3.5\,nm$ with $R_g = 35\,nm$ and fractal dimension equal to (a) $D_f = 1.50$ or (b) $D_f = 2.80$. In both figures the maximum, minimum and average extinction for the group of 50 various aggregates are shown. The standard

deviation divided by the average value of the extinction coefficient $\left(\mathrm{STD}(Q_{a,ext})\times 100 / \bar{Q}_{a,ext}\right)$ is also plotted.

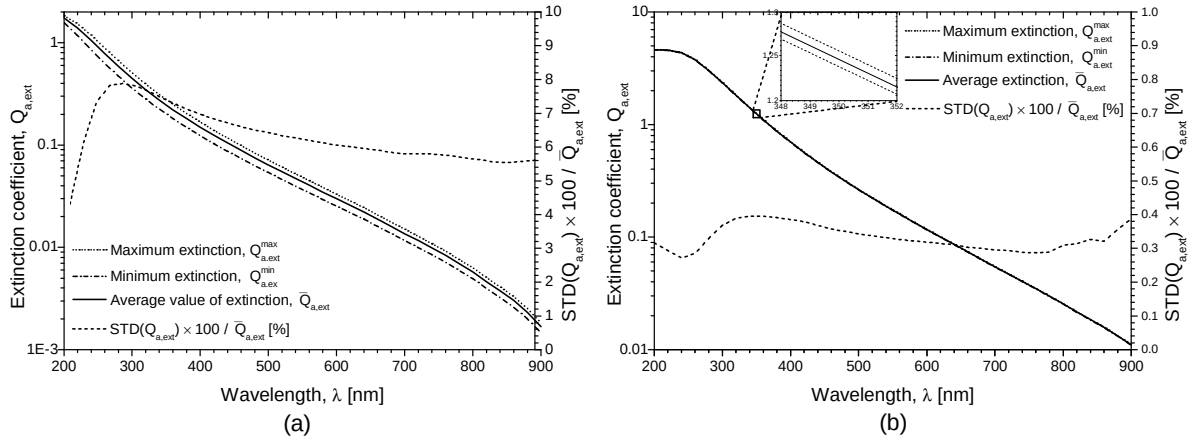

Figure 4.20. Comparison between maximum and minimum extinction coefficients for a group of 50 various aggregates of amorphous silicon monomers with the same parameters: $r_p = 3.5\,nm$, $R_g = 35\,nm$, (a) $D_f = 1.5$, $n_p = 51$ and (b) $D_f = 2.8$, $n_p = 1000$.

It can be seen that the standard deviation is strongly dependent on the fractal dimension. For aggregates with $D_f = 1.50$ its mean value is equal to 6.33% and typically do not exceed 8% for the wavelength ranging from 200 to $900\,nm$. For aggregates with $D_f = 2.80$ the standard deviation is more than one order of magnitude smaller with mean value 0.33%. This behavior of the extinction coefficient is a direct consequence of the fact that dilute aggregates with the same parameters may have much more varied shapes than the compact ones. They can be also situated in numerous different positions regarding the incident wave. It is also worth to notice that for very dense aggregates (as presented in Figure 4.20 (b)) even results of the calculations for one aggregate might be meaningful.

Figure 4.21 presents differences between extinction coefficient of the silicon dioxide aggregates ($r_p = 3.5\,nm$, $R_g = 35\,nm$, $D_f = 1.5$, $n_p = 51$) averaged over 50 and $10-40$ aggregates respectively. It can be seen that relative difference between results averaged over 50 and 40 aggregates is for the entire wavelength range smaller than 0.5%, Moreover, the improvements related to the increasing number of cases by 10 are relatively smaller at each step. It clearly means that averaging over 50 aggregates provides enough high accuracy.

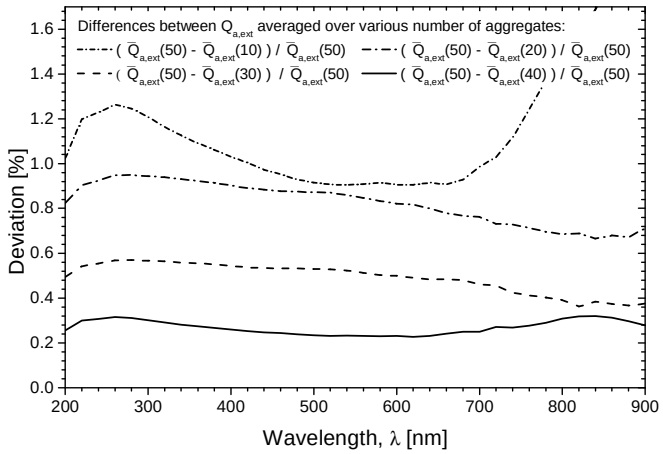

Figure 4.21. Deviation between extinction coefficient of the silicon dioxide aggregates ($r_p = 3.5\ nm$, $R_g = 35\ nm$, $D_f = 1.5$, $n_p = 51$) averaged over various number of aggregates.

4.5.5.4. Extinction cross section of single monomers within fractal aggregates

The effective extinctions of each monomers within an aggregate are also quite different depending on their position in the agregate. As an example Figure 4.22 shows grey-level coded images of the extinction coefficients of the monomers within two aggregates of soot with $n_p = 200$, $r_p = 17.1\ nm$ (a) $D_f = 1.8$, $R_g = 251\ nm$ and (b) $D_f = 2.2$, $R_g = 154\ nm$ for the incident wavelength $\lambda = 300\ nm$ (note that the incident plane wave propagates along the z-axis).

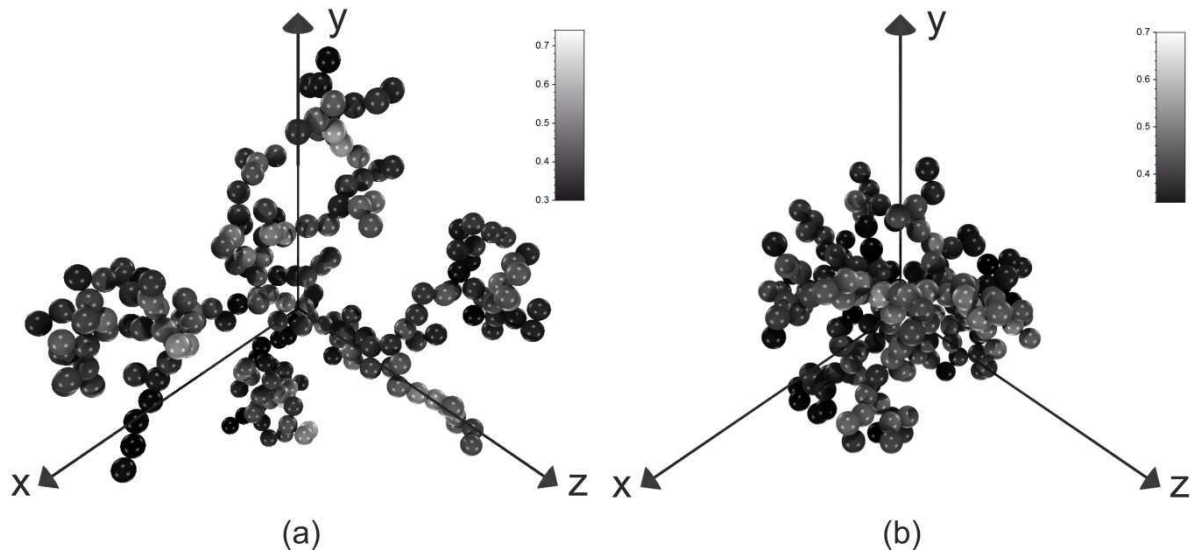

Figure 4.22. Gray-scale images of extinction coefficients of single monomers within aggregates of soot with $n_p = 200$, $r_p = 17.1\ nm$ (a) $D_f = 1.8$, $R_g = 251\ nm$ and (b) $D_f = 2.2$, $R_g = 154\ nm$. Incident wave propagates parallel to the z-axis.

4.5.5.5. Extinction cross section of Buckyballs-like aggregates

Figure 4.23 – Figure 4.25 show the extinction spectra of buckyballs-like aggregates with parameters similar to the ones observed experimentally (see section 6.5): $K30R50$, $K30R25$ and $K30R12$ with radiuses of single monomers $r_p = 40.5\ nm$, $r_p = 33.6\ nm$ and $r_p = 15.7\ nm$ respectively. Each spectra was obtained by averaging the T-Matrix results for the randomly oriented aggregates and 91 wavelengths equally distributed between 200 and $1100\ nm$. The averaging procedure was performed over 100 aggregates.

Figure 4.23 compares extinction coefficients calculated for (i) buckyballs aggregates with an 3D hexagonal compact internal structure (see section 2.5) and (ii) a single spherical particles with a radius equal to the external radius of the buckyballs and the refractive index calculated with an effective medium approximation (i.e. Maxwell-Garnet model (Bohren and Huffman 1998)):

$$\varepsilon_{av} = \varepsilon_m \left[1 + \frac{3f\left(\frac{\varepsilon - \varepsilon_m}{\varepsilon + 2\varepsilon_m}\right)}{1 - f\left(\frac{\varepsilon - \varepsilon_m}{\varepsilon + 2\varepsilon_m}\right)} \right], \tag{4.79}$$

where f is the volume fraction of monomers within the aggregates, ε and ε_m are the relative permittivities of the inclusions (monomers) and the bulk material (i.e. air) respectively. For buckyballs presented in Figure 4.23 – Figure 4.25, we have used a volume fraction of $f = 0.51 - 0.54$ (these values were estimated with the geodesic dome model (Onofri et al. 2012a)).

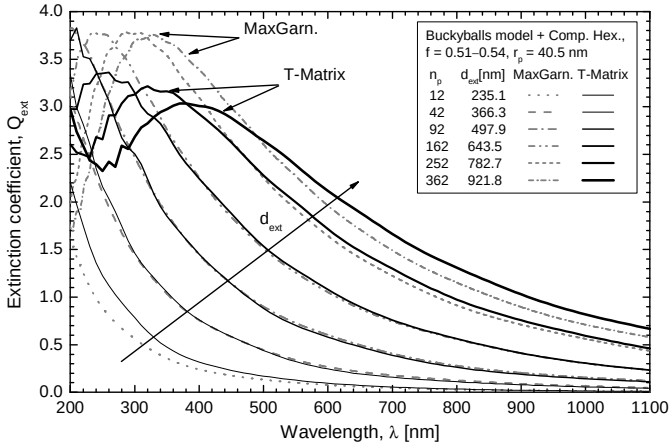

Figure 4.23. Comparison of extinction spectra of buckyballs aggregates (of silica nanobeads) with a 3D hexagonal compact internal structure: T-matrix calculations versus Lorenz-Mie theory with an effective medium approximation, $r_p = 40.5\ nm$.

Surprisingly, we found that results obtained with the Lorenz-Mie theory and the Maxwell-Garnet model fit rather well with the T-Matrix calculations for buckyballs of intermediate size of the aggregates (i.e. with $n_p = 42,\ 92,\ 162$) and for the VIS-NIR spectral range, see Figure 4.23. For the larger and smaller buckyballs significant differences appear when incident

wavelengths shorter than $500\,nm$ is used. Similar conclusions may be drawn from Figure 4.24. Finally, from Figure 4.25 we conclude that for such small aggregates differences between the T-Matrix with a full buckyball model and the Lorenz-Mie theory with the effective refractive index are really small. In the latter case, the mean difference is only of $2.3 \pm 1.2\%$ for buckyballs with $n_p = 362$ (total number of $n_{p,HC} = 749$) monomers to $6.6 \pm 2.5\%$ for $n_p = 162$ (total number of $n_{p,HC} = 249$). Maximum difference equal to 15% was observed for buckyballs with $n_p = 12$ and incident wavelength $\lambda = 200\,nm$. Results presented in the latter figures clearly shows that it is not always necessary to perform very time-consuming T-Matrix calculations.

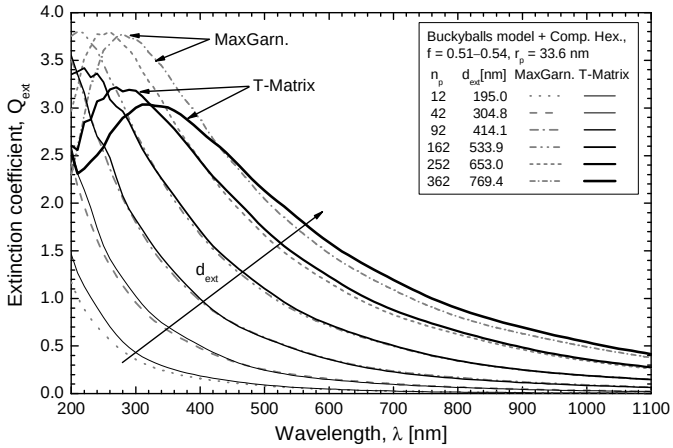

Figure 4.24. Like Figure 4.23 but for $r_p = 33.6\,nm$.

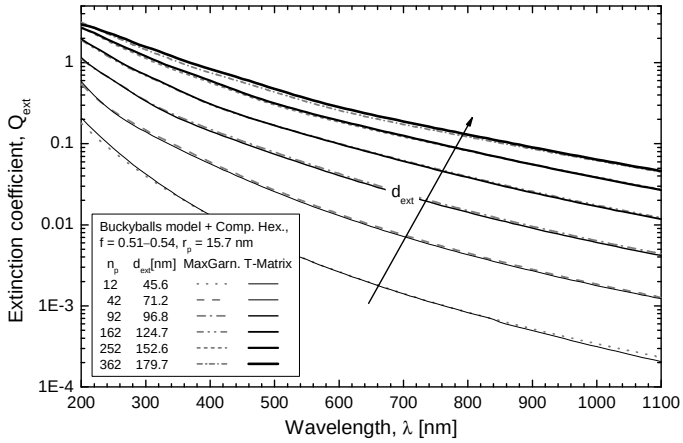

Figure 4.25. Like Figure 4.23 but for $r_p = 15.7\,nm$.

4.5.5.6. Extinction cross section of single monomers within Buckyballs aggregates

Like for fractal aggregates, we can calculate the effective cross section of the each monomers within a buckyballs-like aggregate. Figure 4.26 and Figure 4.27 show the extinction coefficients (i.e. normalized extinction cross section) of each single monomers within a buckyball of $n_p = 252$ monomers filled with a 3D hexagonal compact internal structure

(total number of monomers $n_{p,HC} = 509$), and $n_p = 362$ monomers (total number of monomers $n_{p,HC} = 749$) respectively. The mean radius of the monomers is equal to $r_p = 40.5\ nm$ and the incident wavelength is equal to (a) $\lambda = 300\ nm$, (b) $\lambda = 400\ nm$ and (c) $\lambda = 500\ nm$.

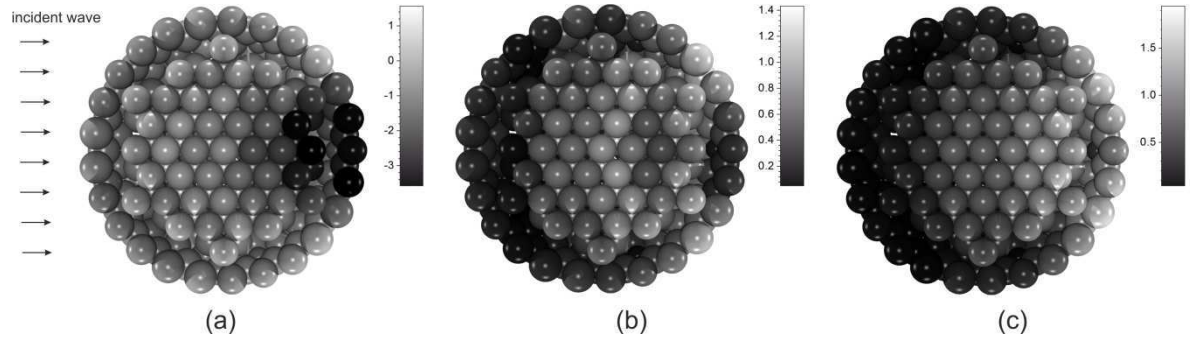

Figure 4.26. Extinction coefficients of each single monomers within the equatorial plan of a buckyball of $n_p = 252$ monomers with a 3D hexagonal internal structure (total number of monomers $n_{p,HC} = 509$) with $r_p = 40.5\ nm$ – (a) $\lambda = 300\ nm$, (b) $\lambda = 400\ nm$, (c) $\lambda = 500\ nm$; external diameter $d_{ext} = 783\ nm$.

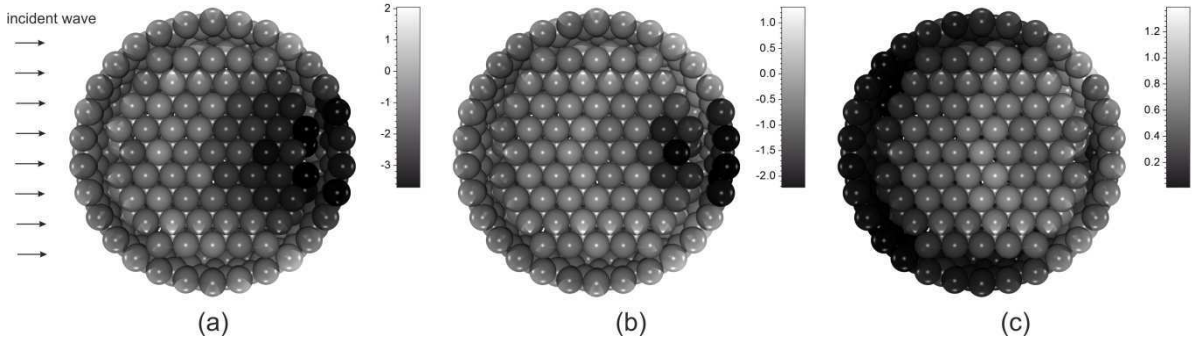

Figure 4.27. Extinction coefficients like in Figure 4.26 for $n_p = 362$ (total number of monomers $n_{p,HC} = 749$); external diameter $d_{ext} = 922\ nm$.

Among the interesting behaviors shown here, we can notice that the monomers exhibit some negative values for the extinction coefficients. They appear when incident wavelength is relatively short comparing to the size of the monomers (see Figure 4.26 (a) and Figure 4.27 (a)-(b)). It is probably the result of some internal multiple scattering and "focusing" effects. It can be noticed that the layout of the extinction cross sections presents some analogy with the one observed for a homogeneous sphere (Barber and Hill 1990).

4.5.5.7. Computational time with the T-Matrix code (Mackowski and Mishchenko 1996)

Another important issue related to the T-Matrix code is the computational time. We have parallelized the Fortran code developed by Mackowski and Mishchenko (Mackowski and Mishchenko 1996; Mishchenko et al. 2012) to get a better compromise between the accuracy and the computational time. This parallel version runs on the computer clusters available in the IUSTI Laboratory (a few dozens of cores were used in general). However, the simulations are still time-consuming and they require large storage capacities. As an example of the typical computational time associated to the T-Matrix, Figure 4.28 shows the time evolution

of the scattering simulations for the aggregates with $D_f = 1.80$ and different size parameters ($x_p = 0.1,\ 0.2,\ 0.5,\ 1.0,\ 2.0$) versus the number of monomers within aggregates ($n_p = 20,\ 40,\ ...,\ 1000$). For a comparison purposes, the calculations presented here were performed on the single, typical up-to date computer (dual core CPU $2 \times 2.8\,GHz$ and $4\,GB$ of RAM memory).

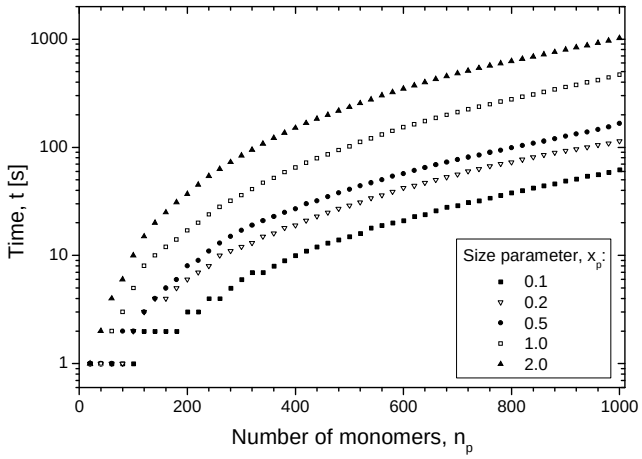

Figure 4.28. Computational time of the T-Matrix code for various size parameters of the aggregate with $D_f = 1.80$ versus number of monomers.

From Figure 4.28 it can be deduced that the computational time of the T-Matrix code strongly depends on the number of monomers within aggregate. However, a non-negligible influence has also the size parameter of the monomers (e.g. the ratio between the computational time for the aggregates with the same properties but $x_p = 2.0$ and $x_p = 0.1$ is higher than 16). It should be noticed that, with the parallelized version, the total computational time is roughly divided by the number of cores being used.

4.6. Conclusion

Despite that numerous light scattering theories and methods to characterize particle systems are available in the literature, only few of them are appropriate when considering the in-situ and time-resolved analysis of fractal aggregates of nanoparticles. In this chapter we briefly introduced only those of them that have been used in the current work.

In fact, only some of the theories (e.g. the LMT theory or the T-Matrix method) provide exact solution of the scattering phenomena, while the others give approximate results with some degree of accuracy (e.g. the RGD or RDG-FA theories). The biggest competition between exact solutions and approximate methods usually relay on the computational time and efficiency. Therefore, each time we have to choose appropriate model regarding size parameters, number of particles and scattering conditions (i.e. wavelength and scattering angles accessible during the analysis) of our problem. It is also necessary to take into account computational time.

Chapter 5

ANALYSIS OF THE SCATTERING DIAGRAMS

5.1. Introduction

For the characterization of fractal-like particle aggregates, the most powerful approach is based on the recording and afterwards the analysis of their visible (X-ray and even neutrons) scattering diagrams with respect to the scattering vector q (see Eq. (4.35)) (e.g. (Sorensen 2001; Bushell et al. 2002). The quantity $I(q)$ is sometimes referred as the "optical structure factor (OSF)" (Sorensen et al. 1992b; Sorensen 2001).

In this chapter we discuss methods and algorithms to estimate the main parameters of fractal-like particle aggregates from their OSF and some related issues. The current chapter is organized as follows. Section 5.2 introduces two main algorithms to analyze OSF. The first one, referenced as the Second Slope Estimation (SSE) method is based on a direct and simple method, but its applicability is limited to aggregates with rather large size parameter and intermediate fractal dimension. The second algorithm, called the First Slope Estimation (FSE) method, requires building calibration curves based on accurate particle agglomeration and particle light scattering models. It allows analyzing the optical structure factor of much smaller aggregates, regardless their fractal dimension and the size of the single particles. Therefore, this algorithm, as well as the introduction of a criteria curve to detect the different scattering regimes, are thought to be powerful tools to perform reliable and reproducible analysis. Section 5.3 presents influence of free monomers (non aggregated) around the aggregates of interest to the results estimated with our algorithms.

Finally, Section 5.4 shows a comparison between scattering diagrams of DLA and DLCA aggregates. It presents numerical results obtained on the ground that both aggregation

algorithms differ from the physical point of view (see section 2.2.2) and therefore it may be questionable if the optical properties of the corresponding aggregates are similar or not. However, we show that scattering characteristics of DLA and DLCA aggregates do not differ significantly as soon as they exhibit a power-law regime.

5.2. Estimation of fractal parameters from scattering diagrams

5.2.1. Introduction

OSF analysis is a powerful approach to estimate parameters of various particles. However, in the literature the method used to process the OSF is never detailed and evaluated, whatever the processing scheme (as it will be shown later on) strongly influence the quality and reliability of the analysis. Regarding the previous remarks, the aim of the present work was to develop reliable algorithms to estimate in a comprehensive and reproducible ways the fractal parameters from OSF (Mroczka et al. 2012).

5.2.2. Light scattering properties

Figure 5.1 (a) shows the numerical simulation of the evolution of the OSF of a water suspension of silicon dioxide aggregates (results averaged over 500 different aggregates with parameters: $n_p = 100$, $D_f = 1.80$, $r_p = 55\,nm$, $R_g = 550\,nm$, $\tilde{m}_p = 1.47 + 0i$). Three scattering regimes (or zones) may be identified in this OSF: namely, the Guinier, the fractal (or power-law) and the Porod zones. Behavior of the OSF in each zone is totally different and related to different aggregate properties. The OSF in the Guinier zone is essentially dependent on the overall size of aggregates (i.e. the length of this zone, with respect to the scattering vector, gives information about R_g). In the fractal zone, the power-law decay of the OSF (and the associated slope) depends mostly on the aggregate's morphology and thus, D_f. The behavior of the OSF in the Porod zone is known to be mainly sensitive to monomers size (Sorensen 2001) but this zone is usually only accessible with X-rays.

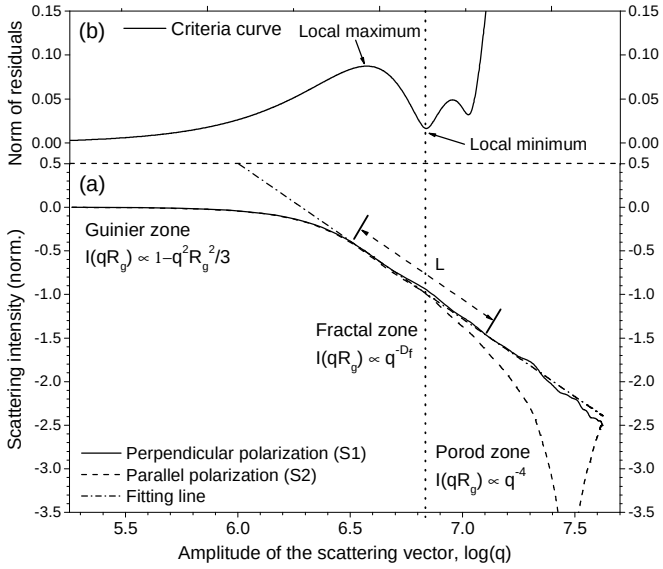

Figure 5.1. (a) Evolution of the optical structure factor (OSF) of silicon dioxide aggregates ($n_p = 100$, $D_f = 1.80$, $r_p = 55\,nm$, $R_g = 550\,nm$) and (b) criteria curve obtained with the FSE algorithm (Mroczka et al. 2012).

5.2.3. Radius of gyration estimation

We basically use the Guinier equation (Sorensen 2001) to estimate the radius of gyration from the normalized OSF:

$$\frac{I(q=0)}{I(q)} \simeq 1 + \frac{R_g^{\,2} q^2}{3}, \quad \text{for} \quad qR_g < 1. \tag{5.1}$$

In the previous equation the power-law term indicates that from the normalized OSF plotted versus q^2 we can estimate directly the radius of gyration. To do so, the algorithm works in a two-step process. Firstly, the OSF is low-pass filtered and normalized. Secondly, a linear least square fitting method is used to estimate the slope coefficient in the Guinier zone (symbolized here by the parameter *a* and the related accuracy Δa). To correctly estimate the radius of gyration it is necessary to use only data in the range $I(q=0)/I(q) < 4/3$. Finally, the radius of gyration is evaluated as $R_g = \sqrt{3a}$, with:

$$\Delta R_g = \frac{\partial R_g}{\partial a}\Delta a = \frac{3}{2\sqrt{3a}}\Delta a. \tag{5.2}$$

5.2.4. Algorithms for estimating the fractal dimension

5.2.4.1. Second Slope Estimation (SSE) Algorithm

In the fractal zone, the power-law decay of the OSF provides both quantitative and qualitative information about the fractal dimension of the aggregates. To get directly the value of D_f, only data values in the range $qR_g > 5$ must be used (Sorensen 2001). In fact, below this limit the power-law regime is not clearly observed. Like previously done for the radius of gyration,

the fractal dimension can be obtained directly from the slope coefficient estimated with a linear least square fitting procedure. However, this procedure and the related algorithm are only valid for rather larger aggregates, i.e. $R_g > (5\lambda)/(4\pi)$.

On the other hand to get a correct estimation of D_f a minimum number of data points are necessary. They must also cover a minimum scattering angles range. Numerical simulations, not reported here, have shown that the criterion introduced by Sorensen must be reinforced at least by a factor of two, $R_g > (5\lambda)/(2\pi)$ and that the predictions obtained are only satisfactory for fractal-like aggregates whose dimension are restricted to the range $D_f = 1.6 - 2.0$.

5.2.4.2. First Slope Estimation (FSE) Algorithm

The "First Slope Estimation (FSE)" algorithm was developed to process OSF with a scattering vector that do not necessarily satisfies the $qR_g > 5$ condition (Mroczka et al. 2012). The biggest advantage of this second algorithm, which uses calibration curves, is its applicability to all kind of aggregates, regardless fractal dimension, wavelength or radius of gyration. This algorithm works in a five-step process.

- *(A) Signal (optical structure factor) interpolation.*

To compensate the huge range of variation of the scattering vector and its non-linearity with respect to the scattering angle (e.g. which both induce a non constant sampling rate of the optical structure factor) the OSF is resampled with a linear interpolation scheme. The number of interpolating points is chosen arbitrary, as a compromise between accuracy and algorithm execution time. Basically, it is set to 1000 points per one order of magnitude of q. So that, depending on the incident wavelength, the OSF is sampled in $2000-3000$ data points.

- *(B) Linear least square fitting.*

One of the most important parts of the FSE algorithm relies on the construction and analysis of a set of criteria curves. The latter uses a local linear least square (LLS) fitting procedure of the OSF. At each iteration step of the algorithm, a moving window with fixed length analyzes the local slope of the OSF. The LLS is performed according to the minimalization procedure described by the equation:

$$\min_x \left\| \mathbf{Ax} - \mathbf{b} \right\|_2, \quad \mathbf{A} \in R^{m \times n}, \tag{5.3}$$

where **x** represents the experimental vector containing windowed data of the OSF and **A**, **b** are matrixes containing regression coefficients. At the beginning of the algorithm, the length of the initial window is set to a relatively large value (usually 600 points) and it may be changed depending on the criteria described at point C.

- *(C) Criteria curve construction.*

For each fitting step, and as a measure of the solution quality, the norm of the overall residual is calculated. Looking for the minimum residual corresponding to each position of the analysis windows, a criteria curve is build. It gives information about fitting results in each part of the optical structure factor. Figure 5.1 (b) shows the best fitting line and criteria curve corresponding to the analysis of the OSF displayed in Figure 5.1 (a). It is easy to notice that the norm of the residuals of Eq. (5.3) varies depending on the window position with respect to the scattering vector, i.e. the scattering regimes. It is close to zero in the Guinier zone, and it increases significantly during the transition between the Guinier and Fractal zones. In the same way, the central part of the fractal zone is well identified by a local minimum. This local minimum is defined as the one that just follows the first local maximum for increasing *q*. The latter maximum identifies the transition between the Guinier and fractal zones. Figure 5.1 (b) shows also that in the Porod zone, the criteria curve is continuously increasing (i.e. the size parameter of these aggregates is too small to allow the observation of the Porod regime). Note that, depending on the width used for the analysis windows, the shape and behavior of the criteria curve may be slightly different. The polarization state of the incoming plane wave influences also the shape of the criteria curve but, in all calculations presented here, we use the perpendicular one since it is more appropriate to detect the fractal regime (the parallel polarization produces harmful oscillations).

- *(D) Analysis of the criteria curve*

To find the best solution from the fitting procedure, it is necessary to select the right local minimum of the criteria curve. An additional criterion is used for this purpose. This local minimum must satisfy the “absolute value criteria” , i.e. the absolute value of the minimum point is at least two times smaller than the value of the first maximum.

- *(E) Algorithm iteration*

If the local minimum detected at the previous step does not satisfy the “absolute value criteria”, the entire procedure (i.e. points B-D) is repeated for smaller and smaller windows widths. If after several iterations this criteria is still not satisfied, the algorithm stops. It usually means that the OSF do not exhibits any characteristic fractal zone. This situation occurs for small size parameters aggregates (i.e. $R_g < \lambda / 2\pi$). Typically, as a limit value that stops algorithm, length of the window 10 times smaller than the initial value is taken (i.e. 60 points of the OSF).

5.2.5. Results and discussion

For computational efficiency, we built an extensive database with the scattering properties of various aggregates. To further demonstrate the validity of the algorithm introduced above, two typical particle systems and parameters were considered:

- An aqueous colloidal suspension of aggregates, composed of silicon dioxide (SiO_2) nanobeads with radius $r_p = 55\ nm$, refractive index $\tilde{m}_p = 1.47 + 0i$ (Sopra.S.A. 2010), radius of gyration $R_g = 110 - 550\ nm$ (with step equal to $11\ nm$), fractal dimension $D_f = 1.4, 1.6, ..., 2.8$, and number of monomers $n_p = 4 - 1000$ (according to the other parameters, see fractal equation, i.e. Eq. (2.13)). The probing beam is a local plane wave with perpendicular polarization and nominal wavelength $\lambda = 409\ nm$ (violet laser diode).
- A gas flow of soot aggregates, composed of carbonaceous monomers with radius $r_p = 25\ nm$, refractive index $\tilde{m}_p = 1.71 + 0.56i$ (Tourbin 2006), $R_g = 188 - 1625\ nm$, $D_f = 1.4, 1.6, ..., 2.8$ and $n_p = 450, 500$ and 550. The probing beam is a local plane wave with perpendicular polarization and nominal wavelength $\lambda = 532\ nm$ (frequency doubled Nd-YAG laser).

5.2.5.1. Estimation of the radius of gyration

To estimate the radius of gyration of the silicon dioxide and soot aggregates, the Guinier zone is first analyzed. Figure 5.2 presents the results of the analysis of 5 colloidal suspensions containing aggregates with increasing radiuses of gyration. The estimated radiuses of gyration were found to be 236, 296, 356, 418 and 595 *nm* for the initial values 220, 275, 330, 385 and 550 *nm* respectively. It should be noticed that, the linear regression fit really well the data points (regression coefficient equal 0.9985, 0.9986, 0.9986, 0.9984 and 0.9983 respectively), even if all the estimated values are slightly, but systematically, overestimated.

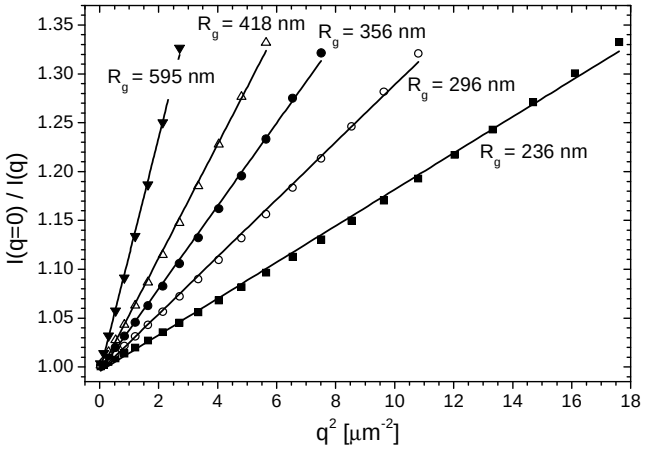

Figure 5.2. Guinier analysis of the SiO_2 aggregates.

Figure 5.3 summaries some results for the radius of gyration of silicon dioxide aggregates versus their initial radiuses of gyration. It can be seen that, as previously reported, the overestimation depends on the fractal dimension. It varies between 3.5% for $D_f = 1.40$ up to 9% for $D_f = 2.80$. Despite the latter bias, we can clearly say that Guinier analysis assures good reliability of the results and that it is fairly accurate.

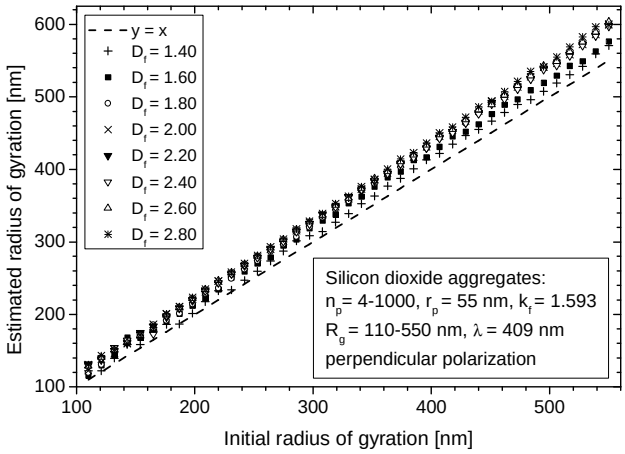

Figure 5.3. Summary of the radiuses of gyration estimated for silicon dioxide aggregates with various parameters.

Table 5.1 resumes the parameters estimated for different systems of soot aggregates with the following parameters: $n_p = 500$, $r_p = 25\,nm$ and $\tilde{m}_p = 1.71 + 0.56i$. Here also the estimated values fit pretty well the expected ones, so that the overestimation of the radius of gyration, similarly as for silicon dioxide aggregates, evolves from 1 to 9% for aggregates having $D_f \leq 2.0$.

Table 5.1. Summary of the radiuses of gyration estimated for soot aggregates of $n_p = 500$ monomers.

Fractal dimension	1.4	1.5	1.6	1.7	1.8	1.9	2.0	2.1
Initial R_g [nm]	1518	1155	909	736	610	515	443	386
Estimated R_g [nm]	1541	1167	954	794	662	540	483	425
R_g accuracy [nm]	73	53	50	41	34	26	23	20

Fractal dimension	2.2	2.3	2.4	2.5	2.6	2.7	2.8
Initial R_g [nm]	341	304	274	250	229	211	195
Estimated R_g [nm]	380	343	312	288	270	255	241
R_g accuracy [nm]	17	16	14	12	11	11	10

5.2.5.2. Estimation of the fractal dimension

Figure 5.4 presents results obtained for the fractal dimension of soot aggregates, with initial fractal dimension $D_f = 1.80$. The fractal dimension estimated with the SSE algorithm, $D_f = 1.82 \pm 0.01$ is in a very good agreement with the expected one. However, as already mentioned, we must keep in mind that the applicability of the SSE method is limited to OSF with $qR_g > 5$. Table 5.2 summarizes the fractal parameters estimated with the SSE algorithm for the soot aggregates with increasing number of monomers. Note that, with the SSE algorithm is was impossible to analyze smaller aggregates than those considered in this table (i.e. due to $qR_g > 5$ limitation). In an opposite way, Figure 5.4 shows also that the raw slope

found in the fractal zone with the FSE algorithm, i.e. 2.74 ± 0.02, differs significantly from the expected fractal dimension.

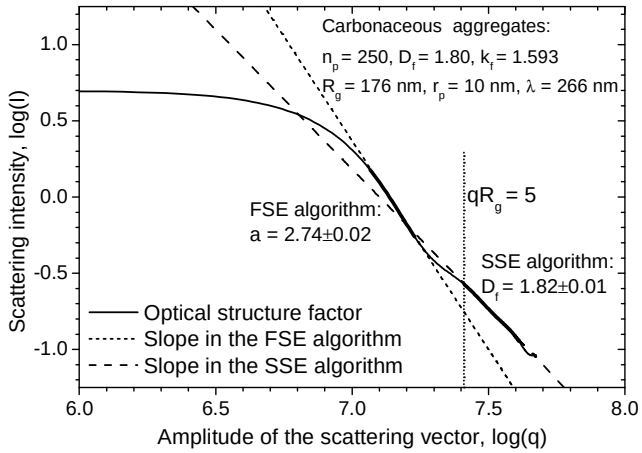

Figure 5.4. Comparison between the SSE and raw FSE (without calibration curves) algorithms for soot aggregates with initial fractal dimension $D_f = 1.8$ and for $r_p = 10nm$ and $n_p = 250$.

Table 5.2. SSE algorithm: estimation of the radius of gyration and fractal dimension of soot aggregates.

Number of monomers, n_p	160	180	200	220	240	242
Radius of gyration R_g [nm]	127.6	137.4	146.1	155.5	163.6	172.1
Initial fractal dimension, D_f	1.80	1.80	1.80	1.80	1.80	1.80
Estimated fractal dimension	1.997	1.941	1.838	1.812	1.772	1.795

Number of monomers, n_p	246	246	248	249	250
Radius of gyration R_g [nm]	172.1	173.9	174.8	175.3	175.7
Initial fractal dimension, D_f	1.80	1.80	1.80	1.80	1.80
Estimated fractal dimension	1.802	1.818	1.828	1.829	1.831

As an example, Figure 5.5 and Figure 5.6 show the fractal dimension estimated with the FSE algorithm for silicon dioxide aggregates. Figure 5.5 presents the optical properties of the aggregates with the radius of gyration increasing from $110\,nm$ to $550\,nm$ and an initial fractal dimension of (a) 1.80 and (b) 2.20. Figure 5.6 shows the various slope coefficients estimated for the aggregates with constant radius of gyration $R_g = 550\,nm$ but different fractal dimensions and number of monomers.

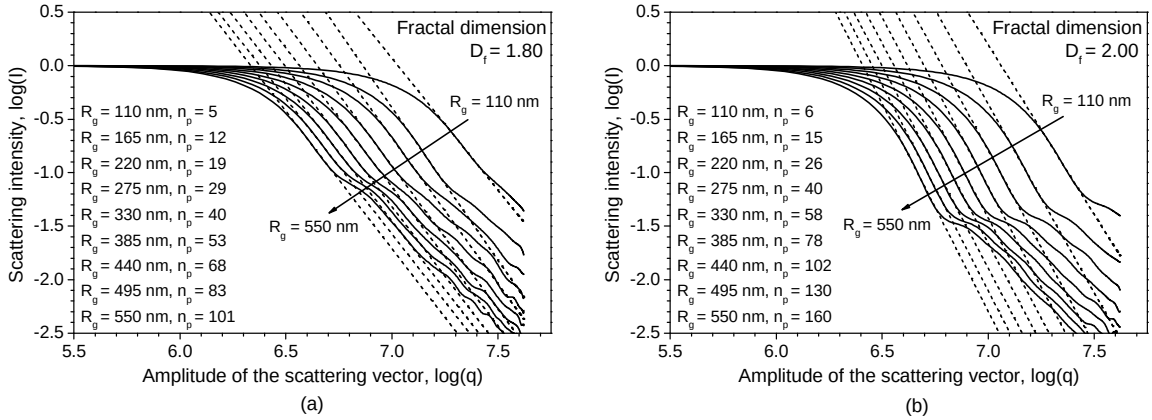

Figure 5.5. Typical results for the fractal dimension estimated for SiO2 particle aggregates with nominal fractal dimension: (a) 1.80, and (b) 2.00.

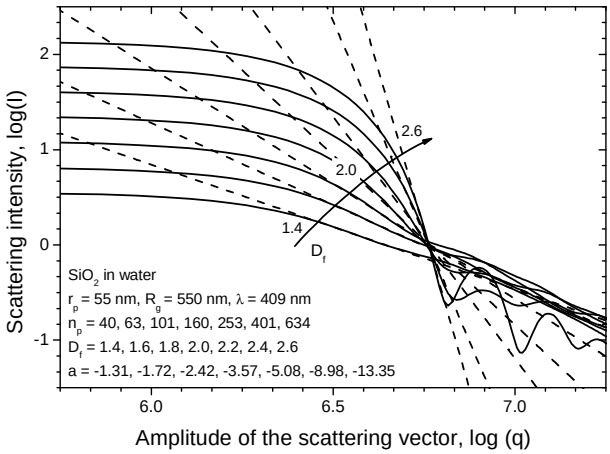

Figure 5.6. Typical results for the fractal dimension estimated for SiO2 particle aggregates with nominal fractal dimension $D_f = 1.80 - 2.60$ and constant radius of gyration $R_g = 550\ nm$.

Figure 5.7. shows the slopes (line equation coefficient) estimated for 8 different fractal dimensions ($D_f = 1.4, 1.6, ..., 2.8$) and a wide range of radiuses of gyration $R_g = 2r_p - 10r_p$ ($R_g = 110 - 550\ nm$). For $D_f = 2.80$, the values estimated with the FSE method were ambiguous and could not be proceed. However, all the other coefficients present clear trends and can be effectively analyzed. It is also worth to notice that as the radius of gyration increases the estimated slope decreases but, later on, for larger aggregates (around $R_g \geq 6r_p = 330\ nm$) it become almost constant.

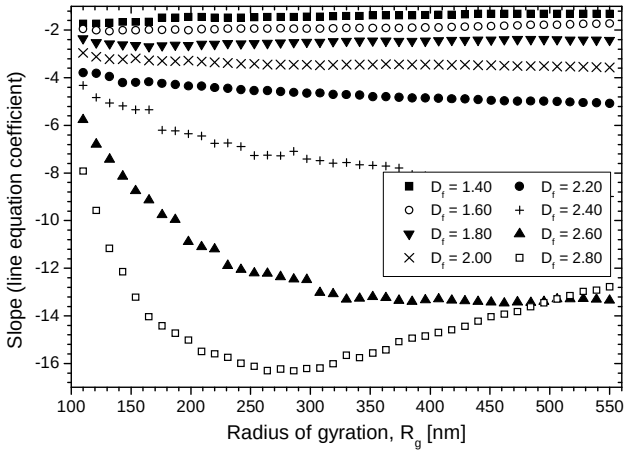

Figure 5.7. FSE algorithm: summary of the slope extraction for aggregates of SiO_2 monomers.

From Figure 5.7 and complementary results (e.g. as depicted in Figure 5.6), we derived calibration curves for the FSE algorithm that relate the raw slope associated to the fractal zone with the nominal fractal dimensions and radiuses of gyration, see Figure 5.8. A 3rd order polynomial fitting improve the resolution of these calibration curves. It should be noticed that, in Figure 5.8 all the curves are almost superimposed for aggregates with radius of gyration higher than $6r_p$, i.e. the fractal dimension of large aggregates can be determined without any prior knowledge (or analysis) of the radius of gyration. Obviously, from Figure 5.7 one may easily deduce that it is also the case for the other fractal dimensions.

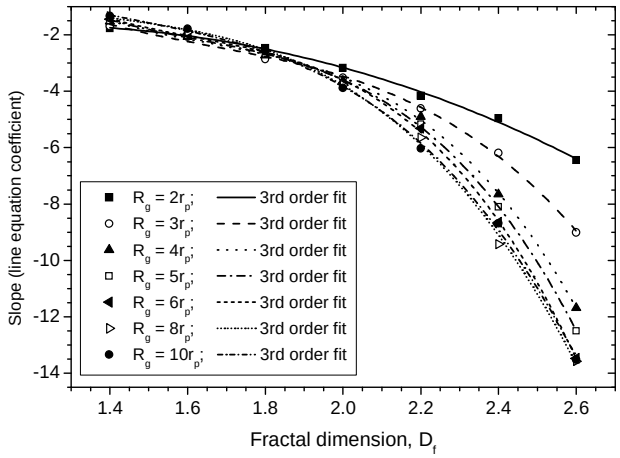

Figure 5.8. Estimated slope as a function of the fractal dimension for silicon dioxide aggregates (the FSE algorithm).

Figure 5.9 shows that by combining the FSE algorithm and the calibration curves (like the ones presented in Figure 5.8), the estimation of the aggregates fractal dimension is significantly improved even when 0.1% and 1% of white noise is added to the OSF. In fact, the fractal dimension is estimated over a large range and with an accuracy of 5% with 0.1% of additive white noise and about 10% for 1% of additive white noise. Additionally, we found

that the accuracy decreases as the fractal dimension decreases, so that this dependency provides even better results for commonly encountered aggregates (e.g. soots).

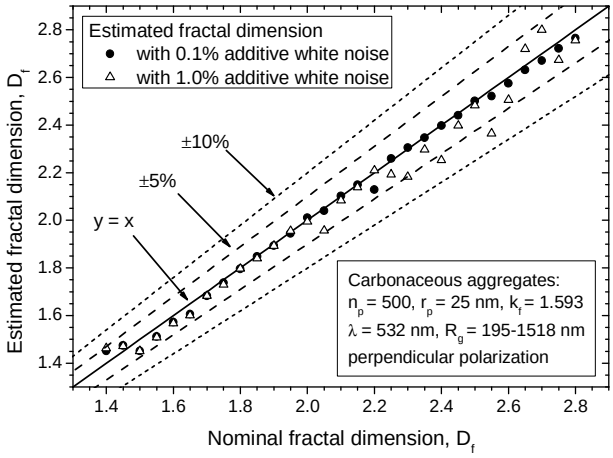

Figure 5.9. FSE algorithm with calibration curves: automatic estimation of the fractal dimensions from noisy optical structure factors. Parameters: soot aggregates with fractal dimension from 1.40 to 2.80 and constant number of 500 monomers.

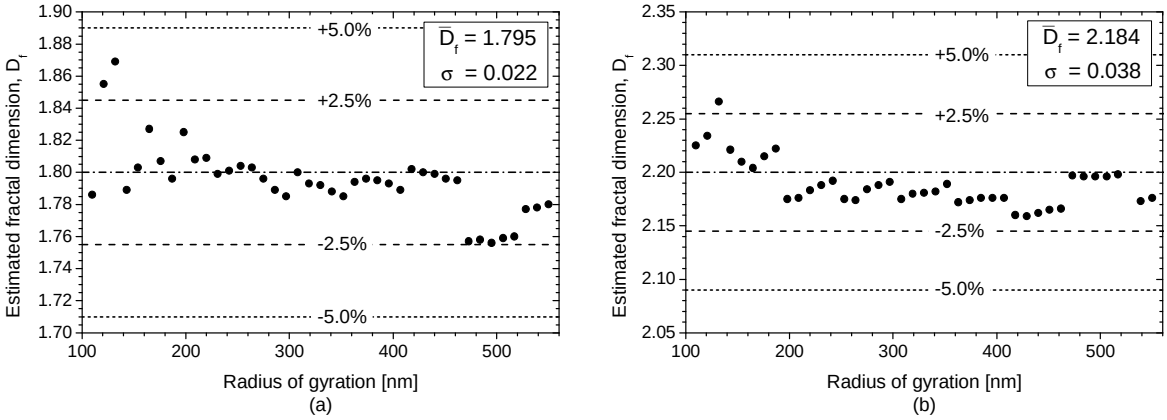

Figure 5.10. Fractal dimensions extracted automatically from the optical structure factors of various aggregates with the FSE algorithm for silicon dioxide aggregates with a constant number of $n_p = 500$ monomers with $r_p = 55\,nm$ and initial fractal dimension (a) $D_f = 1.80$ and (b) $D_f = 2.20$.

In addition to the previous results, Figure 5.10 shows some results for the fractal dimension of silicon dioxide aggregates that were obtained with the FSE algorithm and the calibration curves other than the ones presented in Figure 5.8. The accuracy is here also very good. It is better than 2.5% over almost the entire range of radiuses of gyration. We get about the same accuracy for the mean fractal dimension.

5.2.6. Conclusion

We have introduced a modeling procedure and numerical algorithms to estimate the fractal dimension and radius of gyration of fractal-like aggregates from the analysis of their optical structure factor. All numerical results provided here are based on rigorous particle agglomeration and light scattering models. The Second Slope Extraction (SSE) algorithm is

based on the Guinier analysis. It provides a simple and direct estimation of the fractal dimension. However, its applicability is limited to large size parameters aggregates. The First Slope Extraction (FSE) algorithm can be used to analyze much smaller aggregates than the SSE algorithm, even when we are dealing with the range $qR_g \leq 5$. Its application is more complicated than the SSE algorithm, as it requires to create look-up tables and to produce numerical calibration curves. However, the FSE algorithm is applicable to all kinds of aggregates, regardless their morphology. Therefore, it is thought to be a much more powerful and universal solution. The criteria curves is also a useful approach to identify the different scattering regimes and to obtain more reproducible results. At least all our analysis procedure is described in detail, which is not the case for the works found in the open literature.

5.3. Influence of free monomers on the analysis of the OSF

5.3.1. Physical background

In the open literature, most numerical investigations related to the prediction and the analysis of the OSF are performed on monodisperse aggregates with the same fractal dimension. Very few studies consider the influence of aggregates polydispersion and polymorphology. What may be even more astonishing is that we did not found any work dealing with the influence of free monomers (non aggregated) around the aggregates of interest.

In a combustion system, it means that researcher assumes (consciously or not) that at the measurement point all monomers (primary particles) are already aggregated. One can accept, in some extent, that this could be true in a perfectly laminar flame and far from the reactive zone. But, if we look in details for some TEM images of soot samples (e.g. see chapter 3), it is clear that there is a non-negligible amount of free monomers deposited on TEM grids. These free monomers could be the results of the disintegration of some aggregates, but this is not sure at all. In addition, as most light scattering measurements are performed within the flame (to avoid further aggregation and chemical effects during the exhaust gas cooling phase), we can have some doubts that all monomers are always aggregated at the measuring point. If now we think about dusty plasmas or destabilized colloidal suspensions, where there is no strong convective processes (like in flames), the hypothesize of a fully aggregated system becomes more and more questionable. For colloidal suspensions, where the sedimentation process can be rather slow, the problem appears to be even more drastic. So that, at least, it is necessary to evaluate the influence of the presence of some free monomers onto the analysis of the OSF and this is precisely the aim of this section.

5.3.2. Results and discussion

To fix the idea, Figure 5.11 shows the OSF of a cloud of SiO_2 aggregates surrounded by 20% and 100% (in number) of free monomers (not aggregated). The SiO_2 aggregates are all identical with $n_p = 250$ monomers. They are probed with incident wavelength $\lambda = 266\,nm$. It is clear that even 20% (50 over 250) single monomers change the raw slope coefficient estimated with the FSE method (particularly, from $a = -2.631$ to $a = -2.147$). For 100% of free monomers (250 over 250), the decay constant is divided by a factor of almost 2 ($a = -1.344$).

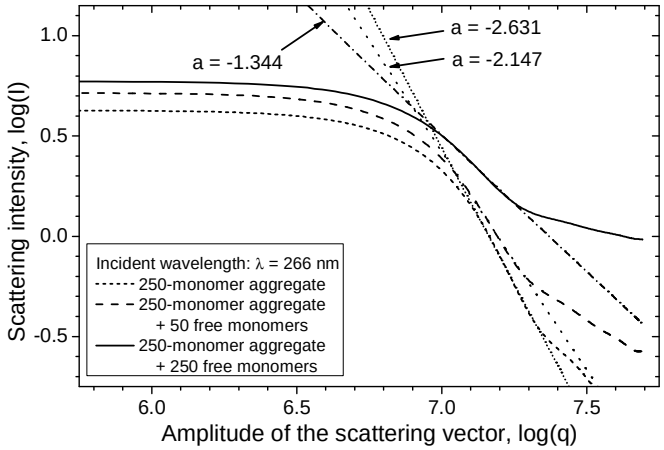

Figure 5.11. Example results of the fractal dimension extraction for aggregates of SiO_2 monomers with fractal dimension 1.80 and various number of free monomers in the experimental setup.

A direct consequence of these results is that the fractal dimension estimated with the FSE method will be strongly biased by the presence of these monomers. In fact, the fractal dimension is more and more overestimated as the number fraction of free monomers increases. To analyze quantitatively this effect, we built an extensive database with different aggregates and number fractions of monomers. This data were processed automatically with the algorithm introduced in the previous section. Figure 5.12 summaries the fractal dimension estimated for SiO_2 aggregates with $D_f = 1.80$ and $n_p = 50 - 250$ versus the number fraction $(2 - 100\%)$ of free monomers. Figure 5.13 and Figure 5.14 show similar results for aggregates having $D_f = 2.00$ and $D_f = 2.20$ respectively.

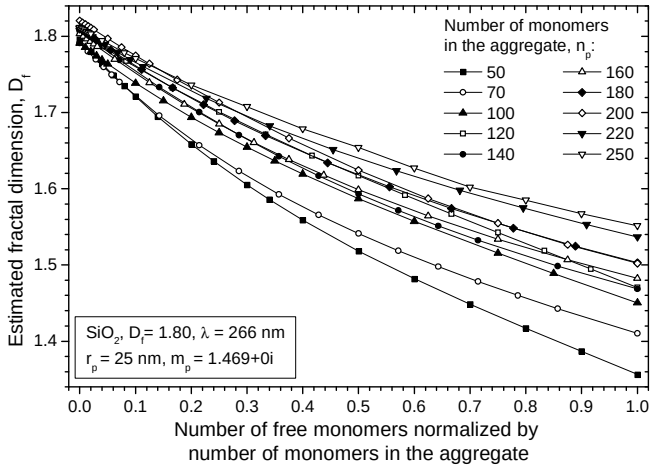

Figure 5.12. Fractal dimensions extracted automatically from the optical structure factor of the aggregates of SiO_2 ($D_f = 1.80$, $r_p = 25\,nm$, $n_p = 50 - 250$) with the FSE algorithm for various number of free monomers in the experimental setup.

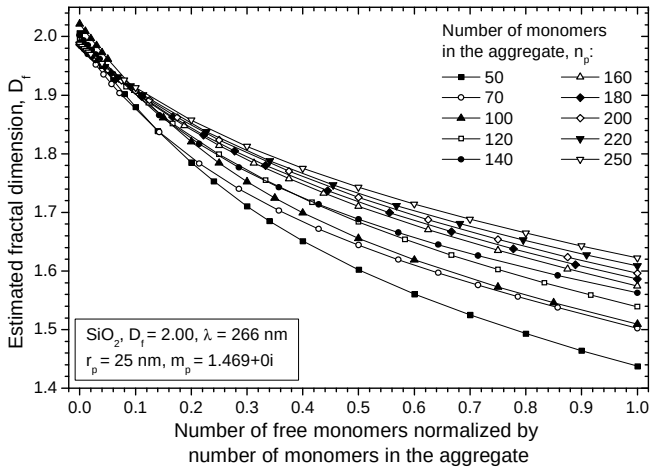

Figure 5.13. Like Figure 5.12 but for $D_f = 2.00$.

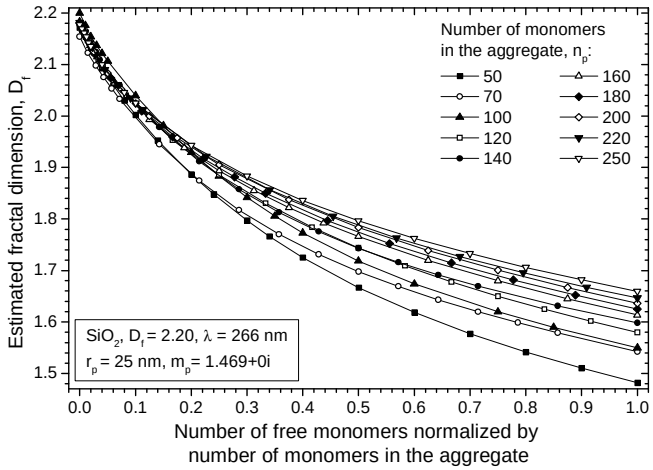

Figure 5.14. Like Figure 5.12 but for $D_f = 2.20$.

Analyzing Figure 5.12 – Figure 5.14 we deduce that influence of the scattering properties of the single monomers to the OSF of the aggregates depends not only on the number of free monomer but also on the total number of monomers within aggregates. Thus, as clearly

shown in Figure 5.12 – Figure 5.14, OSF of the smaller aggregates are much more affected by the scattering properties of the free monomers than the larger ones. As an example, if we compare properties of the aggregates of $n_p = 50$ and $n_p = 250$ monomers with respect to the 50 and 250 free monomers respectively, we can see that estimated fractal dimensions for the initial value of $D_f = 1.80$ are equal to the 1.36 and 1.55. Obviously, a similar trend is observed for the other fractal dimensions. This behavior is the consequence of the fact that the scattering of the aggregate is strongly related to the number of monomers. In the Guinier zone the influence of the monomers is rather weak in comparison to what is observed in the fractal zones. Figure 5.15 shows the corresponding error on the estimated fractal dimension for the aggregates of (a) $n_p = 50$ and (b) $n_p = 200$. The relative error is maximal for $D_f = 2.20$ and minimal for $D_f = 1.80$.

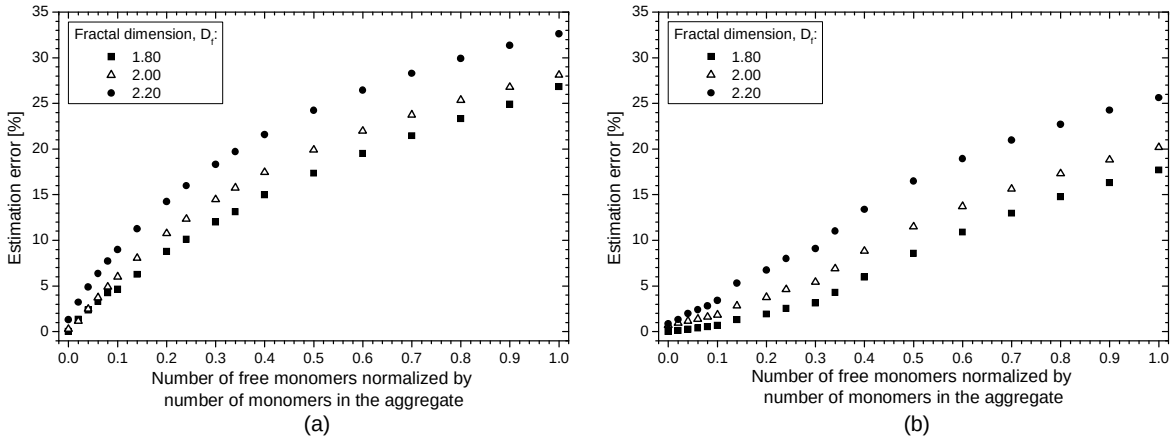

Figure 5.15. Estimation error of the fractal dimension predicted for the optical structure factor of the aggregates of SiO_2 with (a) $n_p = 50$ and (b) $n_p = 200$ with the FSE algorithm for various numbers of free monomers in the experimental setup.

One may argue that an error of $15 - 25\%$ is somewhat acceptable. However, we have to remember that for a large variety of systems (e.g. soots) the fractal dimension varies only in the range 1.60 to 2.00. In the other hand, we can found a large literature discussing improvements of few percent in the determination of D_f whatever this free monomer effects is totally neglected *a priori*. The analysis of OSF without an *a priori* knowledge of the number fraction of free monomers is an interesting perspective of this work.

5.4. A comparison between scattering properties of DLA and DLCA aggregates

To compare scattering properties of DLA and DLCA aggregates from the test sample of DLCA aggregates (Yon et al. 2008) we selected 3 sub-samples with various number of monomers and aggregate whose size is large enough, so that the fractal zone can be observed. The latter criterion is about to be satisfied if $R_g > \lambda / 2\pi$. Therefore, with a significant margin, we selected aggregates with $R_g > 10 r_p$ (i.e. $R_g > 171\,nm$): (1) 31 aggregates with

$D_f = 1.75-180$, (2) 27 aggregates with $D_f = 1.80-1.85$ and (3) 26 aggregates with $D_f = 1.85-1.90$. Several dozens of aggregates are not enough to infer there OSF, therefore each aggregate was randomly rotated 1000 times. Then, using T-Matrix method we calculated the averaged scattering diagrams of all these synthetic samples (referred also as (1); (2) and (3)). To do so, relatively short incident wavelength (quadrupled Nd: YAG laser, $\lambda = 266\,nm$) was used. Next, using our tunable code, we generated DLA aggregates with exactly the same parameters (i.e. n_p, D_f and k_f) as the DLCA aggregates. For this study, the fractal prefactor was set to the value found for the DLCA aggregates $k_f = 1.386$ (see section 2.4). Figure 5.16 compares the OSF of the sample (1) generated with the DLA and DLCA models. Figure 5.17 shows results for the sample (2) and Figure 5.18, for the sample (3).

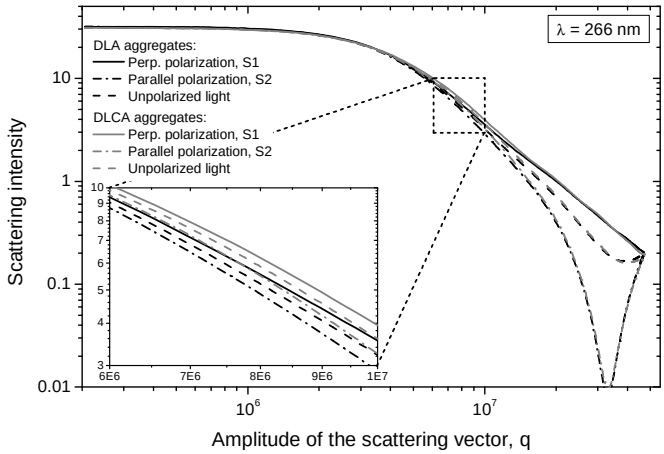

Figure 5.16. Comparison of the OSF of DLA and DLCA aggregates – sample (1): $D_f = 1.75-1.80$ and number of monomers $n_p = 94-916$.

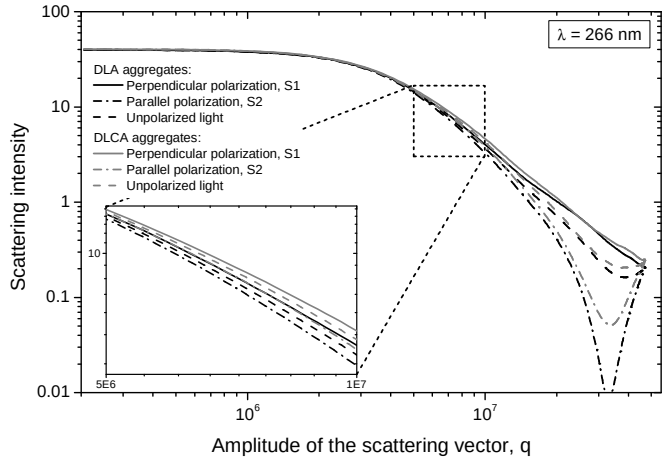

Figure 5.17. A Comparison of the OSF of DLA and DLCA aggregates – sample (2): $D_f = 1.80-1.85$ and number of monomers $n_p = 98-907$.

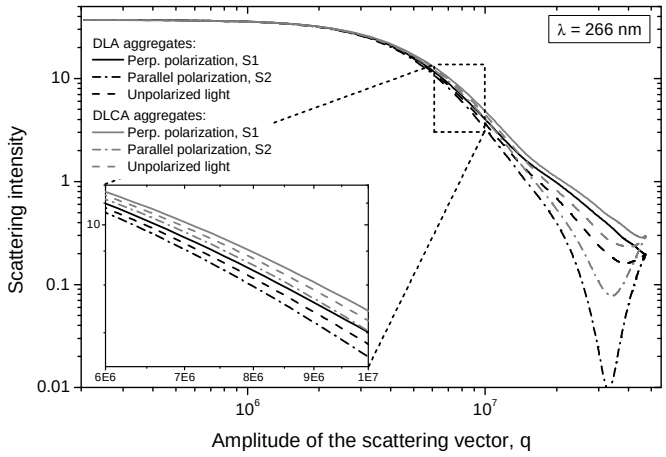

Figure 5.18. Comparison of the OSF of DLA and DLCA aggregates – sample (3): $D_f = 1.85 - 1.90$ and number of monomers $n_p = 112 - 886$.

Comparing OSF presented in Figure 5.16 – Figure 5.18 it can be seen that there are no significant differences between DLA and DLCA aggregates, i.e. the corresponding OSF almost overlap. If some slight and increasing differences can be observed for higher fractal dimensions (compare Figure 5.16 and Figure 5.18), the slopes related to the fractal zone are nearly identical. Thus, through these examples, we can conclude that the global parameters describing an aggregate (i.e. fractal dimension, fractal prefactor, radius of gyration, number and radius of single monomers) are unambiguous regardless aggregation phenomena that leads to their formation.

Our conclusions are in a very good agreement with results presented by Oh and Sorensen (Oh and Sorensen 1998) who compared optical structure factor $I(q)$ of DLA and DLCA aggregates. They reported also that $I(q)$ of DLA aggregates does not show simple scaling behavior described by q^{-D_f} relation in the range $R_g^{-1} \le q \le r_p^{-1}$. However, $I(q)$ is essentially identical for DLA and DLCA aggregates in the range of $q \ge 0.1 r_p^{-1}$. In our case (i.e. for $r_p = 17.1\,nm$ and $\lambda = 266\,nm$) this requirement is satisfied for $q \ge 5.85 \times 10^6$ (i.e. for the scattering angle $\theta \ge 15°$). It also clearly explains the good accuracy found for DLA and DLCA samples over the entire range of the scattering angles. These results emphasize also the generic trend of most results presented in this work (that have been obtained with a DLA model).

5.5. Conclusion

In this chapter we have discussed algorithms and methods to estimate morphological parameters of fractal aggregates from the analysis of their scattering diagrams. The fractal dimension is evaluated from the exponent of the power-law decay of these diagrams in the fractal zone. To evaluate the radius of gyration the Guinier analysis was used. We investigated also the influence of the free monomers (not aggregated) on the conventional analysis of the OSF. As clearly shown, only 20% of free single monomers can significantly

biased estimation of D_f. All the algorithms and methods were tested on two totally different particle systems: colloidal suspensions of optically transparent aggregates (silicon dioxide) as well as clouds of highly absorbing aggregates (carbonaceous soots).

In the last part of the chapter, we compared scattering properties of DLA and DLCA aggregates. The few examples considered here have proven that both aggregation models lead to the aggregates with very similar optical properties. Our conclusions are also in a very good agreement with results presented in the literature (e.g. (Oh and Sorensen 1998)).

Chapter 6

LIGHT EXTINCTION SPECTROMETRY (LES)

6.1. Introduction

For historical reasons, the technique describes in this section is also referred as the turbidimetric technique. However, it is called here the Light Extinction Spectrometry (LES) due to its fundamental analogy with the well known light absorption spectrometry. The latter technique relies on the light molecular absorption, while the LES is based on the particle light extinction (absorption and scattering).

The chapter is organized as follows. To begin with, in section 6.2 we briefly introduce the principle of the LES technique under a single scattering regime. Subsequently, we present the core part of the technique, i.e. the numerical inversion procedure (section 6.3). Next, in section 6.4 we show numerical results (extinction and transmission spectra) obtained for various aerosols and suspensions. After a description of the basic experimental setup, several experimental results are presented (Section 6.5). Section 6.6 is an overall conclusion.

6.2. Principle

Basically, the LES technique measures the extinction spectra of a particle system illuminated by a collimated and polychromatic light beam. Thus, this optical technique requires to pass a beam with spectral intensity $I_0(\lambda_i)$ and wavelengths λ_i through the cloud of particles (monomers, aggregates, etc.) to be analyzed. The transmitted spectral intensity $I(\lambda_i)$ is collected by an optical system (with a small solid angle aperture) and analyzed via a spectrometer. If the multiple scattering phenomenon is negligible (e.g. (Xu 2007)), the beam transmission $T(\lambda_i)$ is given by:

$$T(\lambda_i) = \bar{I}(\lambda_i) / \bar{I}_0(\lambda_i) = \exp(-\tau L) \tag{6.1}$$

where L is the path length of the beam through the cloud of particles and $\tau = C_n \bar{C}_{p,ext}$ is the turbidity of the particulate medium. $\bar{C}_{p,ext}$ is an integral quantity which represents the mean extinction cross section of the particles (Onofri et al. 2009) and C_n is the particle medium concentration in number. If $Q_{p,ext}$ is the extinction efficiency (referred also as the extinction coefficient) of a single spherical particle characterized by its diameter d_p and its refractive index $\tilde{m}_p$ we have that:

$$\bar{C}_{p,ext} = \int_{d_{p,\min}}^{d_{p,\max}} Q_{p,ext}(d_p, \tilde{m}_p) \frac{\pi d_p^2}{4} f(d_p) dd_p. \tag{6.2}$$

A schematic diagram of the LES technique is shown in Figure 6.1 (see also the experimental setup presented in Figure 6.18 and in Figure 6.22).

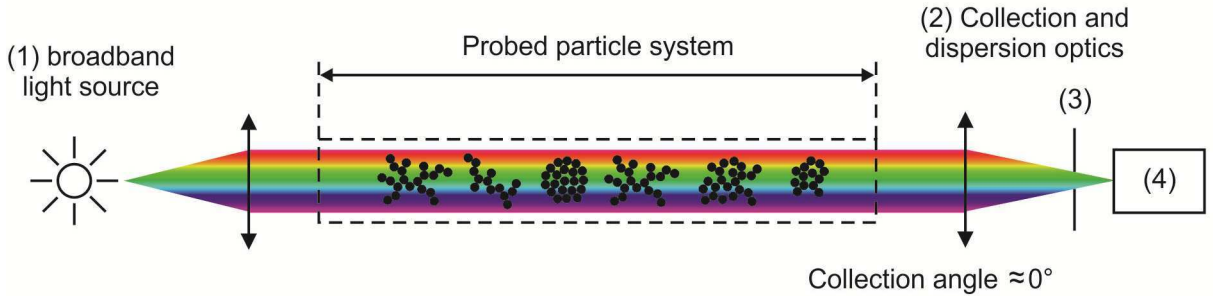

Figure 6.1. Schematic diagram of the Light Extinction Spectrometry: (1) broadband light source, (2) broadband achromatic focusing/collimating optics (3) spatial filter, (4) broadband spectrometer.

LES setup is mainly composed of (1) a broadband light source, (2) broadband achromatic focusing/collimating optics, (3) a spatial filter and (4) a broadband spectrometer for extinction analysis. In principle, LES measurements can be performed using only two optical accesses and at long distance. This is highly suitable to investigate systems with limited optical access, like for instance dusty or fusion plasmas (Shiratani et al. 1999; Onofri et al. 2009). However, this technique has also some drawbacks. Firstly, as mentioned previously, its transmission equation (6.1) is only valid if the collection of multiple scattered photons is negligible (e.g. (Xu 2002)). To ensure partially the validity of the latter requirement, it is necessary to avoid the diffraction peak (the angular aperture of the collection optics must be as small as possible) and the particle diameter cannot exceed several wavelengths. The optical thickness (or turbidity) of the system must also be rather weak. In addition, the LES technique is very sensitive to the particle optical dispersion (complex refractive index over a large spectrum) (e.g. (Onofri et al. 2009)). Finally, when LES is applied to a system with a long optical path, only highly diluted particle systems can be analyzed (Ouf et al. 2008).

6.3. Inversion procedure

The inversion procedure is a key part of the LES technique. It requires to discretize the transmission equation (Onofri et al. 2009; Onofri et al. 2010c) and to minimize the differences between the measured transmission and the numerically predicted one. Eq. (6.2) is a Fredholm integral equation of the first kind (Hansen 1994).

Our goal is to estimate the particle number concentration C_n and the particle number size distribution $f\left(d_p\right)$, from the experimentally measured transmission spectrum $T\left(\lambda_i\right)$. To do so, it is necessary to calculate the kernel of the Fredholm equation $Q_{p,ext}\left(d_p,\tilde{m}_p\right)$. It leads to an ill-posed and predetermined problem (Mroczka and Szczuczyński 2009) that requires regularization and inversion procedures. Generally, a problem is defined as an ill-posed if the solution is not unique or if it is not a continuous function of the data, i.e. if an arbitrarily small perturbation of the data can cause an arbitrarily large perturbation of the solution (Hansen 2008).

Basically, in the literature, there are two main approaches to solve ill-posed problem. In most studies, it is still solved by imposing a model for the PSD (e.g. Log-Normal) and by iterating on the mean diameter and the standard deviation. The second approach is more powerful as it does not impose strong constraints onto the PSD. However, it is numerically unstable and it requires a specific regularization scheme to stabilize the inversion procedure (e.g. (Hansen 2008)). Applying the second approach it is preferable to use the particle concentration in volume rather than in number. If, as an equivalent particle model, the spherical one is used, the particle size distribution in volume $V\left(d_p\right)$ depends on the particle number concentration as follows (Onofri et al. 2010a; Onofri et al. 2010b):

$$V\left(d_p\right)=C_v v\left(d_p\right)=C_n\left(\pi/6\right)d_p^3 f\left(d_p\right) \tag{6.3}$$

where $v\left(d_p\right)$ is the normalized particle size distribution in volume. If we introduce the constant $\Lambda=3L/2$, Eq. (6.2) can be rewritten in the following linear form:

$$-\ln\left[T\left(\lambda_i\right)\right]=\Lambda\int_{d_{p,\min}}^{d_{p,\max}} Q_{p,ext}\left(\lambda_i,d_p,\tilde{m}_p\right)\frac{V\left(d_p\right)}{d_p}. \tag{6.4}$$

The above equation may be discretized as follows:

$$\int_{d_{p,\min}}^{d_{p,\max}} \frac{Q_{p,ext}\left(\lambda_i,\tilde{m}_p,d_p\right)}{d_p}V\left(d_p\right)dd_p=\sum_{j=1}^{M}S_{i,j}V_j, \tag{6.5}$$

where the vector V_j to be determined is the discrete form of $V\left(d_p\right)$, with $j=1,\ 2,\ ...,M$. The element $S_{i,j}$ is equal to $S_{i,j}=Q_{p,ext}\left(\lambda_i,\tilde{m}_p,d_{p,j}\right)/d_{p,j}$ for wavelengths λ_i, $i=1,\ 2,...,N$. $\mathbf{S}$ is a $N\times M$ matrix referenced here as the "extinction matrix", which has to be calculated only once with:

$$S_{i,j}=\int_{d_{p,j-1}}^{d_{p,j}}\frac{Q_{p,ext}\left(\lambda_i,\tilde{m}_p,d_p\right)}{d_p}dd_p. \tag{6.6}$$

If we represent a measured transmission spectrum as a vector $\bar{\mathbf{T}}$ whose element $\bar{T}_i$ corresponds to the beam transmission for the wavelength λ_i and a cloud of particles with size distribution in volume $\mathbf{V}$; then, to find $\mathbf{V}$, the following linear algebraic equation has to be solved:

$$\bar{\mathbf{T}} \equiv \mathbf{S} \cdot \mathbf{V}. \tag{6.7}$$

Solution of the equation is given as:

$$\mathbf{V} \equiv \left(\mathbf{S}^{\mathrm{T}}\mathbf{S}\right)^{-1}\mathbf{S}^{\mathrm{T}}\bar{\mathbf{T}}. \tag{6.8}$$

The ratio between the largest and the smallest nonzero singular values of matrix $\mathbf{S}$ is large. This implies that the matrix $\mathbf{S}$ is ill-conditioned and numerically unstable, i.e. that the solution is potentially very sensitive to perturbations. A way to solve this problem is to iteratively minimize the square of the difference $\mathbf{S}\cdot\mathbf{V} - \bar{\mathbf{T}}$ taking into account that the PSD is always a nonnegative function. It leads to a minimalization procedure of a Non-Negative Least-Square problem: $\underset{V>0}{Min}\left\|\mathbf{S}\cdot\mathbf{V} - \bar{\mathbf{T}}\right\|^2_{2-LSQ}$. This can be done using orthogonal numerical algorithms (Lawson and Hanson 1974; Hansen 1994; Hansen 2008).

LES deals with particles sizes ranging from the Rayleigh to the Mie scattering regimes (Onofri et al. 2009), therefore extinction coefficients can vary of several orders of magnitude from the lower to the upper boundary of the PSD. It leads to a large condition number of the matrix $\mathbf{S}$. To limit the underlying problems, it is convenient to introduce a smoothing (or regularization) matrix $\mathbf{H}$ and a Lagrangian parameter (i.e. smoothing factor (Twomey 1979)). The corresponding algebraic equation is then expressed by:

$$\left(\mathbf{S}^{\mathrm{T}}\mathbf{S} + \gamma\mathbf{H}\right)\mathbf{V} = \mathbf{S}^{\mathrm{T}}\bar{\mathbf{T}}. \tag{6.9}$$

Finally, the solution of the discretized ill-posed problem may be found by minimization of the following quantity:

$$\underset{V>0}{Min}\left\|\left(\mathbf{S}^{\mathrm{T}}\mathbf{S} + \gamma\mathbf{H}\right)\mathbf{V} - \mathbf{S}^{\mathrm{T}}\bar{\mathbf{T}}\right\|^2_{2-LSQ}. \tag{6.10}$$

This can be performed using several numerical tools, we did it under MATLAB environment. As mentioned previously, the algebraic solution of this inverse problem requires to compute the extinction matrix. To do so, depending on the particle morphology and size range, different methods and theories can be used. In the present study, for spheres we used the Lorenz-Mie theory, while for aggregates of nanospheres (fractal-like aggregates as well as buckyballs aggregates), we used essentially the T-Matrix method (Mackowski and Mishchenko 1996). As mentioned previously, this code is very time-consuming (see section 4.5.5.7), so it cannot be used on-line to inverse the measured spectra. However, it was used to calculate look-up tables.

6.4. Numerical results

6.4.1. Extinction spectra and scattering diagrams

In the current section we present and discuss results of T-Matrix calculations for the extinction and scattering cross sections of a cloud of various aggregates. We consider aggregates composed of amorphous silicon and silicon dioxide monomers with radius 3.5, 40.5 and $55\,nm$. We show also transmission spectra for different number concentrations of aggregates. From the T-Matrix code and an aggregate of n_p monomers we get an extinction coefficient (i.e. extinction cross section normalized by the surface of the sphere with volume equivalent to the one of the aggregate):

$$Q_{a,ext}^{T-M} = C_{a,ext}^{T-M} / \pi R_v^2, \tag{6.11}$$

where the radius in volume R_v of the equivalent sphere is given by:

$$R_v = n_p^{1/3} r_p. \tag{6.12}$$

Using Eqs. (6.11) and (6.12) we get the extinction cross section of the aggregate:

$$C_{a,ext}^{T-M} = \pi r_p^2 n_p^{2/3} Q_{a,ext}^{T-M} \tag{6.13}$$

By analogy, the scattering and absorption cross sections may be calculated too.

To compare extinction and scattering spectra of aggregates with various parameters, we show the evolution of the extinction and scattering coefficients rather than cross sections. It should be noticed also that calculations of the extinction spectra is a very time-consuming task. As an example, to perform simulations for the wavelengths ranging from 200 to $1000\,nm$ with $10\,nm$ step and an averaging procedure over 50 aggregates, we have to compute 4050 different cases. If we consider large aggregates (e.g. with $n_p = 1000$ monomers) with large monomers (e.g. $r_p = 55\,nm$) it takes 1000 hours (about 15 minutes for each case) on an up-to date computer and one full day on a cluster of 40 cores (see section 4.5.5).

6.4.1.1. Aggregates of Amorphous Silicon

Figure 6.2 shows the results of the T-Matrix calculations for the mean extinction coefficient of a cloud of monodisperse aggregates composed of amorphous silicon nanoparticles, versus the incident wavelength. In both subfigures the fractal dimension and the number of monomers increase from 1.5 to 2.8 and 51 to 1000 respectively, whereas the radius of gyration is kept constant (equal to $R_g = 10 r_p$). The radius of single monomers equal to $r_p = 3.5\,nm$ corresponds to particles generated in a low-pressure Argon-Silane discharge (Boufendi and Bouchoule 1994; Onofri et al. 2011b).

Figure 6.2 (a) shows the evolution of the extinction coefficient versus the wavelength while (b) shows the sensitivity of the extinction coefficient to the fractal dimension. This sensitivity is defined as the ratio of the extinction coefficient of the aggregates with the extinction coefficient of a single monomer. Both figures indicates that extinction is not very sensitive to

the fractal dimension, in contrary to the scattering diagrams (Farias et al. 1996; Sorensen 2001).

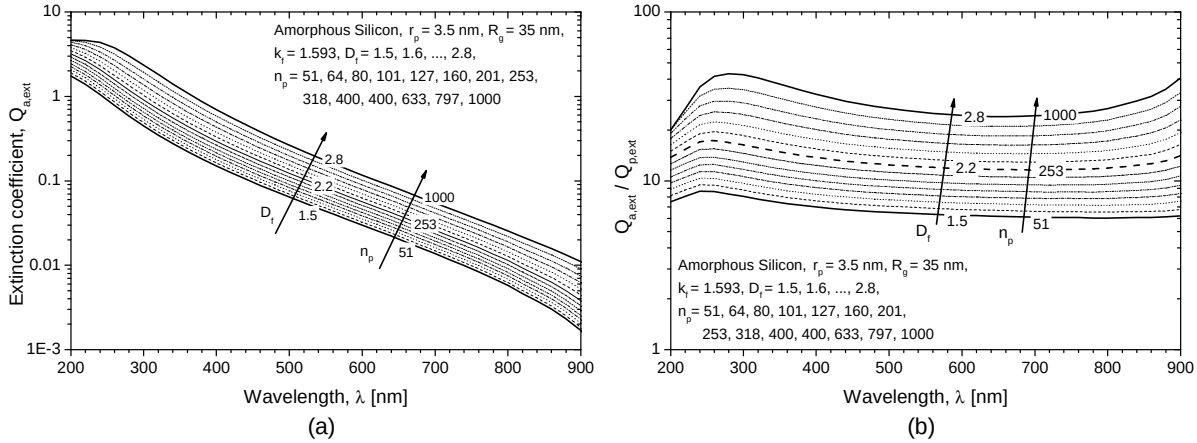

Figure 6.2. Extinction spectra of aggregates of amorphous silicon for various fractal dimensions and numbers of monomers but with a constant radius of gyration: (a) raw extinction coefficient and (b) sensitivity to the fractal dimension.

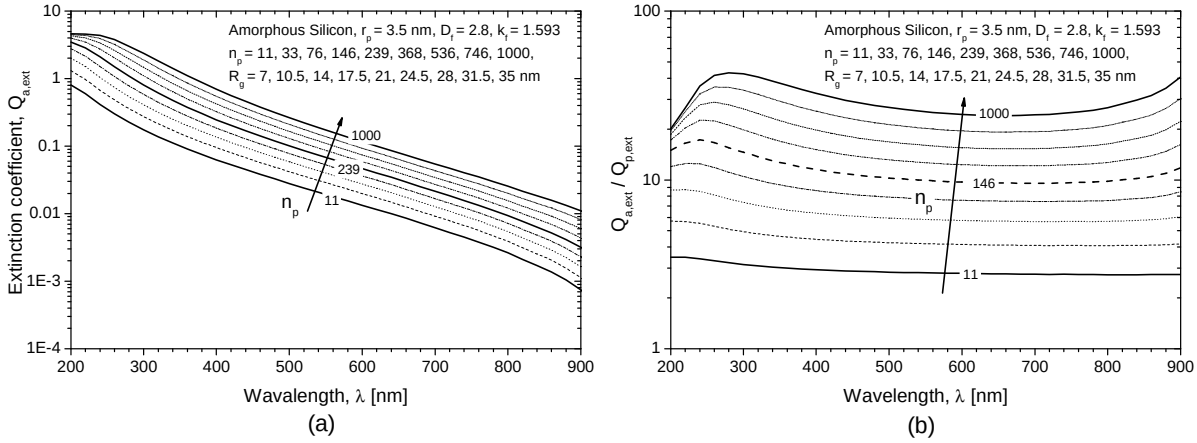

Figure 6.3. Extinction spectra of aggregates of amorphous silicon with various sizes (i.e. different numbers of monomers and radiuses of gyration) but constant fractal dimension: (a) raw extinction coefficient and (b) sensitivity to the size of the aggregates.

Figure 6.3 shows the (a) evolution of the extinction coefficient versus the wavelength and (b) its sensitivity to the size of the aggregates; amorphous silicon monomers with $r_p = 3.5\ nm$. In the presented case, the fractal dimension remains constant $D_f = 2.80$, while the size of the aggregates increases (i.e. number of monomers and radius of gyration). Comparing Figure 6.2 and Figure 6.3 it turns out that extinction is more sensitive to the radiuses of gyration of aggregates than to their morphology. It is also interesting to notice that the sensitivity of the extinction is different depending on the wavelength. It is significantly higher for wavelengths above $\lambda = 750\ nm$ and below $\lambda = 450\ nm$ than in the intermediate zone. For large wavelength, due to the small size of the aggregates compare to the wavelengths, only macroscopic properties of the aggregates seems to be important, while for the wavelength below $\lambda = 750\ nm$ more physical insight about the aggregates morphology is probably accessible.

Analyzing Figure 6.2 and Figure 6.3 we must also remember that extinction spectra are changing not only due to the geometrical properties of the aggregates (size and shape) but also due to the dispersion spectra of the particle material. The latter effect is particularly important for amorphous silicon since its refractive index is rapidly changing in the range $\lambda = 200 - 900\ nm$, see Figure 6.4.

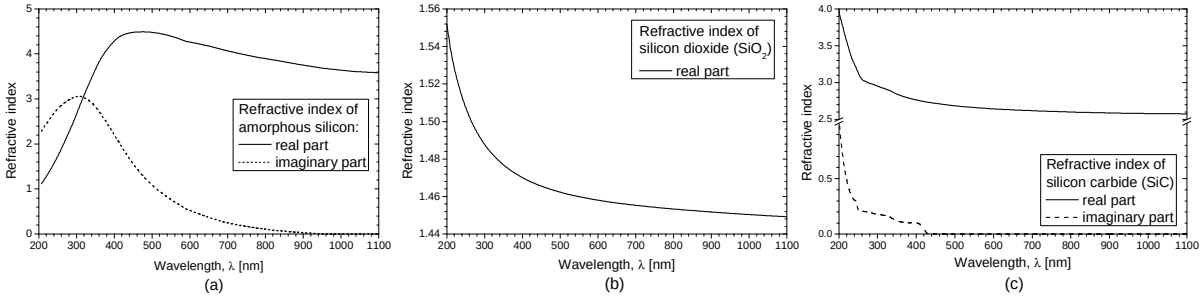

Figure 6.4. Dispersion spectra used for (a) amorphous silicon, (b) silicon dioxide and (c) silicon carbide particles (Sopra.S.A. 2010).

The influence of the imaginary part of the refractive index can be seen when extinction coefficients presented in Figure 6.2 and Figure 6.3 are compared with scattering coefficients calculated for exactly the same aggregates, see Figure 6.5 and Figure 6.6 respectively. These figures confirms what is predicted by the RDG-FA model: for small aggregates, the extinction coefficient is mainly sensitive to the imaginary part of the refractive index of monomers.

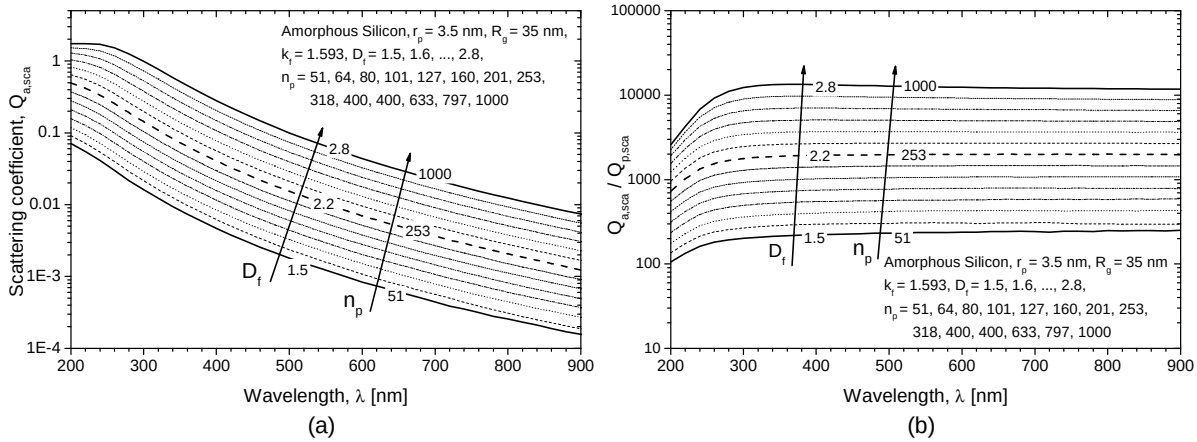

Figure 6.5. Scattering coefficient of aggregates of amorphous silicon with various fractal dimensions and number of monomers but a constant radius of gyration: (a) raw coefficient and (b) sensitivity to the fractal dimension.

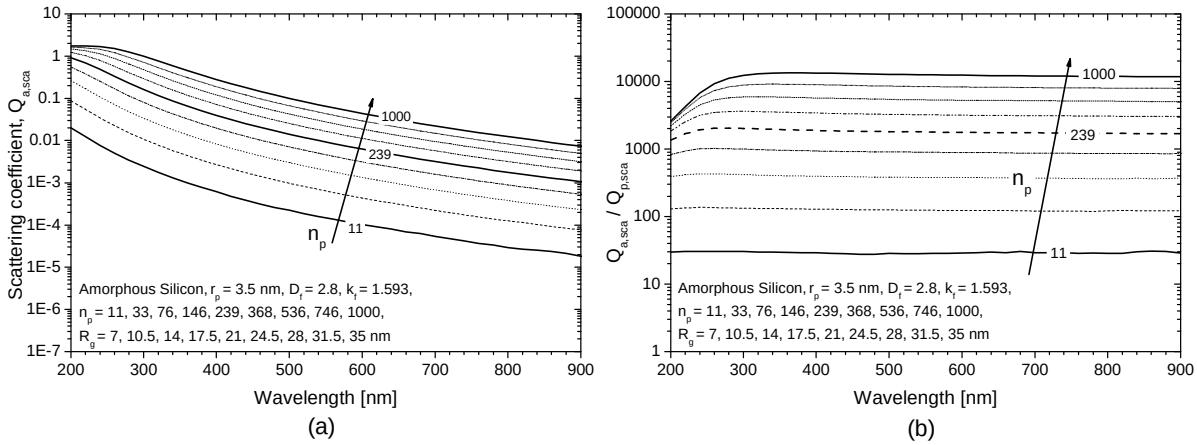

Figure 6.6. Scattering coefficient of aggregates of amorphous silicon with various sizes (i.e. different numbers of monomers and radiuses of gyration) but constant fractal dimension: (a) raw coefficient versus the wavelength and (b) sensitivity to the size of the aggregate.

6.4.1.2. Aggregates of Silicon Dioxide

Figure 6.7 (a) shows the evolution of the extinction coefficient of a cloud of aggregates composed of silicon dioxide monomers. The fractal dimension and the number of monomers increase from 1.5 to 2.8 and 51 to 1000 respectively, whereas the radius of gyration is kept constant (equal to $R_g = 10 r_p$). The radius of single monomers is equal to $r_p = 40.5\,nm$ and corresponds to the particles generated in our experimental setup (see section 6.5.2). Figure 6.7 (b) shows the same results but with linear-logarithmic scales.

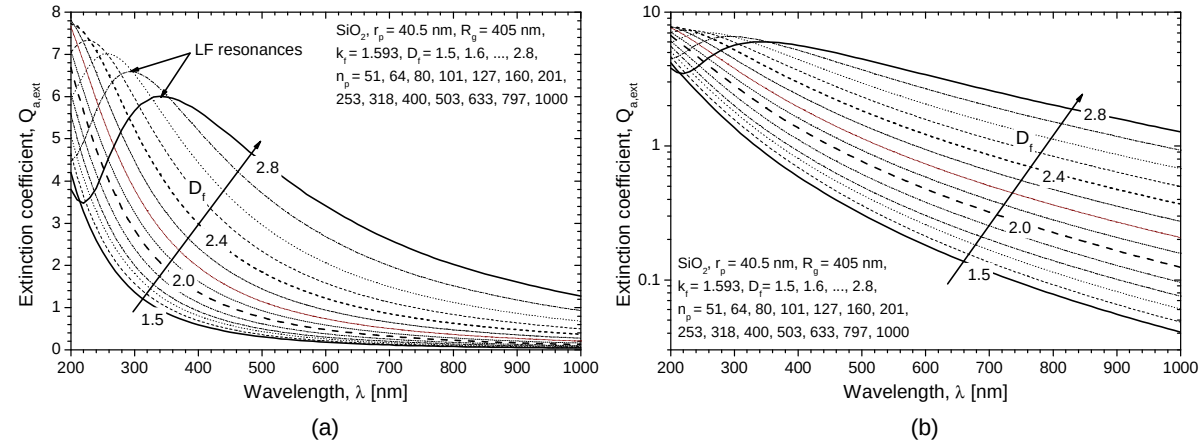

Figure 6.7. Extinction coefficient of aggregates of silicon dioxide monomers with various fractal dimensions and number of monomers but constant radius of gyration: (a) linear scale and (b) linear-logarithmic scale.

Figure 6.8 shows similar evolution of the extinction coefficient for the aggregates with constant fractal dimension $D_f = 2.80$ but various sizes (i.e. different numbers of monomers $n_p = 12 - 1000$ and radiuses of gyration $R_g = 110 - 550\ nm$) and slightly larger radius of single monomers $r_p = 55\ nm$.

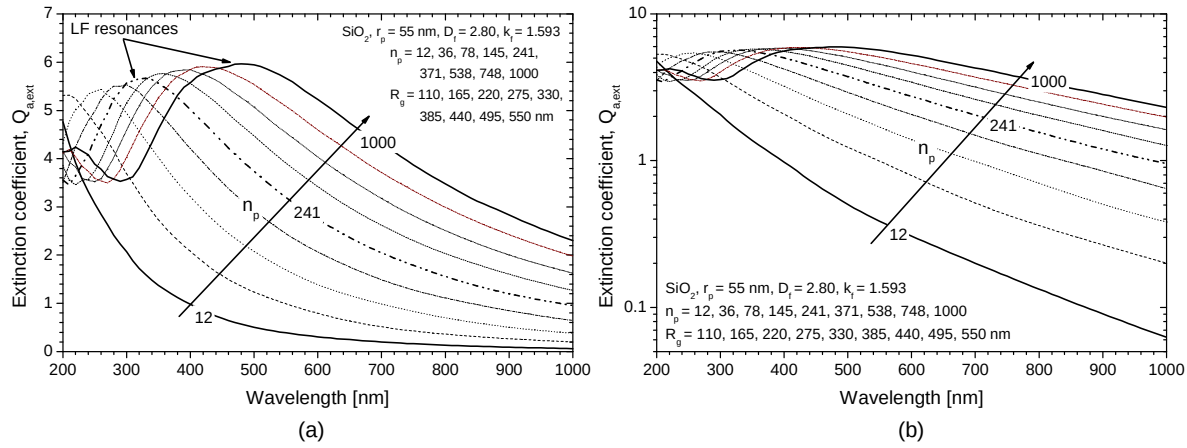

Figure 6.8. Extinction coefficient of aggregates of SiO_2 with various sizes (i.e. numbers of monomers and radiuses of gyration) but constant fractal dimension: (a) linear and (b) linear-logarithmic scale.

In addition to the rapid increases of the extinction coefficients with the number of monomers, the most interesting result shown in Figure 6.7 and Figure 6.8 is that, like for spheres, some low frequency (LF) resonances appear in the extinction diagrams. They can be clearly observed when the size of aggregates is large enough compare to the wavelength and when aggregates are sufficiently dense. Resonances appear in Figure 6.7 when the fractal dimension is higher than $D_f = 2.50$ and for the wavelength $\lambda \sim R_g / 2$. For aggregates with $D_f = 2.80$ the position of the first resonance is significantly related to the total size of the aggregate. It appears when aggregate is about the wavelength $\lambda \sim R_g$.

Figure 6.9 (a) compares the sensitivity of the extinction coefficient to the fractal dimension of the aggregates composed of silicon dioxide monomers with $r_p = 40.5\ nm$ (like in Figure 6.7). Figure 6.9 (b) shows the sensitivity of the extinction coefficient to the total size of the aggregates, for a constant fractal dimension $D_f = 2.80$, $r_p = 55\ nm$ and for various size of the aggregates (like in Figure 6.8).

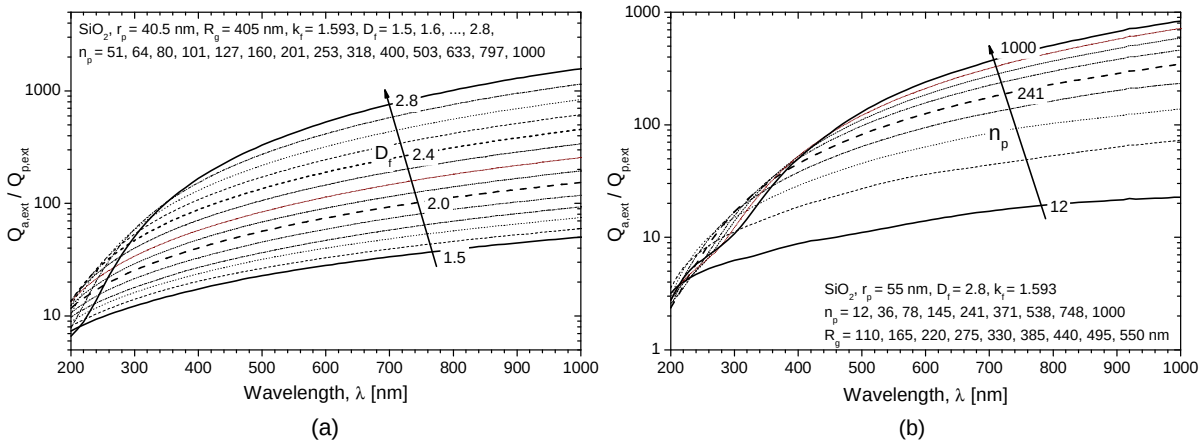

Figure 6.9. (a) Sensitivity of the extinction coefficient to the size of the aggregates composed of silicon dioxide monomers with $r_p = 40.5\ nm$ and (b) sensitivity to the total size of the aggregates for constant fractal dimension of aggregates with $r_p = 55\ nm$.

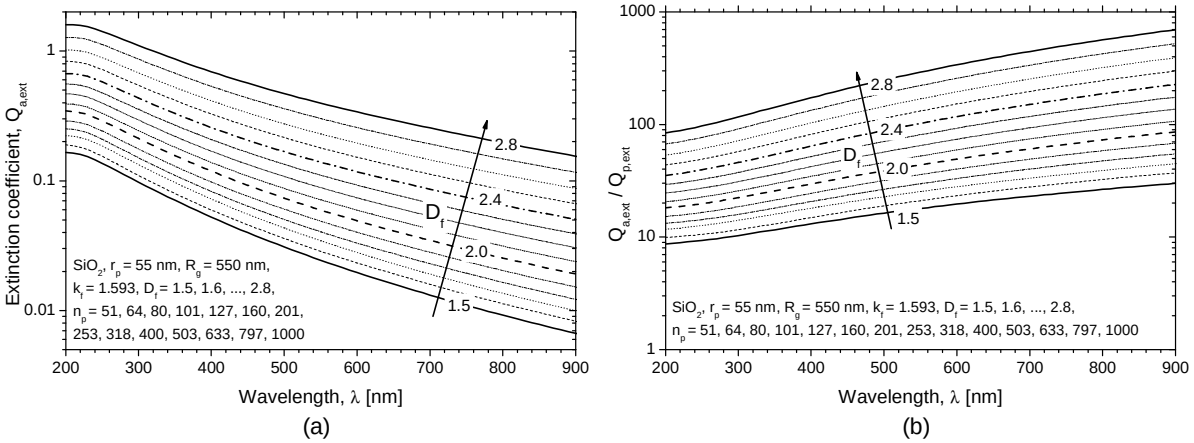

Figure 6.10. Extinction coefficient of aggregates of silicon dioxide in water: (a) evolution of the extinction coefficient versus the wavelength and (b) sensitivity to the fractal dimension.

Figure 6.10 shows results for an aqueous suspension of silicon dioxide aggregates. Figure 6.10 (a) shows the evolution of the extinction coefficient, while Figure 6.10 (b) shows its sensitivity to the fractal dimension. Like previously, in both figures the fractal dimension and the number of monomers increase from 1.5 to 2.8 and from 51 to 1000 respectively, whereas the radius of gyration is kept constant (equal to $R_g = 10 r_p$). Radius of single monomers is equal to $r_p = 55\ nm$. The most interesting conclusion that can be drawn from both subfigures, when they are compared to Figure 6.7, is that we do not observe resonances. Moreover, the maximum of the extinction coefficient is strongly reduced compared to the previous case. Figure 6.11 presents the evolution of the extinction coefficient predicted for aggregates with a 3D hexagonal compact (HC) structure and an increasing number of monomers (i.e. aggregates growing with a constant shape, see Figure 6.12). In this case, the resonances are clearly more intense. For these aggregates the first low frequency oscillation appears when the size of the aggregates is about the wavelength ($R_g \sim \lambda$). Additionally, we can observe high frequency oscillations (in some extent, like for a sphere).

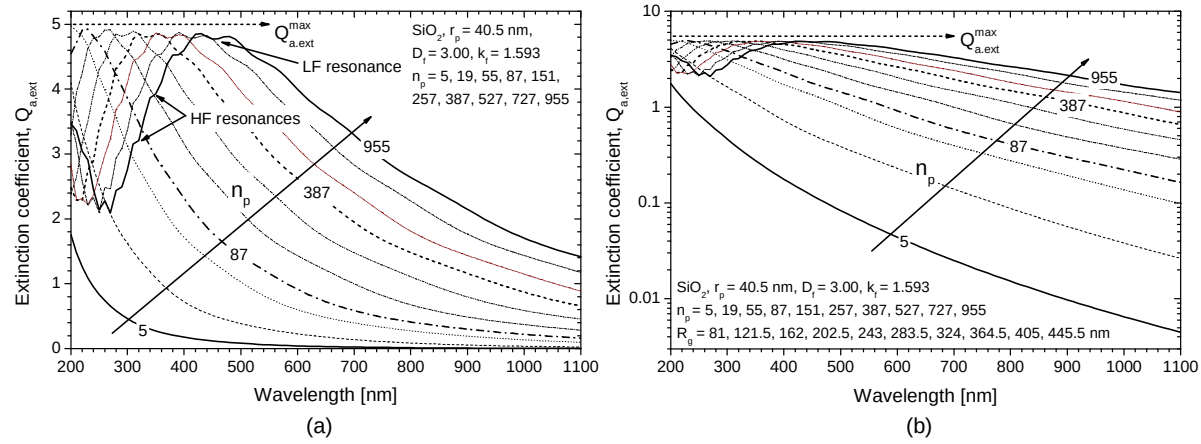

Figure 6.11. Evolution of the extinction coefficient of 3D hexagonal compact aggregates of silicon dioxide monomers versus the wavelength: (a) linear and (b) linear-logarithmic scale.

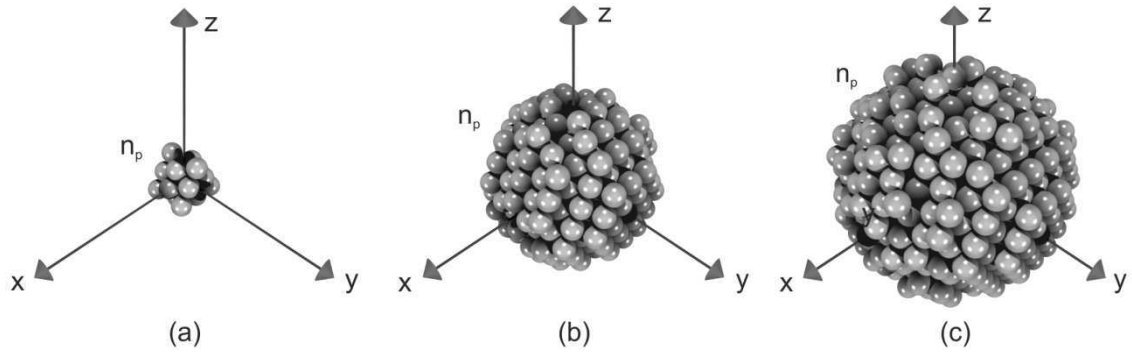

Figure 6.12. 3D hexagonal compact aggregates ($D_f = 3.00$, $k_f = 1.593$) with different numbers of monomers and different external radiuses: (a) $n_p = 19$, $R_e = 3r_p$, (b) $n_p = 387$, $R_e = 8r_p$ and (c) $n_p = 955$, $R_e = 11r_p$.

In contradiction to the previous results, the ones presented in Figure 6.11 were averaged not for 50 different aggregates but for 50 random orientation of the same 3D hexagonal compact aggregate with $n_p = 5$, 19, 55, 87, 151, 257, 387, 527, 727 and 955. Averaging is necessary even for so dense aggregates due to their high internal symmetry. Moreover, the external surface is not smooth, which has strong influence especially for small aggregates.

6.4.1.3. Aggregates of Silicon Carbide

Figure 6.13 shows the evolution of the extinction spectra of diluted aqueous suspension of silicon carbide aggregates (SiC) in water. In both subfigures the fractal dimension and the number of monomers increase from 1.7 to 2.5 and 80 to 503 respectively, whereas the radius of gyration is kept constant (equal to $R_g = 10r_p$). Radius of single monomers is equal to $r_p = 55\,nm$. For wavelengths shorter than $\lambda \simeq 450\,nm$, the spectra exhibit large oscillations. They are caused by a rapid decay of both the real and the imaginary parts of the refractive index of silicon carbide (see Figure 6.4 (c)).

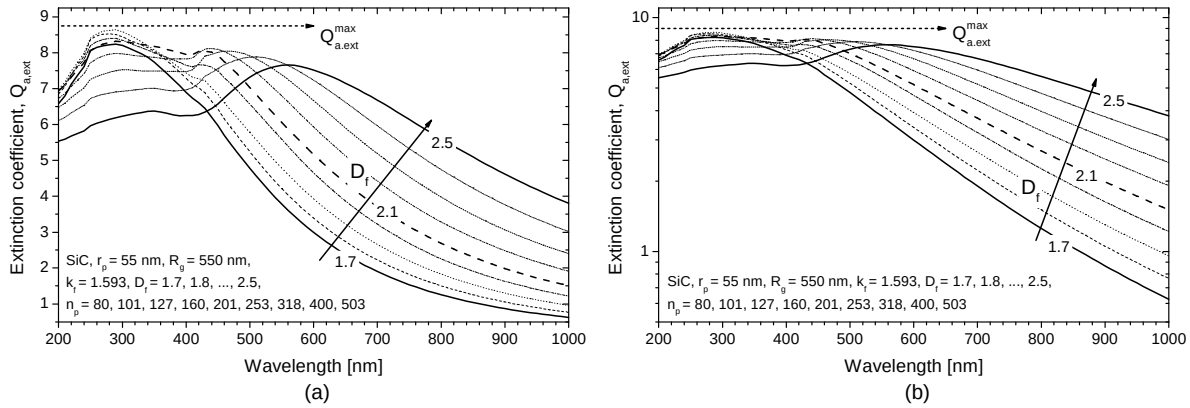

Figure 6.13. Extinction coefficient of aggregates of silicon carbide monomers with various fractal dimensions and numbers of monomers but constant radiuses of gyration: (a) linear and (b) linear-logarithmic scale.

6.4.2. Spectral transmission

With the above calculations, we can predict the transmission spectra of various particle systems at different concentrations. For this purpose we use equation (6.1). We have also assumed that the optical thickness of the particulate media is small enough to limit multiple scattering phenomena, $\tau^{-1} < L$ (Xu 2002). To do so, we used particles concentrations in number in the range $1\times10^{11} - 2\times10^{13}\ m^{-3}$ (depending on the diameter of the monomers and the total size of the aggregates) for a probing length of $L = 1\ m$, which corresponds to the typical length of our experimental setup (see section 6.5.1).

As an example, Figure 6.14 shows simulated transmissions for amorphous silicon aggregates with $r_p = 3.5\ nm$ and (a) various fractal dimensions and numbers of monomers but constant radius of gyration and (b) various sizes but constant fractal dimension. We assumed particles concentration in number $C_n = 2\times10^{13}\ m^{-3}$. Figure 6.15 shows transmission for aggregates of silicon dioxide with various fractal dimensions and numbers of monomers but constant radius of gyration and $C_n = 1\times10^{11}\ m^{-3}$: (a) $r_p = 40.5\ nm$ in air and (b) $r_p = 55\ nm$ in water.

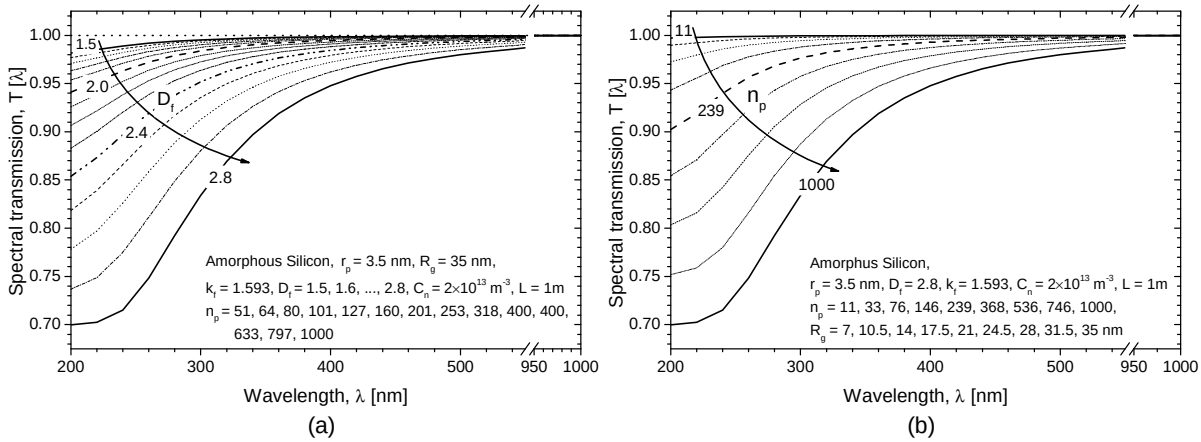

Figure 6.14. Simulated transmissions for amorphous silicon aggregates with (a) various fractal dimensions and numbers of monomers and (b) various sizes with constant fractal dimension.

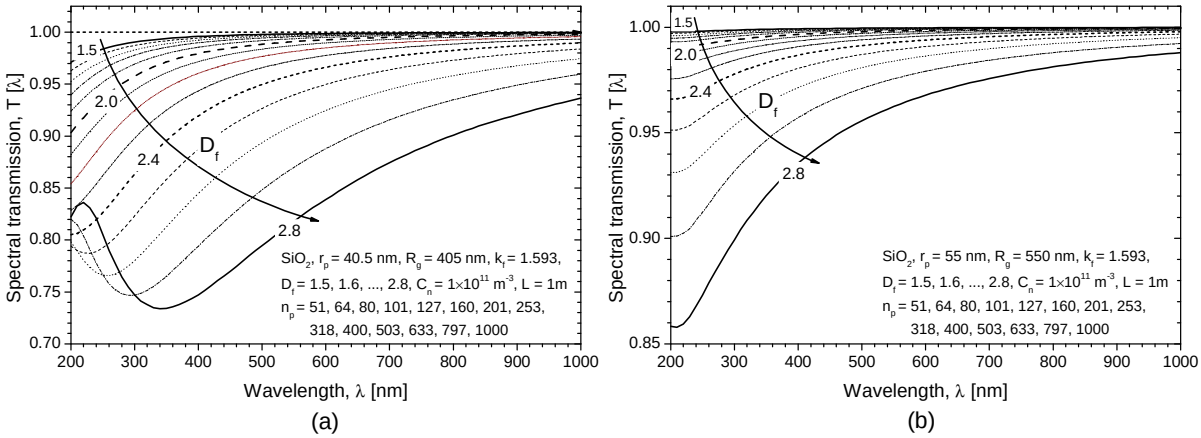

Figure 6.15. Simulated transmissions for silicon dioxide aggregates with various fractal dimensions and numbers of monomers: (a) $r_p = 40.5\ nm$ in air and (b) $r_p = 55\ nm$ in water.

Figure 6.16 shows transmission spectra of silicon dioxide aggregates with various sizes (i.e. different numbers of monomers and radiuses of gyration) but (a) constant fractal dimension $D_f = 2.80$ and (b) compact hexagonal internal structure ($D_f = 3.00$). These spectra exhibit also some oscillations trends.

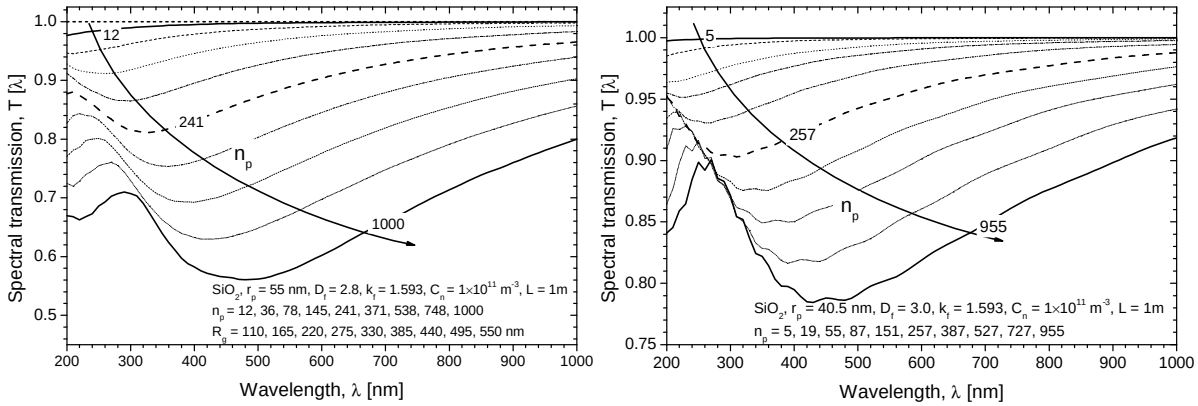

Figure 6.16. Simulated transmissions for silicon dioxide aggregates with various size (i.e. different numbers of monomers and radiuses of gyration) but (a) constant fractal dimension $D_f = 2.80$ and (b) compact hexagonal internal structure.

Figure 6.17 presents transmission spectra of fractal aggregates of silicon dioxide with fractal dimension (a) $D_f = 1.80$ and (b) $D_f = 2.80$ but various particle concentrations in number ranging from 1×10^{10} to 1×10^{11} m^{-3}. The main effect of particle concentration is the scale down or up the transmissions.

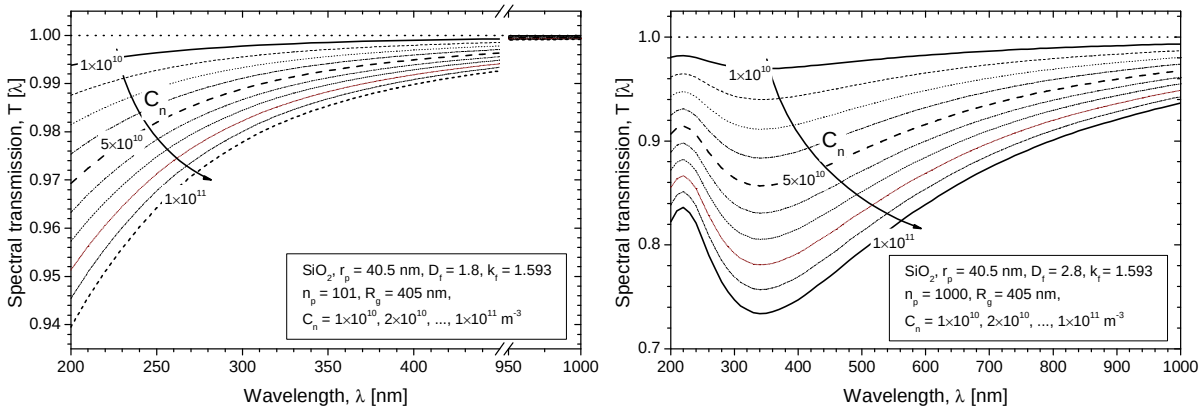

Figure 6.17. Simulated transmissions for various concentrations in number of silicon dioxide aggregates with the same radius of gyration and number of monomers: (a) $D_f = 1.80$ and (b) $D_f = 2.80$.

6.5. Experimental investigations

During this Ph.D. work, we have developed a LES-optical setup that have been tested on different particle systems: aerosols of buckyballs of silica nanobeads with various radiuses of single monomers and eternal diameters, aerosols of tungsten aggregates, as well as silicon aggregates produced by low-pressure discharges (plasma system).

6.5.1. Optical setup

Figure 6.18 shows an overall schematic diagram of the LES-optical setup. The latter is mainly composed of (1) a stabilized Halogen-Deuterium lamp (see also Figure 6.19 (a)), (2) solarized UV-NIR fibers, (3) an on-line intensity attenuator (see also Figure 6.19 (b)), (4) several coupling and positioning optics (see also Figure 6.20), (5) achromatic optics ($50\,mm$ focal length parabolic mirrors) to collimate and collect (6) the probing beam (with diameter $5\,mm$) that passes through (7) silica optical windows, (8) an high quantum efficiency and low noise UV-NIR spectrometer (see also Figure 6.19 (b)) and (9) a computer with acquisition and processing software. The intensity attenuator might be also situated between coupling optics and spectrometer (see Figure 6.22).

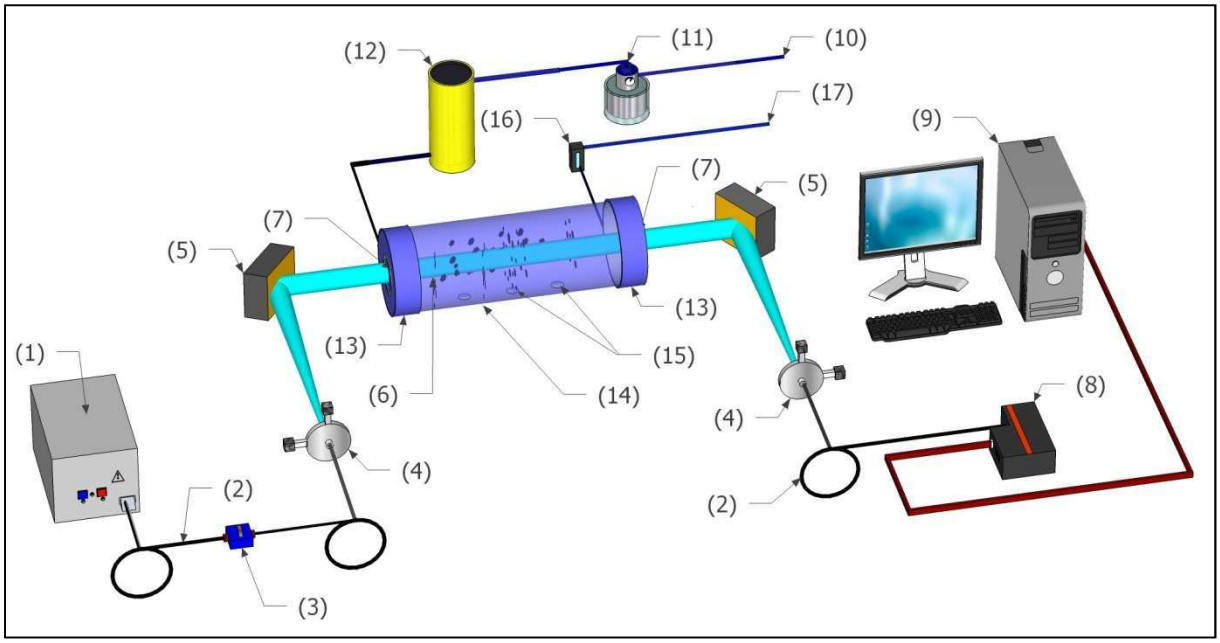

Figure 6.18. Schematic diagram of the experimental setup to generate and analyze aerosol of nanoparticle aggregates: (1) stabilized Halogen-Deuterium lamp, (2) solarized UV-NIR fibers, (3) on-line intensity attenuator, (4) coupling and positioning optics, (5) achromatic optics (50 mm focal length parabolic mirrors) to collimate and collect (6) the probing beam, (7) silica optical windows to close test chamber, (8) UV-NIR spectrometer, (9) computer with acquisition and post-processing software, (10) pressurized air source, (11) atomizer, (12) drier, (13) multiple inlets and outlets, (14) experimental chamber made of Plexiglas, (15) bottom traps to collect TEM/SEM samples, (16) pressure gauges, (17) suck-up air pump.

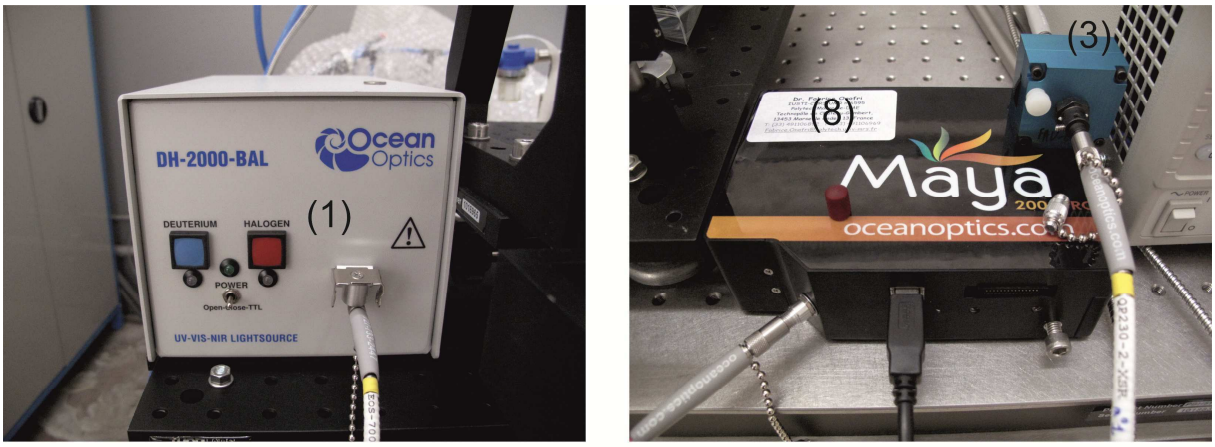

(a) (b)

Figure 6.19. (a) Stabilized Halogen-Deuterium lamp and (b) UV-NIR spectrometer Maya 2000 Pro.

In the LES experimental setup we use a Balanced Deuterium Tungsten Halogen Light Source DH-2000-BAL produced by Ocean Optics (see Figure 6.19 (a)). It provides stable output with spectral range $\lambda = 215 - 2000\ nm$ ($\lambda = 215 - 400\ nm$ on deuterium bulb and $\lambda = 360 - 2000\ nm$ on tungsten halogen bulb). Figure 6.20 presents picture of the optical part of the experimental setup. It consists of (2) solarized UV-NIR fibers (transmission from UV to NIR: $\lambda = 180 - 1150\ nm$), (4) coupling and positioning optics and (5) achromatic mirror that are used to collimate and collect the probing beam. Achromatic mirrors are used rather than lenses to limit chromatic aberrations. For acquisition of the experimental spectra we use a spectrometer Maya 2000 Pro produced by Ocean Optics (see Figure 6.19 (b)). It measures the input signal with a spectral range $175 - 1050\ nm$ and a global half-height optical resolution of $2 - 3\ nm$. Detector with 2068×70 pixels (active 2048×64) and A/D converter provide $16 - bit$ accuracy and integration time between $6.2\ ms$ and $5\ s$.

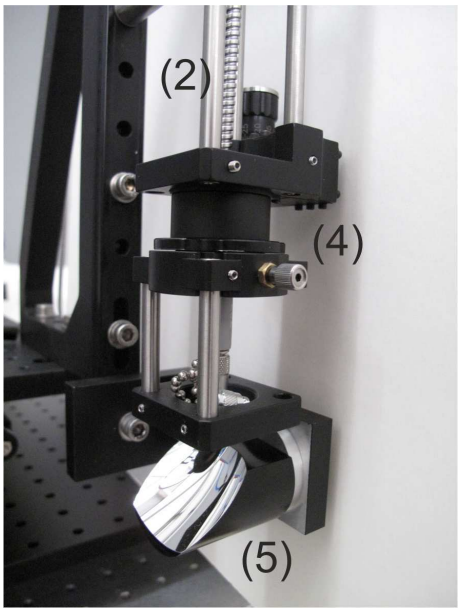

Figure 6.20. Details of the LES emission and collection optics: (2) solarized UV-NIR fibers, (4) coupling and positioning optics, (5) parabolic mirrors.

To control the spectrometer as well as to perform acquisition and data processing, and to prepare look-up tables for data inversion, we developed MS-Windows based software under Delphi-Borland Environment. Figure 6.21 shows a screen copy of the main window of the developed tool. It allows to record single and multiple spectra (finite or infinite loop), remove dark and background noises, record reference and calculate transmission spectra. The software enables also to average results over several spectra and control spectrometer integration time, and to inverse the extinction spectra.

In practice, the experimental transmission is measured as:

$$T(\lambda_i) = \frac{I(\lambda_i) - I_{dark}(\lambda_i) - I_{back}(\lambda_i)}{I_0(\lambda_i) - I_{dark}(\lambda_i) - I_{back}(\lambda_i)}, \tag{6.14}$$

where I_{dark} and I_{back} refer to the dark and background noises of the spectrometer respectively. Similarly as previously, $I(\lambda_i)$ and $I_0(\lambda_i)$ are the probing and the reference spectra in air (without particles in the test chamber) respectively.

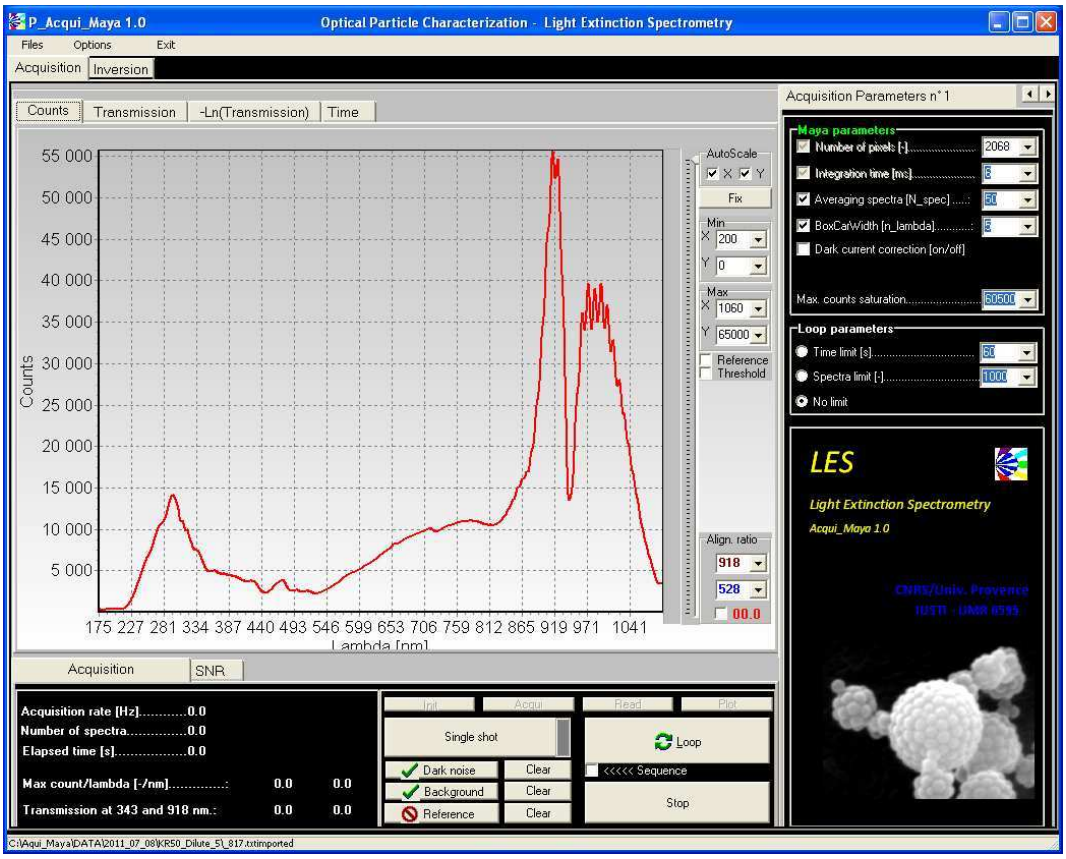

Figure 6.21. “Acqui Maya” – acquisition and preprocessing software.

6.5.2. Aerosol of silicon dioxide buckyballs

6.5.2.1. Setup: fluid loop and colloidal suspensions

Figure 6.22 presents a picture of the entire experimental setup. Aerosol of aggregates of nanoparticles is generated using (10) pressurized air with (11) a Laskin nozzle aerosol generator (ATM220 by TOPAS company, see also Figure 6.23 (a)) using various colloidal silica suspensions. A cloud of nano- and micro droplets containing both water and nanoparticles is obtained at (11) the atomizer output. To fully evaporate water, the cloud is directed to (12) a drier filled with silica gel. The aerosol of dried aggregates is then injected into the test chamber. The latter is made of Plexiglas, and it is mainly composed of a tube

with a circular internal diameter of $90\,mm$ and a length of $L=1000\,mm$. The (13) test chamber is equipped with multiple (14) inlets and outlets with mixing grids to create a homogeneous aerosol across the test chamber. On the bottom side of the test chamber additional (15) traps to collect samples for the reference TEM and SEM measurements. The one used aerosol flow-rate is measured by (16) pressure gauges at the chamber output as it is sucked out with (17) an air pump. Figure 6.23 presents (a) the Laskin nozzle aerosol generator and (b) the drier filled with silica gel.

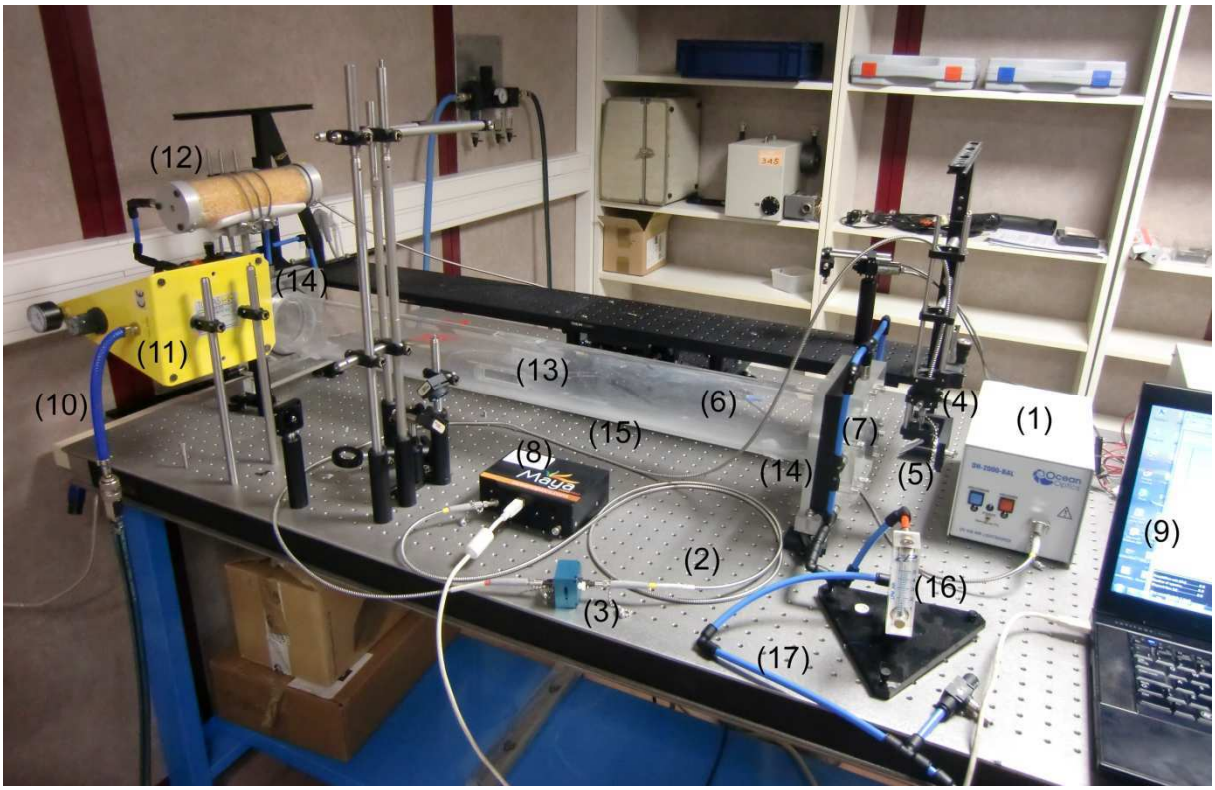

Figure 6.22. Picture of the experimental setup: (1) stabilized Halogen-Deuterium lamp, (2) solarized UV-NIR fibers, (3) on-line intensity attenuator, (4) coupling and positioning optics, (5) achromatic optics to collimate and collect the (6) probing beam, (7) silica optical windows to close test chamber, (8) UV-NIR spectrometer, (9) computer with acquisition and post-processing software, (10) pressurized air source, (11) atomizer, (12) drier, (13) experimental chamber made of Plexiglas equipped with (14) multiple inlets and outlets, (15) bottom traps to collect TEM/SEM samples, (16) pressure gauges, (17) suck-up air pump.

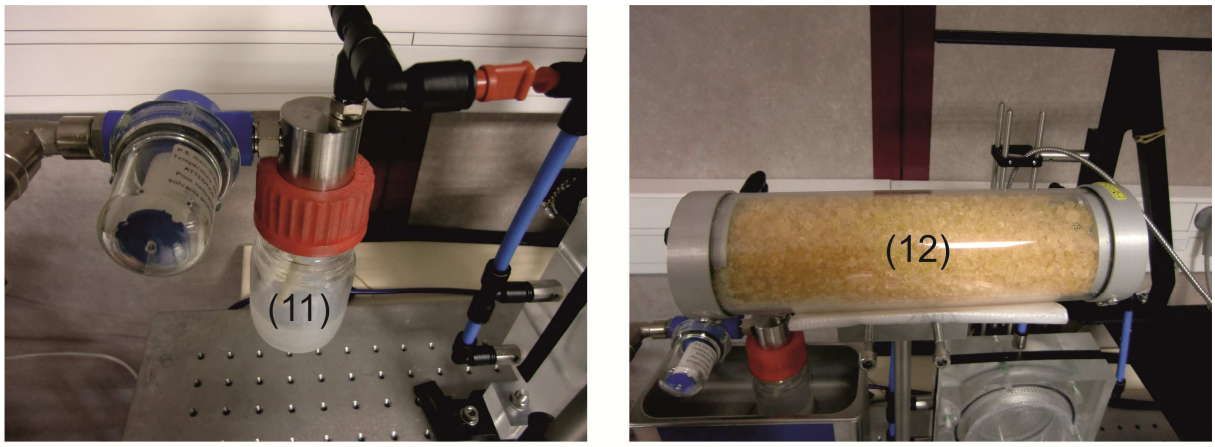

Figure 6.23. (a) Laskin nozzle aerosol generator and (b) drier filled with silica gel.

Figure 6.24 shows typical LES transmissions (i.e. $-\ln(T(\lambda))$, see Eq. (6.4)) measured with the experimental setup. Comparing the reference spectra in air and the probing one it can be seen, that the presence of particles within the test chamber is more clear in the deep UV zone. On the other hand, in this spectral range, LES sensitivity to the particle shape and material is expected to be higher. Therefore, special care must be taken when deep UV is used to reconstruct the PSD (Onofri et al. 2011b).

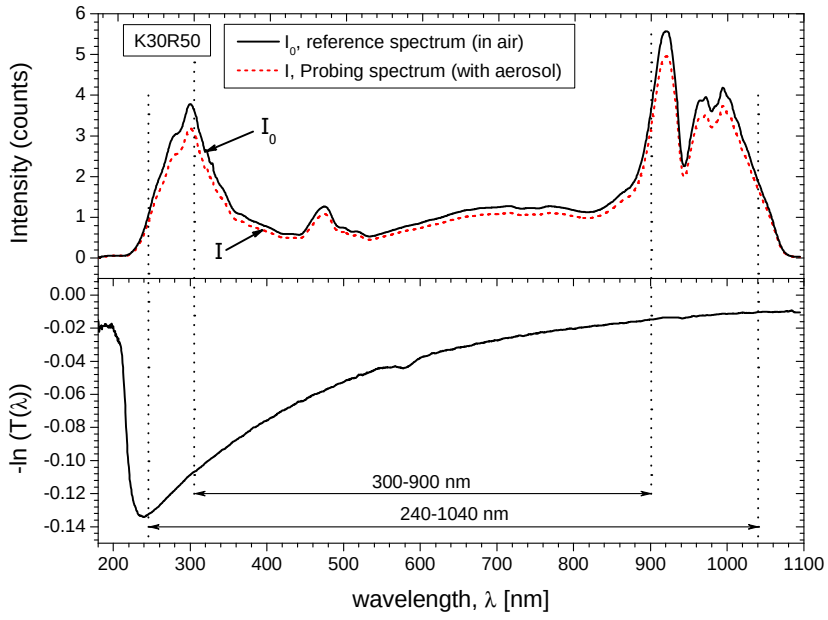

Figure 6.24. LES: Typical spectra and transmission

During experimental studies we considered three different suspensions. They all contain silica nanobeads at 30% in mass, but with a mean diameter centered, according to the manufacturer specifications on (i) 25, (ii) 50 and (iii) 100 *nm*. These suspensions are referenced further on as $K30R12$, $K30R25$ and $K30R50$ respectively. It should be noticed that our TEM and SEM analyze (see section 6.5.2.4) have shown that the mean diameters of the particles is

significantly different from the values given by the manufacturer, so we have found $\bar{d}_p = 31.4 \pm 5.6nm$, $\bar{d}_p = 67.2 \pm 6.6\ nm$ and $\bar{d}_p = 81 \pm 16\ nm$ respectively. In addition, to prepare various aerosols of nanoparticles, we used water dilution of the initial suspensions.

6.5.2.2. Inversion procedure

To inverse experimental spectra we have developed necessary procedures according to Eqs. (6.7) – (6.10) under MATLAB environment. They might be used independently or as an executable file in the "Acqui Maya" software.

To inverse spectra recorder for various aerosols of silica aggregates, the following parameters were used: spherical silicon dioxide particles with dispersion spectra (see also Figure 6.4 (a)) according to the database provided by Sopra S.A. (Sopra.S.A. 2010), particles diameter in the range $1-1000\ nm$ and a probing distance of $L = 1000\ mm$. To calculate extinction matrix we applied a wavelength range spanning from 175 to $1100\ nm$ and discretized in 926 bands. To inverse data we used $20-40$ size classes for the size boundaries $1-1200\ nm$. The Lagrangian parameter was set constant with $\gamma = 10^{-8}$. It should be noticed here that the number of size classes was reduced to prevent the instability of the inversion procedure. The latter drastically increases when the spectral bandwidth of the incident beam is not significantly larger that the PSD width (indeed, it is the case with the aerosols generated here). LES inversion is rather unstable for widely polydisperse PSD.

6.5.2.3. Sampling procedure and electron microscopy analyses

As a reference for the LES analysis, the aggregates produced in the test chamber are analyzed with Transmission Electron and Scanning Electron Microscopes (TEM and SEM). For this purpose, aggregates samples are collected on carbon tips after a sedimentation process (several hours). Usually, for images of single particles it is possible to proceed them automatically with a blob analysis (classical 2D image processing and measuring tools). However, for silica aggregates the aforementioned processing methods were not suitable, so we were obliged to process the images "manually". It is also important to keep in mind that with SEM analyses the statistics are always poor (no more than several dozen up to few hundred of aggregates were analyzed for each case) and it is impossible to ensure that we are analyzing exactly the same aggregates, in shape and number, than the ones that are present in the test chamber when the aerosol is flowing in.

6.5.2.4. Experimental results

Suspension of K30R50

During the experiment we used various input pressures (1, 2 and $3\ bar$) and a fixed pressure of the output (sucking out the air from the test chamber) equal to $200\ mbar$. Typical spectra

for different pressures of the aerosol $K30R50$ pure silica suspension (without any previous dilution) are shown in Figure 6.25 (a). Figure 6.25 (b) presents aerosol transmissions versus time for three selected wavelengths ($\lambda = 300,\ 600$ and $800\ nm$) when the pump pressure was gradually increasing.

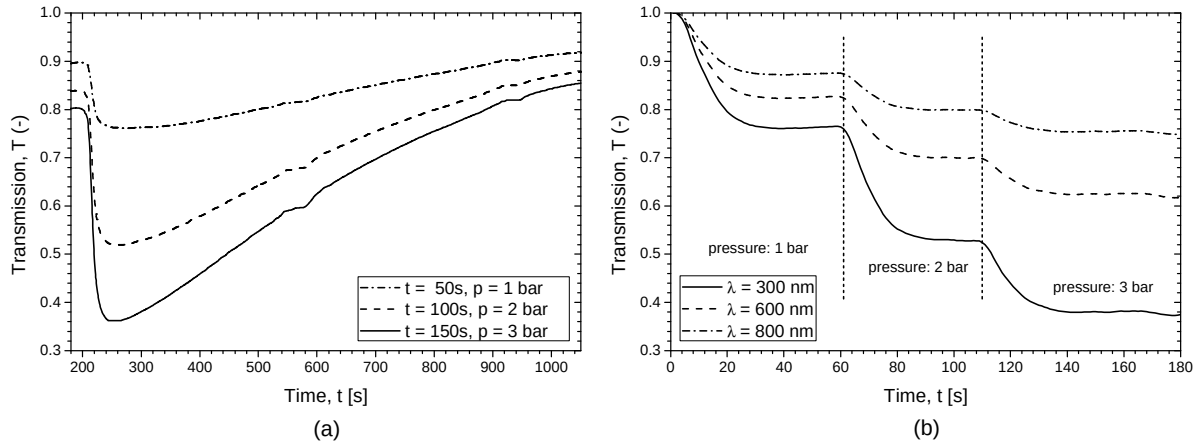

Figure 6.25. Typical spectra measured for aerosol of $K30R50$ with a dilution $1:5$ (a) raw spectra for various pressures of atomizer and (b) transmissions for three selected wavelengths.

It should be noticed that for an input pressure of only $3\ bar$ the transmission is very small, just little larger than $T(\lambda_i) = e^{-1}$ for $\lambda \simeq 250\ nm$. Transmissions higher than the given value clearly indicates that the optical thickness of the particulate media is weak enough to satisfy the multiple scattering criteria $\tau^{-1} < L$ (Xu 2002).

As previously introduced, during the experiment we collected samples for the SEM and TEM reference analysis. In the present case sedimentation time was equal to 3 hours and 30 minutes. We analyzed collected images manually by measuring the diameter of 229 different TEM and SEM images of aggregates (Barbosa et al. 2011). Figure 6.26 and Figure 6.27 show respectively some SEM and TEM images of the collected aggregates.

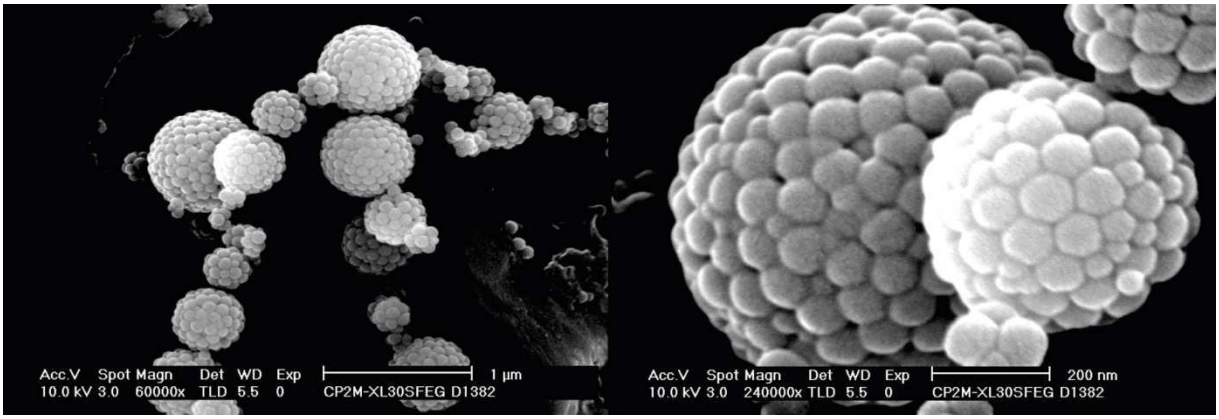

Figure 6.26. Example SEM images of aggregates of $K30R50$.

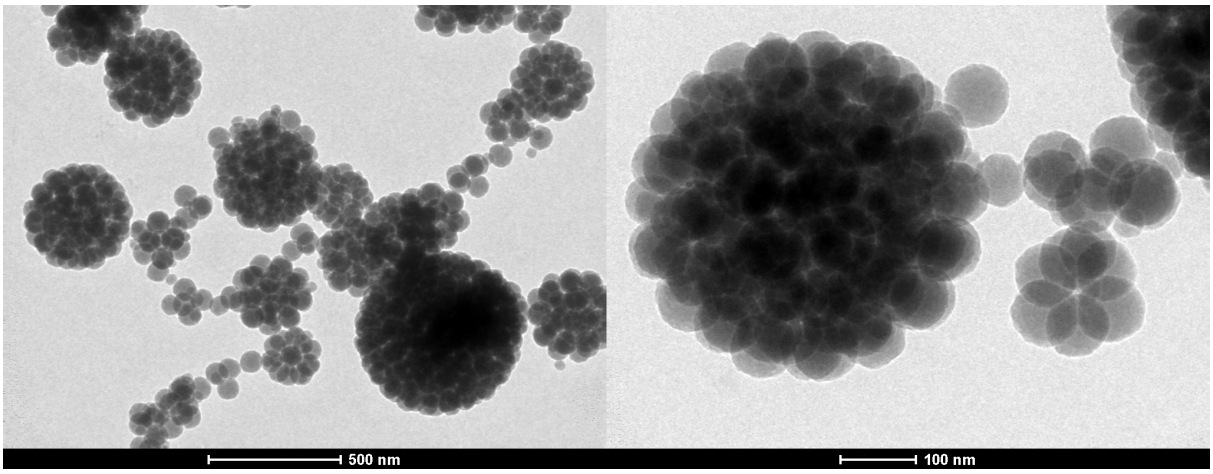

Figure 6.27. Example TEM images of aggregates of $K30R50$.

Figure 6.28 and Figure 6.29 illustrate the different steps used to inverse experimental LES spectra. Figure 6.28 (a) presents a typical LES spectrum measured for the aerosol of $K30R50$ suspension and an input pressure of $3\ bar$. Figure 6.28 (b) shows the wavelengths selected to inverse the spectrum. It can be seen that the raw spectrum and the reconstructed one match almost perfectly (i.e. the residual norm is lower than 3×10^{-7}). Figure 6.29 presents the "raw" extinction matrix $\mathbf{S}$ and (b) the filtered extinction matrix $\left(\mathbf{S}^{\mathrm{T}}\mathbf{S}+\gamma\mathbf{H}\right)\mathbf{V}$.

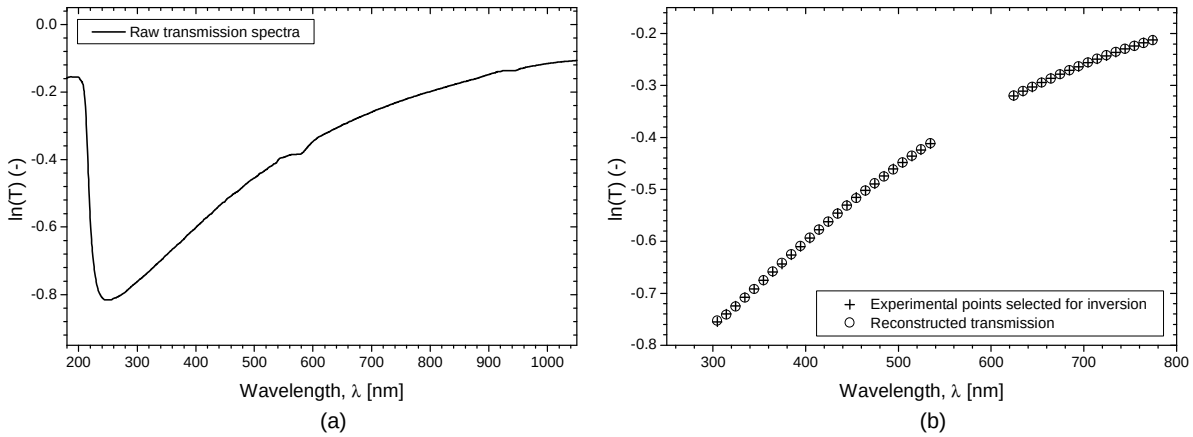

Figure 6.28. Experimental spectrum measured for an aerosol $K30R50$: (a) raw spectrum and (b) wavelengths selected for the inversion procedure.

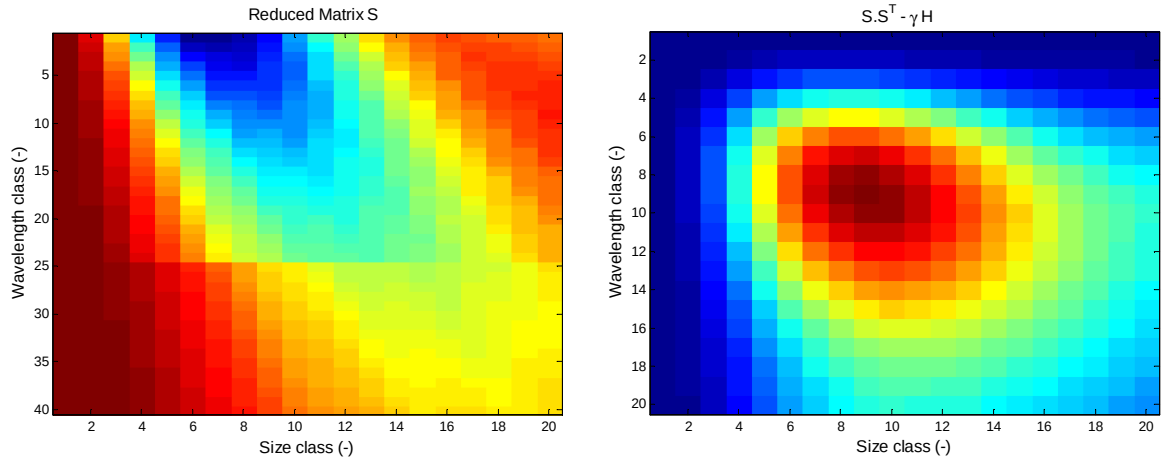

Figure 6.29. (a) The "raw" extinction matrix $\mathbf{S}$ corresponding to the wavelengths selected to inverse experimental spectra and the related (b) filtered extinction matrix $\left(\mathbf{S}^{\mathbf{T}}\mathbf{S} + \boldsymbol{\gamma}\mathbf{H}\right)\mathbf{V}$.

Figure 6.30 compares the PSD in volume and number estimated by TEM off-line analyses with on-line and real-time LES. The PSD measured with the LES system, in volume, is also converted in a particle distribution number (assuming a spherical particle model). For the PSD measured with TEM analyses, in particle number, a reverse procedure was applied. In Figure 6.30 we depicted also the mean and median values as well as the corresponding standard deviations.

Table 6.1 compares statistics of TEM and LES measurements for various experimental conditions. Note that with TEM analysis it is impossible to estimate the particle concentration neither in number, nor in volume.

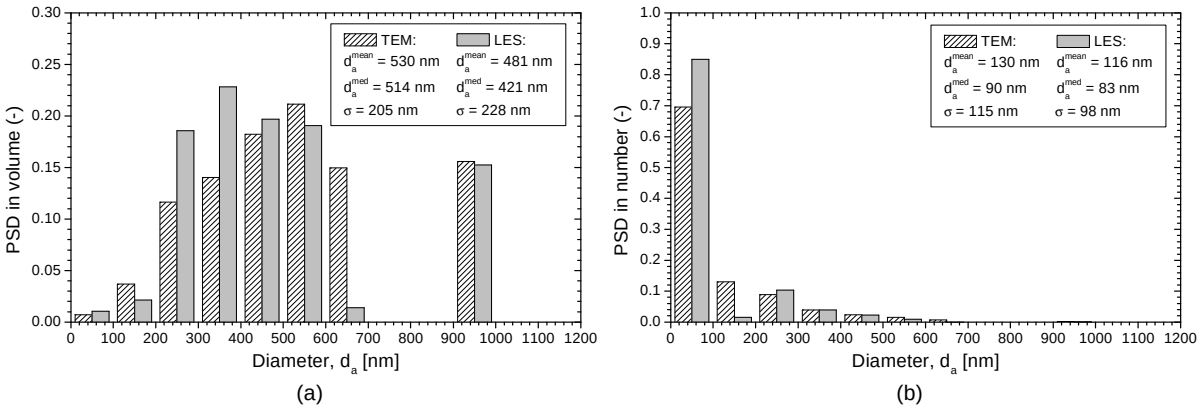

Figure 6.30. Comparison between TEM and LES analysis of the aerosol of $K30R50$ without initial dilution: (a) PSD in volume and (b) PSD in number.

Table 6.1. Comparison of TEM and LES statistics for the aerosol of $K30R50$ without initial dilution.

Pressure	Volume				Number			
	d_a^{mean} $[nm]$	d_a^{med} $[nm]$	σ_a $[nm]$	C_v $[m^3/m^3]$	d_a^{mean} $[nm]$	d_a^{med} $[nm]$	σ_a $[nm]$	C_n $[part/m^3]$
1 *bar*	644	520	249	1.5×10^{-6}	370	283	170	3.2×10^{13}
2 *bar*	544	503	245	2.9×10^{-6}	293	249	130	1.2×10^{14}
3 *bar*	481	421	228	3.1×10^{-6}	116	83	98	3.5×10^{15}
TEM (3*bar*)	438	466	216	---	130	90	115	---

The most interesting result shown in Table 6.1 is that for an increasing pressure in the test chamber the mean diameter of the aggregates decreases. It concerns both results in volume and number. Although the increasing particle concentrations are rather obvious consequences of the increasing pressure in the test chamber, the estimated values clearly proof the capabilities of the developed method.

Suspension of K30R50 with dilution 1:5

Figure 6.31 shows a few TEM images of obtained for the $K30R50$ suspension. These aggregates were produced by atomizing $5\,ml$ of the $K30R50$ silica suspension diluted with $25\,ml$ of water. Samples for the TEM analysis were collected after 3 hours of sedimentation. 133 aggregates have been analyzed (Barbosa et al. 2011).

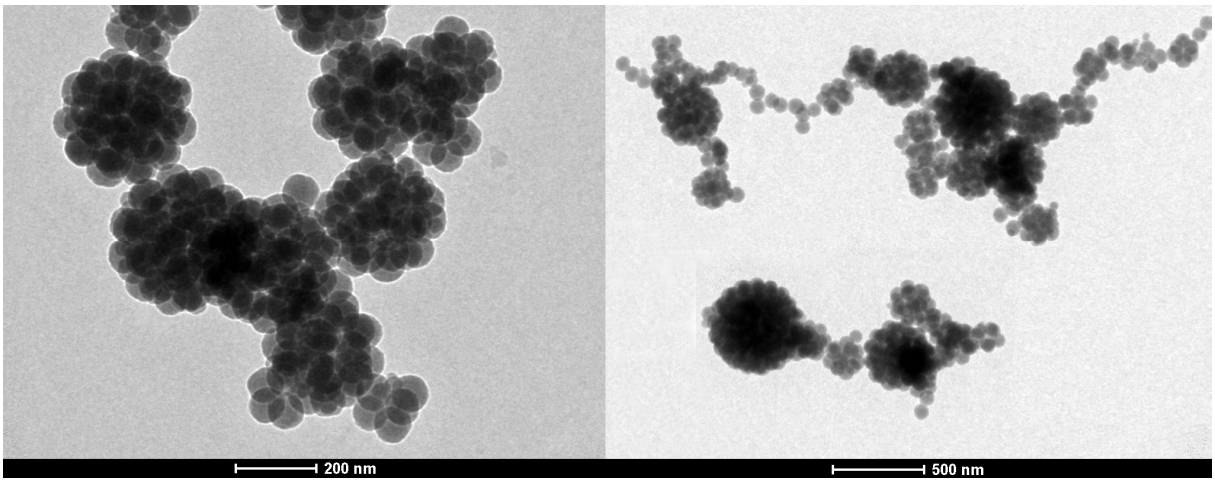

Figure 6.31. TEM images of aggregates of $K30R50$ (dilution $1:5$).

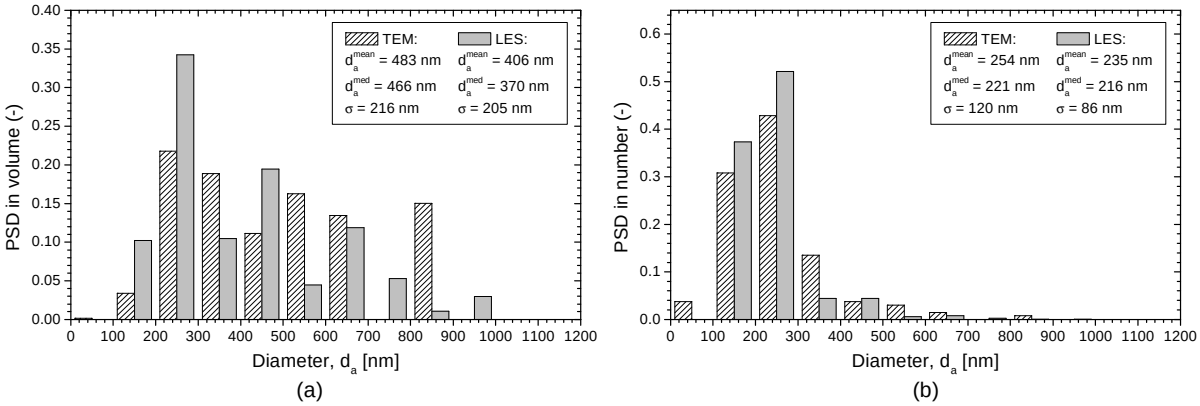

Figure 6.32. Comparison between TEM and LES analysis of the aerosol of $K30R50$ – dilution $1{:}5$: (a) PSD in volume and (b) PSD in number.

Figure 6.32 compares results of the off-line TEM analysis with the LES results for a pressure of $2\ bars$: (a) PSD in volume and (b) PSD in number. The mean and median values as well as the corresponding standard deviations are reported. Table 6.2 compares TEM and LES statistics for various experimental conditions. Here also, we note that an increasing pressure produces smaller aggregates at a higher concentration.

Table 6.2. Comparison of TEM and LES statistics for the aerosol of $K30R50$ with dilution $1{:}5$.

Pressure	Volume				Number			
	d_a^{mean} $[nm]$	d_a^{med} $[nm]$	σ_a $[nm]$	C_v $[m^3/m^3]$	d_a^{mean} $[nm]$	d_a^{med} $[nm]$	σ_a $[nm]$	C_n $[part/m^3]$
1 *bar*	479	465	247	3.3×10^{-7}	267	242	96	2.1×10^{13}
2 *bar*	406	370	205	7.8×10^{-7}	235	216	86	7.4×10^{13}
3 *bar*	379	307	192	1.0×10^{-6}	247	233	78	9.4×10^{13}
TEM (3 *bar*)	438	466	216	---	254	221	120	---

Suspension of K30R50 with dilution 1:20

Figure 6.33 shows some TEM images of the $K30R50$ aggregates obtained after a dilution of $1{:}20$ and 15 hours of sedimentation. We analyzed 46 different aggregates (Barbosa et al. 2011).

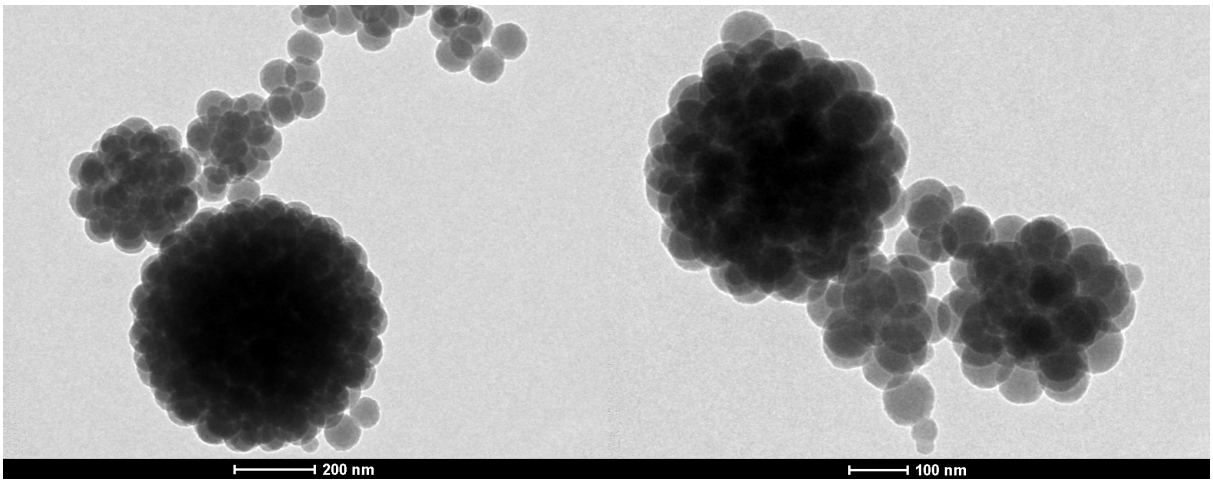

Figure 6.33. TEM images of aggregates of $K30R50$ (dilution $1:20$).

Figure 6.33 compares results of the off-line TEM analysis with LES inversion procedure for the atomizer pressure $3\,bar$. It shows histograms of the (a) PSD in volume and (b) PSD in number for both measurement methods. The related statistics are shown in Table 6.3.

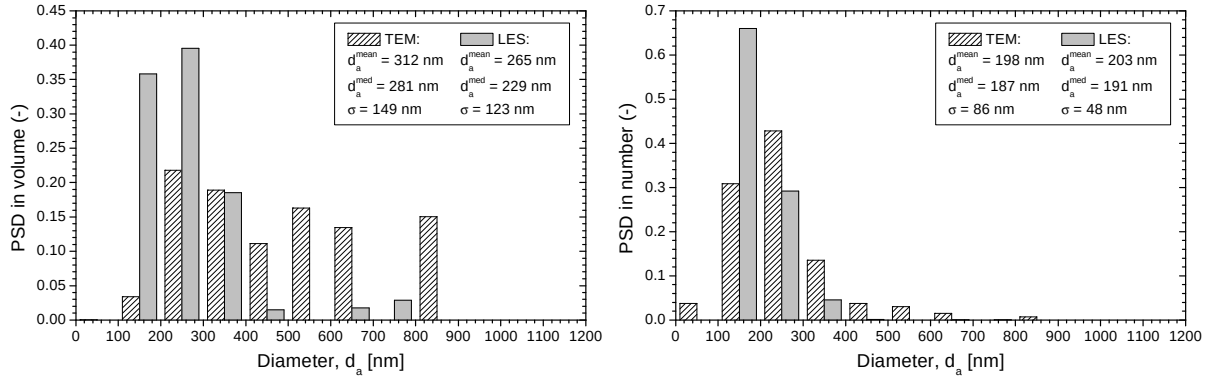

Figure 6.34. Comparison between TEM and LES analysis of the aerosol of $K30R50$ after a dilution $1:20$: (a) PSD in volume and (b) PSD in number.

Table 6.3. Comparison of TEM and LES statistics for the aerosol of $K30R50$ with dilution $1:20$.

Pressure	Volume				Number			
	d_a^{mean} $[nm]$	d_a^{med} $[nm]$	σ_a $[nm]$	C_v $[m^3/m^3]$	d_a^{mean} $[nm]$	d_a^{med} $[nm]$	σ_a $[nm]$	C_n $[part/m^3]$
1 *bar*	276	213	122	5.7×10^{-8}	194	181	53	1.2×10^{13}
2 *bar*	235	223	128	1.5×10^{-7}	145	131	48	6.7×10^{13}
3 *bar*	265	229	123	1.9×10^{-7}	203	191	48	6.1×10^{13}
TEM (3 *bar*)	312	281	149	---	198	187	86	---

Suspension of K30R25

Figure 6.35 and Figure 6.36 show SEM and TEM images of the $K30R25$ aggregates (no dilution). For TEM analysis, 168 different aggregates were investigated for a sedimentation time of 3 hours (Barbosa et al. 2011). Figure 6.37 compares the PSD (a) in volume and (b) in number at 2 *bars*. The statistics are shown in Table 6.4.

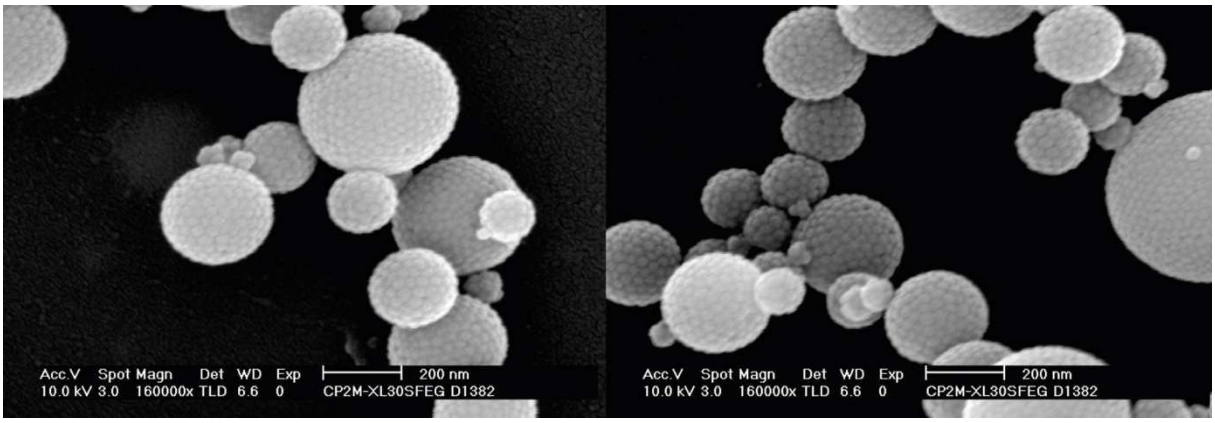

Figure 6.35. SEM images of aggregates of $K30R25$ (no dilution).

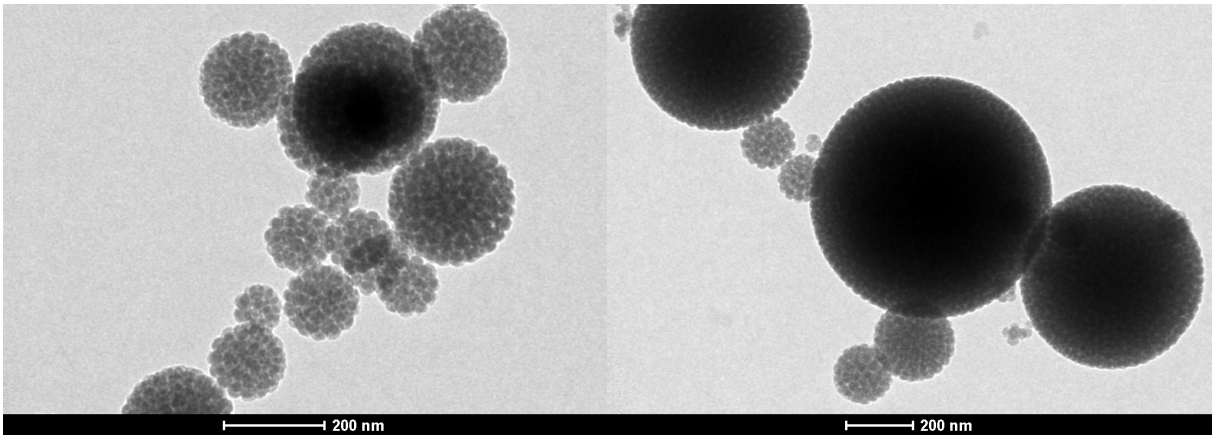

Figure 6.36. TEM images of aggregates of $K30R25$ (no dilution).

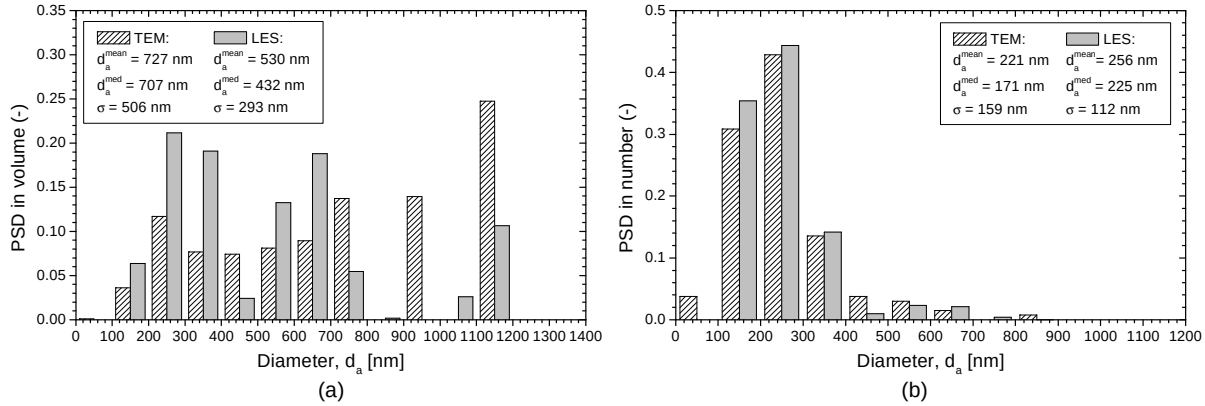

Figure 6.37. Comparison between TEM and LES analyses of the aerosol of $K30R25$ (no dilution): (a) PSD in volume and (b) PSD in number.

Table 6.4. Comparison of SEM and LES statistics for the aerosol of $K30R25$ without dilution.

Pressure	Volume				Number			
	d_a^{mean} $[nm]$	d_a^{med} $[nm]$	σ_a $[nm]$	C_v $[m^3/m^3]$	d_a^{mean} $[nm]$	d_a^{med} $[nm]$	σ_a $[nm]$	C_n $[part/m^3]$
1 *bar*	479	465	247	2.3×10^{-6}	224	190	104	1.9×10^{14}
2 *bar*	530	432	293	3.2×10^{-6}	256	225	112	2.0×10^{14}
3 *bar*	447	486	238	3.8×10^{-6}	218	193	91	3.9×10^{14}
TEM (3 *bar*)	727	707	506	---	221	171	159	---

Comparing results presented in Table 6.1 - Table 6.4, one can notice that, for a few experiments there exist some discrepancies between TEM/SEM and LES analyses. But, it would be an error to consider TEM/SEM results as the true ones, since they are necessarily biased by the sampling procedure and their accuracy is strongly limited by the limited size of the samples analyzed. The collection of samples by a sedimentation process is probably not the more appropriate procedure and we even came recently to the conclusion that a sedimentation time of 3 hours is not enough (even if we have developed a correction method, based on the Stokes sedimentation regime, to correct this problem (Toure 2010)). Nevertheless, it is also clear is that the aggregates generated with the non-diluted suspensions are pretty large, and probably very close to the limit that can be managed with the LES system operating only in the UV-NIR range. The previous results show also that the LES technique, with the appropriate model and inversion procedures, can be already used to perform time resolved and non-invasive investigations, concentration measurements and parametric studies that are definitely not possible with SEM/TEM analyses (very time consuming or basically impossible).

6.5.3. Aerosol of tungsten aggregates

The goal of the study presented in this section was to bring some insights about the capabilities of the LES technique to characterize, in fusion devices and more particularly for ITER, tungsten aggregates at the vicinity of plasma-facing components (PFC, i.e. tiles) or realized by laser cleaning methods. This section gives only a very short overview of the results obtained. More details can be found in the published work (Onofri et al. 2012b).

6.5.3.1. Setup: fluid loop and powders

We basically use the same setup than for silicon dioxide buckyballs, the main difference was that we use water-ethanol suspensions of spherical tungsten nanoparticles (supplied by SkySpring Nanomaterials, Inc.). One additional difference is that a metallic plate was

introduced in the test chamber to test the wall proximity on LES probing beam and thus, on its capabilities to size particles at the vicinity of plasma facing materials (PFC). In the same way, to test the influence of shock waves and the broadband emission induced by laser cleaning method, we use a pulsed ($5\ ns$, $25\ Hz$) and frequency doubled high-energy Nd:YAG laser ($110\ mJ$, $\lambda = 532\ nm$) to generate plasma plumes (i.e. laser induced breakdown of air) within the test chamber (Onofri et al. 2011a; Onofri et al. 2012b).

6.5.3.2. Inversion procedure

The inversion procedure was similar to the one described for silicon dioxide buckyballs, except that we use the fractal equation to describe the morphology of the tungsten aggregates. The fractal dimension of the letters was estimated to $D_f = 2.7$, with a log-normal distribution for the number-weighted PSD for both, the primary particles ($d_p = 31 \pm 41\ nm$) and aggregates ($d_a = 45 \pm 37\ nm$).

Figure 6.38 shows three synthetic TEM images over the 30 000 numerical aggregates with morphological properties (fractal dimension and PSDs) similar to the experimental ones. This figure shows also the relation between the radius of gyration of these aggregates and their external radius (i.e. geometrical radius). This database of numerical aggregates was also used to calculate their light extinction matrix **S** (i.e. 30 size classes and 30 wavelength bands) averaged over 300 orientations. For the refractive index of tungsten, we use the data base provided by the Ioffe Institute (Ioffe.Institute 2012).

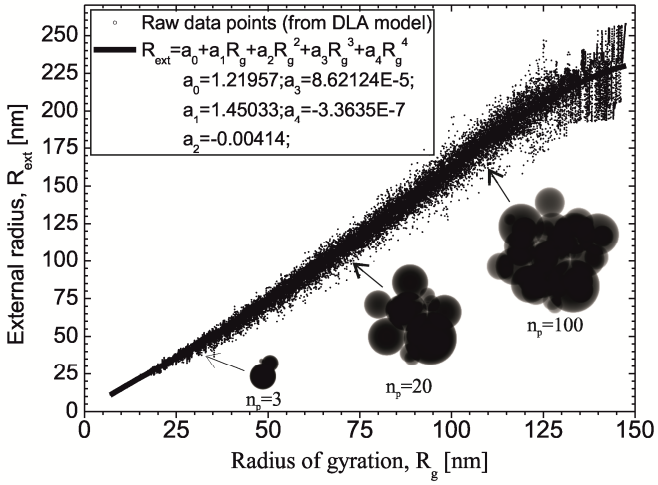

Figure 6.38. Numerical aggregates (simulated TEM images) with morphological parameters similar to the experimental tungsten aggregates, and relation between two of their characteristic radiuses.

6.5.3.3. Example results

Figure 6.39 shows a comparison of the PSDs of tungsten aggregates, measured with the LES and SEM techniques. The results are in a pretty good agreement (see the discussion on bias

induced by our electron microcopy sampling procedure). In this study we have also shown that LES measurements are not significantly affected by the proximity of a wall, as well as the broadband emission, the shock wave and gas expansion induced by a plasma plume (Onofri et al. 2012b).

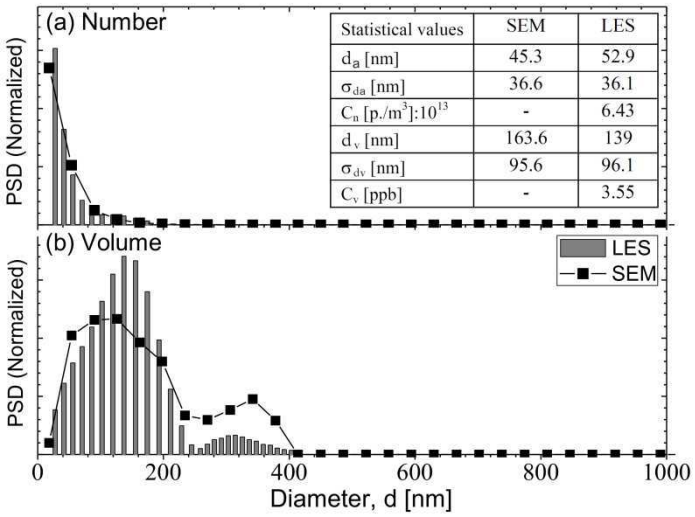

Figure 6.39. Comparison of LES and SEM results for the PSDs of an aerosol of tungsten aggregates with fractal dimension equal to $D_f = 2.7$.

6.5.4. Low-pressure discharge (dusty plasma)

6.5.4.1. Background of the study

This study was performed in the framework of the project "CARMINA" between four laboratories and institutes, supported by the French National Research Agency (ANR). The results presented in this section were obtained in cooperation with Prof. Laifa Boufendi and his research group (GREMI UMR n°6606 CNRS, Université d'Orléans). They deal with the one-line, and time-resolved, characterization of the growing rate of nanoparticles and aggregates in a dusty plasma (low pressure Argon-Silane discharge) (Boufendi and Bouchoule 1994).

Reactive plasmas lead to the formation of nanoparticles that tend to grow and aggregate, by complex series of chemical and physical reactions (e.g. (Berndt et al. 2009)). Depending on the physical conditions and reactive gas being used, the shape and the size of these aggregates may differ significantly (e.g. (Schweigert et al. 1995; Ozaki et al. 1999; Fortov et al. 2005)). In this study we have investigated the formation of cauliflower-like aggregates of typically $5-100\ nm$ produced by gas mixtures of Argon and Silane (SiH_4, i.e. reactive gas) at different pressures, temperatures and for different electrical powers.

As an example, Figure 6.40 shows a transmission electron microscopy image of aggregates produced in a Argon-Silane low-pressure after 20s. Note that, according to Orleans' group, in

the plasma reactor the aggregates (the small aggregates with a cauliflower-shape) are not agglomerated like their appear to be on TEM image. They agglomerate during deposition due to some residual charges and latter on, Coulomb's attractive forces.

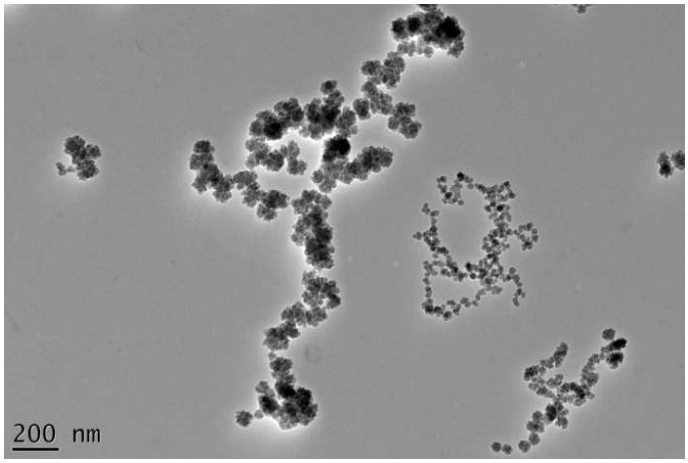

Figure 6.40. TEM of the aggregates produced by a low-pressure Argon-Silane discharge after 20s. Note that in the plasma, the aggregates (with a cauliflower-shape) are not agglomerated like in this image.

Scientifically, the starting point of this work is the results obtained by the group in Orleans in 1994, from the off-line analysis of TEM samples collected from the low-pressure discharge (Boufendi and Bouchoule 1994). This pioneer work, which was one of the first to report the dust formation phenomena, is referred below as "TEM-1994" results, whereas their common analyses of TEM samples are referred as "TEM-2011" results.

6.5.4.2. Setup: plasma reactor and optical setup

The reactor used in this experiment produce a capacitive discharge generated by a radiofrequency generator. It was designed for the study of silicon dust particle formation in low pressure cold plasmas. The pressure can range from 10 to 100 Pa and the electrical power can vary from 10 to 50 W. At low power, it is possible to slow down the particle formation in order to follow in real time their growth and to study the transition from one growth phase to another.

To perform measurements we rebuild the initial LES experimental setup. The main improvements consist of mechanical changes, particularly we added a special frame, optical choppers and adjusting system to ensure optical access to plasma reactor (see Figure 6.41 and Figure 6.42). The optical part of the system was not modified. Figure 6.42 shows a picture of the LES setup during measurements of the Low-pressure discharge.

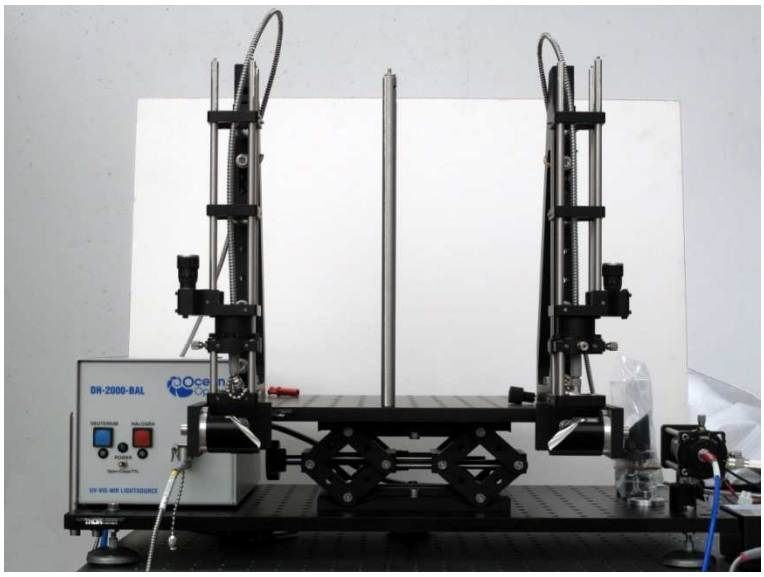

Figure 6.41. Picture of the experimental setup adapted to the LES analysis of the low-pressure discharge (plasma system).

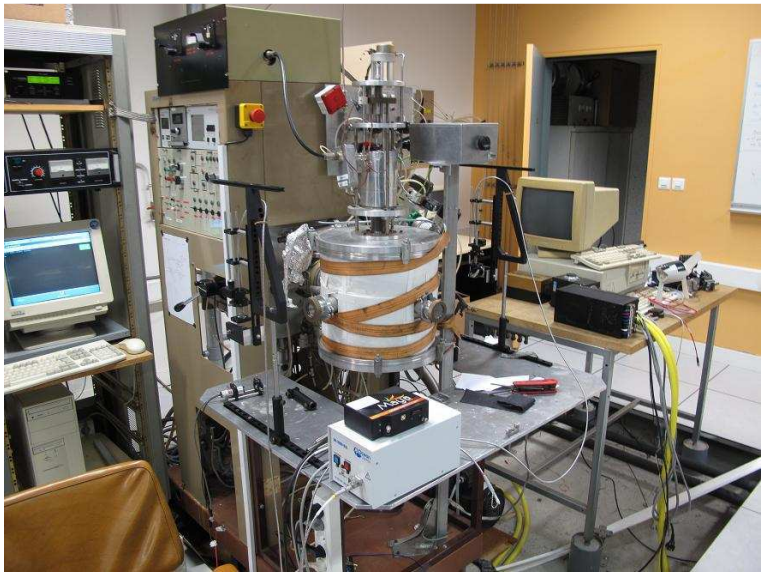

Figure 6.42. LES measurements in a Low-pressure discharge (plasma reactor in GREMI UMR n°6606 CNRS, Université d'Orléans).

6.5.4.3. Experimental results

As an example, Figure 6.43 (a) presents typical LES transmission spectra measured in a low-pressure Argon-Silane discharge. ΔT refers to the starting time of the plasma discharge. To inverse these data, the following parameters were used: spherical amorphous silicon particles with diameter in the range $1-1000\,nm$ and a probing distance of $L=130\,mm$. To calculate extinction matrix we choose refractive index (dispersion spectra) of amorphous silicon according to the database provided by Sopra S.A. (Sopra.S.A. 2010).

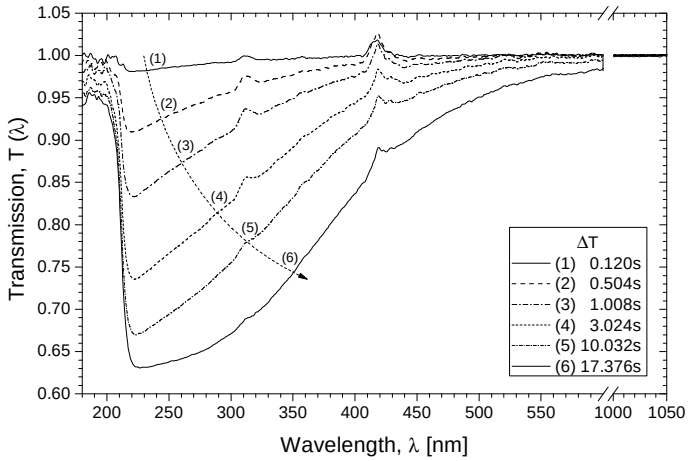

Figure 6.43. Light Extinction Spectrometry of low-pressure Argon-Silane discharge: transmissions for different operating times.

Figure 6.44 and Figure 6.45 illustrate the different steps used in the inversion procedure of the experimental data. Figure 6.44 shows (a) a spectrum obtained for $\Delta T = 3.024\,s$, as well as the wavelengths selected for the inversion procedure; while (b) shows the corresponding reconstructed PSD. Figure 6.45 (a) illustrates the "raw" extinction matrix $\mathbf{S}$ as well as the reduced (i.e. selected points) and (b) the filtered extinction matrix $\left(\mathbf{S}^{\mathrm{T}}\mathbf{S} + \gamma\mathbf{H}\right)\mathbf{V}$.

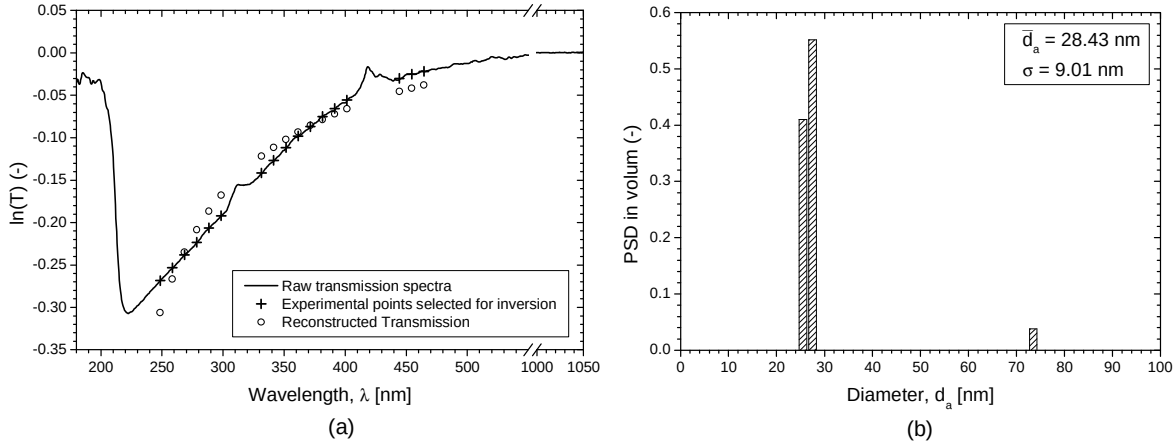

Figure 6.44. Example (a) experimental and reconstructed spectra measured in Argon-Silane low pressure discharge and (b) the corresponding reconstructed PSD.

Important issue encountered during the inversion procedure is that exact value of the refractive index of the aggregating monomers is not precisely known. As mentioned previously to calculate extinction matrix, we use the one of amorphous silicon. However, the internal composition of the monomers produced in the low-pressure Argon-Silane discharge is complex, so they might contain various chemical elements. Difficulties with obtaining the real value of the refractive index induce some differences between experimental spectra and the inversed ones. As can be seen in Figure 6.44 (a) they can differ significantly and induce instabilities.

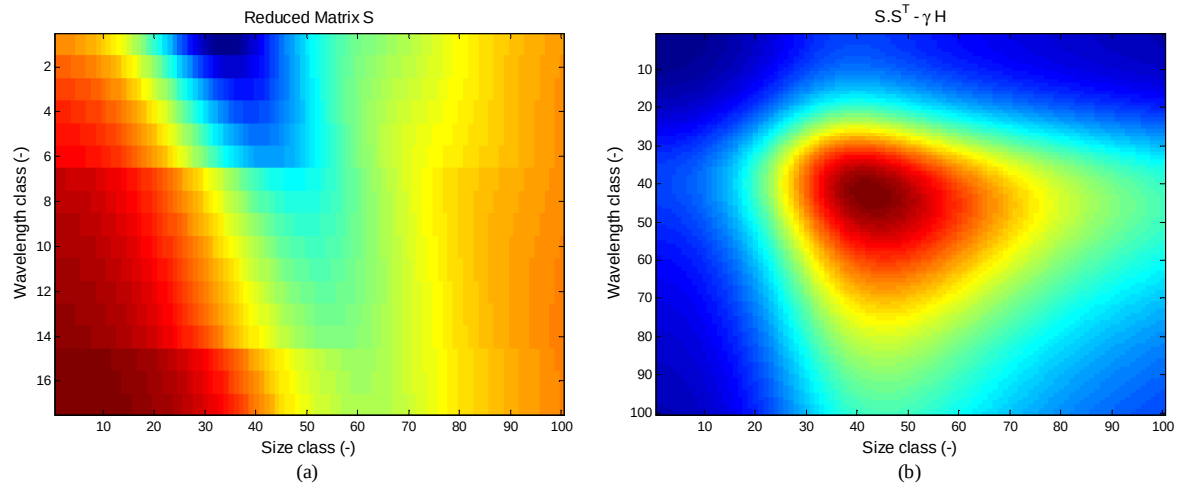

Figure 6.45. (a) The "raw" extinction matrix $\mathbf{S}$ reduced to the selected points of the transmission spectra and (b) the filtered extinction matrix $\left(\mathbf{S^T S} + \gamma \mathbf{H}\right)\mathbf{V}$.

Figure 6.46 compares LES on-line measurements, with the off-line SEM analysis (Boufendi and Bouchoule 1994), for the aggregates mean volume-diameter and standard deviation, d_a and σ_d respectively. Results of the LES analysis were obtained by the inversion of 1155 transmission spectra recorded during the measurement sequence lasting $17.37s$ from the start of the plasma discharge. The particle number and volume concentrations estimated with LES, are also shown. Clearly speaking, in Figure 6.46 LES results match rather well SEM results (Onofri et al. 2011b).

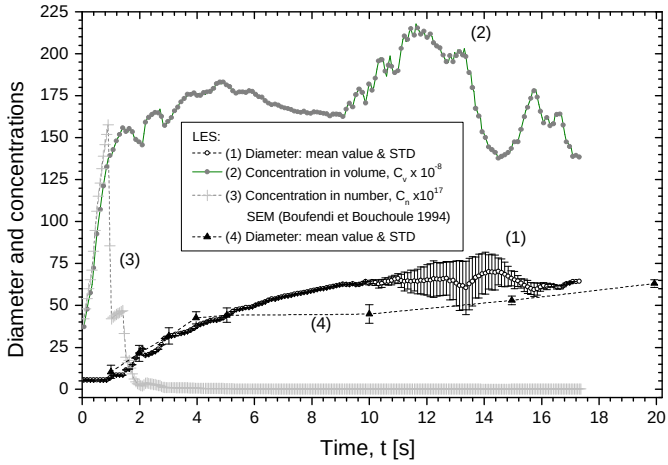

Figure 6.46. Light Extinction Spectrometry: temporal evolution of the particle size and concentrations measured in a low-pressure Argon-Silane discharge

Important drawback of these experiments is that they are not synchronized with plasma reactor and thus it is impossible to fix exactly the starting point of the plasma discharge and the optical analysis. As an example, Figure 6.47 shows the temporal evolution of the particle size measured in the low-pressure Argon-Silane plasma but for two different reference points. In addition to the previous figure, results of the LES measurements are compared also with the recent off-line TEM analysis of the Orleans' group (refereed as TEM-2011 and have not

published yet). It can be seen that result of the LES match better when the starting point is adjusted.

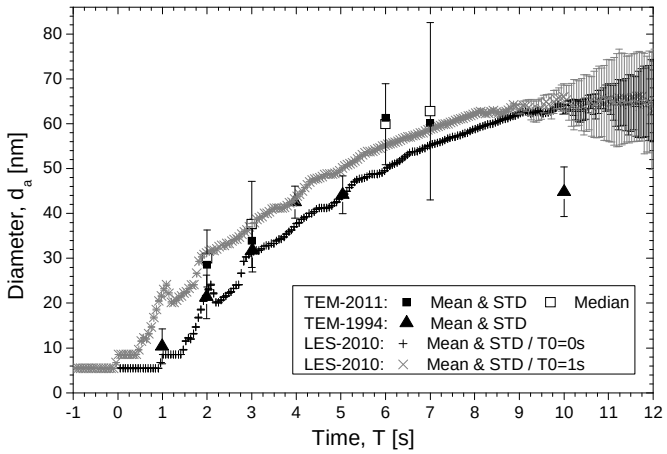

Figure 6.47. Temporal evolution of the particle size measured in a low-pressure Argon-Silane discharge for two different reference points.

6.6. Conclusion

In this chapter we have introduced the principle of the Light Extinction Spectrometry (LES). As shown previously, this technique relies on the analysis of the total extinction spectra of all particles illuminated by a collimated and polychromatic beam. It leads to an ill-posed problem requiring inversion of a Fredholm integral of the first kind, which was solved with a least-square algorithm with a non-negative constraint. We have proved that LES technique can be successfully apply to characterize the PSD and to estimate the concentration in nanoparticles aggregates with totally different optical properties. Despite that, there are some limitations in the applicability of the LES (concerning particles concentration and refractive index), we have proved that it is a powerful technique. Although we do not know exactly refractive index of the monomers aggregating in low-pressure Argon-Silane discharge, we are still able to accurately estimate aggregation dynamics as well as particles concentration and PSD. Both particle systems have been investigated with a well agreement to the off-line TEM and SEM reference analysis.

Further developments of the LES technique requires improvements of the inversion procedure, particularly application of the different regularization schemes (e.g. (Mroczka and Szczuczyński 2010; Mroczka and Szczuczyński 2012)). The latter works present the constrained regularized least-squares (CRLS) method introduced by means of an active set algorithm of quadratic programming. This approach shows considerably better results than the typical regularized least-squares (RLS) method for reconstruction of PSD in terms of better fidelity and smaller uncertainties. Therefore, its application may be profitable for the inversion procedures presented in this chapter.

Chapter 7

GENERAL CONCLUSION AND PERSPECTIVES

This manuscript presents the Ph.D. work completed as a co-shared thesis (French: “Cotutelle”) between the laboratory IUSTI UMR CNRS n°7343, Aix-Marseille University in Marseille, France, and the Chair of Electronic and Photonic Metrology Wrocław University of Technology in Wrocław, Poland.

The main objective of this work was to develop electromagnetic models and experimental methods to characterize the morphology of nanoparticles and their aggregates. The latter are commonly encountered in systems of high scientific and technological interest: sooty flames, aerosols, suspensions, dusty plasmas, etc.

The first part of this Ph.D. work was devoted to review aggregation phenomena, and more particularly, Diffusion-Limited, Diffusion-Limited Cluster and Reaction-Limited Cluster Aggregation. We developed a fully adjustable (tunable) DLA-type code to generate fractal-like aggregates with precisely defined morphological parameters, strict self-similarity and thus scale-invariant properties at each scale. To model very dense and highly opaque aggregates observed in aerosol of nanoparticles, a completely new Buckyballs-like model was developed. As a reference for scattering techniques and aggregates modelling, we have developed two TEM-based methods. Among them, a newly introduced algorithm (Modified Box-Counting Method, MBC) for the analysis of self-similarity properties of each aggregate was compared with an average, multi-scale analysis (widely used in the literature). The MBC method provides less noisy estimation for the evolution of the fractal dimension with the size of aggregates, giving at the same time a criterion to reject the aggregates with insufficient self-similarity properties.

The second part of this Ph.D. was devoted to the simulation of the light scattering properties by aggregates of various particles. To do so, several light scattering theories were considered. Particularly, we compared results of the Lorenz-Mie theory, Rayleigh-based approximations (RGD, RDG-FA), as well as the T-Matrix solution. We have found that the T-Matrix theory is the only one that is sufficiently accurate to describe all the scattering problems encountered in this work. To estimate parameters of the fractal aggregates from the scattering diagrams we developed several algorithms. Additionally, we investigated also the influence of the presence of free monomers on the estimation of the fractal parameters. The latter task, although quite intuitive, is surprisingly missing in the literature.

In the third part of this Ph.D. we review various optical techniques to characterize particle systems. It appears that, a few of them allow in-situ and time-resolved analyses with limited optical accesses. In the framework of various projects related to the plasma we developed a Light Extinction Spectrometry (LES) technique.

Finally, the last part of this Ph.D. work was focused on the application of all the models and methods we have developed to study nanoaerosols (nanosilica beads and tungsten), combustion systems and dusty plasmas. Thus, the results obtained during this analysis clearly proofs the validity of developed algorithms and shows the potential of our experimental methods.

This Ph.D. was performed in the framework of collaborative work. Therefore, some results presented in this thesis were achieved in a cooperation with different researchers and with support of my supervisors. So that, in this paragraph, I would like to point out my main contributions.

I performed all the numerical results presented in this manuscript. Particularly, it includes development of the DLA and TEM-modeling software, methods to fill and optimize buckyballs aggregates, algorithms to derive morphological parameter of fractal aggregates from TEM pictures, as well as algorithms to analyze optical structure factors and to perform the Guinier analysis of fractal aggregates. I carried out also the light scattering simulation presented in this manuscript. I developed numerous applications using various light scattering theories whose results are presented.

Experimental part of this thesis concerning LES analysis of various particle systems was performed in a cooperation with the other researchers. My participation in this work includes numerical study of the light scattering properties of particles corresponding to the experimental systems, as well as contributions in the laboratory work. Particularly, it concerns taking part in building, preparation and development of the experimental setup, performing various measurements as well as collecting samples for reference TEM/SEM analysis.

It includes also data gathering, post-processing and inversion with different particle models. Finally, I performed analysis and interpretation of the presented results.

Further perspectives of this Ph.D. include the use the Discrete Dipole Approximation (DDA) to calculate scattering properties of the fractal-like and buckyballs-like aggregates. Subsequently, these results will be compared with the T-Matrix predictions. We suppose that such a validation should be especially interesting for highly melted particles in combustion systems or plasma. In the case of the aggregates produced by the aerosol drying method, the T-Matrix algorithm seems to be more accurate since the shape of single monomers within aggregates is nearly spherical.

Perspectives for the development of the LES technique assume improvements of the inverse method being used. Particularly, it is highly interesting to advance the non-negative least square algorithm by different regularization schemes (e.g. Tikhonov Regularization, various SVD algorithms or iterative methods). Further perspectives include also extended tests of the LES technique for aerosols of various nanoparticles. It is important to perform additional validations and experiments in order to investigate capabilities of the LES method to study different plasma systems.

Chapter 8

REFERENCES

References

Arnas C., Dominique C., Roubin P., Martin C., Laffon C., Parent P., Brosset C. and Pegourie B. (2005). Experimental Study of Different Carbon Dust Growth Mechanisms, *Journal of Nuclear Materials*, 337-339: 69-73.

Auger J.-C., Martinez V. and Stout B. (2007). Absorption and Scattering Properties of Dense Ensembles of Non-spherical Particles, *Journal of the Optical Society of America A*, 24: 3508–3516.

Babu S., Gimel J. C. and Nicolai T. (2008). Diffusion Limited Cluster Aggregation with Irreversible Slippery Bonds, *The European Physical Journal E*, 27 (3): 297-308.

Barber P. W. and Hill S. S. (1990). Light Scattering by Particles: Computational Methods, Singapore, *World Scientific*.

Barbosa S., Onofri F. R. A. and **Woźniak M.** (2011). TEM Analysis of Buckyballs Aggregates. Internal Report, Marseille, Aix-Marseille University.

Barbosa S., Onofri F. R. A., **Woźniak M.**, Touré O. and Grisolia C. (2012). Optical Characterization of Highly Ordered Aggregates of Colloidal Nanobeads, *International Conference Lasers and Interactions with Particles (LIP2012)*, March 26-30th, Rouen, France.

Barton J. P., Alexander D. R. and Schaub S. A. (1988). Internal and Near-Surface Electromagnetic Fields for a Spherical Particle Irradiated by a Focused Laser Beam, *Journal of Applied Physics*, 64: 1632-1639.

Bau S., Witschger O., Gensdarmes F., Rastoix O. and Thomas D. (2010). A TEM-based Method as an Alternative to the BET Method for Measuring off-line the Specific Surface Area of Nanoaerosols, *Powder Technology*, 200 (3): 190-201.

Berndt J., Kovacevic E., Stefanovic I., Stepanovic O., Hong S. H., Boufendi L. and Winter J. (2009). Some Aspects of Reactive Complex Plasmas, *Contributions to Plasma Physics*, 49 (3): 107-133.

Binek P. (2007). Analysis of the Optically Dense Systems with Matrix T, Wrocław, *Wrocław University of Technology*, Ph.D. thesis (in Polish).

Bird G. A. (1994). Molecular Gas Dynamics and the Direct Simulation of Gas Flows, *Oxford University Press*.

Boffa V., Castricum H. L., Garcia R., Schmuhl R., Petukhov. A. V., Blank D. H. A. and Elshof J. E. (2009). Structure and Growth of Polymeric Niobia-Silica Mixed-Oxide Sols for Microporous Molecular Sieving Membranes: a SAXS Study, *Chemistry of Materials*, 21 (9): 1822–1828.

Bohren C. F. and Huffman D. R. (1998). Absorption and Scattering of Light by Small Particles, *John Wiley and Sons, Inc.*

Boufendi L. and Bouchoule A. (1994). Particle Nucleation and Growth in a Low-Pressure Argon-Silane Discharge, *Plasma Sources Science and Technology*, 3 (3): 262-267.

Brasil A. M., Farias T. L. and Carvalho M. G. (1999). A Recipe for Image Characterization of Fractal-like aggregates, *Journal of Aerosol Science*, 30 (10): 1379-1389.

Braun A., Huggins F. E., Seifert S., Ilavsky J., Shah N., Kelly K. E., Sarofim A. and Huffman G. P. (2004). Size-Range Analysis of Diesel Soot with Ultra-Small Angle X-ray Scattering, *Combustion and Flame*, 137 (1-2): 63-72.

Bushell G. C., Yan Y. D., Woodfield D., Raper J. and Amal R. (2002). On Techniques for the Measurement of the Mass Fractal Dimension of Aggregates, *Advances in Colloid and Interface Science*, 95 (95): 1-50.

Buzea C., Pacheco I. I. and Robbie K. (2007). Nanomaterials and Nanoparticles: Sources and Toxicity, *Biointerphases*, 2 (4): 17-71.

Cai J., Lu N. and Sorensen C. M. (1995). Analysis of Fractal Cluster Morphology Parameters: Structural Coefficient and Density Autocorrelation Function Cutoff, *Journal of Colloid and Interface Science*, 171 (2): 470-473.

Chakrabarty R. K., Moosmuller H., Arnott W. P., Garro M. A., Slowik J. G., Cross E. S., Han J.-H., Davidovits P., Onasch T. B. and Worsnop D. R. (2007). Light Scattering and Absorption by Fractal-Like Carbonaceous Chain Aggregates: Comparison of Theories and Experiment, *Applied Optics*, 46 (28): 6990-7006

Chakrabarty R. K., Moosmuller H., Arnott W. P., Garro M. A., Tian G., Slowik J. G., Cross E. S., Han J.-H., Davidovits P., Onasch T. B. and Worsnop D. R. (2009). Low fractal Dimension Cluster-Dilute Soot Aggregates from a Premixed Flame, *Physical Review Letters*, 102 (23): 235504.

Cohen R. J. and Benedek G. B. (1982). Equilibrium and Kinetic Theory of Polymerization and the Sol-Gel Transition, *Journal of Chemical Physics*, 86: 3696–3714.

Dalzell W. H. and Sarofim A. F. (1969). Optical Constants of Soot and Their Application to Heat-Flux Calculations, *Journal of Heat Transfer*, 91 (1): 100-104.

De-Iuliis S., Cignoli F. and Zizak G. (2005). Two-Color Laser-Induced Incandescence (2C-LII) Technique for Absolute Soot Volume Fraction Measurements in Flames, *Applied Optics*, 44 (34): 7414-7423.

Desgroux P., Mercier X., Lefort B., Lemaire R., Therssen E. and Pauwels J. F. (2008). Soot Volume Fraction Measurement in Low-Pressure Methane Flames by Combining Laser-Induced Incandescence and Cavity Ring-Down Spectroscopy: Effect of Pressure on Soot Formation, *Combustion and Flame*, 155 (1-2): 289–301.

Dobbins R. A. and Megaridis C. M. (1991). Absorption and Scattering of Light by Polydisperse Aggregates, *Applied Optics*, 30: 4747-4754.

Doicu A., Wriedt T. and Eremin Y. A. (2006). Light Scattering by Systems of Particles, *Springer*.

Draine B. T. and Flatau P. J. (1994). Discrete Dipole Approximation for Scattering Calculations, *Journal of the Optical Society of America A*, 11 (4): 1491-1499.

Einstein A. (1956). Investigations of the Theory of Brownian Movement, New York, *Dover Publications Inc.*

Farias T. L. (1997). Evaluation of Light Scattering Theories for Fractal Aggregates, Lisbon, *Universidade Tecnica de Lisboa*, Ph.D. thesis (in English).

Farias T. L., Koylu U. O. and Carvalho M. G. (1996). Range of Validity of the Rayleigh-Debye-Gans Theory for Optics of Fractal Aggregates, *Applied Optics*, 35 (33): 6560-6567.

Foroutan-pour K., Dutilleul P. and Smith D. L. (1999). Advances in the Implementation of the Box-Counting Method of Fractal Dimension Estimation, *Applied Mathematics and Computation*, 105: 195-210.

Forrest S. R. and Witten T. A. (1979). Long Range Correlations in Smoke Particle Aggregates, *Journal of Physics A: Mathematical and General*, 12 (5): L109-L117.

Fortov V. E., Ivlev A., Khrapak S., Khrapak A. and Morfill G. (2005). Complex (Dusty) Plasmas: Current Status, Open Issues, Perspectives, *Physics Reports*, 421: 1-103.

Glenzer S. H. and Redmer R. (2009). X-ray Thomson Scattering in High Energy Density Plasmas, *Reviews of Modern Physics*, 81 (4): 1625–1663.

Goodman J. (1996). Introduction to Fourier Optics, New-York, *McGraw-Hill*.

Gouesbet G. (2009). Generalized Lorenz-Mie theories, the Third Decade: A Perspective, *Journal of Quantitative Spectroscopy and Radiative Transfer*, 110 (14-16): 1223-1238.

Gouesbet G., Maheu B. and Grehan G. (1988). Light Scattering From a Sphere Arbitrarily Located in a Gaussian Beam, Using a Bromwich Formulation, *Journal of the Optical Society of America A*, 5 (9): 1427-1443.

Guenadou D., Lorcet H., Brothier M., Gramondi P., U.Michon, Onofri F., Vardelle M. and G.Mariaux (2008). *7th International Symposium of High Temperature Air Combustion and Gasification*, Phuket, Thailand (HiTACG 2008, Phuket).

Hansen P. C. (1994). Regularization Tools: a Matlab Package for Analysis and Solution of Discrete Ill-Posed Problems, *Numerical Algorithms*, 6: 1-35.

Hansen P. C. (2008). Regularization Tools. A Matlab Package for Analysis and Solution of Discrete Ill-Posed Problems. Version 4.1 for Matlab 7.3. Informatics and Mathematical Modelling Building 321, Technical University of Denmark DK-2800 Lyngby, Denmark.

Heinson W. R., Sorensen C. M. and Chakrabarti A. (2010). Does Shape Anisotropy Control the Fractal Dimension in Diffusion-Limited Cluster-Cluster Aggregation?, *Aerosol Science and Technology*, 44 (12): i-iv.

Hessler J. P., Seifert S. and Winans R. E. (2002). Spatially Resolved Small-Angle X-ray Scattering Studies of Soot Inception and Growth, *Proceedings of the Combustion Institute*, 29 (2): 2743-2748.

Holland B. T., Blanford C. F. and Stein A. (1998). Synthesis of Macroporous Minerals with Highly Ordered Three-Dimensional Arrays of Spheroidal Voids, *Science*, 281 (5376): 538-540.

Hong S. and Winter J. (2006). Size Dependence of Optical Properties and Internal Structure of Plasma Grown Carbonaceous Nanoparticles Studied by in Situ Rayleigh-Mie Scattering Ellipsometry, *Journal of Applied Physics*, 100 (6): 064303.

Ioffe.Institute (2012). Refractive Indexes Database, http://www.ioffe.ru/SVA/NSM/nk/.

Jullien R. and Botet R. (1987). Aggregation and Fractal Aggregates, Singapore, *World Scientific*.

Kaye B. H. (1994). A Random Walk Through Fractal Dimensions, New York, *Weinheim*.

Kerker M. (1969). The Scattering of Light and Other Electromagnetic Radiation, New York, *Academic Press*.

Kim A. Y., Hauch K. D., Berg J. C., Martin J. E. and Anderson R. A. (2003). Linear Chains and Chain-Like Fractals from Electrostatic Heteroaggregation, *Journal of Colloid and Interface Science*, 260: 149-159.

Koylu U. O. and Faeth G. M. (1992). Structure of Overfire Soot in Buoyant Turbulent Diffusion Flames at Long Residence Times, *Combustion and Flame* 89 (3): 140-156.

Koylu U. O. and Faeth G. M. (1994). Optical Properties of Overfire Soot in Buoyant Turbulent Diffusion Flames at Long Residence Times, *Journal of Heat Transfer*, 116 (1): 152-159.

Koylu U. O., Faeth G. M., Farias T. L. and Carvalho M. G. (1995). Fractal and Projected Structure Properties of Soot Aggregates, *Combustion and Flame*, 100 (4): 621-633.

Lapuerta M., Martos F. J. and Martín-Gonzalez G. (2010). Geometrical Determination of the Lacunarity of Agglomerates with Integer Fractal Dimension, *Journal of Colloid and Interface Science*, 346 (1): 23-31.

Lawson C. L. and Hanson R. J. (1974). Solving Least Squares Problems, Englewood Cliffs, *Prentice-Hall*.

Lin M. Y., Lindsay H. M., Weitz D. A., Ball R. C., Klein R. and Meakin P. (1989). Universality of Fractal Aggregates as Probed by Light Scattering, *Proceedings of the Royal Society of London*, 423 (1864): 71-87.

Mackowski D. W. and Mishchenko M. I. (1996). Calculation of the T-Matrix and the Scattering Matrix for Ensembles of Spheres, *Journal of the Optical Society of America A*, 13 (11): 2266-2278.

Martin P. A. (2006). Multiple scattering: interaction of time-harmonic waves with N obstacles, Cambridge, *Cambridge University Press*.

Meakin P. (1983). Formation of Fractal Clusters and Networks by Irrevesible Diffusion-Limited Aggregation, *Physical Review Letters*, 51 (13): 1119-1122.

Meakin P. (1984). Effects of Cluster Trajectories on Cluster-Cluster Aggregation: a Comparison of Linear and Brownian Trajectories in Two- and Three-dimensional simulations, *Physical Review A*, 29 (2): 997-999.

Megaridis C. M. and Dobbins R. A. (1990). Morphological Description of Flame-Generated Materials, *Combustion Science and Technology*, 71 (1-3): 95-109.

Melton L. (1984). Soot Diagnostics Based on Laser Heating, *Applied Optics*, 23 (13): 2201-2208.

Meyer W. V., Cannell D. S., Smart A. E., Taylor T. W. and Tin P. (1997). Multiple-Scattering Suppression by Cross Correlation, *Applied Optics*, 36 (30): 7551-7558.

Michelsen H., Liu F., Kock B., Bladh H. and Boiarciuc A. (2007). Modeling Laser-Induced Incandescence of Soot: a Summary and Comparison of LII Models, *Applied Physics B*, 87 (3): 503-521.

Mie G. (1908). Beiträge zur Optik Trüber Medien, Speziell Kolloidaler Metallösungen, *Annalen der Physik*, 330 (3): 377–445.

Mishchenko M., Hovenier J. and Travis L. (2000). Light Scattering by Non-spherical Particles, San Diego, *Acad. Press*.

Mishchenko M., Travis L. D. and Mackowski D. W. (2012). T-matrix Codes for Computing Electromagnetic Scattering by Nonspherical and Aggregated Particles. Retrieved 1.04.2009, from http://www.giss.nasa.gov/staff/mmishchenko/t_matrix.html.

Mishchenko M. I. (2009). Electromagnetic Scattering by Nonspherical Particles: a Tutorial Review, *Journal of Quantitative Spectroscopy and Radiative Transfer*, 110: 808–832.

Mishchenko M. I., Travis L. D. and Mackowski D. W. (1996). T-Matrix Computations of Light Scattering by Nonspherical Particles: a Review, *Journal of Quantitative Spectroscopy and Radiative Transfer*, 55 (5): 535-575.

Mitchell J. B. A., Stasio S., LeGarrec J. L., Florescu-Mitchell A. I., Narayanan T. and Sztucki M. (2009). Small Angle X-ray Scattering Study of Flame Soot Nanoparticle Aggregation and Restructuring, *Journal of Applied Physics* 105 (12): 124904-124904-9.

Mokhtari T., Sorensen C. M. and Chakrabarti A. (2005). Multiple-Scattering Effects on Static Light-Scattering Optical Structure Factor Measurements, *Applied Optics*, 44 (36): 7858-7861.

Mroczka J. and Szczuczyński D. (2009). Inverse Problems Formulated In Terms Of First-Kind Fredholm Integral Equations In Indirect Measurements, *Metrology And Measurement Systems*, 16 (3): 333-357.

Mroczka J. and Szczuczyński D. (2012). Simulation Research on Improved Regularized Solution of the Inverse Problem in Spectral Extinction Measurements, *Applied Optics*, 51 (11): 1715-1723.

Mroczka J. and Szczuczyński D. K. (2010). Improved Regularized Solution of the Inverse Problem in Turbidimetric Measurements, *Applied Optics*, 49 (24): 4591-4603.

Mroczka J., **Woźniak M.** and Onofri F. R. A. (2012). Algorithms and Methods for the Analysis of the Optical Structure Factor of Fractal Aggregates, *Metrology and Measurement Systems*, 19 (3): 459-470.

Nieminen T. A., Loke V. L. Y., Stilgoe A. B., Knoner G., Branczyk A. M., Heckenberg N. R. and Rubinsztein-Dunlop H. (2007). Optical Tweezers Computational Toolbox, *Journal of Optics A 9*: S196-S203.

Oh C. and Sorensen C. M. (1997). The Effect of Overlap Between Monomers on the Determination of Fractal Cluster Morphology, *Journal of Colloid and Interface Science*, 193 (1): 17-25.

Oh C. and Sorensen C. M. (1998). Structure Factor of Diffusion-Limited Aggregation Clusters: Local Structure and Non-self-similarity, *Physical Review E*, 57 (1): 784-790.

Onofri F. R. A. (2007). Light Scattering Properties of Clusters of Particles as a Model of Inter Stellar Dusts, IUSTI-UMR 6595 CNRS-University of Provence, Marseille: 17.

Onofri F. R. A., Barbosa S., Toure O., **Woźniak M.** and Grisolia C. (2012a). Sizing buckyballs-like aggregates of colloidal nanoparticles by light extinction spectroscopy, *Journal of Quantitative Spectroscopy and Radiative Transfer*, http://dx.doi.org/10.1016/j.jqsrt.2012.08.018.

Onofri F. R. A., Barbosa S., **Woźniak M.** and Acosta P. (2010a). Optical Characterization of micro- and nanoparticle systems. Proceedings of the International Conference on Plasma Diagnostics, Pont-à-Mousson, France, paper 11.

Onofri F. R. A., Barbosa S., **Woźniak M.**, Mroczka J., Vrel D. and Grisolia C. (2012b). In Situ Characterization of Dust Mobilized by Laser Cleaning Methods and Loss of Vacuum Accidents, *Fusion Science and Technology*, 62 (1): 39–45.

Onofri F. R. A., Barbosa S., **Woźniak M.**, Toure O. and Mroczka J. (2010b). Optical Characterization of Nanoparticles and Aggregates: Light Extinction Spectrometry, *15th Int. Symp on Appl. Laser Techniques to Fluid Mechanics*, July 5–8, 2010, Lisbon, Portugal.

Onofri F. R. A., Barbosa S., **Woźniak M.**, Vrel D. and Grisolia C. (2011a). In-situ Characterization of Dust Mobilized by Laser Claening Methods and Loss of Vacuum Accident, *15th International Conference on Fusion Reactor Materials (ICFRM-15)*, Charleston, USA.

Onofri F. R. A., Bergounoux L., J. L. Firpo and Mesguish-Ripault J. (1999). Velocity, Size and Concentration Measurements of Optically Inhomogeneous Cylindrical and Spherical Particles, *Applied Optics*, 38 (21): 4681-4690.

Onofri F. R. A., Grehan G. and Gouesbet G. (1995). Electromagnetic Scattering From a Multilayered Sphere Located in an Arbitrary Beam, *Applied Optics*, 34 (30): 7113-7124.

Onofri F. R. A., Krzysiek M., Barbosa S., **Woźniak M.**, Mroczka J., Yijia Y. and Ren K.-F. (2010c). Inverse Near-critical-angle Scattering as a Tool to Characterize Bubble Clouds, *Proceedings of SPIE*, 7588.

Onofri F. R. A., Ren K. F. and Grisolia C. (2009). Development of an in Situ ITER Dust Diagnostic Based on Extinction Spectrometry: Dedicated Light Scattering Models *Journal of Nuclear Materials*, 390-391: 1093-1096.

Onofri F. R. A., **Woźniak M.** and Barbosa S. (2011b). On the Optical Characterisation of Nanoparticle and their Aggregates in Plasma Systems, *Contributions to Plasma Physics*, 51 (2-3): 228-236.

Ouellette N. T., Xu H. and Bodenschatz E. (2006). A Quantitative Study of Three-Dimensional Lagrangian Particle Tracking Algorithms, *Experiments in Fluids*, 40 (2): 301-313.

Ouf F., Vendel J., Coppalle A., Weill M. and Yon J. (2008). Characterization of soot particles in the plumes of over-ventilated diffusion flames, *Combustion Science and Technology*, 180 (4): 674–698.

Ouf F. X. (2006). Caracterisation des Aerosols Emis Lors d'un Incendie, Rouen.

Ouf F. X., Yon J., Ausset P., Coppalle A. and Maille M. (2010). Influence of Sampling and Storage Protocol on Fractal Morphology of Soot Studied by Transmission Electron Microscopy, *Aerosol Science and Technology*, 44 (11): 1005 - 1017.

Ozaki R., Uchida G., Lizuka S. and Sato N. (1999). Frontiers in Dusty Plasmas, *Proceedings 2nd Int. Conf. Phys. Dusty Plasmas* Elsevier, Hakone, Japan,.

Pierce F., Sorensen C. M. and Chakrabarti A. (2006). Computer Simulation of Diffusion-Limited Cluster-Cluster Aggregation with an Epstein Drag Force, *Physical Review E*, 74 (2): 1539-3755.

POV-Ray (2004). Persistence of Vision Pty. Ltd., Persistence of Vision Raytracer (Version 3.6) [Computer Software]: Retrieved from http://www.povray.org/download/.

Puri R., Richardson T. F., Santoro R. J. and Dobbins R. A. (1993). Aerosol Dynamic Processes of Soot Aggregates in a Laminar Ethene Diffusion Flame, *Combustion and Flame*, 92 (3): 320-333.

Ren K. F., Grehan G. and Gouesbet G. (1997). Scattering of a Gaussian Beam by an Infinite Cylinder in GLMT-Framework, Formulation and Numerical Results, *Journal of the Optical Society of America A*, 14 (11): 3014-3025

Rieker T. P., Hindermann-Bischoff M. and Ehrburger-Dolle F. (2000). Small-angle X-ray Scattering Study of the Morphology of Carbon Black Mass Fractal Aggregates in Polymeric Composites, *Langmuir*, 16 (13): 5588–5592.

Roduner E. (2006). Size Matters: Why Nanomaterials are Different *Chemical Society Reviews*, 35: 583-592.

Samson R. J., Mulholland G. W. and Gentry J. W. (1987). Structural Analysis of Soot Agglomerates, *Langmuir*, 3 (2): 272–281.

Schulz C., Kock B. F., Hofmann M., Michelsen H. and Will S. (2006). Laser-Induced Incandescence: Recent Trends and Current Questions, *Applied Physics B*, 83 (3): 333-354.

Schweigert V. A., Alexandrov A. L., Morokov Y. N. and Bedanov V. M. (1995). MINDO/3 Study of the Interaction of Small Carbon Clusters, *Chemical Physics Letters*, 238 (1-3): 110-115.

Sharpe J. P., Rohde V., Team A.-U. E., Sagara A., Suzuki H., Komori A. and Motojima O. (2003). Characterization of Dust Collected From ASDEX-Upgrade and LHD, *Journal of Nuclear Materials*, 313-316: 455-459.

Shiratani M., Fukuzawa T. and Watanabe Y. (1999). Particle Growth Kinetics in Silane RF Discharges, *Japanese Journal of Applied Physics*, 38 (7B): 4542.

Smoluchowski M. (1906). The Kinetic Theory of Brownian Molecular Motion and Suspensions, *Annals of Physics*.

Sopra.S.A. (2010). Optical Data from Sopra S.A. Refractive Indexes Database, http://www.sopra-sa.com.

Sorensen C. M. (2001). Light Scattering by Fractal Aggregates: A Review, *Aerosol Science and Technology*, 35: 648-687.

Sorensen C. M., Cai J. and Lu N. (1992a). Light-scattering Measurements of Monomer Size, Monomers per Aggregate, and Fractal Dimension for Soot Aggregates in Flames, *Applied Optics*, 31 (30): 6547-6557

Sorensen C. M., Cai J. and Lu N. (1992b). Test of Static Structure Factors for Describing Light Scattering From Fractal Soot Aggregates, *Langmuir*, 8: 2064-2069.

Sorensen C. M., Hageman W. B., Rush T. J., Huang H. and Oh C. (1998). Aerogelation in a Flame Soot Aerosol, *Physical Review Letters*, 80 (8): 1782-1785.

Sorensen M. and Roberts G. C. (1997). The Prefactor of Fractal Aggregates, *Journal of Colloid and Interface Science*, 186 (2): 447-452.

Stanislas M., Westerweel J. and Kompenhans J. (2004). Particle Image Velocimetry, Berlin, *Springer*.

Stasio S., Konstandopoulos A. G. and Kostoglou M. (2002). Cluster–Cluster Aggregation Kinetics and Primary Particle Growth of Soot Nanoparticles in Flame by Light Scattering and Numerical Simulations, *Journal of Colloid and Interface Science*, 247 (1): 33-46.

Tamanai A., H.Mutschke, Blum J. and Neuha R. (2006). Experimental Infrared Spectroscopic Measurement of Light Extinction for Agglomerate Dust Grains, *Journal of Quantitative Spectroscopy and Radiative Transfer*, 100 (1-3): 373–381.

Tang S., Preece J. M., McFarlane C. M. and Zhang Z. (2000). Fractal Morphology and Breakage of DLCA and RLCA Aggregates, *Journal of Colloid and Interface Science*, 221 (1).

Theiler J. (1990). Estimating Fractal Dimension, *Journal of the Optical Society of America A*, 7 (6): 1055-1073.

Tourbin M. (2006). Caracterisation Comportement de Suspensions Concentrees de Nanoparticules Sous Ecoulement: Application aux Processus d'agregation et de Rupture, Toulouse, *National Polytechnique de Toulouse*, Ph.D. thesis (in French).

Toure O. (2010). Caractérisation de Nano-aérosols par Spectrométrie d'extinction, Marseille, *Aix-Marseille University*, M.Sc. thesis (in French).

Twomey S. (1979). Introduction to the Mathematics in Remote Sensing and Indirect Measurement New York, *Elsevier*.

van der Hulst H. C. (1957). Light Scattering by Small Particles, New York, *Wiley*.

Vander-Wal R. L. (2009). Laser-Induced Incandescence: Excitation and Detection Conditions, Material Transformations and Calibration, *Applied Physics B*, 96 (4): 601-611.

Wang G. M. and Sorensen C. M. (1999). Diffusive Mobility of Fractal Aggregates Over the Entire Knudsen Number Range, *Physical Review E*, 60 (2): 3036-3044.

Waterman P. C. (1965). Matrix Formulation of Electromagnetic Scattering, *Proceedings of the IEEE*, 53 (8): 805-812.

Weitz D. A., Huang J. S., Lin M. Y. and Sung J. (1985). Limits of the Fractal Dimension for Irreversible Kinetic Aggregation of Gold Colloids, *Physical Review Letters*, 54 (13): 1416–1419.

Weitz D. A. and Oliveria M. (1984). Fractal Structures Formed by Kinetic Aggregation of Aqueous Gold Colloids, *Physical Review Letters*, 52 (16): 1433-1436.

Wentzel M., Gorzawski H., Naumann K. H., Saatho H. and Weinbruch S. (2003). Transmission Electron Microscopical and Aerosol Dynamical Characterization of Soot Aerosols, *Journal of Aerosol Science*, 34 (10): 1347-1370.

Witten T. A. and Sander L. M. (1981). Diffusion-Limited Aggregation, a Kinetic Critical Phenomenon, *Physical Review Letters*, 47 (19): 1400-1403.

Woźniak M., Onofri F. R. A., Barbosa S., Yon J., Caumont C. and Mroczka J. (2012a). Detecting correlations between the morphological parameters of multi-fractal samples of fractal-like aggregates, *European Aerosol Conference*, poster, 2–7 September 2012, Granada, Spain.

Woźniak M., Onofri F. R. A., Barbosa S., Yon J. and Mroczka J. (2012b). Comparison of Methods to Derive Morphological Parameters of Multifractal Samples of Particle Aggregates from TEM Images, *Journal of Aerosol Science*, 47: 12-26.

Wriedt T. (2009). Light Scattering Theories and Computer Codes, *Journal of Quantitative Spectroscopy and Radiative Transfer*, 110 (11): 833-843.

Xu F. (2007). Diffusion d'un Faisceau Quelconque par un Sphéroïde et Mesure en Ligne de la Vapeur Humide par l'extinction Spectrale de la Lumière, Rouen, *University of Rouen*, Ph.D. thesis (in French).

Xu R. (2002). Particle Characterization: Light Scattering Methods, New York, *Kluwert Academic Publisher*.

Yon J., Lemaire R., Therssen E., Desgroux P., Coppalle A. and Ren K. F. (2011). Examination of Wavelength Dependent Soot Optical Properties of Diesel and

Diesel/Rapeseed Methyl Ester Mixture by Extinction Spectra Analysis and LII Measurements, *Applied Physics B*, 104 (2): 253-271.

Yon J., Roze C., Girasole T., Coppalle A. and Mees L. (2008). Extension of RDG-FA for Scattering Prediction of Aggregates of Soot Taking Into Account Interactions of Large Monomers, *Particle and Particle Systems Characterization*, 25 (1): 54–67.

Zift R. M., McGrady E. D. and Meakin P. (1985). On the Validity of Smoluchowski's Equation for Cluster-Cluster Aggregation Kinetics, *Journal of Chemical Physics*, 82: 5269-5274.

RÉSUMÉ EN FRANCAIS
(ABSTRACT IN FRENCH LANGUAGE)

Chapitre 1: Introduction

On observe la formation ou la présence de nanoparticules dans de très nombreux systèmes naturels ou industriels (voir la Figure F.1) : aérosols, suspensions colloïdales, flammes, plasmas (froids thermiques et de fusion), les milieux interstellaires,... Les propriétés particulières des nanoparticules, par rapport à celles de leur matériau (échelle macroscopique), sont souvent liées aux effets dits, de surface, et aux effets quantiques (Buzea et al. 2007).

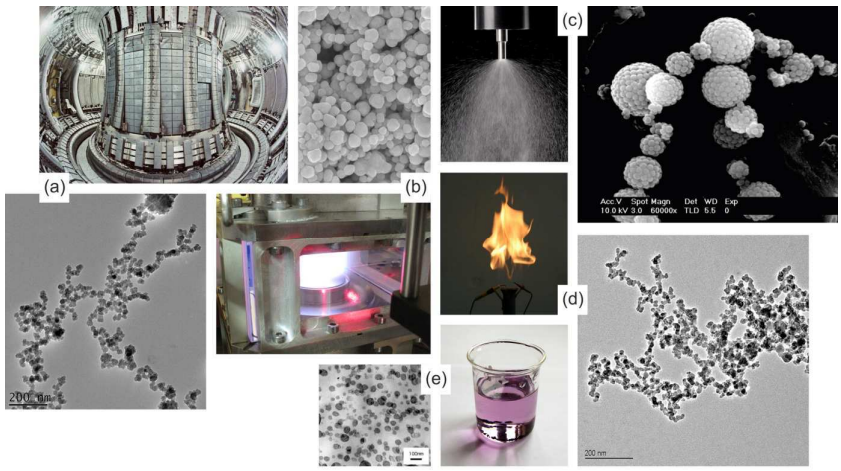

Figure F.1. Les systèmes nano particulaires sont observés dans milieux très différents : (a) réacteurs de fusion (tokamak JET) ; (b) décharges dans un gaz à basse pression ; (c) certaines pulvérisations ; (d) flammes et (d) suspensions colloïdales déstabilisées.

Ces effets confèrent aux systèmes nano particulaires une réactivité chimique, des propriétés thermo physiques, mécaniques, optiques, électriques et magnétiques inégalées et parfois très insolites. Les effets de surface sont liés à la fraction importante d'atomes à l'interface avec le

milieu environnant, qui est sans commune mesure avec ce que l'on peut obtenir à l'échelle microscopique et, à fortiori, macroscopique. Les effets quantiques sont directement liés aux dimensions de ces particules, dont certaines, comme les *quantum dots,* ne sont composées que de quelques dizaines ou centaines d'atomes ou molécules (Roduner 2006). Dans ce dernie cas, c'est le confinement des électrons qui est à l'origine des bandes étroites d'absorption et d'émission (Buzea et al. 2007).

Pour comprendre, produire et contrôler ces systèmes, il faut disposer d'outils de caractérisation et notamment, de leur granulométrie et de leur concentration. Les techniques de laboratoire (comme la microscopie électronique) ne répondent que partiellement à ce besoin, dans la mesure où elles sont très intrusives et peu adaptées à des études paramétriques résolues temporellement. Les résultats obtenus peuvent également être biaisés par la procédure de prélèvement, la taille limitée de l'échantillon ou même la difficulté d'analyser de manière statistique les images obtenues (comme nous le montrons dans ce travail).

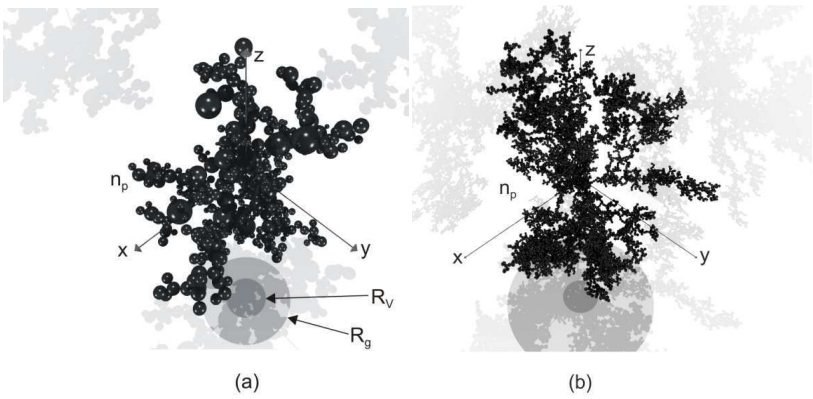

Figure F.2. Agrégats fractals composés de (a) 500 monomères polydisperses (distribution log-normale, $\sigma_p = 0.5$) avec $R_v = 7.94$, $D_f = 2.00$, $R_v = 17.71$; (b) 10000 monomères monodisperses avec $D_f = 2.00$ et $R_g = 79.22$.

Pour l'analyse des systèmes micro particulaires (Xu 2002), il existe de nombreuses techniques optiques qui permettent de s'affranchir des limites que nous venons d'évoquer. Les choses se compliquent à l'échelle nanométrique de par la complexité morphologique des agrégats formés par les nanoparticles ; la nécessité de disposer à la fois de modèles de particules, de modèles de diffusion de la lumière et procédures d'inversion ad hoc, ainsi que d'une instrumentation adaptée. C'est précisément l'objectif de ce travail de thèse que d'apporter différentes solutions dans ce domaine avec, comme contrainte supplémentaire, de privilégier un diagnostic pouvant opérer à longue distance et sur des systèmes aussi différents que des suspensions, des aérosols et des plasmas poussiéreux.

En accord avec cette démarche, le chapitre 2 introduit deux modèles permettant de décrire simplement la morphologie d'agrégats fractals ou réguliers. Le chapitre 3 présente les travaux réalisés pour améliorer les analyses morphologiques reposant sur la microscopie électronique et ceci, afin de pouvoir mieux comparer ces résultats avec ceux des techniques optiques. Le

chapitre 4 décrit et commente les différentes approximations physiques et théories utilisées pour modéliser les propriétés de diffusion et d'absorption de la lumière par des agrégats de formes complexes. Le chapitre 5 introduit et valide numériquement les deux modèles développés pour analyser les diagrammes de diffusion (facteur de structure optique) de systèmes nano particulaires. Le chapitre 6 présente les travaux numériques et expérimentaux menés sur la spectrométrie d'Extinction (LES). Le chapitre 7 est une conclusion générale avec perspectives.

Chapitre 2: Modèles d'agrégats de particules

Pour calculer puis inverser les propriétés optiques de nano-agrégats, il nous faut au préalable disposer d'un modèle les décrivant le plus simplement possible. Après quelques rappels sur les phénomènes d'agrégation, ce chapitre présente les deux modèles d'agrégats développés : un modèle d'Agrégation Limité par la Diffusion (DLA) (Woźniak et al. 2012b) et un modèle de dôme géodésique (*Buckyballs*) (Onofri et al. 2012a).

Agrégation Limité par la Diffusion (DLA)

En résumé, le modèle DLA repose sur une description : de la morphologie des agrégats, basée sur l'équation fractale (Witten and Sander 1981); et sur les hypothèses que les monomères (particules primaires constituant l'agrégat) ont une marche aléatoire (Brownienne) et qu'elles s'agrègent au premier contact, avec $n_p = k_f \left(R_g / r_p \right)^{D_f}$. Où n_p et r_p représentent le nombre et le rayon des monomères de l'agrégat en cours de formation, D_f et R_g la dimension fractale et le rayon de giration de ce dernier, et k_f un pré-facteur fractal (ou coefficient de structure). A titre d'exemple, la Figure F.2 montre, pour deux agrégats, une visualisation 3-D (créé avec le logiciel POV-Ray (POV-Ray 2004)), les projections 2D associées ainsi que celles des rayons de giration et en volume (disques). Ce modèle et le code de calcul associé prennent en compte différents effets, comme l'interpénétration des monomères (pour simuler un phénomène de frittage), une polydispersion du rayon de ceux-ci (type : log-normale), la distance d'apparition des monomères, etc. Une étude numérique a été conduite pour qualifier ce modèl et comparer différentes représentations utilisées pour définir les caractéristiques des agrégats (voir par exemple la Figure F.3).

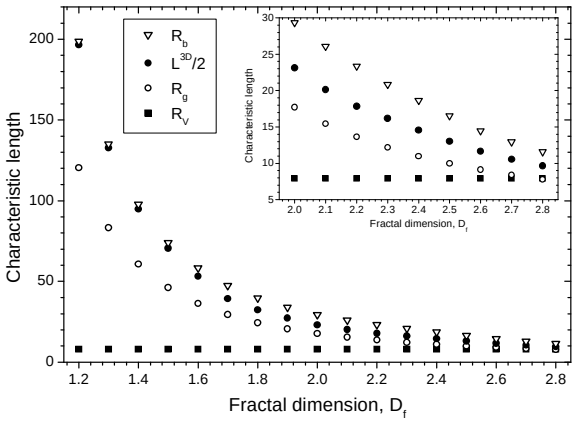

Figure F.3. Comparaison de quatre longueurs caractéristiques d'agrégats générés avec le code DLA : rayons de giration R_g, rayons en volume R_v, rayons de la sphère circonscrite R_b et longueur maximale de l'agrégat L^{3D}) ; $n_p = 500$.

Modèle de dôme géodésique (Buckyballs)

Ce modèle a été développé pour décrire la structuration en réseau, pentagonal et hexagonal, des agrégats de silice formés par évaporation de suspensions colloïdales (voir la Figure F.4). En effet, l'analogie formelle avec les fullerènes (ou Buckyballs), nous a conduit à modéliser ces agrégats comme des dômes géodésiques basés sur l'icosaèdre (composé de $n_{Face} = 20$ faces, $n_{Edg.} = 30$ segments et $n_{Vert.} = 12$ sommets) (Toure 2010). Dans ce modèle, les côtés de l'icosaèdre sont divisés en $n_i + 1$ segments de même longueur. Ces derniers servent à la définition des triangles réguliers qui divisent les faces de l'icosaèdre. Nous avons montré qu'en plaçant une nano sphère à chaque sommet du polyèdre ainsi formé, on forme une Buckyballs de n_p monomères : $n_{p,n_i=0} = n_{Ver}$; $n_{p,n_i>0} = n_{Ver} + n_i (n_i + 2) n_{Face} / 2$. Celle-ci est inscrite dans une sphère (ou diamètre externe de la Buckyball) dont l'expression du rayon a été établie. Vient ensuite une étape de projection des centres des nano sphères sur cette sphère circonscrite et une étape d'ajustement des diamètres des monomères, de façon à maximiser le nombre de contacts entre les monomères.

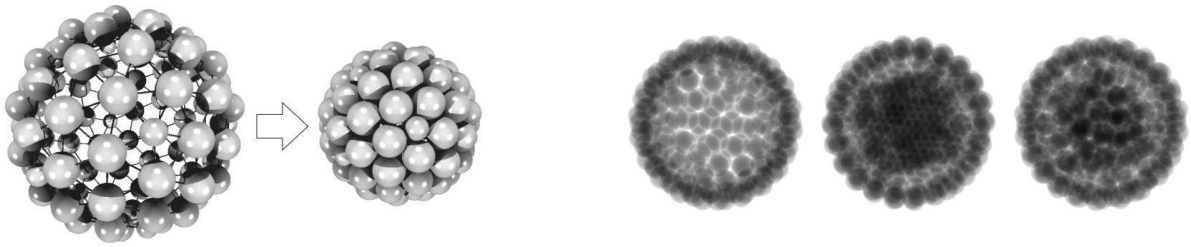

Figure F.4. A gauche : buckyball de $n_p = 92$ nano particules (forme dilatée et forme compacte) ; A droite, image MET synthétiques de buckyballs (a) creuse ($n_p = 162$), ou pleines : (b) Cœur hexagonal compact ($n_p = 162 + 113$ sphères, fraction volumique 52%) ou (c) Cœur fractal ($n_p = 162 + 72$ sphères, $D_f = 2.88$, fraction volumique 49%).

Chapitre 3: Modèles pour l'analyse fractale des images obtenues par microscopie électronique en transmission

L'analyse de la morphologie des agrégats, fractals ou non, est encore essentiellement basée sur le traitement d'images obtenues par microscopie électronique en transmission (MET). En effet, bien que les résultats obtenus sont souvent biaisés par la procédure d'analyse (Koylu et al. 1995; Chakrabarty et al. 2009; Ouf et al. 2010), cette approche permet d'accéder directement aux projections 2D de la morphologie des agrégats, tout en étant peu sensible aux propriétés de leur matériau (souvent mal connues). Ajoutons que les analyses fractales couramment réalisées sont incapables d'appréhender correctement les agrégats multi-fractals et les échantillons non homogènes. Dans la mesure où les résultats des techniques optiques sont souvent comparées aux analyses MET, ce chapitre est consacré à la remise à plat de la technique d'analyse fractale la plus utilisée, et l'introduction d'une nouvelle technique de traitement des images MET (Woźniak et al. 2012b). La résolution de ces techniques est testée sur des échantillons synthétiques et sur des données expérimentales (i.e. des suies formées par une flamme diesel (Yon et al. 2011)).

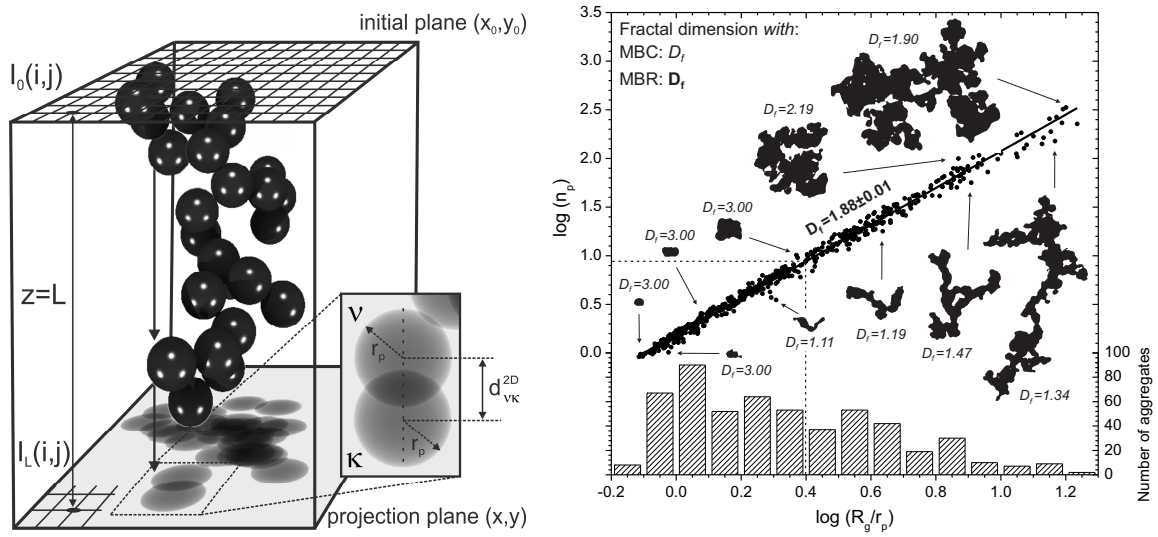

Figure F.5. (a) Visualisation avec le logiciel POV-Ray et image TEM simulée d'un agrégat synthétique avec $D_f = 1.50$, $n_p = 25$, $R_g / r_p = 6.27$; (b) Résultat de l'analyse des images-MET d'un échantillon expérimental de suies; avec les méthodes MBR et MBC (**Woźniak** et al. 2012b);

Modélisation des images MET

Dans une première partie, nous détaillons un modèle très simplifié de la formation des images MET. Dans celui-ci, le code DLA est utilisé pour produire des agrégats synthétiques dont les images en transmission sont déterminées à l'aide d'une loi d'absorption (des électrons) de type Beer-Lambert. Différents effets sont étudiés numériquement, comme les superpositions induites par la projection 2D, le seuillage des images MET, l'extraction de longueurs caractéristiques, etc.

Méthode d'analyse basée sur les caractéristiques du rectangle circonscrit (MBR)

La première méthode repose sur l'extraction et l'analyse des caractéristiques du rectangle circonscrit (MBR, longueur L^{2D} et largeur W^{2D}) à chaque agrégat fractal (Samson et al. 1987). Nous montrons que la relation couramment utilisée pour obtenir le rayon de giration des agrégats $R_g = \sqrt{L^{2D}W^{2D}} / \beta$, avec $\beta \approx 2.34$ (Koylu et al. 1995), n'est valable que pour de très petits agrégats dont la dimension fractale est de l'ordre de $\beta \approx 1.80$. De même, nous avons clairement établi que la dimension fractale, déduite de la pente d'une relation (linéaire) du type $\ln n_p = f\left(\sqrt{L^{2D}W^{2D}} / r_p\right)$ est une estimation fortement biaisée par la présence de monomères et très petits agrégats (dont la nature fractale est mise en doute). Ces travaux ont également permis d'obtenir des courbes de calibration numériques qui peuvent être utilisées pour corriger en partie ces biais (dépendance de β avec la dimension fractale mais aussi le nombre de monomères) (Woźniak et al. 2012b).

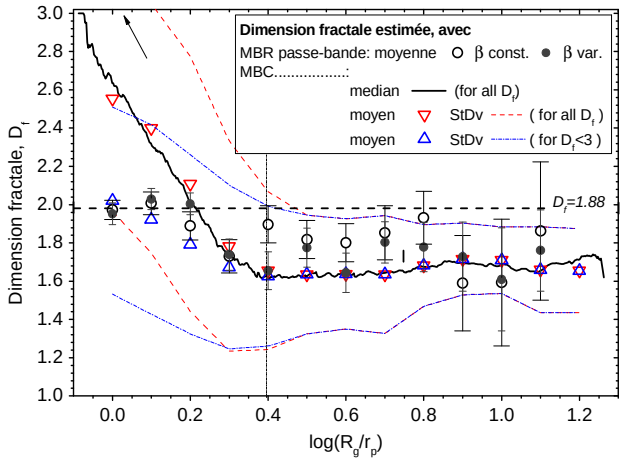

Figure F.6. Évolution de la dimension fractale d'échantillons de suies en fonction de leur granulométrie, selon la technique MBC et la technique MBR.

*Méthode basée sur une modification de la méthode par comptage de **boîtes** (MBC).*

La méthode par comptage de boîtes (Theiler 1990) consiste à établir le taux d'occupation d'un agrégat au sein du rectangle qui lui est circonscrit et ceci, à différentes échelles (analyses avec des boîtes de plus en plus petites : N_s boîtes à d'échelle L_s) : $D_f = -\lim_{L_s \to 0}\left(\ln N_s / \ln L_s\right)$. L'intérêt fondamental de cette approche est qu'elle permet de déterminer la dimension de chaque agrégat observé. En principe, elle permet donc d'analyser directement des échantillons non homogènes. En pratique, cette analyse multi-échelle est limitée par la taille finie des monomères et de l'agrégat lui-même. Pour pallier ces problèmes, nous avons introduit différents modifications à l'algorithme originel : les images MET des agrégats ne sont plus analysées que dans chaque rectangle circonscrit, les boîtes ne sont plus générées suivant un maillage cartésien mais suivant un schéma aléatoire (pour limier les effets de bord) et à chaque échelle le nombre de boîtes est normalisé; la dimension fractal n'est plus déduite du calcul d'une limite (physiquement inaccessible, (Foroutan-pour et al. 1999)) mais de la pente

de la courbe associée); au final, le code DLA est utilisé pour générer des courbes de calibration reliant cette pente à la dimension fractale attendue (Woźniak et al. 2012b).

Comparaison des deux méthodes

Toute une étude numérique est réalisée, à l'aide d'agrégats synthétiques, pour déterminer la résolution que l'on peut espérer avec ces deux méthodes (Figure F.6). Ces dernières ont également été testées sur un échantillon expérimental (suies, voir également les Figures F.1 et F.5). Les résultats de la Figure F.6 sont emblématiques de tous ceux obtenus. Avec la méthode MBR, l'estimation est anormalement bruitée et totalement différente suivant que l'on traite globalement l'échantillon ou que l'on réalise des analyses sur des sous-échantillons. A contrario, la méthode MBC restitue une estimation beaucoup plus continue (et donc physique), par ailleurs la dimension fractale estimée pour les agrégats intermédiaires et grands est également beaucoup plus faible ($D_f = 1.66 \pm 0.02$) que celle obtenue avec la méthode MBR globale ($D_f = 1.88 \pm 0.02$). Ce résultat va dans le sens de travaux récents reposant sur une approche différente (Chakrabarty et al. 2009).

Chapitre 4: Théories électromagnétiques et modèles de diffusion

Ce chapitre passe en revue les différents outils utilisés dans ce travail, pour modéliser les propriétés de diffusion des agrégats et inverser les données expérimentales.

La théorie de Lorenz-Mie

Cette théorie fait référence dans bien des domaines et notamment, pour la caractérisation optique de systèmes particulaires. La diffusion d'une onde plane harmonique par un diffuseur sphérique, isotrope, homogène, à matériau linéaire et sans propriété magnétique est résolu avec une méthode de séparation des variables. Cette théorie s'applique à des particules de toutes tailles et de tous indices, mais uniquement sphériques.

Théories de Rayleigh et Rayleigh-Gans-Debye (RGD)

Ces modèles asymptotiques ne sont validents que pour des particules dont le paramètre de taille x et l'indice complexe $\tilde{m}_p$ sont tels que, respectivement, $x \ll 1, \left|\tilde{m}_p\right| x \ll 1$ et $\left|\tilde{m}_p - 1\right| \ll 1$, $kd_p \left|\tilde{m}_p - 1\right| \ll 1$. En principe, la forme de la particule peut s'écarter de celle de la sphère. Leurs avantages principaux résident surtout dans la rapidité du calcul des diagrammes de diffusion et des section efficaces, ainsi que la description des comportements asymptotiques (p. ex. l'extinction des très petites particules est surtout liée à leur absorption avec $C_{p,abs} \propto r_p^3$ et $C_{p,sca} \propto r_p^6$).

Théorie de Rayleigh-Debye-Gans théorie pour les agrégats fractals (RDG-FA)

Cette théorie est une extension de la Théorie de Rayleigh-Debye-Gans. Elle permet de prendre en compte la nature fractale d'une particule. Pour ce faire, et en résumé, Dobbins et

Megaridis (Dobbins and Megaridis 1991) introduisent un facteur de forme $f\left(q,R_g\right)$ qui corrige, des effets morphologiques, les relations obtenues avec la RGD classique. On obtient notamment pour l'intensité diffusée par des agrégats éclairés par une onde de polarisation parallèle ou perpendiculaire: $I_{a,\perp}(\theta)=n_p^2 I_{p,\perp}(\theta) f\left(q,R_g\right)$; $I_{a,\parallel}(\theta)=I_{a,\perp}(\theta)\cos^2\theta$ et les sections efficaces correspondantes : $C_{a,abs}=n_p C_{p,abs}$; $C_{a,sca}=n_p^2 C_{p,sca} G\left(k,R_g,D_f\right)$; $C_{a,ext}=C_{a,abs}+C_{a,sca}$. Avec pour le facteur de forme, selon que l'on est dans le régime de Guinier $\left(q^2R_g^2\le 1.5D_f\right)$: $f\left(q,R_g\right)=\exp\left(-q^2R_g^2/3\right)$ ou fractal $\left(q^2R_g^2>1.5D_f\right)$: $f\left(q,R_g\right)=\left(q^2{R_g}^2\right)^{-D_f/2}$, où $q=2k\sin(\theta/2)$ est le vecteur diffusion, k et θ le vecteur d'onde et l'angle de diffusion respectivement. Nous avons mené une étude numérique pour évaluer le domaine de validité de la RDG-FA, en utilisant les résultats de la T-Matrice (voir plus loin) comme référence. Conformément aux hypothèses de base de la RGD (qui s'applique uniquement aux objets déphasant), on retrouve que ce domaine est très réduit et qu'il se limite aux agrégats petits et/ou peu denses (faible dimension fractale).

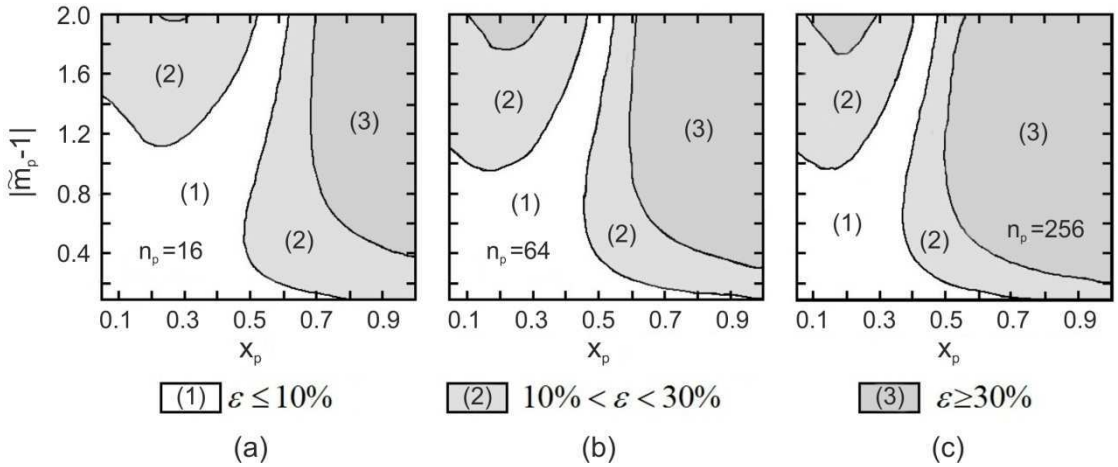

Figure F.7. Section efficace d'absorption de suies de dimension fractale $D_f=1.8$: écart entre les prédictions de la RDG-FA et ceux de la T-Matrice.

Théorie (ou méthode) de la T-Matrice

Cette méthode introduite par Watermann (Waterman 1965), qualifiée aussi de méthode d'annulation du champ (null-field method), permet de calculer les propriétés de diffusion des ondes électromagnétiques par des particules complexes (Mishchenko et al. 1996; Bohren and Huffman 1998; Auger et al. 2007). Elle est fondée sur le principe d'équivalence selon lequel le champ électromagnétique à l'extérieur d'une surface régulière *S*, est équivalent à celui qui serait produit par une distribution de courants superficiels électrique et magnétique portée par la surface *S*. A l'intérieur de *S*, les sources produisent un champ nul. On peut ainsi exprimer le champ total (incident + diffusé) à l'extérieur de *S* sous la forme d'intégrales de surfaces. Les champs incidents et la fonction de Green sont développés en harmoniques sphériques. Ce développement n'est pas valable sur *S* ; il l'est à l'intérieur d'une sphère inscrite dans *S*, ou à l'extérieur d'une sphère circonscrite à *S*. On fait alors l'approximation d'écrire les courants superficiels équivalents comme la somme des *N* premières harmoniques sphériques avec des

coefficients inconnus. A l'intérieur de la sphère inscrite, l'équation *E=0* se transforme en un système linéaire qui relie les coefficients inconnus des courants aux coefficients connus des champs incidents. On obtient d'autres relations en utilisant les conditions aux limites. Les coefficients du système matriciel (T-Matrice) résultant sont des combinaisons d'intégrales d'harmoniques sphériques sur *S*. Une fois ce système résolu, on connaît les courants superficiels et donc le champ diffusé. Le nombre *N* à utiliser dépend de la forme, de la taille et de l'indice de réfraction du diffuseur (sphère, ellipsoïde, cylindre tronqué, agrégat de sphères).

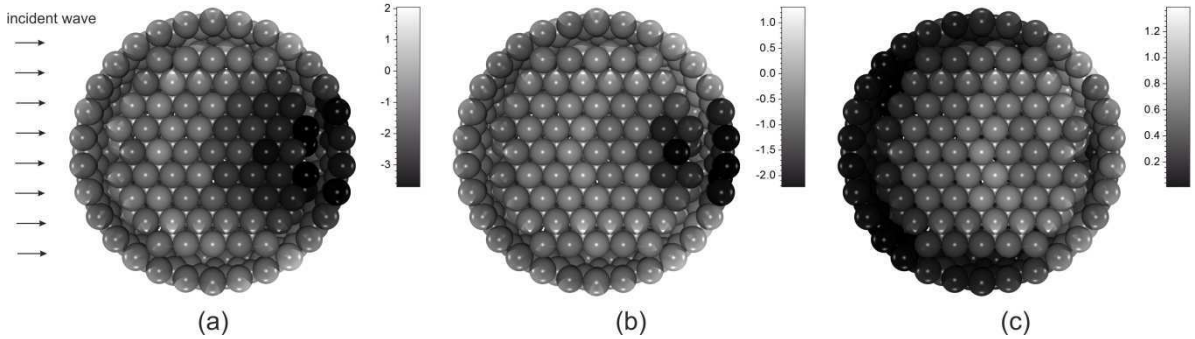

Figure F.8. Visualisations, dans le plan équatorial, du coefficient d'extinction net (positif ou négatif) des monomères au sein d'un buckyball composé de $n_{p,HC} = 749$ monomères de rayon $r_p = 40.5nm$; (a) $\lambda = 300nm$, (b) $\lambda = 400nm$, (c) $\lambda = 500nm$.

Différents codes de calcul sont en libre accès, pour ce travail nous avons utilisé celui développé par Mackowski et Mishchenko (Mackowski and Mishchenko 1996) et qui est mis à disposition sur le site internet du Goddard Institute for Space Studies de la NASA. Ce code, que nous avons nous même parallélisé, permet de calculer les propriétés globales de diffusion et d'absorption d'agrégats composés de plusieurs centaines de nano sphères. Il permet également de calculer les sections effectives d'extinction de chaque nano sphères, voir par exemple la Figure F.8.

Chapitre 5: Analyse des diagrammes de diffusion d'agrégats fractals

Ce chapitre traite de l'analyse des diagrammes de diffusion d'agrégats fractals, dans le but d'en déduire laeur dimension fractale et leur rayon de giration. Cette approche peut sembler très classique, néanmoins, dans la littérature, on ne trouve aucun détail sur une quelconque procédure d'extraction de ces deux quantités. Le but de ce chapitre est donc également de proposer des solutions (automatisées et reproductibles) et des éléments de réflexion sur cette approche.

Dans une première partie, nous introduisons deux algorithmes pour extraire la dimension fractale. Le premier algorithme, désigné par l'acronyme SSE (pour *Second Slope Estimation*), consiste à déduire directement la dimension fractale de l'analyse du taux de décroissance du diagramme de diffusion (ou Facteur Optique de Structure, OSF), au centre de la zone fractale. Cette dernière est simplement définie comme la zone située entre la zone de Guinier et la zone

de Porod. Le rayon de giration est obtenu à l'aide de l'analyse dite de Guinier (voir la Figure F.9 (a)), qui est bien documentée dans la littérature (Sorensen 2001). Cette approche ne donne des résultats satisfaisants que pour des agrégats dont le paramètre de taille est important $(qR_g > 5)$. Le second algorithme, désigné par l'acronyme FSE (pour *First Slope Estimation*), intègre une méthode itérative de recherche du centre de la zone fractale et l'utilisation de courbes de calibration (basées sur le modèle DLA et les résultats de la T-Matrice). Plus lourd à mettre en oeuvre que l'algorithme SSE, il est plus précis et permet d'analyser des agrégats beaucoup plus petits. De ce fait, le modèle FSE est considéré comme plus universel (voir la Figure F.9 (b)).

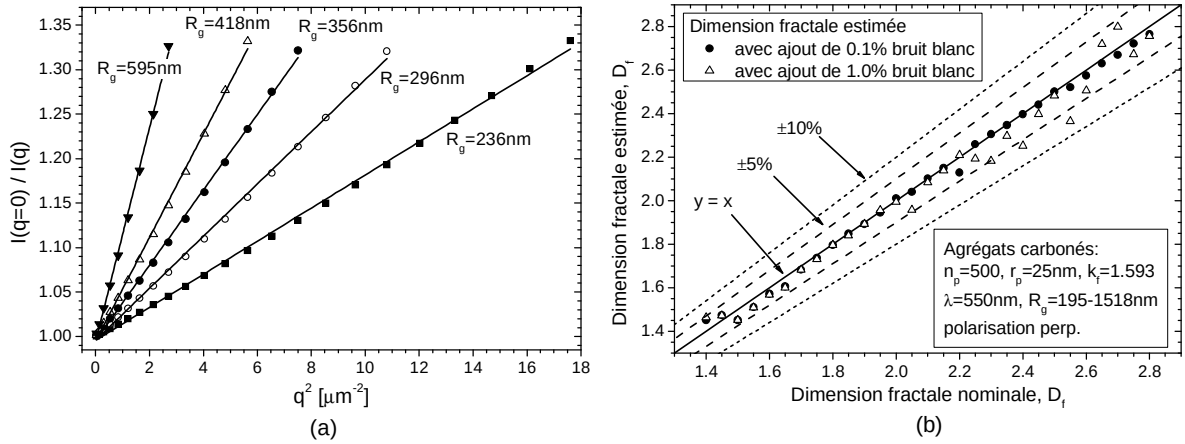

Figure F.9. (a) Analyse de Guinier d'agrégats fractals de SiO_2 ; (b) Dimension fractale estimée avec l'algorithme FSE (avec ou sens ajout d'un bruit blanc ; agrégats fractals de suies composées de 500 monomères).

Dans la deuxième partie de ce chapitre, nous nous intéressons à un problème qui semble avoir été totalement négligé dans la littérature : l'existence (et donc l'influence) de monomères libres sur l'analyse des diagrammes de diffusion des agrégats. Nos travaux révèlent l'importance des monomères libres. En effet, pour un taux de : un monomère libre pour un agrégat, la dimension fractale des agrégats peut en effet être sous-estimée de près 25%. Ces résultats préliminaires pourraient remettre en question bon nombre de travaux publiés.

Chapitre 6: Spectrométrie d'extinction

Ce chapitre détaille les travaux numériques et expérimentaux réalisés sur la spectrométrie d'extinction (LES), pour obtenir la distribution granulométrique et la concentration de différents systèmes nano particulaires.

Principe et principe d'inversion des spectres de la technique LES

En résumé, la technique LES repose sur une mesure de la transmission spectrale d'un faisceau collimaté, à large spectre, ayant traversé le milieu particulaire (défini par sa largeur, la concentration et l'extinction des particules). En régime de diffusion simple, cette transmission

est simplement modélisée par une loi de type Beer-Lambert. L'extinction d'un nuage polydisperse est décrite comme une intégrale de Fredholm du premier type qui dépend de la distribution granulométrique et des propriétés optiques intrinsèques des particules. Le noyau (matrice d'extinction) de l'intégrale est calculé en utilisant la T-Matrice avec au choix, le modèle DLA ou celui des Buckyballs, voire celui d'une sphère (milieu effectif). La procédure de régularisation principale repose repose sur la méthode introduite par Twomey-Philips (Twomey 1979). L'inversion est réalisée au moyen d'une méthode de moindres carrés à solutions positives.

Résultats numériques

Une étude numérique apporte des éléments d'appréciation sur l'évolution des spectres d'extinction et de transmission avec la dimension fractale, le rayon de giration et l'indice de réfraction des agrégats. Celle-ci montre que la LES est assez peu sensible à la dimension fractal des agrégats. En régime de diffusion simple, la plage de mesure des concentrations est de l'ordre de $1\times10^{13}-5\times10^{15}$ en nombre et $5\times10^{-8}-5\times10^{-6}$ en volume (ces concentrations sont données, à titre indicatif, pour les buckyballs de silice et une distance de 1m).

Études expérimentales

Après une description du montage optique, cette dernière partie présente les travaux expérimentaux réalisés avec la technique LES sur des aérosols de *buckyballs* et des agrégats de nano particules de tungstène, puis sur des nano agrégats formés dans des plasmas poussiéreux.

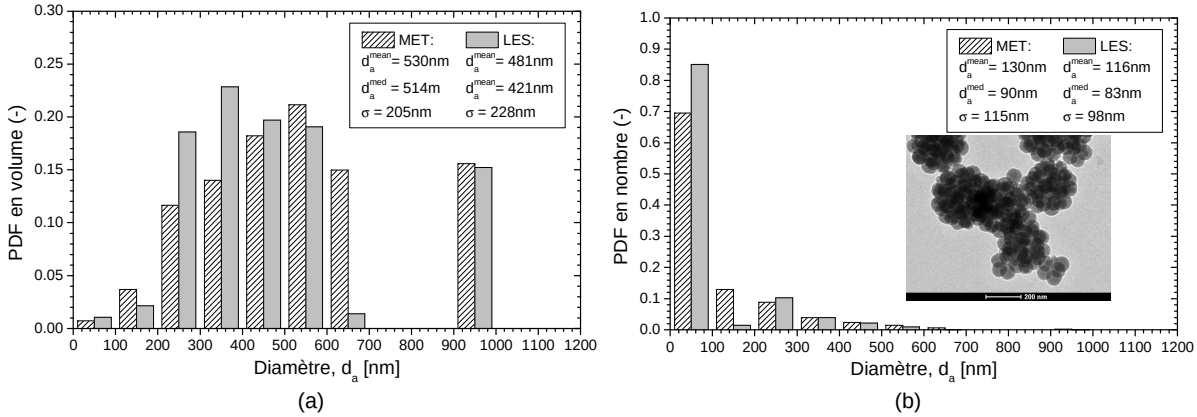

Figure F.10. Granulométrie des Buckyballs selon les analyses MET et LES : (a) en volume et (b) en nombre.

Les premiers agrégats sont formés par pulvérisation, sous forme de gouttelettes microniques, de différentes suspensions colloïdales de silice. Il semble que nous ayons été les premiers à avoir observé et proposé un mécanisme de formation de ces agrégats dotés d'un pavage de surface pentagonal/hexagonal. Nous qualifions ceux-ci de *buckyballs* de silice (voir aussi les Figures F.1, F.5 et F8). La Figure F.10 montre une comparaison type entre analyses MET et

LES (Barbosa et al. 2012). Les travaux expérimentaux, plutôt satisfaisants, ont également confirmé la nécessité d'augmenter la plage spectrale (vers l'infrarouge) de nos analyses si l'on veut pouvoir caractériser les agrégats produits par les suspensions non diluées (diamètres supérieurs au micromètre).

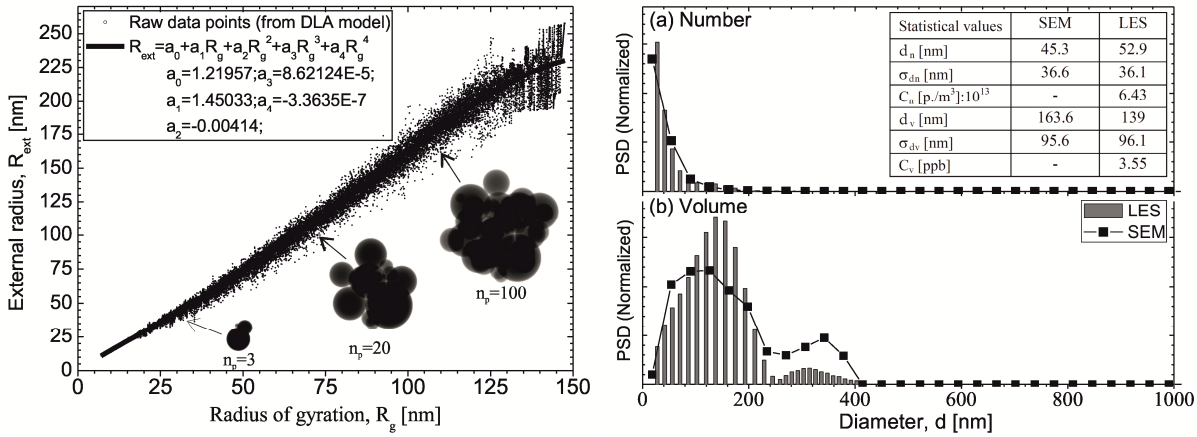

Figure F.11. Exemple de courbe de calibration numérique et comparaisons des analyses granulométriques MEB/LES des agrégats de tungstène.

L'étude expérimentale menée sur les agrégats de tungstène avait pour but d'apporter des éléments d'appréciation sur l'applicabilité de la technique LES à la caractérisation d'agrégats (poussières) de tungstène au voisinage des composants faces au plasma (parois des tokamaks) et/ou lors du nettoyage de ces surfaces par les techniques d'ablation laser. Les aérosols de tungstènes étaient formés par évaporation de suspensions de nano billes de tungstène. La forte luminance et les ondes de choc générées par les techniques d'ablation ont été simulées par la génération de plumes (à l'aide d'un laser Nd-YAG de forte fluence) juste au-dessus d'une paroi métallique. Ces investigations ont établi que la technique LES fonctionne très bien en proche paroi (malgré le blocage et la diffraction de plus de 80% de l'énergie du faisceau sonde) et que, pour les paramètres testés, les effets induits par la plume étaient négligeables (a l'exception de la raie d'émission du laser de puissance, dont la contribution au spectre LES doit être soustraite avant inversion). La Figure F.11 illustre deux résultats types des analyses morphologiques (analyses d'images MEB et d'agrégats synthétiques) et granulométrique (à plus de 10mm de la paroi) (Onofri et al. 2012b).

Dans le cadre d'une collaboration avec l'équipe du prof. Boufendi, nous avons réalisé différentes études sur les mécanismes de croissance des poudres dans un plasma poussiéreux (décharge Argon-Silane basse pression, (Boufendi and Bouchoule 1994)). La technique LES possède l'incomparable avantage, face aux analyses MEB/MET classiques, de permettre un suivi temporel de la croissance des poudres, et de restituer des concentrations en nombre et volume. Elle nous a également permis de mener des études paramétriques (variation de la puissance électrique, mélange et pression des gaz,...) qui seraient quasiment impossibles à réaliser avec les analyses par prélèvement. La Figure F.12 montre une image TEM des

poudres obtenues après 10 s, ainsi qu'un profil de croissance type. On constate que l'accord est très bon (le décrochage vers 10 s est attribué aux analyses MEB). Ces travaux ont également montré qu'à l'avenir, il serait souhaitable de mener études ciblées sur la détermination de la l'indice de réfraction des poudres (Onofri et al. 2011b).

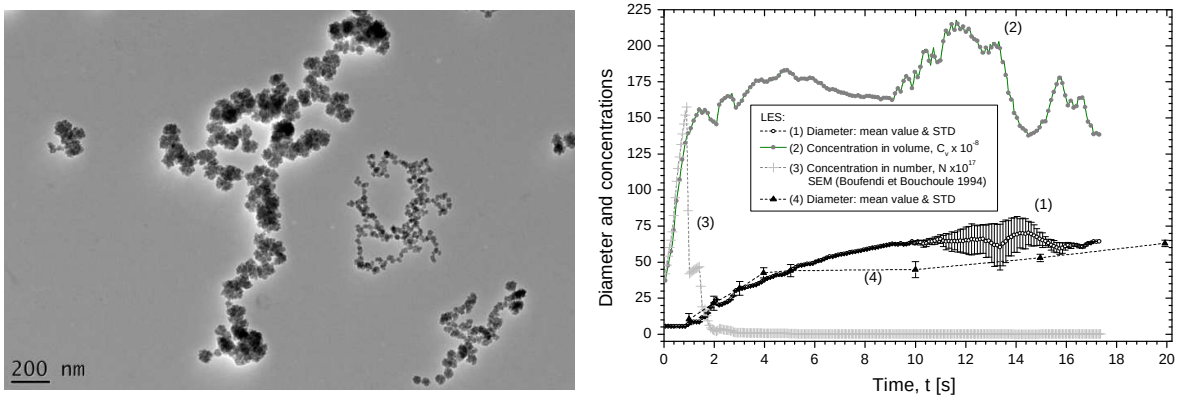

Figure F.12. A gauche : image TEM des poudres déposées (et agrégées) sur la grille d'analyse ; A droite : comparaison des analyses TEM par prélèvement des mesures LES in-situ dans une décharge Argon-Silane basse pression.

Chapitre 7: Conclusion et Perspectives

Ce travail de thèse évalue et apporte différentes solutions pour caractériser optiquement la granulométrie et la concentration de suspensions, aérosols et plasmas poussièreux. Différents outils ont ainsi été développés pour décrire la morphologie d'agrégats à partir d'images de microscopie électronique. Ces outils ont également été utilisés pour produire des agrégats synthétiques, eux-mêmes utilisés pour comparer les prédictions des modèles de diffusion. Nous avons également developpé différentes solutions et algorithmes pour analyser de manière reproductible les diagrammes de diffusion (facteur de structure optique) ainsi que pour inverser les spectres d'extinction. Les tests expérimentaux réalisés avec la technique LES (aérosols de silice et tungstène, aggrégats de silicium) ont confirmé le bien fondé de notre démarche et les potentialités de la technique LES. Outre les applications, les perspectives à ce travail portent sur l'amélioration des techniques de régularisation et d'inversion, des études expérimentales sur la détermination de l'indice de réfraction complexe des nano agrégats.

ABSTRAKT W JĘZYKU POLSKIM (ABSTRACT IN POLISH LANGUAGE)

Rozdział 1: Wstęp

Nanocząstki i agregaty nanocząstek są obecnie przedmiotem intensywnego zainteresowania ośrodków naukowych na całym świecie. Jest to ściśle związane z ich unikalnymi i niezwykle interesującymi właściwościami znajdującymi coraz szersze zastosowanie w wielu dziedzinach życia. Istnieją dwa zasadnicze czynniki, które sprawiają, że nanocząstki wykazują odmienne właściwości od materiałów makroskopowych: efekty powierzchniowe oraz efekty kwantowe (Buzea et al. 2007). Na rysunku P.1 przedstawiono przykładowe agregaty nanocząstek.

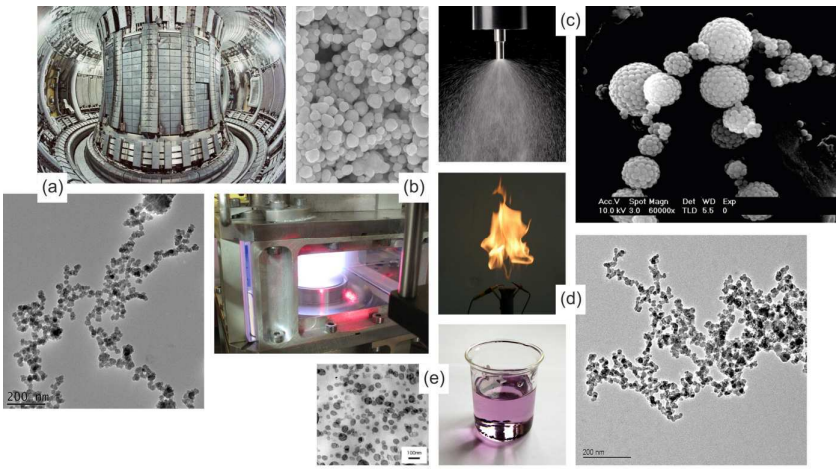

Rysunek P.1. Występowanie nanocząstek: (a) reaktor termojądrowy (tokamak), (b) piec plazmowy do produkcji nanoproszków, (c) aerozol nanocząstek, (d) płomień i sadza, (e) roztwór koloidalny i przebiegający w nim proces agregacji.

Efekty powierzchniowe są ściśle związane z bardzo dużym stosunkiem powierzchni czynnej nanocząstek do ich objętości. Sprawia to, że substancje chemiczne w postaci nanocząstek są znacznie bardziej reaktywne niż te same związki w postaci makroskopowej. Efekty kwantowe są natomiast spowodowane niewielkimi rozmiarami cząstek i objawiają się jako szereg

zjawisk, które zwykle charakteryzują atomy lub molekuły (Roduner 2006). Przykładowo, podobnie jak pojedyncze atomy, kropki kwantowe przyjmują określone wartości spektrum energetycznego z uwagi na pułapkowanie elektronów, a zmiany ich całkowitego ładunku są możliwe jedynie o skwantowane wartości (Buzea et al. 2007).

Kluczowym zadaniem niezbędnym do zrozumienia i monitorowania, a co za tym idzie kontroli mechanizmów agregacji nanocząstek w różnych systemach jest charakterystyka rozkładu wielkości cząstek (particle size distribution, PSD) oraz ich koncentracji (C_n). Do niedawna najczęściej stosowanymi metodami w charakterystyce właściwości nano- i mikrocząstek były próbkowanie i analiza off-line (np. mikroskopia elektronowa, dyfrakcja elektromagnetyczna, itp.). Niemniej jednak dla bardzo reaktywnych i delikatnych obiektów jakimi są omawiane agregaty, niezawodność i powtarzalność tego typu pomiarów jest wysoce dyskusyjna. Dlatego też optyczne układy pomiarowe jako nieinwazyjne i wystarczająco szybkie zapewniają większą dokładność pomiarów.

Opracowano szereg różnych metod optycznych umożliwiających analizę układów cząstek (Xu 2002). Ich wykorzystanie do opisu agregatów nie jest jednak zadaniem łatwym. Analiza optyczna wymaga bowiem zastosowania odpowiedniego modelu morfologicznego cząstek występujących w analizowanym układzie oraz właściwego modelu rozproszenia światła.

Rozdział 2 niniejszej pracy wprowadza dwa modele opisujące morfologię agregatów nanocząstek: model fraktalny i tzw. model „Buckyballs". W rozdziale 3 przedstawiono algorytmy zrealizowane w celu udoskonalenia opartych na mikroskopii elektronowej sposobów analizy agregatów. Opracowane metody stanowią punkt odniesienia dla wyników uzyskiwanych technikami optycznymi. Rozdział 4 omawia różne teorie i aproksymacje wykorzystywane do modelowania właściwości rozproszenia i absorpcji światła przez agregaty cząstek. Rozdział 5 wprowadza dwa algorytmy opracowane w celu analizy diagramów rozproszenia i estymacji parametrów fraktalnych. Rozdział 6 pracy omawia numeryczne i eksperymentalne wyniki uzyskane za pomocą Spektrometrii Ekstynkcji Światła (LES) dla różnych ośrodków doświadczalnych. Rozdział 7 zawiera wnioski i rekomendacje dla przyszłych prac badawczych wynikające z niniejszej pracy.

Rozdział 2: Modele agregatów cząstek

Rozdział 2 niniejszej pracy przedstawia fizyczne podstawy procesu agregacji nanocząstek. W szczególności traktuje on o agregacji limitowanej dyfuzją (DLA), agregacji klastrów limitowanej dyfuzją (DLCA) oraz agregacji klastrów limitowanej reakcją (RLCA). W celu opisu morfologii agregatów nanocząstek zrealizowano optymalizowane oprogramowanie DLA oraz opracowano model do opisu tzw. agregatów „Buckyballs".

Agregacja Limitowana Dyfuzją (DLA)

Klasyczny model DLA zakłada mniej lub bardziej dokładną, symulację zjawisk zachodzących w układzie cząstek (ruchy Browna, kolizje, nierozerwalne łączenie się pojedynczych cząstek, itp.), lecz nie kontroluje parametrów agregatów na etapie ich tworzenia. Optymalizowane oprogramowanie wykonane w ramach niniejszej pracy umożliwia natomiast zachowanie wszystkich parametrów fraktalnych (z określoną dokładnością) na każdym etapie agregacji. Pozwala to na uniknięcie generacji multi-fraktali (tzn. agregatów o różnych parametrach w różnej skali bądź różnym obszarze agregatu) oraz zapewnia powtarzalność uzyskiwanych wyników. Aby opisać matematycznie morfologię agregatów cząstek wykorzystano tzw. równanie fraktalne (Witten and Sander 1981):

$$n_p = k_f \left(\frac{R_g}{r_p} \right)^{D_f}, \tag{P.1}$$

w którym n_p jest liczbą pojedynczych cząstek w agregacie (zwanych również monomerami), r_p średnim promieniem cząstek, D_f wymiarem fraktalnym, k_f współczynnikiem skalującym, a R_g promieniem bezwładności agregatu. Promień bezwładności jest wymiarem charakterystycznym agregatu określającym w ogólny sposób rozkład masy w jego strukturze. Definiowany jest on jako średniokwadratowa odległość cząstek od środka masy układu:

$$R_g = \sqrt{\frac{1}{n_p} \sum_{n=1}^{n_p} (\mathbf{r_0} - \mathbf{r_n})^2}, \tag{P.2}$$

gdzie r_0 i r_n są wektorami określającymi odpowiednio pozycję środka masy układu i n-tego monomeru w trójwymiarowej przestrzeni euklidesowej. Wobec licznych rozbieżności występujących w literaturze dotyczących wartości współczynnika skalującego k_f, przyjęto jego stałą wartość $k_f = 1.593$ wyznaczoną z wykorzystaniem układu heksagonalnego monodyspersyjnych cząstek (wymiar fraktalny agregatu $D_f = 3.00$). Rysunek P.2 przedstawia przykładowe agregaty wygenerowane za pomocą wykonanego oprogramowania.

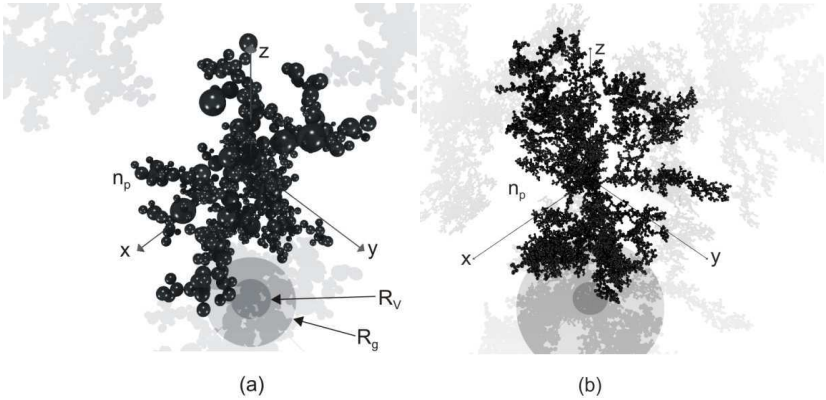

Rysunek P.2. Wygenerowane numerycznie agregaty fraktalne o następujących parametrach: (a) $n_p = 500$ monomerów (rozkład logarytmiczno-normalny, $\sigma_p = 0.5$), $D_f = 2.00$, $R_g = 17.71$, (b) $n_p = 10000$ monomerów monodyspersyjnych, $D_f = 2.00$, $R_g = 79.22$.

Na rysunku P.3 porównano różne wymiary charakterystyczne agregatów wygenerowanych za pomocą oprogramowania DLA: promień bezwładności R_g, promień objętości R_v, promień najmniejszej sfery ograniczającej agregat R_b, oraz maksymalną długości agregatu w przestrzeni L^{3D}.

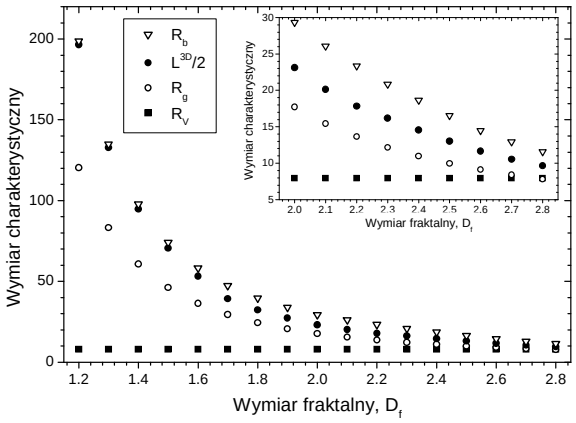

Rysunek P.3. Porównanie różnych wymiarów charakterystycznych agregatów zawierających $n_p = 500$ monomerów wygenerowanych z wykorzystaniem oprogramowania DLA: promień bezwładności R_g, promień objętości R_v, promień najmniejszej sfery ograniczającej agregat R_b oraz maksymalnej długości agregatu w przestrzeni L^{3D}.

Model „Buckyball”

Gęsto upakowane agregaty o regularnej strukturze (patrz rysunek P.1 (c)) wytworzono na stanowisku pomiarowym podczas osuszania aerozolu zawierającego roztwór koloidalny dwutlenku krzemu (krzemionki) (Onofri et al. 2012a). Do opisu ich morfologii opracowano model oparty na dwudziestościanie foremnym (Toure 2010). Umożliwia on budowanie szeregu agregatów o skwantowanej liczbie cząstek. Pierwszy z szeregu jest agregat zawierający $n_p = 12$ monomerów. Powstaje on przez umieszczenie pojedynczych monomerów w każdym wierzchołku dwudziestościanu. W celu budowy większego agregatu, każda krawędź dwudziestościanu jest dzielona na $n_i + 1$ odcinków równej długości, gdzie $n_i \geq 0$ jest liczbą naturalną określającą nową liczbę wierzchołków wprowadzanych na każdej krawędzi. Nowe wierzchołki są łączone za sobą za pomocą linii równoległych do istniejących krawędzi. W ten sposób na każdej ścianie powstaje n_i^2 -nowych trójkątów równobocznych, a całkowita liczba wierzchołków jest równa n_p. Można zauważyć, że liczba n_p zmienia się w następujący sposób:

$$n_{p,n_i=0} = n_{Vert.}; \quad n_{p,n_i>0} = n_{Vert.} + n_{Face}\left(\frac{3n_i}{2} + n_{c,n_i}\right), \tag{P.3}$$

gdzie $n_{Vert.}$ oznacza liczbę wierzchołków, n_{Face} liczbę ścian, a n_{c,n_i} jest liczbą nowych wierzchołków powstałych na ścianie dwudziestościanu foremnego. W celu uzyskania dużych agregatów o kształcie sferycznym wierzchołki trójkątów równobocznych znajdujące się wewnątrz ścian dwudziestościanu są rzutowane na sferę opisaną na dwudziestościanie. Ostatnim elementem algorytmu jest optymalizacja promienia monomerów, który jest

zwiększany iteracyjnie od zera do momentu aż nastąpi styk monomeru, z którymś z sąsiadujących.

Podczas prac eksperymentalnych zauważono, że większość agregatów jest wypełniona monomerami, dlatego też opracowano dwie metody wypełniania pustych struktur. Pierwsza z nich polega na wykorzystaniu agregatu fraktalnego o największym możliwym do wygenerowania wymiarze fraktalnym w opracowanym oprogramowaniu DLA ($D_f = 2.88$). Druga wykorzystuje agregat o układzie heksagonalnym monomerów ($D_f = 3.00$). Rysunek P.4 przedstawia przykładowy agregat zawierający $n_p = 92$ monomery oraz syntetyczne obrazy TEM wykonane za pomocą opracowanego oprogramowania.

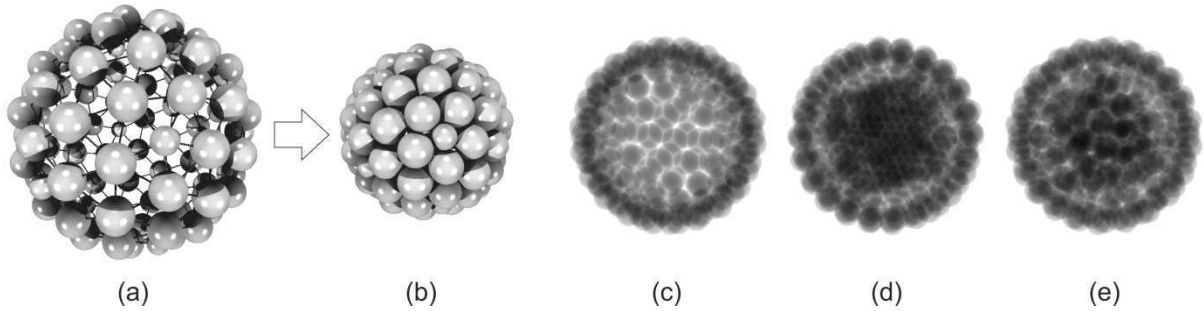

Rysunek P.4. Agregat „Buckyball" o $n_p = 92$ monomerów: (a) rozszerzony, (b) właściwy agregat. Sztuczne obrazy TEM wykonane z wykorzystaniem zrealizowanego oprogramowania: (c) pusty agregat, (d) agregat wypełniony heksagonalną strukturą monomerów ($n_p = 162 + 113$) oraz (e) model wypełniony agregatem fraktalnym ($n_p = 162 + 72$).

Rozdział 3: Metody analizy agregatów fraktalnych oparte na zdjęciach TEM

W rozdziale 3 niniejszej pracy omówiono dwie metody wykrywania zależności pomiędzy wielkością oraz wymiarem fraktalnym niewielkich agregatów cząstek w oparciu o dwuwymiarowe zdjęcia z Transmisyjnej Mikroskopii Elektronowej (TEM) (Woźniak et al. 2012b). Zostały one opracowane jako metoda referencyjna dla pomiarów wykorzystujących rozproszenie światła. Pierwsza z metod (powszechnie stosowana w literaturze) nazwana w pracy metodą Najmniejszego Kwadratu Ograniczającego (MBR) oparta jest na całkowitej analizie wszystkich agregatów w różnej skali, podczas gdy druga z nich (Zmodyfikowany Algorytm Pudełkowy, MBC) polega na analizie samopodobieństwa każdego z agregatów. Obie metody zostały przetestowane z wykorzystaniem próbek eksperymentalnych agregatów sadzy (Yon et al. 2011) jak również obrazów TEM wygenerowanych numerycznie z pomocą wykonanego oprogramowania.

Rysunek P.5 (a) przedstawia wizualizację 3D wygenerowanego numerycznie agregatu fraktalnego oraz powstawanie syntetycznego obrazu TEM. Rysunek P.5 (b) przedstawia wyniki pomiarów dla 543 agregatów z badanej próbki, w szczególności: (i) rozkład wielkości znormalizowanego promienia bezwładności, (ii) typowe obrazy agregatów po binaryzacji

wraz z wymiarami fraktalnymi wyznaczonymi z użyciem algorytmu MBC oraz (iii) wymiar fraktalny całej próbki wyznaczony z użyciem konwencjonalnej metody MBR. Wykorzystując algorytm MBR oszacowano typowy dla agregatów sadzy (Diesel soot) wymiar fraktalny: $D_f = 1.88 \pm 0.01$ (np. (Yon et al. 2011)). Już na pierwszy rzut oka można przypuszczać, że najmniejsze agregaty mają znacznie większy wymiar fraktalny niż największe. W celu sprawdzenia czy taka korelacje faktycznie istnieje (tzn. próbki eksperymentalne są multifraktalami) należy wyznaczyć wymiar fraktalny agregatów w różnej skali, jak to ma miejsce w przypadku algorytmu MBC.

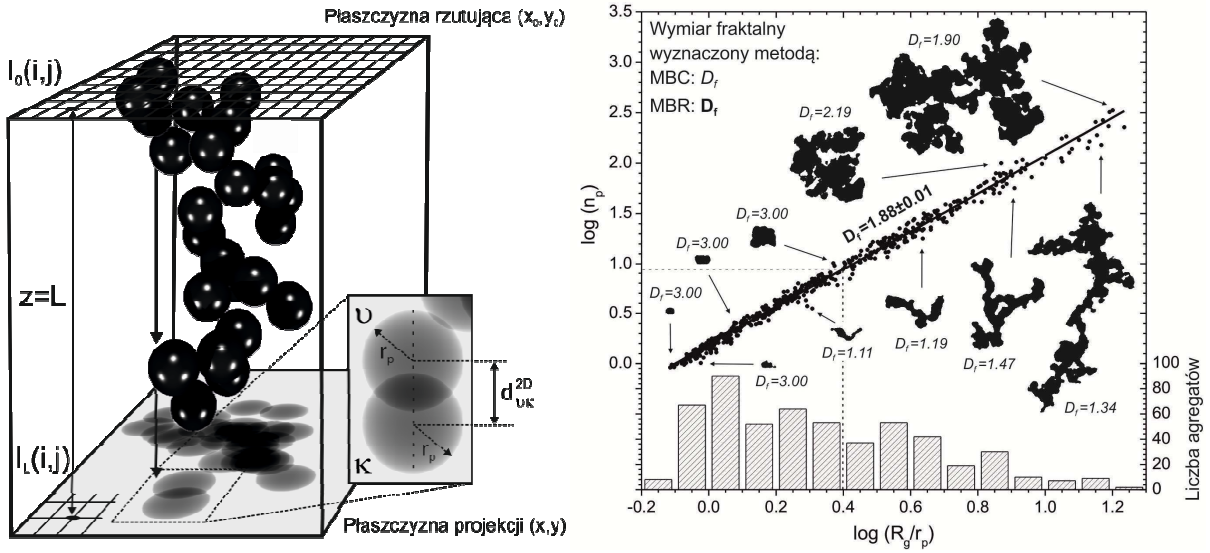

Rysunek P.5. (a) Wizualizacja 3D wygenerowanego numerycznie agregatu fraktalnego (parametry: $D_f = 1.50$, $n_p = 25$, $R_g / r_p = 6.27$) oraz powstawanie syntetycznego obrazu TEM, (b) Analiza TEM eksperymentalnych próbek agregatów sadzy (diesel soot): rozkład wielkości znormalizowanego promienia bezwładności oraz estymacja wymiaru fraktalnego z wykorzystaniem metod MBR i MBC (Woźniak et al. 2012b).

Rysunek P.6 przedstawia wyniki pomiarów eksperymentalnych próbek agregatów sadzy z wykorzystaniem algorytmów MBR i MBC. W analizie MBR wartość średnia, mediana oraz odchylenia standardowe D_f zostały wyznaczone dla mniejszych przedziałów o szerokości pasma $\log\left(R_g / r_p\right) = \pm 0.05$. W celu oszacowania wartości średniej rozważono dwa przypadki: brano pod uwagę wszystkie agregaty lub tylko te, które spełniają założenie $D_f < 3$ (punkty poza danym obszarem były traktowane jako błędy metody MBC).

Na podstawie przedstawionych wyników można wyciągnąć kilka ważnych wniosków. Przede wszystkim, dla małych agregatów $\left(\log\left(R_g / r_p\right) \le 0.4\right)$ średnia wartość wymiaru fraktalnego rośnie ze spadkiem wartości R_g / r_p. Przykładowo, dla $\log\left(R_g / r_p\right) \approx 0$ uzyskano $D_f \approx 2.05$ oraz $D_f \approx 2.55$ w zależności tego czy brane były pod uwagę wszystkie punkty pomiarowe czy tylko te spełniające założenie $D_f < 3$. Podobna zależność była zauważona przy analizie z wykorzystaniem algorytmu MBR. Dla średnich i dużych agregatów, rysunek P.6 pokazuje, że wykorzystując algorytm MBC nie uzyskano jednak stałej wartości wymiaru fraktalnego

$D_f = 1.66 \pm 0.04$ dla $\log\left(R_g / r_p\right) \geq 0.4$ oszacowanej wcześniej jako średnia z wszystkich pomiarów.

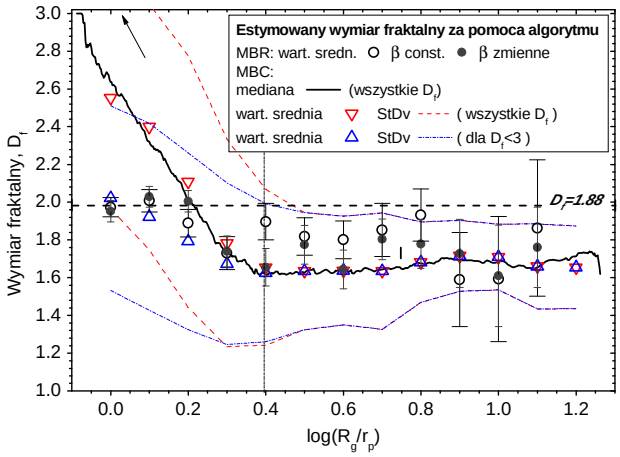

Rysunek P.6. Algorytm MBC i pasmowy MBR zastosowane do próbek eksperymentalnych: porównanie zmian w wymiarze fraktalnym w funkcji znormalizowanego promienia bezwładności.

Na podstawie przedstawionych pomiarów i symulacji zauważono, że algorytm MBC zapewnia mniej zaszumioną estymację zmian wymiaru fraktalnego w funkcji wielkości agregatów, dając równocześnie kryterium do odrzucenia agregatów nie spełniających wymogów samopodobieństwa. Stosując tę metodę uzyskano średni wymiar fraktalny w próbce sadzy znacznie mniejszy ($D_f = 1.66 \pm 0.02$) niż w klasycznej analizie ($D_f = 1.88 \pm 0.02$).

Rozdział 4: Teorie i modele rozproszenia światła

Rozdział 4 stanowi przegląd teorii i metod wykorzystywanych do wyznaczania rozproszenia światła przez różnego rodzaju cząstki. W szczególności skupiono się na algorytmach pozwalających wyznaczenie charakterystyk rozproszenia światła przez agregaty nanocząstek. Przedstawiono zatem teorię Lorenza-Mie oraz oparte na teorii Rayleigha aproksymacje, tj. RGD i RDG-FA. W ostatniej części rozdziału 4 omówiono teorię T-Matrix oraz pokazano przykładowe wyniki uzyskane z jej wykorzystaniem.

Teoria Lorenza-Mie (LMT)

Teoria LMT jest jedną z najpopularniejszych teorii rozproszenia światła. Często stosowana jest jako rozwiązanie referencyjne podczas tworzenia nowych teorii i aproksymacji. W celu wyznaczenia rozproszenia światła przez sferyczną, izotropową, homogeniczną cząstkę, LMT wykorzystuje metodę separacji zmiennych w sferycznym układzie współrzędnych. Teoria ta może być używana w celu opisu rozproszenia światła przez cząstki wykonane z różnych materiałów, o różnej wielkości i dla bardzo szerokiego zakresu długości padającej fali świetlnej. Największym ograniczeniem jest kształt cząstek, który może być tylko sferyczny.

Teoria Rayleigha

Zakłada, że homogeniczna i izotropowa cząstka sferyczna, której promień jest dużo mniejszy od długości padającej fali świetlnej, może być traktowana jako oscylujący dipol generujący fale elektromagnetyczne w określonym kierunku. Warunki stosowalności teorii Rayleigha wyrażają następujące zależności (Bohren and Huffman 1998; Xu 2002): $x_p \ll 1$ oraz $\left|\tilde{m}_p\right| x_p \ll 1$, gdzie $x_p = 2\pi r_p / \lambda$ oraz $\tilde{m}_p$ wyrażają odpowiednio parametr Mie oraz zespolony współczynnik załamania światła danej cząstki.

Teoria Rayleigha-Gansa-Debyea (RGD)

Teoria RGD jest rozwinięciem teorii Rayleigha poszerzającą możliwości jej stosowania. Powstała w celu opisu układów, w których cząstki są na tyle duże, że nie mogą być traktowane jako pojedyncze dipole. Jeżeli jednak cząsteczka spełnia warunki wyrażone przez następujące równania: (Bohren and Huffman 1998): $\left|\tilde{m}_p - 1\right| \ll 1 \quad kd_p \left|\tilde{m}_p - 1\right| \ll 1$ (w których d_p określa średnicę cząstki a $k = 2\pi / \lambda$ jest tzw. liczba falową), to może być analizowana jako zbiór pojedynczych dipoli i po uwzględnieniu elementu określającego przesunięcie fazowe, rozproszenie światła da się opisać za pomocą relatywnie prostych zależności. Największą zaletą teorii RGD jest możliwość wyznaczania diagramów rozproszenia oraz profili ekstynkcji w bardzo krótkim czasie. Dla małych cząstek w porównaniu do długości padającej fali świetlnej ekstynkcja wynika głównie z absorpcji ($C_{p,abs} \propto r_p^3$ oraz $C_{p,sca} \propto r_p^6$).

Teoria Rayleigha-Debya-Gansa dla agregatów fraktalnych (RDG-FA)

Teoria RDG-FA stanowi rozszerzenie teorii RGD umożliwiające analizę agregatów nanocząstek. Idea leżąca u podstaw teorii RDG-FA zakłada, że do analizy agregatów nie jest konieczna znajomość położenia wszystkich monomerów. Parametry agregatu są opisane w sposób „globalny" za pomocą parametrów fraktalnych takich jak D_f, k_f, R_g, n_p oraz r_p.

Zgodnie z aproksymacją RDG-FA natężenie światła rozproszonego w funkcji kąta rozproszenia θ, może zostać wyznaczone dla prostopadłej i równoległej polaryzacji światła jako (Dobbins and Megaridis 1991):

$$\begin{aligned} I_{a,\perp}(\theta) &= n_p^2 I_{p,\perp}(\theta)\, f\left(q, R_g, D_f\right) \qquad \text{(a)} \\ I_{a,\parallel}(\theta) &= I_{a,\perp}(\theta)\cos^2\theta \qquad \text{(b)} \end{aligned} \tag{P.4}$$

gdzie $I_{p,\perp}(\theta)$ wyraża rozproszenie światła dla pojedynczej cząstki sferycznej według teorii Rayleigha. Funkcja $f\left(q, R_g, D_f\right)$ w zależności od analizowanego obszaru (Dobbins and Megaridis 1991), (tj. (a) w obszarze Guiniera (dla małych kątów rozproszenia) oraz (b) w obszarze fraktalnym (dla dużych kątów rozproszenia)) dana jest równaniem:

$$\begin{aligned} f\left(q, R_g, D_f\right) &= \exp\left(-\frac{q^2 R_g^2}{3}\right), \quad q^2 R_g^2 \le 1.5 D_f \text{ (obszar Guiniera)} \qquad \text{(a)} \\ f\left(q, R_g, D_f\right) &= \left(q^2 R_g{}^2\right)^{-D_f/2}, \quad q^2 R_g^2 > 1.5 D_f \text{ (obszar fraktalny)} \qquad \text{(b)} \end{aligned} \tag{P.5}$$

gdzie q jest amplitudą wektora rozproszenia opisaną zależnością $q = k\sin(\theta/2)$, w której k i θ oznaczając odpowiednio liczbę falową i kąt rozproszenia. Całkowita absorpcja, rozproszenie i ekstynkcja światła dla agregatu zawierającego n_p cząstek są opisane następującą zależnością:

$$\begin{aligned} C_{a,abs} &= n_p C_{p,abs} && \text{(a)} \\ C_{a,sca} &= n_p^2 C_{p,sca} G\left(k, R_g, D_f\right) && \text{(b)} \\ C_{a,ext} &= C_{a,abs} + C_{a,sca} && \text{(c)} \end{aligned} \qquad \text{(P.6)}$$

gdzie $C_{p,abs}$ oraz $C_{p,sca}$ są absorpcją i rozproszeniem pojedynczej cząstki, a funkcja $G\left(k, R_g, D_f\right)$ jest dla agregatów fraktalnych wyrażona jako (Dobbins and Megaridis 1991):

$$G\left(k, R_g, D_f\right) = \left(1 + \frac{4}{3D_f} k^2 R_g^2\right)^{-D_f/2}. \qquad \text{(P.7)}$$

W niniejszej pracy przeprowadzono symulacje określające stosowalność teorii RDG-FA dla różnych przypadków przyjmując wyniki uzyskane w symulacjach T-Matrix za źródło odniesienia. Jako przykład uzyskanych wyników, rysunek P.7 przedstawia błąd aproksymacji RDG-FA absorpcji światła względem metody T-Matrix przez agregaty fraktalne $D_f = 1.80$ dla różnej wartości parametru Mie (x_p) i różnej liczby cząstek w agregacie: (a) $n_p = 16$, (b) $n_p = 64$ and (c) $n_p = 256$ monomerów. Parametr Mie i współczynnik załamania światła zmieniają się według następujących zależności $x_p = 0.01 - 1.00$, $\left|\tilde{m}_p - 1\right| = 0.1 - 2.0$ (gdzie $\tilde{m}_p = m_p + ik_p$ oraz $\tilde{m}_p = k_p + 1$).

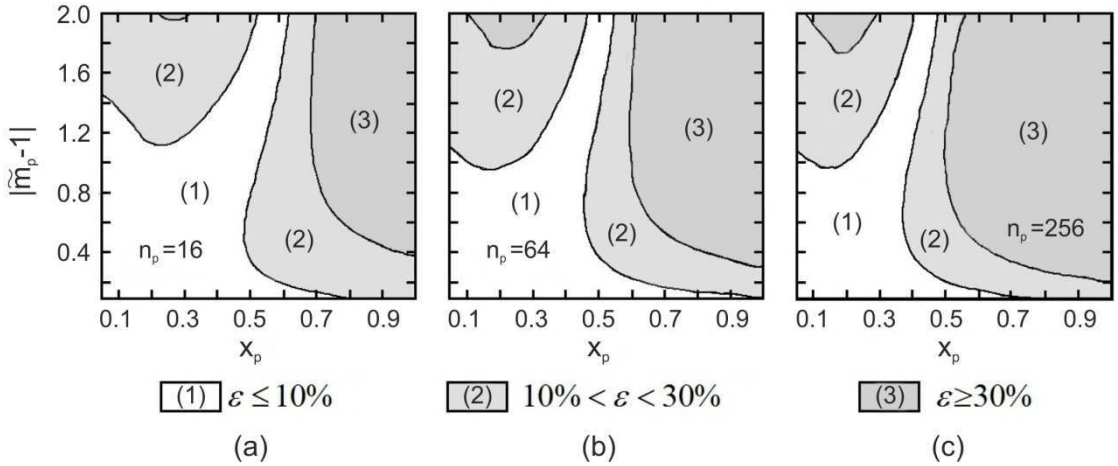

Rysunek P.7. Błąd aproksymacji RDG-FA absorpcji światła względem metody T-Matrix przez agregaty fraktalne $D_f = 1.80$ dla różnej wartości parametru Mie (x_p) i różnej liczby cząstek w agregacie.

Teoria (metoda) T-Matrix

Rozwiązanie T-Matrix wprowadzone przez Watermana (Waterman 1965) do wyznaczenia właściwości światła rozproszonego przez różne cząstki jest również zwane metodą zerowego pola (null-field method). (Mishchenko et al. 1996; Bohren and Huffman 1998, Auger et al. 2007). Teoria T-Matrix polega na bezpośrednim rozwiązaniu równań falowych Maxwella,

dzięki czemu wyniki otrzymane przy jej pomocy są uznawane za dokładne. T-Matrix umożliwia badanie rozproszenia światła zarówno na cząsteczkach o bardzo zróżnicowanym kształcie. Największą zaletą rozwiązania jest niezależność elementów macierzy **T** od padającej i rozproszonej fali świetlnej, a jedynie ich powiązanie z parametrami analizowanych cząstek: kształtem, parametrem Mie, współczynnikiem załamania światła oraz orientacją cząstek w przestrzeni. Pozwala to na wyznaczenie macierzy przejścia **T** jedynie raz dla danego zagadnienia, a następnie wykorzystanie dla dowolnych kątów padania i rozproszenia światła.

W literaturze dostępne są różne kody wykonane w oparciu o algorytm T-Matrix. W niniejszej pracy wykorzystano oprogramowanie napisane w języku Fortran przez Maćkowskiego i Mischenko (Mackowski and Mishchenko 1996) dostępne na stronie internetowej Goddard Institute for Space Studies NASA (Mishchenko et al. 2012). W celu przyspieszenia symulacji kod ten został zrównoleglony z wykorzystaniem protokołu MPI i był wykorzystywany na klastrze obliczeniowym dostępnym w laboratorium IUSTI.

Wykorzystując oprogramowanie T-Matrix można wyznaczyć diagramy rozproszenia, całkowite rozproszenie, absorpcję i ekstynkcję światła, jak również parametry światła rozproszonego przez pojedyncze cząstki wchodzące w skład agregatów. Jako przykład, rysunek P.8 przedstawia ekstynkcję światła dla pojedynczych monomerów w płaszczyźnie przekroju agregatu Buckyball zawierającego $n_p = 252$ monomerów na powierzchni, wypełnionego układem heksagonalnym (całkowita liczba $n_{p,HC} = 509$) o promieniu $r_p = 40.5\ nm$ dla długości fali padającej (a) $\lambda = 300\ nm$, (b) $\lambda = 400\ nm$, (c) $\lambda = 500\ nm$.

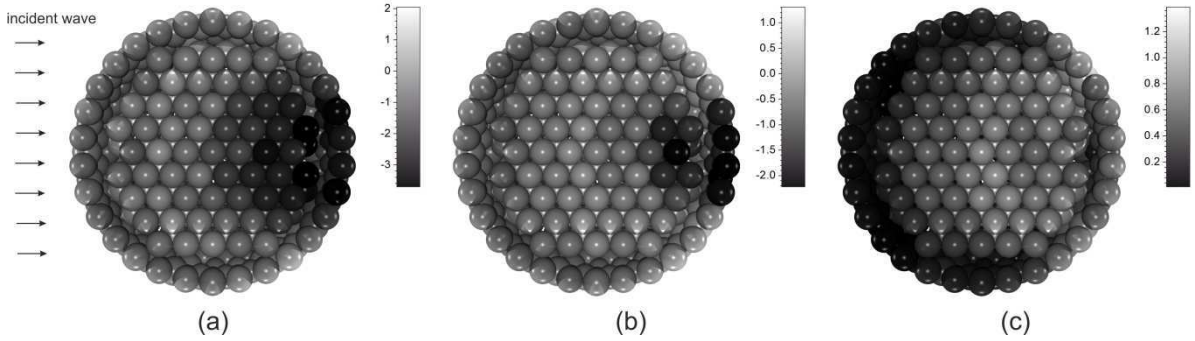

Rysunek P.8. Znormalizowana ekstynkcja pojedynczych monomerów w płaszczyźnie przekroju agregatu Buckyball zawierającego $n_p = 252$ monomerów na powierzchni wypełnionego układem heksagonalnym monomerów (całkowita liczba monomerów $n_{p,HC} = 509$) o promieniu $r_p = 40.5\ nm$ dla długości fali padającej (a) $\lambda = 300\ nm$, (b) $\lambda = 400\ nm$, (c) $\lambda = 500\ nm$; średnica zewnętrzna $d_{ext} = 783\ nm$.

Rozdział 5: Analiza diagramów rozproszenia

Rozdział 5 omawia wykorzystanie diagramów rozproszenia światła w funkcji amplitudy wektora rozproszenia światła q (zwanych w literaturze Optycznymi Współczynnikami Struktury, OSF) do wyznaczenia parametrów agregatów. W pracy wprowadzono dwa

algorytmy umożliwiające wyznaczenie wymiaru fraktalnego D_f w oparciu o nachylenie charakterystyki w obszarze fraktalnym OSF (Mroczka et al. 2012). Promień bezwładności agregatów R_g oszacowano za pomocą algorytmu wykorzystującego tzw. analizę Guiniera.

Pierwszy z opracowanych algorytmów, nazwany SSE (Second Slope Estimation) z uwagi na analizę drugiej części obszaru fraktalnego (dla większych kątów rozproszenia) oparty jest na założeniu podanym przez Sorensena (Sorensen 2001) mówiącym, że spadek natężenia w obszarze fraktalnym OSF równy jest liczbowo wymiarowi fraktalnemu agregatu gdy spełnione jest założenie $qR_g > 5$. Algorytm ten może być zatem stosowany jedynie dla stosunkowo dużych agregatów o dużych wartościach parametru Mie. Jego działanie polega na zastosowaniu regresji liniowej dla punktów OSF spełniających podane kryterium.

Drugi z opracowanych algorytmów, nazwany FSE (First Slope Estimation) z uwagi na analizę pierwszej części obszaru fraktalnego OSF umożliwia pomiary agregatów niezależnie od wartości R_g oraz promienia pojedynczych monomerów r_p. Wymaga on jednak zastosowania bardziej złożonej metody poszukiwania prostej najlepiej dopasowanej do OSF w obszarze fraktalnym oraz krzywych kalibracyjnych łączących oszacowane nachylenie charakterystyki i rzeczywistym wymiarem fraktalnym.

Na rysunku P.9 (a) przedstawiono przykładowe wyniki wyznaczania promienia bezwładności agregatów za pomocą analizy Guiniera. Rysunek P.9 (b) przedstawia wykorzystanie algorytm FSE do automatycznego wyznaczenia wymiaru fraktalnego z zaszumionych OSF. Parametry agregatów: cząsteczki sadzy, $D_f = 1.40 - 2.80$, $n_p = 500$.

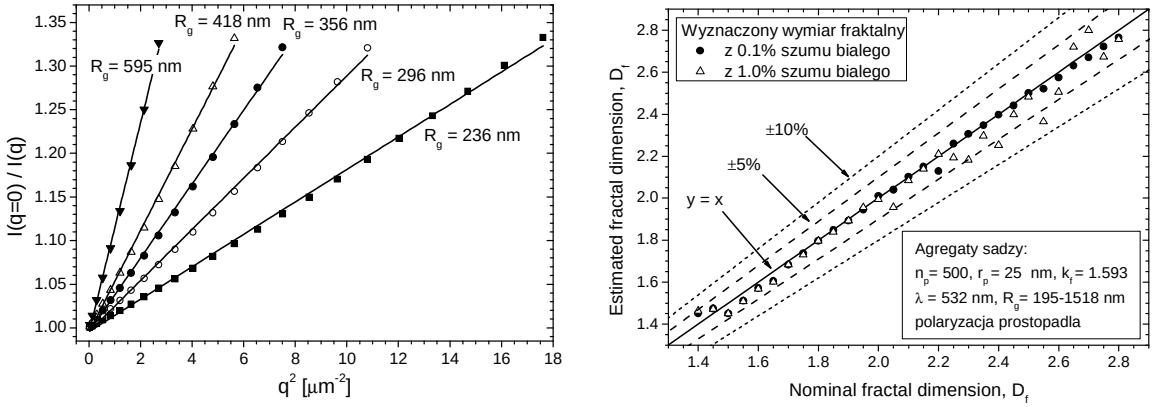

Rysunek P.9. (a) Wyznaczanie promienia bezwładności agregatów za pomocą analizy Guiniera, (b) algorytm FSE z krzywymi kalibracyjnymi: automatycznie wyznaczony wymiar fraktalny z zaszumionych OSF. Parametry: agregaty sadzy o wymiarze fraktalnym 1.40 do 2.80 oraz stałej liczbie 500 monomerów (Mroczka et al. 2012).

W drugiej części niniejszego rozdziału skupiono się na problemie zaniedbywanym w literaturze: wpływie pojedynczych monomerów, które nie uległy agregacji, a znajdują się w układzie pomiarowym na dokładność pomiarów z wykorzystaniem OSF. Przykładowo, stosunek pojedynczych monomerów do monomerów w agregacie sadzy o $n_p = 50$ i $D_f = 1.80$ równy 1:1 powoduje niedoszacowanie wartości wymiaru fraktalnego o ok. 25%.

Rozdział 6: Spektrometria Ekstynkcji Światła (LES)

Z powodów historycznych metoda pomiarowa opisana w tym rozdziale bywa nazywana turbidymetrią. Niemniej jednak jest ona tutaj nazwana Spektrometrią Ekstynkcji Światła (Light Extinction Spectrometry, LES) z uwagi na fundamentalną analogię do powszechnie stosowanej spektrometrii absorpcji światła (Light Absorption Spectrometry). Spektometria absorpcji światła wykorzystuje absorpcję molekularną cząstek, podczas gdy LES ekstynkcję (absorpcję i rozproszenie) światła.

Zasada działania LES polega na analizie całkowitej ekstynkcji (osłabienia) światła po przejściu przez badany układ cząstek oświetlony przez skolimowaną i polichromatyczną wiązkę promieniowania elektromagnetycznego (Onofri et al. 2010b). Dlatego też technika ta wymaga, aby wiązka o natężeniu $I_0(\lambda_i)$ i długościach fali λ_i przebiegała przez chmurę cząsteczek (monomerów, agregatów, itp.) które chcemy analizować. Natężenie promieniowania po przejściu przez ośrodek $I(\lambda_i)$ jest zbierane przez układ optyczny, a następnie analizowane przez spektrometr. Jeżeli zjawisko wielokrotnego odbicia jest pomijalnie małe (np. (Xu 2007)), transmitancja wiązki jest dana równaniem:

$$T(\lambda_i) = \overline{I}(\lambda_i) / I_0(\lambda_i) = \exp(-\tau L) \tag{P.8}$$

gdzie L jest długością drogi optycznej przez chmurę cząstek oraz $\tau = C_n \overline{C}_{p,ext}$ określa turbidymetrię medium. $\overline{C}_{p,ext}$ jest wielkością całkową, która wyraża średnią ekstynkcję cząstek (Onofri et al. 2009) oraz C_n jest koncentracją cząstek. Jeżeli $Q_{p,ext}$ to efektywność ekstynkcji (zwana również współczynnikiem ekstynkcji) pojedynczej cząsteczki sferycznej opisanej przez jej promień d_p i współczynnik załamania światła $\tilde{m}_p$, to mamy:

$$\overline{C}_{p,ext} = \int_{d_{p,\min}}^{d_{p,\max}} Q_{p,ext}\left(d_p, \tilde{m}_p\right) \frac{\pi d_p^2}{4} f(d_p) dd_p. \tag{P.9}$$

Procedura inwersji numerycznej jest najważniejszą częścią techniki LES. Wymaga ona dyskretyzacji równania transmitancji ośrodka (Onofri et al. 2009) oraz minimalizacji różnic pomiędzy transmitancją mierzoną eksperymentalnie i przewidzianą numerycznie. Problem ten może zostać wyrażony matematycznie przez równanie (P.9), zwane w literaturze równaniem całkowym Fredholma pierwszego rodzaju (Hansen 1994).

Jeżeli zmierzona transmitancja przedstawiona zostanie w postaci dyskretnej jako wektor $\overline{\mathbf{T}}$, którego elementy $\overline{T}_i$ odpowiadają transmitancji wiązki dla długości fali świetlnej λ_i, a objętościowy rozkład wielkości cząstek wyrazimy jako $\mathbf{V}$; to aby znaleźć $\mathbf{V}$, musi zostać rozwiązane następujące liniowe równanie algebraiczne: $\overline{\mathbf{T}} = \mathbf{SV}$, w którym $\mathbf{S}$ jest wyznaczoną numerycznie macierzą ekstynkcji. Rozwiązanie omawianego problem odwrotnego sprowadza się do minimalizacji następującej wielkości:

$$\underset{V>0}{Min} \left\| \left(\mathbf{S}^{\mathbf{T}}\mathbf{S} + \gamma\mathbf{H}\right)\mathbf{V} - \mathbf{S}^{\mathbf{T}}\overline{\mathbf{T}} \right\|_{2-LSQ}^2, \tag{P.10}$$

które może zostać znalezione z wykorzystaniem różnych narzędzi numerycznych, w szczególności środowiska MATLAB.

Wyniki symulacyjne

Przeprowadzone w pracy badania symulacyjne dotyczyły określenia wpływu wymiaru fraktalnego, promienia bezwładności oraz współczynnika załamania światła badanych agregatów na zmiany widma absorpcji, ekstynkcji i rozproszenia światła, jak również transmitancje ośrodka. Uzyskane wyniki pokazują, że LES nie jest bardzo wrażliwa na zmiany wymiaru fraktalnego, lecz jedynie na całkowitą wielkość agregatów.

LES może być wykorzystywana przy koncentracji cząstek w zakresie $1\times10^{13}-5\times10^{15}$ oraz objętości $5\times10^{-8}-5\times10^{-6}$ (parametry oszacowane dla agregatów dwutlenku krzemu oraz długości komory pomiarowej 1 m).

Wyniki eksperymentalne

Badania eksperymentalne techniką LES przedstawione w niniejszej pracy zostały wykonane dla agregatów Buckyballs dwutlenku krzemu oraz wolframu, jak również dla agregatów nanocząstek w zanieczyszczonej plazmie.

Pierwszą grupą cząstek analizowaną w niniejszej pracy były tzw. agregaty Buckyballs. Są one wytwarzane za pomocą rozpylania i osuszania mikrokropelek zawierających roztwory koloidalne krzemionki o różnym stężeniu i różnej wielkości pojedynczych monomerów, ($r_p = 15.7\ nm$, $r_p = 33.6\ nm$ oraz $r_p = 40.5\ nm$. Rysunek P.10 przedstawia porównanie analizy LES i TEM (tj. przeprowadzonej w oparciu o zdjęcia z mikroskopii transmisyjnej) (Barbosa et al. 2012). Jak można zauważyć wyniki LES w znacznym stopniu pokrywają się z pomiarami TEM.

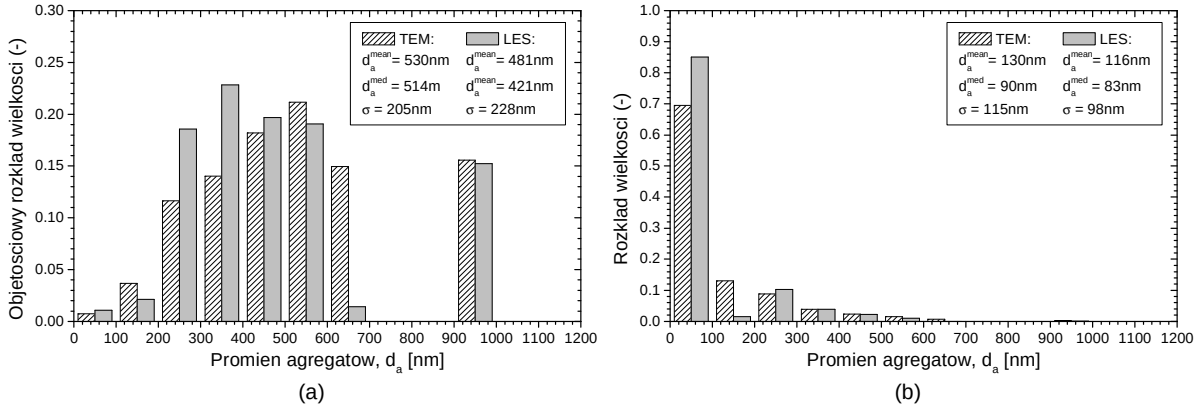

Rysunek P.10. Porównanie analizy TEM i LES aerozolu zawierającego agregaty nanocząstek dwutlenku krzemu: (a) objętościowy rozkład wielkości oraz (b) liczbowy rozkład wielkości.

Drugą grupą cząstek analizowaną w niniejszej pracy były agregaty wolframu. Badania miały na celu sprawdzenie wpływu bliskość przeszkód na pomiary LES, jak również na jej zdolności do analizy wielkości cząstek w plazmie, w szczególności w reaktorze ITER. Badane agregaty został wygenerowane z wykorzystaniem wodno-alkoholowego roztworu sferycznych nanocząstek wolframu. W układzie pomiarowym dodatkowo zainstalowano poprzeczną płytkę metalową mającą na celu sprawdzenie wpływu sąsiedztwa przeszkody

(wall proximity) na pomiary LES. Dodatkowo, w celu weryfikacji wpływu fali uderzeniowej oraz emisji szerokopasmowej generowanej przez metodę czyszczenia laserem użyto impulsowego lasera ($5\,ns$, $25\,Hz$) o wysokiej mocy (Nd:YAG, $110\,mJ$, $\lambda = 532\,nm$) do generowania plazmy (Onofri et al. 2011a; Onofri et al. 2012b).

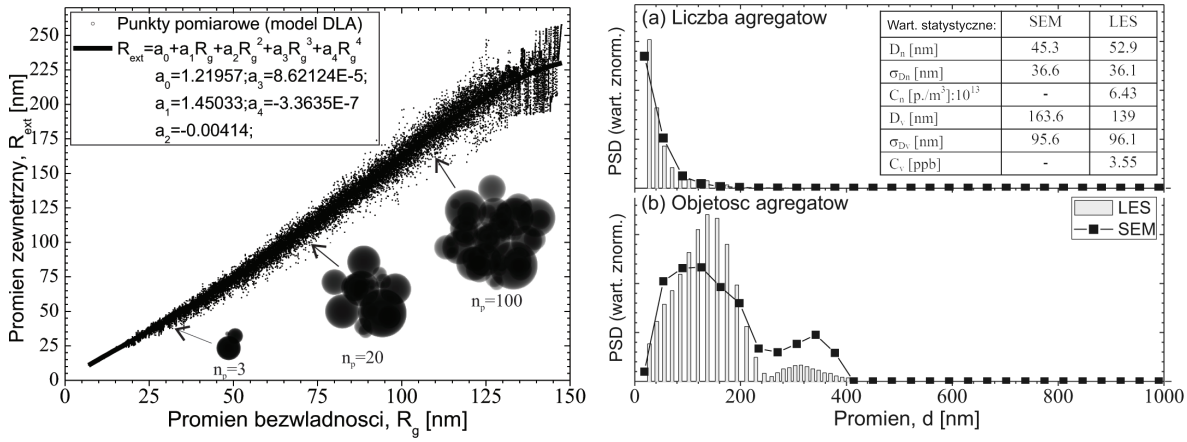

Rysunek P.11. Przykładowa krzywa kalibracyjna oraz porównanie rozkładów wielkości agregatów wyznaczonych z wykorzystaniem techniki SEM I LES.

Na podstawie przeprowadzonych pomiarów stwierdzono, że technika LES działa bardzo efektywnie w sąsiedztwie przeszkód (nawet w przypadku blokowania lub dyfrakcji ok. 80% energii wiązki pomiarowej) oraz, że jest odporna na efekty związane z emisją plazmy. Podczas pomiarów należy jedynie zwrócić uwagę na widmo lasera, które musi zostać usunięte z całkowitego widma analizowanego przez spektrometr przed wykonaniem inwersji. Rysunek P.11 przedstawia dwa typowe wyniki pomiarów: (a) numerycznie wygenerowane obrazy SEM agregatów odpowiadających tym na stanowisku pomiarowym, oraz (b) porównanie rozkładów wielkości agregatów uzyskanych za pomocą analizy LES i SEM.

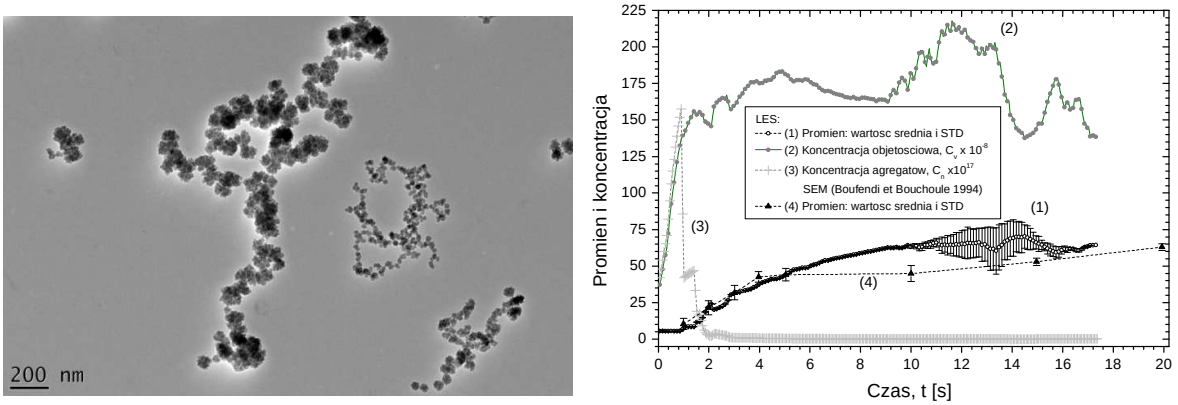

Rysunek P.12. LES: zmiana rozmiaru cząstek oraz ich koncentracji podczas niskociśnieniowego wyładowania argonowo-silanowego.

Trzecią grupą agregatów analizowaną w niniejszej pracy były cząsteczki ulegające agregacji w zanieczyszczonej plazmie. Rysunek P.12 (a) przedstawia zdjęcie TEM przykładowych agregatów powstających podczas niskociśnieniowego wyładowania w plazmie argonowo-

silanowej. Na rysunku przedstawiono również zmiany koncentracji oraz rozkładu wielkości agregatów w funkcji czasu. Analizując uzyskane wyniki stwierdzono dużą zgodność pomiędzy pomiarami TEM i LES. Ponadto wykazano, że niniejsza technika pomiarowa jest bardzo czuła na niedokładność określenia współczynnika załamania światła analizowanych agregatów (Onofri et al. 2011b).

Rozdział 7: Podsumowanie i wnioski

W niniejszej pracy przedstawiono różne rozwiązania mające na celu analizę rozkładu wielkości oraz stężenia agregatów nanocząstek z wykorzystaniem technik rozproszenia światła. Do opisu morfologii agregatów wykorzystano model fraktalny oraz tzw. model Buckyballs. Ponadto w celu pomiarów referencyjnych opracowano algorytmy i modele umożliwiające dokładną analizę agregatów w oparciu o zdjęcia TEM.

Dodatkowo, opracowano algorytmy umożliwiające analizę diagramów rozproszenia w funkcji amplitudy wektora rozproszenia q. Przeprowadzono również symulacje mające na celu określenie wpływu pojedynczych monomerów, które nie uległy agregacji, a znajdują się w układzie pomiarowym na dokładność uzyskiwanych wyników.

Opracowana została technika pomiarowa LES. Polega ona na analizie całkowitej ekstynkcji światła po przejściu przez badany układ cząstek oświetlony polichromatyczną wiązkę promieniowania elektromagnetycznego. Walidacja eksperymentalna została przeprowadzona dla różnych aerozoli zawierających agregaty krzemionki i wolframu oraz dla cząstek ulegających agregacji w zanieczyszczonej plazmie.

Perspektywy dalszego rozwoju przeprowadzonych badań zakładają udoskonalenie metod inwersji zastosowanych w technice LES, w szczególności aplikację różnych metod regularyzacji odwracanych numerycznie macierzy (Hansen 1994). Ponadto planuje się wykorzystanie Dyskretnej Aproksymacji Dipolowej (Discrete Dipole Approximation, DDA) do wyznaczenia charakterystyk światła rozproszonego przez agregaty nanocząstek.

Słowa kluczowe:

nanocząsteczki, agregaty fraktalne, multifraktalne, rozproszenie światła, diagramy rozproszenia, ekstynkcja, Spektrometria Ekstynkcji Światła, LES, T-Matrix, problem odwrotny, TEM, aerozol, roztwór koloidalny, plazma, ITER.

SHORT ABSTRACT AND KEYWORDS

This Ph.D. work provides and evaluates various solutions to characterize, with optical/electromagnetic methods nanoparticles and aggregates of nanoparticles found in suspensions, aerosols and dusty plasmas. Two main models are introduced to describe the morphology of particle aggregates with fractal-like (for particles in plasmas and combustion systems) and Buckyballs-like (aerosols, suspensions) shapes. In addition, the author proposes various solutions and methods (T-Matrix, Rayleigh type approximations) to calculate the scattering diagrams (optical structure factors) of fractal aggregates as well as algorithms to inverse extinction spectra. As a reference case for the performed analysis, several tools to describe the morphology of fractal aggregates from electron microscopy images have been also developed. The experimental validation carried out with the Light Extinction Spectrometry (LES) technique (for nano silica beads, tungsten, dusty plasma and silicon aggregates) clearly proves the validity of the algorithms developed as well as the potential of the LES technique.

Keywords:

nanoparticles, fractal aggregates, multifractals, buckyballs, light scattering, scattering diagrams, extinction, Light Extinction Spectrometry, LES, T-Matrix, inverse problem, TEM, aerosols, colloidal suspensions, dusty plasma, ITER